Synthesis and structural exploration of 4-amino-3,5-bis(pyridin-2-yl)-1,2,4-triazole based ligands and their transition metal complexes.

Jake Ridley Connor Musselle-Sexton

A thesis submitted in partial fulfilment of the requirements for the award of

Doctor of Philosophy

School of Natural & Environmental Sciences

(Chemistry)

Newcastle University

Supervisors Dr Michael Probert and Dr Jon Sellars

Abstract

This thesis focuses on the synthesis and modification of substituted 1,2,4-triazole systems, along with structural investigations of their complexation to metal ion species.

To begin, a high-pressure study was conducted on polymorph *D* of the literature system $[Fe(abpt)_2(NCS)_2]$ (abpt = 4-amino-3,5-bis(pyridin-2-yl)-1,2,4-triazole). Crystals of this form display a phenomenon known as spin crossover, in which the spin state of the metal ions can switch upon exposure to external stimuli. In the case of polymorph *D*, where two crystallographically independent metal centres exist in the high spin state under ambient conditions, thermal switching of only one of the metal centres has previously been shown. Nevertheless, this work expands upon prior publications and demonstrates that, using high pressure as the external stimulus, it is possible to access the phase space in which both metal centres are switched to the low spin state.

To expand on the exploration of this interesting phenomenon and using the knowledge of the accessibility of variable spin states for 'abpt' based complexes, thirteen new substituted 1,2,4-triazoles were prepared. The preparation of these novel systems was approached using a synthetic route with a common backbone, requiring only minor modifications, to produce the desired product. This work was conducted alongside the preparation of eight known literature compounds.

The resultant 1,2,4-triazoles were coordinated to various metal salts and crystallised to enable interrogation of their solid-state structures. The analyses of any resultant crystals were performed through the use of single crystal X-ray diffraction, allowing detailed investigation of even subtle structural properties, particularly those that are known to be connected to the spin crossover phenomenon.

Five new organometallic systems were discovered which demonstrated interesting structural properties, including spin crossover, solvent mediated spin crossover and unexpected migration characteristics. Additionally, many other metal complexes produced during this research were structurally characterised with these systems exposed to the same level of structural interrogation. This has built a body of work leading to a greater understanding of the driving forces involved in the generation of exotic materials that have useful characteristics.

Acknowledgements

I would like to thank both Dr Michael Probert and Dr Jon Sellars for their continued support throughout my time at Newcastle and giving me the opportunity to undertake this project. Thank you for answering all my questions no matter how small and ridiculous they may have been and helping me grow as a scientist.

To my parents, Simon and Tonia who helped support me throughout all of my studies and putting up with me during my time studying. They have given me the platform to chase my goals and try to better myself both academically and as a person.

Thanks to Dr Paul Waddell for being the days when it was just us in the office and allowing me to chat absolute nonsense all the time without judging me too harshly and your help with everything crystallography related.

Thanks to Liam Mistry, Ollie Glenister, Natalie Johnson, Charlie McMonagle, Andrew Tyler, Lucy Hunter, Amhed Aljohani, Lok Ho, Jake Weatherston and Tom Smith who have provided so much friendship and entertainment over the years.

Lastly, I would like to show my gratefulness to Alexandra Longcake for her support in all things which helped me become a better person, putting up with me moping about during the COVID-19 lockdowns.

Declaration

The work described in this thesis was carried out by Jake R.C. Musselle-Sexton at Newcastle University under the supervision of Dr M.R. Probert and Dr J.D. Sellars, except where acknowledged by reference to other sources. It has not been submitted in whole or in part, for any other degree.

Contents

List of Figures

List of Tables

List of Schemes

Chapter 1 Introduction

The development of novel functional materials for new technologies *e.g.* those possessing unique and useful physical properties, is a large and vibrant field of research.[1] There is an increasing demand for electronics worldwide, a situation that is forcing the need for new materials that demonstrate increased efficiency and have lower environmental impact. Some of these functional materials possess the ability to display switchable states, one category of these materials are known as spin crossover (SCO) systems. These materials, due to their fundamental physical characteristics, have the potential to be used in many areas of modern technological development such as to create new display devices, sensors and applications in novel data storage with the potential capability of competing with the increasing amount of data being generated in both the private and commercial sector.[1]

Spin crossover compounds have the capability to switch spin states, at a molecular level, under external stimuli.[2] These changes in spin states can have a large impact on the physical characteristics of the material, such as the metal ion to ligand bond lengths and distortions of the octahedral structure. Under stimuli such as temperature[2], light irradiation[3–5] and pressure[6,7] the metal centres within SCO compounds can transition between high spin and low spin configurations (see section 1.2). These systems possess a wide variety of properties, and the transitions can be reversible and often contain a thermal hysteresis. This is where the system displays different behaviour when cooling and heating through the transition, resulting in the temperature that the transition occurs being different. These properties can lead to a bistability that has been proposed to be of use as the mechanism for data storage and display devices for three decades, increasing the interest in these compounds.[8] Ideally these systems would display spin state transitions with a large thermal hysteresis centred near room temperature and be fully reversible, allowing for these properties to be exploited in potential uses in new technologies (see section 1.4).

The discovery of the SCO phenomenon originates in the 1930s when Cambi *et al.* noticed unusual magnetic behaviour in the form of changing of spin states with a

variation of temperature in dithiocarbamato iron(III) complexes.[9] However, it was not until the 1960s that the first examples of iron(II) and cobalt(II) complexes were demonstrated to exhibit thermally induced transitions and, before this, only iron(III) systems had been reported.[2] The discovery of these new complexes, along the realisation that this was an exploitable field, increased the interest in this area of solid state structural science.[2]

The field has seen large, continued, growth since the 1960s, with new discoveries such as the first two-stepped transition reported in an iron(III) complex in 1981 driving further interest.[10] Pressure induced transitions were discovered in an iron(III) complex in 1963,[11] whereas, light induced transitions were not realised until 1984.[3] The field has expanded since then to utilise many new techniques in the synthesis and analysis of SCO complexes.

Historically, magnetic techniques have been one of the primary tools used to analyse the bulk properties of potential SCO systems. However, the physical properties can be studied using various techniques that enable the investigation of structural changes that are coupled to the phenomenon. One set of demonstrative structural change that can be monitored are the large changes in the bond lengths and volumes of the molecular entities as well as the macroscopic effects on the crystal. Single crystal X-ray diffraction (SC-XRD) has become a prominent method applied to analyse these compounds due to the accuracy and precision of structural investigation enabled by the technique.

The design of different SCO systems has been approached from many directions as interest in the field has increased. Variations in the metal centres (Fe(II/III) Co(II/III)) and the ligands used to complete the coordination spheres around them are a subset that continue to be investigated.[12–14] Much of the focus of these studies is adapting the principal ligands, and their binding motifs, in attempts to tune the energy of the octahedral splitting (Δ_o) (see section 1.1). Indeed, this method has become a mechanism to investigate the properties of the ligands that are required to enable the synthesis of new, more useful, SCO systems. Archetypal ligands such as 1,10-phenanthroline[15] and 2,6-di(pyrazol-3-yl)pyridine[16] (figure 1.1), have offered the most

commonly explored ligand backbone for these investigations. This concentration of studies around ligands based on a small number of molecular backbones has left a large array of compounds relatively unexplored. In turn this yields a large number of modifications, and design routes, possible that are yet to be explored.

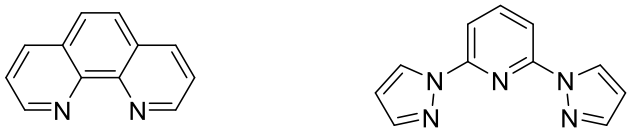

1 2

Figure 1.1. Molecular representation of ligands 1) 1,10-phenanthroline and 2) 2,6-di(pyrazol-3-yl)pyridine

Synthesising new compounds based on the principles from ligand field theory (LFT) and crystal field theory (CFT), provides a concrete basis for the foundations of any new study. These simple theories can be used to explain the interactions between the coordinating ligands and the various metal ion centres. The strength of the interactions is known to fundamentally impact the energies correlated to Δ_o and offer a mechanism to carefully tune this parameter.

The work described herein will focus on the synthesis of novel 1,2,4-triazole based ligands and their coordination with various metal salts in chapters 4 – 7. These chapters will discuss some of the unique organometallic complexes that have been successfully generated along with some of their interesting structural features and properties. Furthermore, a discussion of other complexes synthesised during this work, in attempts to generate new SCO systems will follow. Finally, a summary and outlook will be given for potential directions to follow of from these studies, that should offer the most relevant avenues for continued research in the area.

1.1 Ligand Field Theory

Ligand field theory constitutes a simple basis for understanding the structure and interactions between ligand and metal centres based upon the interactions of atomic and molecular orbitals in metal organic complexes. LFT stems from molecular orbital (MO) theory when applied to transition metals and can be used to understand the various dynamics of these systems such as bonding, reactivity and structural features/properties.

In the case of perfectly octahedral coordination complexes containing d^4-d^7 metal ions, a transition metal ion has five *d* orbitals. These orbitals are degenerate in energy, for the discrete metal ions, until the approach of ligands. The interactions between the metal and the ligand orbitals cause the degeneracy to be lost. The result is that the orbitals split into two sets, one higher in energy and one lower, known as the t_{2g} set (largely non-bonding) and e_g set (anti-bonding) respectively, as displayed in figure 1.2.

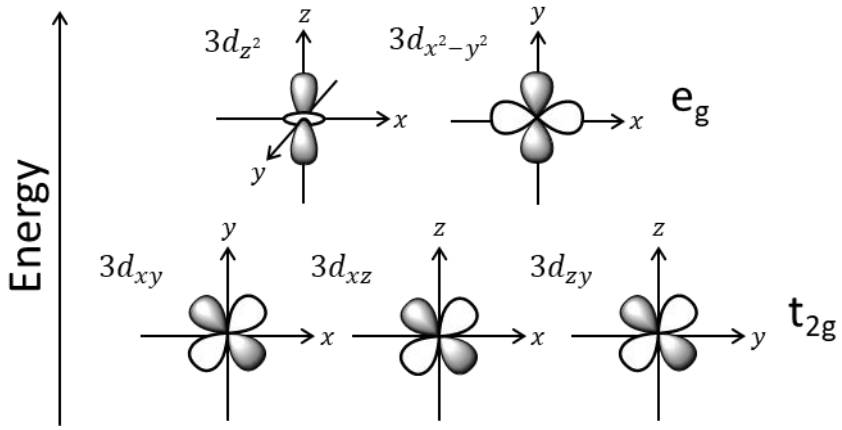

Figure 1.2. The representation of the five *d*-orbitals split into e_g and t_{2g} sets, of a transition metal in a Cartesian coordinate system.

The *d*-orbitals, designated d_z^2 and d_x^2-$_y^2$ as shown in figure 1.2, belong to the e_g set. These orbitals are oriented along the vectors towards ligands and will raise in energy relative to the barycentre, the energy of the metal d-orbitals in the isolated ion and upon ligand approach due to electron-electron repulsion. The remaining *d*-orbitals the d_{xy}, d_{xz} and d_{zy} in the t_{2g} set, are oriented with lobes between the axis of ligand approach. This results in the ligands coordinating to the metal, having direct access to the charged centre and they do not suffer from the same repulsion effects as the e_g set. This results in a lowering of the energy with respect to the barycentre.

The energy gap between the t_{2g} and e_g sets is defined as crystal field splitting parameter (Δ_o) or ligand field strength. The size of Δ_o when compared to electron pairing energy (*P*) will determine if a system exists in high spin or low spin state. In the case of a large Δ_o and small total pairing energy term, the system will exist in the low spin (LS) state. If Δ_o is small and the total *P* term is large then the result will be a system in the high spin (HS) state.

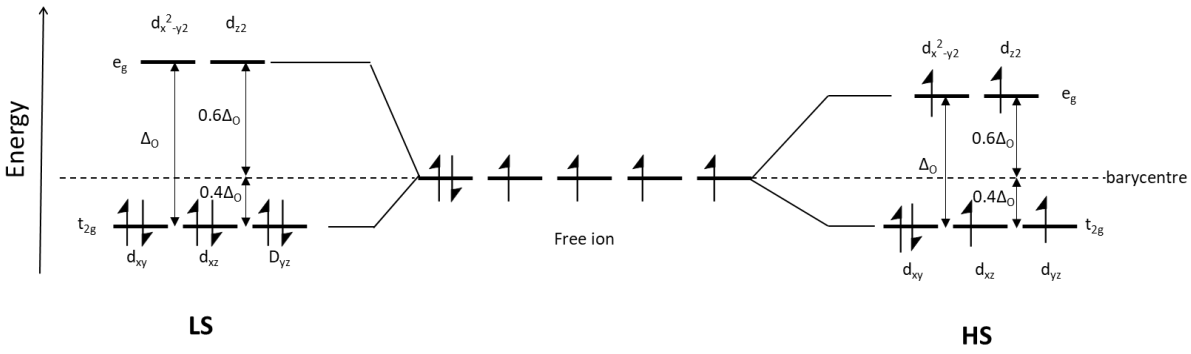

Figure 1.3. Effect of ligand field strength on Δ_o and spin state configurations for high spin and low spin for a d^6 metal ion.

For systems where the metal ion and oxidation state remain the same, the strength of the coordinating ligands interactions with the metal centre will determine the size of Δ_o. One example that demonstrates the importance of these interactions can be shown through the two Fe(II) complexes, $[Fe(H_2O)_6]^{2+}$ and $[Fe(CN)_6]^{4-}$. The first of these exists in the HS state, whereas the latter is found to occupy a LS state. These highlight examples of a weak field strength ligand (H_2O) and strong field strength ligand (CN^-).[17] Classical ligands have been analysed and placed into an order known as the spectrochemical series. This shows the order of the respective ligand field strengths from weakest to strongest derived from classical measurements of magnetic behaviour.

$I^- < Br^- < S^{2-} < SCN^- < Cl^- < N_3^- < F^- < NCO^- < OH^- < C_2O_4^{2-} < O^{2-} < H_2O <$ $acac^- < NCS^- < CH_3CN <$ gly < py < NH_3 < en < bipy < phen < NO_2^- < PPh_3 < CN^- < CO

Weak field ligands are more likely to form HS complexes where electrons are unpaired due to the dominance of the *P* with respect to the Δ_o term, whereas strong field ligands form LS complexes due to the opposite effect. The ligands in the spectrochemical series contain different donor and acceptor properties in the form of *σ*-donors or π-donors/acceptors. A *σ* bond is formed by the overlap between metal and ligand orbitals in an end-to-end fashion, whereas π bonds occur when this overlap is side-by-side.

The overlap between metal and ligand ligands has different effects depending on the acceptor/donating nature of the ligand. In the case of π-acceptors ligands, metals donate electrons to the ligand orbitals. Conversely, π-donor ligands have electrons present in their orbitals, this allows donation of electron density to the metal centre. π-Donor ligands cause a decrease in Δ_o due to the energy of the orbitals being lower than the metal *d* orbitals, causing the overlap between the ligand π orbitals and metal t_{2g} orbitals to be lower in energy than the ligand orbitals. π-Acceptors that have empty *d*-orbitals will increase the magnitude of Δ_o, due to the energy of these orbitals being greater than the metal d orbitals. The changes made to the interactions between orbitals can be reflected in the physical structure and, therefore, the properties for a given metal complex.

MO theory can be used to explain various structural properties observed in metal complexes. The first of these is the metal – ligand distance to the bound atoms. The bond lengths increase with increasing occupancy of the anti-bonding e_g orbitals.[17] This effect can most clearly be demonstrated in the octahedral Fe(II) metal centred complexes that have a nitrogen based coordination sphere. These systems have characteristic Fe – N bond lengths depending on the spin state of the metal ion centre. The bond lengths change by ~10% from ~2.0 Å in the low spin cases to ~2.2 Å in high spin cases. Furthermore, the impact of spin state changes on the metal centre can be studied through the accompanied variation in the octahedron volume, associated to the bond length changes. This distortion of the octahedral volume is in the order of~10 $Å^3$ for low spin to ~13 $Å^3$ for high spin.[18]

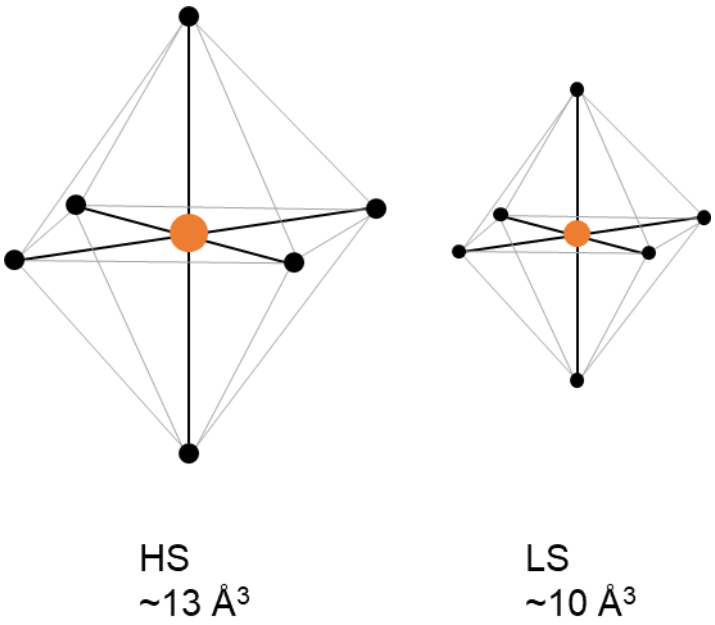

Figure 1.4. Representation of the relative sizes of the octahedron volume for a first-row transition metal ions in the HS and LS states.

Systems where the magnitude of the energies for the *P* and Δ_o terms are similar have both of the HS and LS states accessible. These cases are often the most interesting as the conversion between one spin state and the other can usually be triggered by an external stimulus such as temperature, pressure or light irradiation.[2] These principles allow for the design of new metal complexes with targeted properties, with the synthesis of new ligands designed to tune Δ_o to allow conversion between spin states to potentially create new materials with desired properties.

1.2 Spin Crossover

One outdated hypothesis proposed around the mechanisms involved in accessing different spin states of a metal ions was that it was only possible through changing the coordinating ligands based on their ligand field strength.[19] However, the study by L. Cambi and L. Szego in the 1930's highlighted that differences in the magnetic susceptibility measurements were observable purely through changes in the temperature, leaving the chemical entity unchanged.[2] This phenomenon is now known as spin crossover in that the populations of orbitals around the metal centre in a complex can be switched *via* external stimuli such as temperature, pressure and light [2,4,20,21], thus allowing alteration of the electronic spin state of the system. There are a

multitude of stimuli that have now been observed to induce spin state swapping in these types of material. Many of these methods are displayed in figure 1.5, along with the primary references relating to the method's discovery.

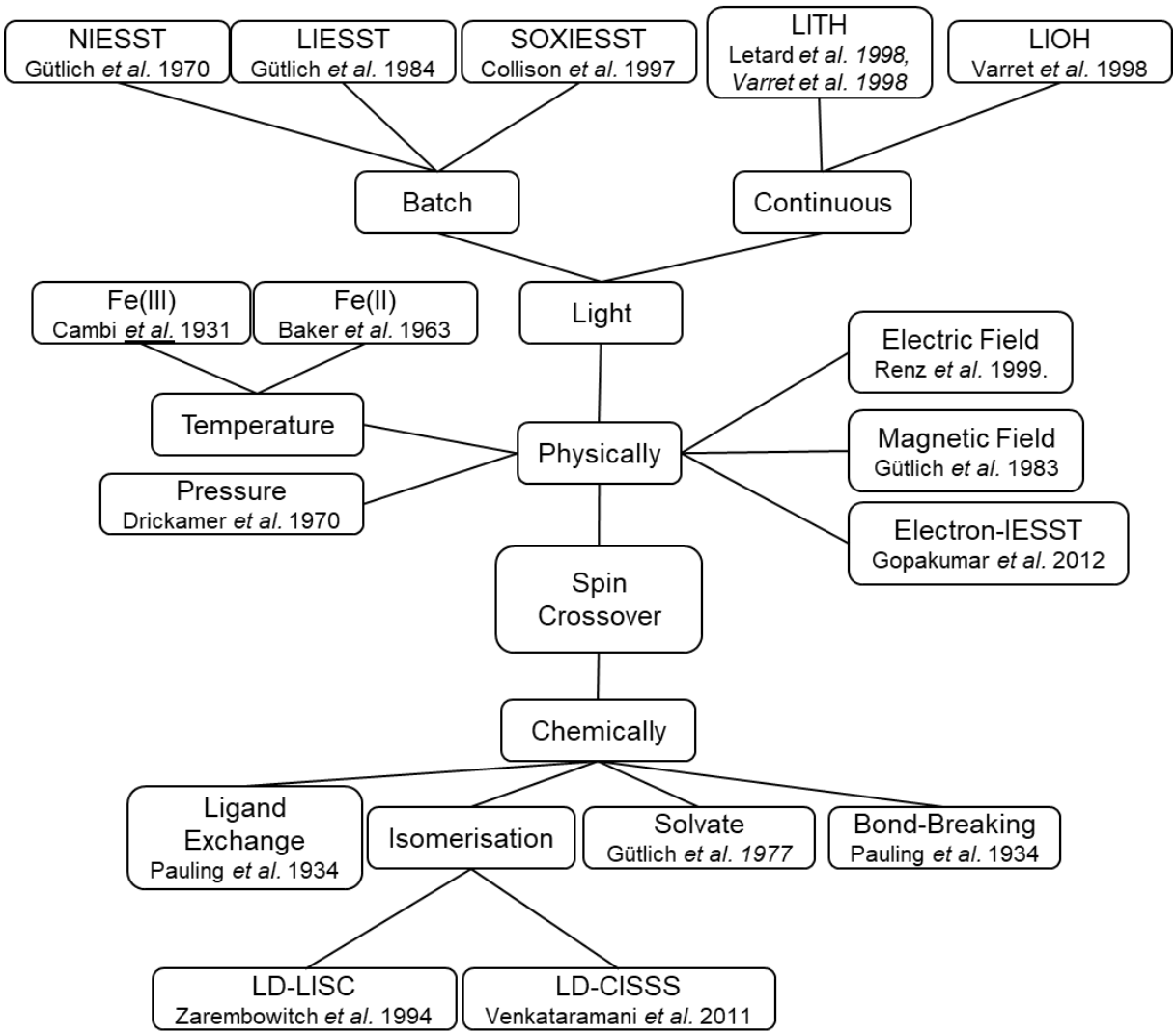

Figure 1.5. Various methods and stimuli capable of inducing spin crossover, (image based upon Renz *et al.*[22]). Cambi *et al.*[9], Baker *et al.*[15], Gütlich *et al.*[3,23–25], Collison *et al.*[26] Letard *et al.*[27], Varret *et al.*[28] Renz *et al.*[29], Gopakumar *et al.*[30], Pauling *et al.*[31], Zarmembowitch *et al.*[32], Venkataramani *et al.*[33]

Since the discovery of the SCO phenomenon, the field has grown from a few cases observed in Fe(III) to a broad field of research, encompassing many metals and select oxidation states. Currently, $3d^6$ Fe(II) based systems dominate the research landscape with the largest number of published examples. This is due to the relative size of the energy gap between *P* and Δ_o compared to other metal ions and oxidation states. The most commonly exploited coordination environment in Fe(II) SCO systems consists of

6 nitrogen atoms in an approximately octahedral geometry. These nitrogen atoms are generally supplied from coordinated ligands in the form of heterocyclic rings and N-thiocyanato groups.[34] Other examples of metal ions that can display SCO include Mn(II), Mn(III), Co(II) and Co(III) with the latter also being of a $3d^6$ configuration. However, Co(III) octahedral metal complexes tend towards LS state arrangements.[35]
A summary of the majority of spin crossover systems observed in first-row transition metals is displayed in in table 1.1. There are cases of second row transition metal SCO although these are significantly rarer due to the lower spin pairing energy and the stronger field ligands.[35] This is quantifiable for metal ions in the same group and oxidation state with identical ligand coordination spheres. The ligand field strength increases by ~50% between 3d and 4d, with little variation in P. This results in the general observation of LS states being favourable for 4d complexes and this trend is seen to continue into the 5d elements.[2]

Table 1.1. Electronic configurations for both HS and LS states for first row octahedral d^4-d^7 transition metal ions.

Configuration	LS	HS	Metal ion
$3d^4$	S = 1	S = 2	Cr(II), Mn(III)
$3d^5$	S = ½	S = 5/2	Mn(II), Fe(III)
$3d^6$	S = 0	S = 2	Fe(II), Co(III)
$3d^7$	S = ½	S = 3/2	Co(II)

Increasing the oxidation state of the metal ion in an octahedral complex while retaining all other properties increases the ligand field strength, with a 40% increase between Fe(II) and Fe(III) complexes.[2]

1.2.1 Thermal Spin Crossover

The most commonly observed form of SCO for the systems under consideration, and studied to date, are thermal transitions, inducing a change from high spin to low spin as the temperature is reduced. One important parameter that has become prevalent in the field is that of $T_{½}$. This is defined as the temperature that the ratio of the high spin state population is equal to the ratio of the low spin state population. This value of $T_{½}$

is then used as a reference point in SCO systems that are undergoing a thermal transition. In the simplest example of SCO behaviour, that of a single step transition, the $T_{½}$ value can be used to quantify the transition.

In order for the spin crossover phenomenon to be observable, the difference in zero-point energy between the two states ($\Delta E^0_{HL} = E^0_{HS} – E^0_{LS}$) must be within range of the thermally accessible energies (k_BT) ($\Delta E^0_{HL} = \Delta E^0_{HS} - \Delta E^0_{LS} \approx k_BT$). This is displayed schematically in figure 1.6.[17,19] If this criterion is met, all complexes would occupy a LS state at low temperatures and at higher temperatures they would be in a HS state.

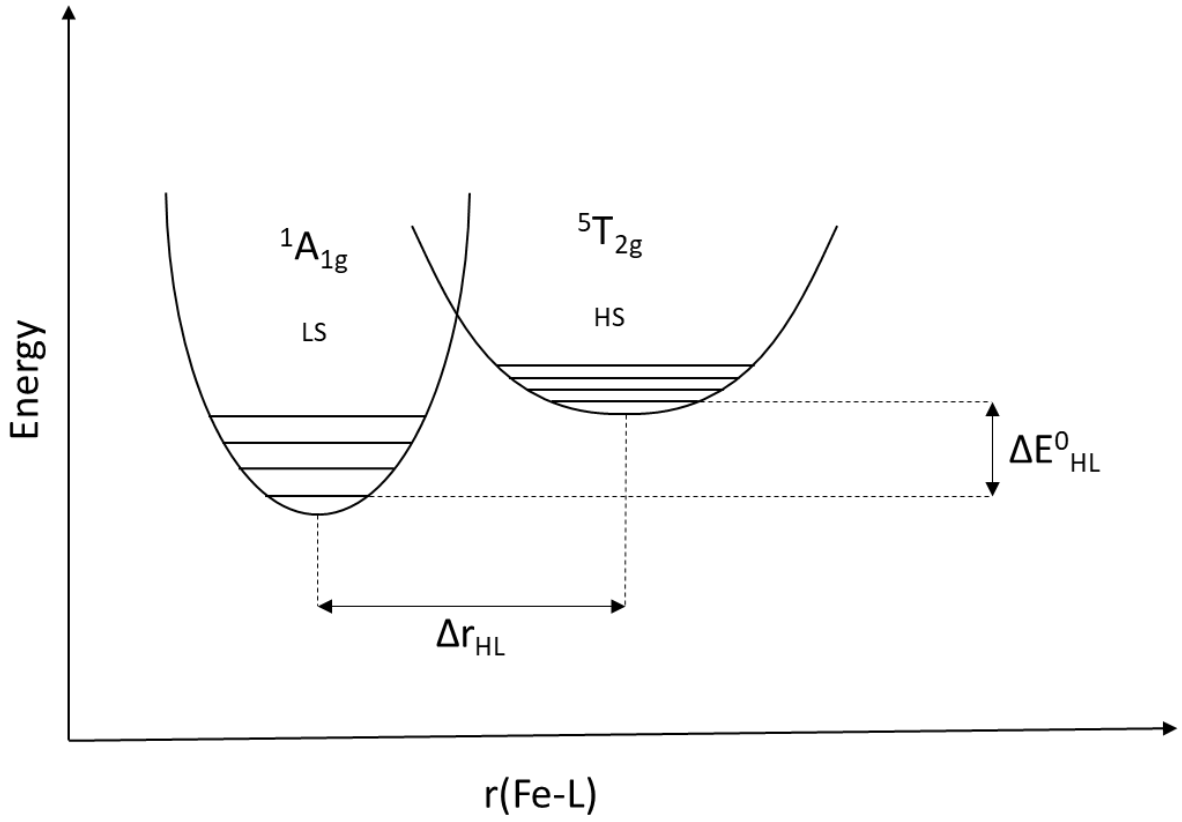

Figure 1.6. Potential wells for the HS ($^5T_{2g}$) and LS ($^1A_{1g}$) states in a octahedral iron(II) spin crossover system related to Fe-L stretching vibration.[17]

Thermal transitions can be split into subclasses based upon their behaviour. Whist $T_{½}$ can be used to denote where SCO occurs in the case of a simple single stepped transition, this is not the case in general. Systems that display increasingly complex SCO behaviour require further information to fully describe the transition(s). Examples of various types of spin transition curves are displayed in figure 1.7: these diagrams represent plots of the high spin fraction of a complex vs the temperature of the

observation. The behaviour of various systems is affected by multiple sources however it is proposed that the degree of cooperativity between the metal centres in the solid state plays a significant role in determining the type of transition and if it is globally accessible.[10] The degree of cooperativity known as “Elasticity theory” and it was developed in 1989 by Spiering and Willenbacher.[36] The theory explains that, due to the large change in bond lengths that occur on switching between high spin and low spin states, it leads to defects within the crystal structure. In turn these defects create an “internal pressure” and this leads other SCO molecules to “feel” this pressure induced by change in spin state of one or more centres, enabling a propagation throughout the crystal. The simplest forms of thermal spin crossover are shown in figure 1.7.

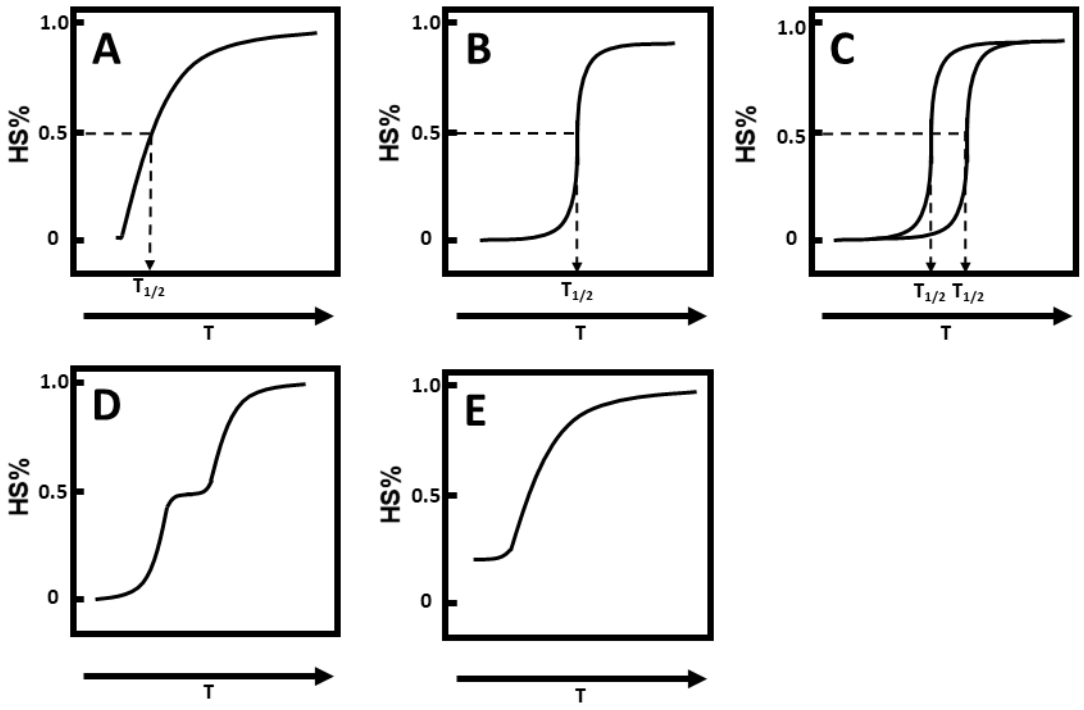

Figure 1.7. Spin transition curves observed in SCO systems. A: gradual, b: abrupt, C: Hysteresis, D: multistep and E: incomplete (ref)

Single step transitions can appear as gradual transitions where there is a lack of, or severely reduced cooperativity between metal centres. This leads to a transition that can occur over tens to hundreds of Kelvin. If the cooperation between metal centres is increased, the rate of the propagation of the transition can also be increased and this

leads to a more abrupt SCO. In cases where systems display abrupt spin transitions, a hysteresis in the temperature of the transition can often also be observed. A hysteresis in the spin transition is where the change in spin state from HS to LS and the return from LS to HS occur at different temperatures, *i.e.* hysteresis occurs when there is a difference in $T_{½}$ of the transition between heating and cooling the sample. This hysteresis has been proposed to be of fundamental importance in the potential applications where the bistability of the system can be exploited. An abrupt transition that contains a moderately wide hysteresis that is centred around room temperature can be considered the optimal situation and a design goal for potential applications of SCO systems.[37] (see section 1.4).[8] Multi-step transitions are observed when a percentage of the metal centres switch spin states throughout a given temperature range, before a break in the transition where the percentage of HS/LS is stable. This is followed by further heating/cooling that enables another group of metal centres to switch and so on until the transition is complete. This can occur in systems with two or more similar but independent metal centres. Incomplete transitions, as the name implies, are relatively straightforward to describe as the system never fully switches to the LS state with changes in temperature, although the reason behind this is less clear. These changes in behaviour are believed to be largely linked to the cooperativity of the system and should be taken into consideration during the design of new systems.

Analysis of the effects of weak interactions in systems that display the SCO phenomenon has often been completed in attempts to provide insights into the mechanism of cooperation between metal centres. In the solid state it is known that increasing the cooperativity between molecules can be achieved through enhanced exploitation of intermolecular interactions, both strong and weak, for example hydrogen bonding and π-π stacking. These interactions can be demonstrated by considering the case of 2,2'-bi-4,5-dihydrothiazine (Bta), dipyrido[3,2-a:2'3'-c]phenazine (Dpp) and 1,10-phenanthroline (Phen).[38–40] These ligands, when coordinated to iron(II) bis-isothiocyanate, form trans $[Fe(L)_2(NCS)_2]$ systems, their crystal packing can be compared to one another. The three ligands display different levels of π-π stacking with Dpp displaying the most overlap (figure 1.8), and Bta the least. The impact of this trend can be observed in their spin transitions. Dpp displays an abrupt thermal

transition with a hysteresis, Phen also displays an abrupt transition whereas Bta only displays a very gradual transition.

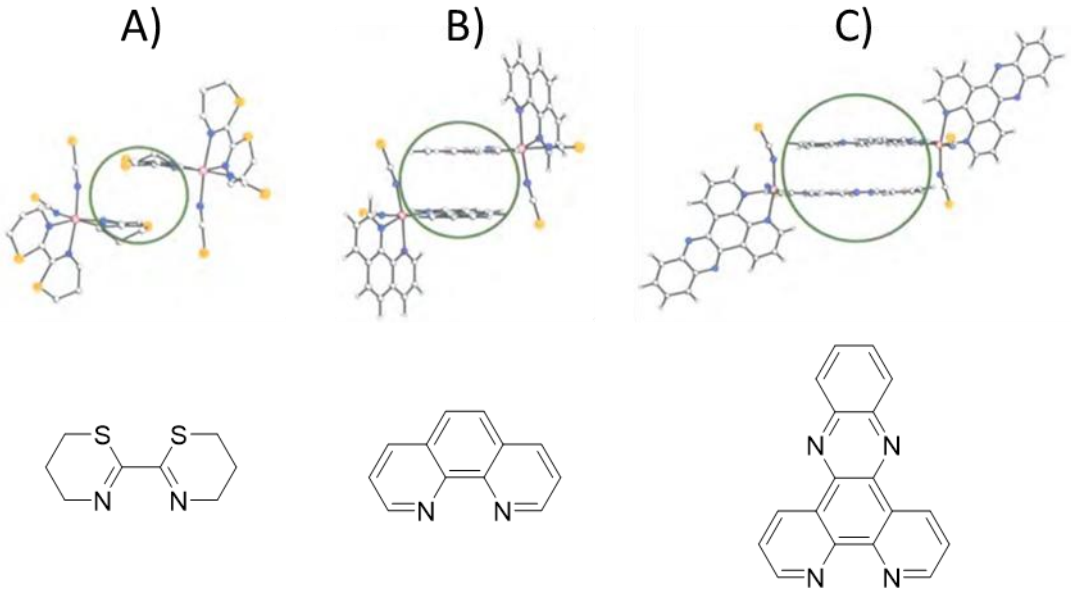

Figure 1.8. Image representing the π-π stacking interactions caused by ligand overlap in the crystal structures of A) bta, B) Phen and C) Dpp

1.2.2 Light Induced Spin Transitions

Light irradiation as a route to inducing SCO behaviour was first observed over 50 years after the original discovery of SCO. This mechanism of induction is most associated with a phenomenon now called light induced excited spin state trapping (LIESST). This is where samples are irradiated with a, usually, high-powered light source at low temperature to reverse the impact of slow cooling. The aim is to induce the transition from the occupied low spin state to a metastable high spin state. This LIESST effect is only present for a subset of materials that undergo spin transitions, and most commonly seen in those that are thermally induced. The first observation of this interesting characteristic of some SCO systems was by Gütlich *et al* in 1984 with the system $[Fe(Ptz)_6][BF4]_2$ (Ptz = 1-propyltetrazole) .[3] The discovery of light induced transitions again increased the interest in the SCO field in the 1980s as it was observed that at low temperatures it is possible to be able to produce full conversion from LS to metastable high spin (HS*) state with lifetimes exceeding 24 h. After the initial

discovery it was shown that previous examples that displayed thermal SCO behaviour could also display the LIEEST effect.[4,5]

Two years later, it was noted that these metastable states at low temperature when irradiated with a light of a different wavelength could be reverted to the LS state. This effect was labelled “reverse-LIESST”.[41] The mechanics of a system displaying both thermal and LIESST behaviour is shown in figure 1.9.

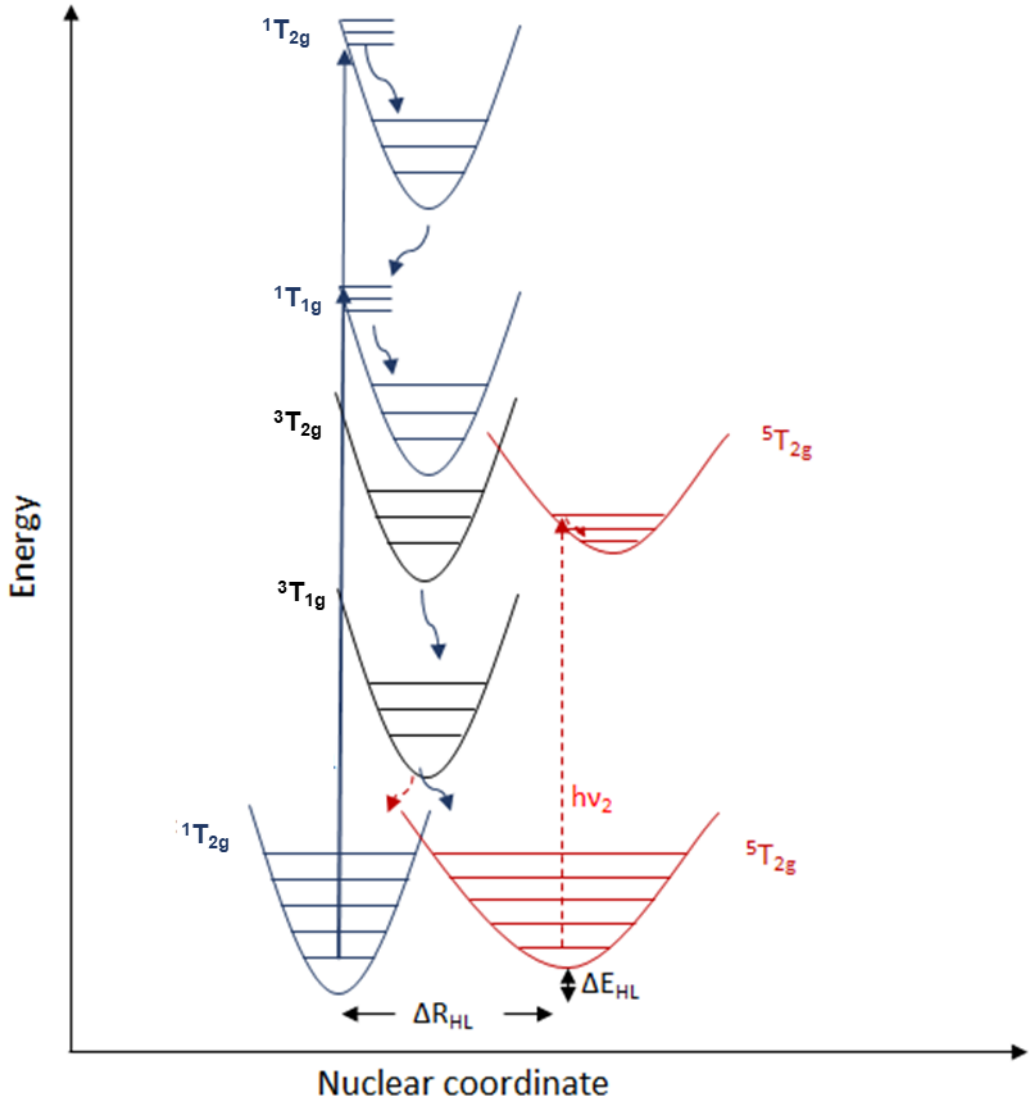

Figure 1.9 Mechanism of LIESST and reverse-LIESST for an Fe(II) ion, highlighting the electronic transitions involved in the transformations

Like thermal transitions, the behaviour of this LIESST effect can be plotted as the percentage of the HS state vs temperature. Figure 1.10 highlights the archetypal profile for the LIESST effect in terms of an example spin transition curve of a system that displays abrupt thermal SCO behaviour and LIESST at low temperature. As the sample is heated the HS* state will relax back to the LS state. The temperature that the compound reverts back to the LS ground state is referred to as T_{LIESST}.

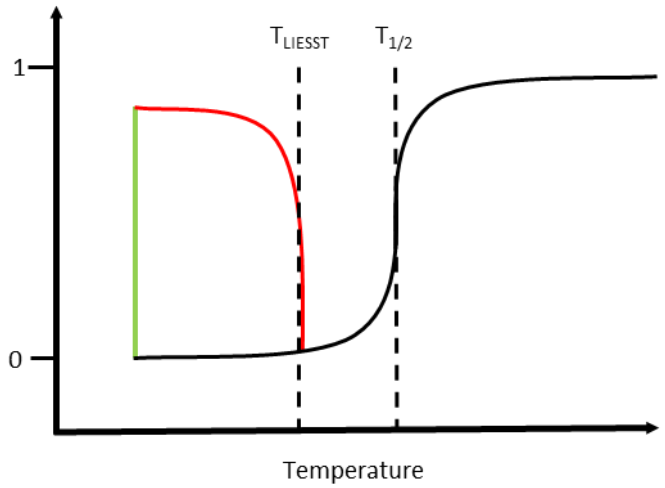

Figure 1.10 Example spin transition curse for a system that displays both thermal and LIESST phenomena. Black represents the decrease in mole fraction of high spin sample with temperature. Green displays sample light irradiated at a singular temperature. Red is the relaxation of the metastable state as the light source is switched off and sample is warmed up.

This phenomenon is only present at low temperature, with the highest temperature of 135 K recorded for a Fe(II) mononuclear metal complex, $[FeL(CN)_2]\cdot H_2O$ (L=[2,13-dimethyl-6,9-dioxa-3,12,18-triazabicyclo[12.3.1]octadeca-1(18),2,12,14,16-pentaene).[42] The low temperatures at which this phenomenon is displayed limit the opportunity of using these systems in proposed potential applications. Ideally, a meta stable HS state near to room temperature would be ideal for a switchable device.

LIESST is just one of the light induced spin state switching behaviour that has been discovered. One other light irradiation technique is called LD-LISC (Ligand-driven light induced spin change) that utilises ligands with photo-active groups to change the ligand field strength upon light irradtiation.[32,43] This process is coupled to structural

change in the photo responsive ligands. Another notable difference from SCO is that the HS and LS are both ground states of their respective structures.[43] Unlike LIESST, LD-LISC has been observed to occur at room temperature. The downside is that this has been observed mainly in solution studies and this is considerably less optimal for modern applications, there are however, a few examples of LD-LISC observed in the solid state.[44,45]

In a similar vein to the study of thermal transitions there has been research into the effect of different ligands and their respective complexes' ability to undergo light induced transitions and how they can be manipulated to produce new systems for analysis. To further understand the relationships between thermal, photoinduced transitions and the coordinated ligands, a study of Fe(II) SCO systems was conducted.[46] The study used different ligands that have different denticity: mono, bi, tri and quadridentate (figure 1.11). The $T_{½}$ and T_{LIESST} of these compounds were plotted against one another. A trend was observed with increasing denticity where the $T_{½}$ and T_{LIESST} of these compounds were located at higher temperatures. The relationship was proposed as the formula: $T_{LIESST} = T_0 – 0.3\ T_{½}$, where T_0 is the value of T_{LIESST} when $T_{½}$ tends to 0 for a group of metal complexes related by ligands. Therefore, in the design of SCO systems that display LIESST, some measure of control can be exerted on the T_{LIESST} via the denticity of the coordinating ligands.

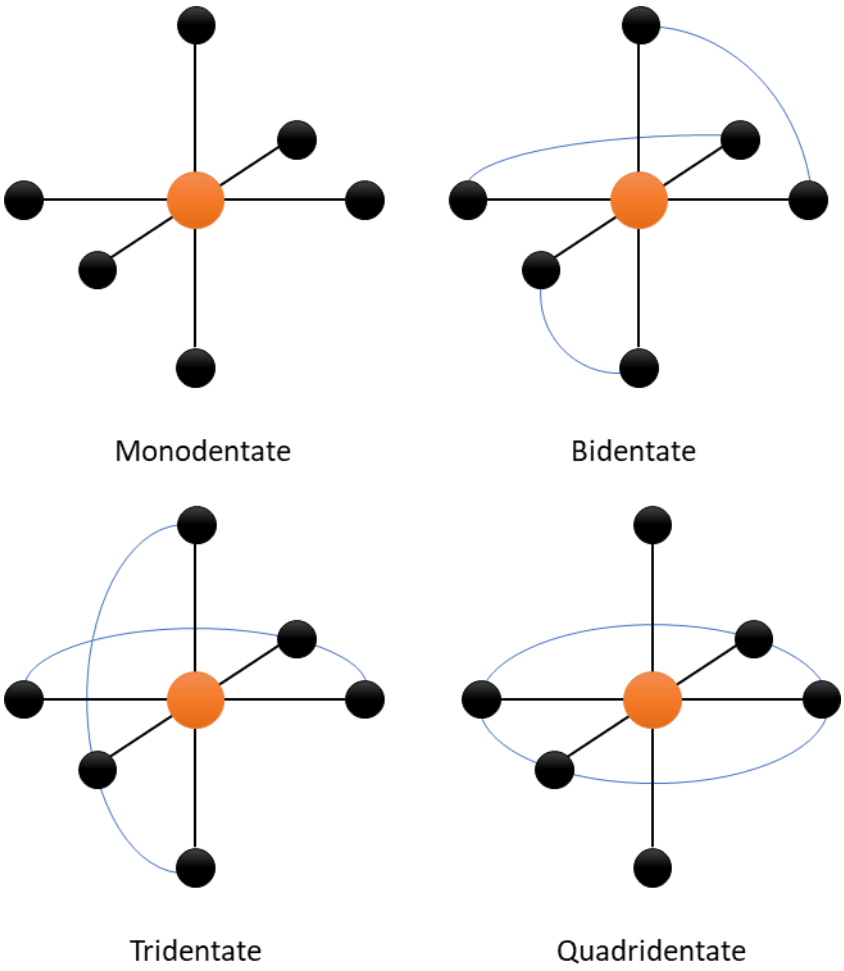

Figure 1.11. Representation of ligands with different denticity in an octahedral metal complex.

Another light induced mechanism is light induced thermal hysteresis (LITH) where it's possible to use laser irradiation on a sample held within its thermal hysteresis of a SCO system to promote a transition.[27,28] The first case of this was a study of the metal complex $[FeL(CN)_2]\cdot H_2O$ (L = N_3O_2 Schiff based macrocyclic ligand) which was irradiated with a laser within the hysteresis loop producing a metastable HS state.[47] While similar to LIESST it is noted in the literature to be mechanically different and rarely observed.[47–50]

1.2.3 Pressure Induced Spin Crossover

The final mechanism to induce SCO behaviour discussed in this body of work is the use of pressure. This process is observed in nature with spin transitions occurring in materials such as perovskites in the Earth's lower mantle.[51] High pressure studies have been used to induce spin transitions in single crystal samples. To accomplish this

specialised equipment is required, X-ray diffraction experiments are conducted with the sample encased in a diamond anvil cell (DAC), that are used to generate elevated pressures. Experiments on single crystals using high-pressure has given scientists the ability to access transitions that were previously inaccessible via thermal experimentation alone.[52]

Increasing pressure on a system causes a vertical distortion and an increase in the energy of the $^5T_2$ (HS) potential well (figure 1.12). This causes a difference in the zero-point energies for samples at a higher pressure and a lowering of the activation barrier (ΔW).

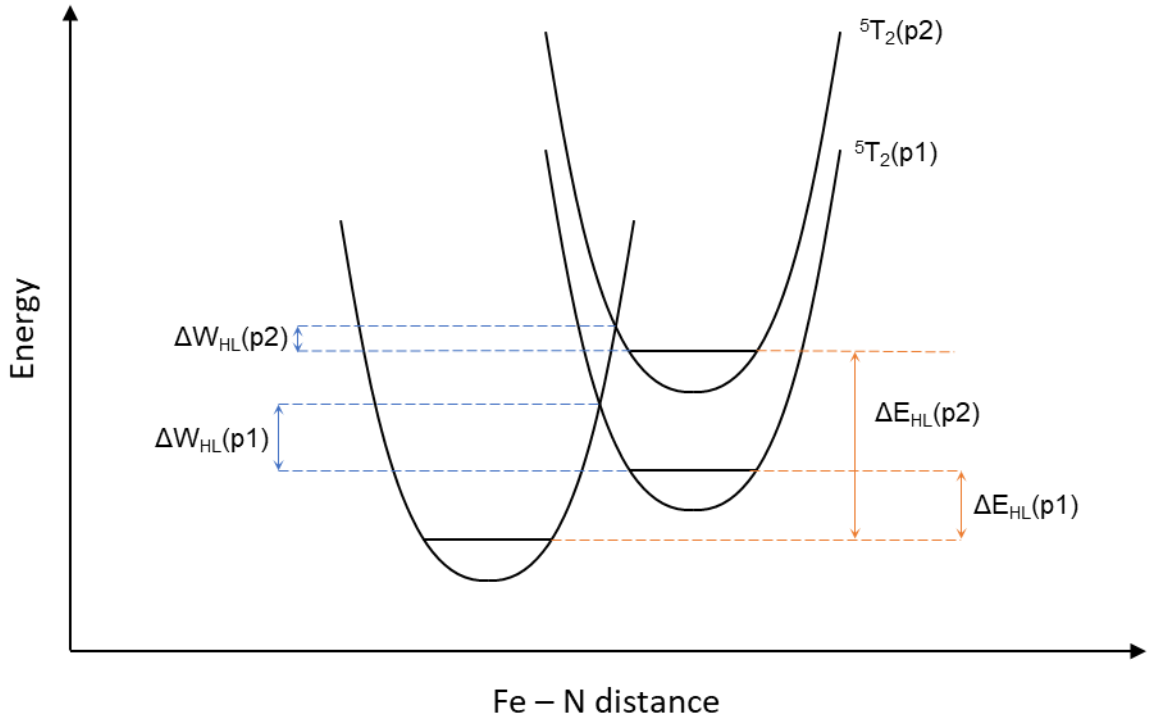

Figure 1.12. Diagram displaying the effect of pressure (p2>p1) on the position of the potential wells for a Fe(II) compound.

The LS state has shorter bond lengths and a smaller volume so pressure applications should favour LS conformations. The first examples of high pressure SCO studies were completed in 1960s by Drickamer *et al.* using Mössbauer spectroscopic detection to detect changes in spin state.[52] The increase in pressure displayed effects on the behaviour of the spin transition such as shifting the temperature induced transition in

a compound by ~15 kbar.[53] Some studies have shown an increase in the width of hysteresis in systems while under increased pressure.[6] Examples of pressure induced solid state phase transitions have been shown to occur in the systems [Fe(PM-BiA)$_2$(NCS)$_2$] and [Fe(PM-AzA)$_2$(NCS)$_2$] where PM-BiA = (*N*-(2'-pyridylmethylene)-4-aminobiphenyl) and PM-AzA = (*N*-(2'-pyridylmethylene)-4-(azophenyl)aniline.[54,55] In more recent experiments, the previously reported compound [Fe(abpt)$_2$(NCS)$_2$], has been extensively studied due to its four polymorphs, each displaying individual SCO behaviour and has shown new results with high-pressure experiments. Polymorph A displays thermal transitions that have been shown to undergo pressure induced transitions.[56] Polymorph B displays no thermal SCO behaviour at ambient pressures and has been shown to undergo a thermal transition with temperature variation while the sample is held at an increased pressure (>4.4 kbar) to a fully LS state that was previously inaccessible.[57]

The development of the diamond anvil cell (DAC) began in the 1950s[58] and allowed crystallographers access to high pressure experiments with multiple techniques including X-ray crystallography with the key being the generation of an X-ray accessible high pressure chamber.

The diamond anvil cell is comprised of two diamonds separated by a metal gasket, generally made from stainless steel or tungsten. The sample and one or more ruby chips (or spheres) are held within the gasket pressure transmitting media (PTM) that allows for hydrostatic pressure, *i.e.* uniform in all directions, to be exerted on the sample (figure 1.13). Each PTM has specific operating characteristics such as a hydrostatic limit, the pressure they can reach before they no longer apply uniform pressure. While pressures of up to 300 GPa have been obtained, routinely accessed pressures in-house are typically lower than <10 GPa, particularly for molecular systems that tend to undergo amorphization at much lower pressures than mineral or elemental systems. Pressure is applied by increasing the load (force) to the back of the diamond that is then transmitted to the smaller front face (culet), inducing a significant increase in the force per unit area within the cell. Due to the large difference in size an extremely large pressure can be obtained simply upon the tightening of two screws (figure 1.14). The screws are carefully tightened, allowing for controlled

increases in pressure to reach the approximate desired value. Greater control of the pressure increases can be obtained by using finer pitch screw threads.

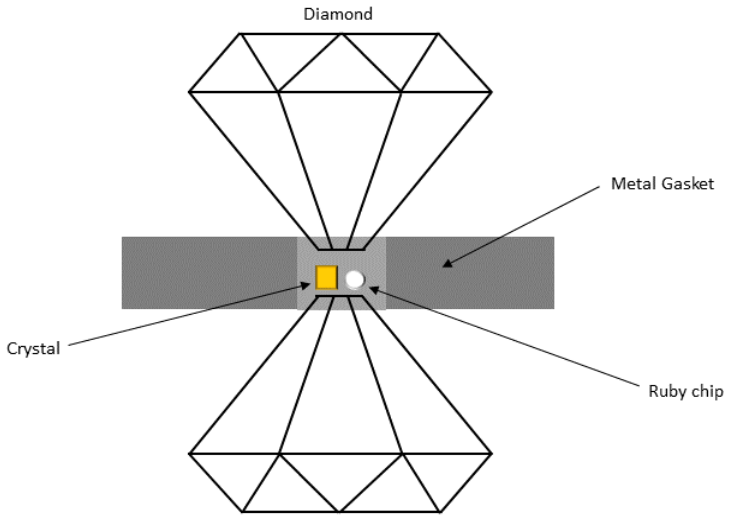

Figure 1.13. Sample environment in a DAC. The single crystal of the sample sits alongside ruby spheres between two diamond faces filled with a hydrostatic medium, the body and backing plates of the cell have been omitted for clarity.

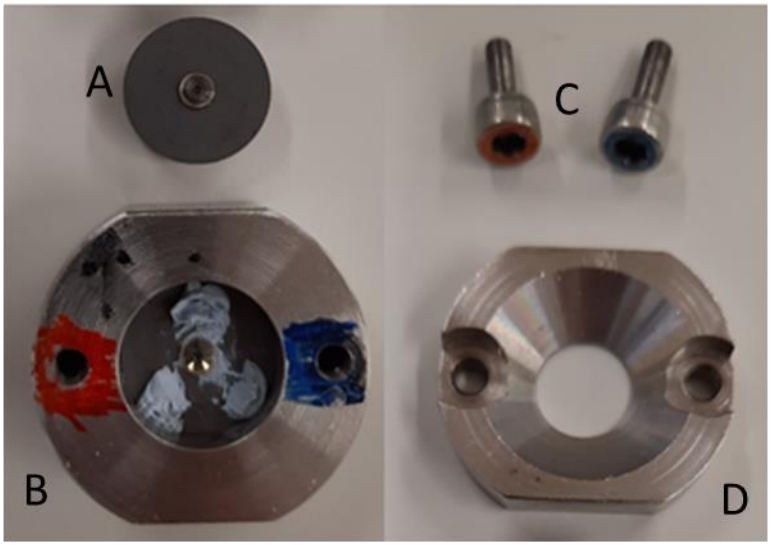

Figure 1.14. Diamond anvil cell used at Newcastle University, A) The top diamond and backing plate, B) the base containing the second diamond and backing plate, C) Screws and D) the top plate.

The diamonds in the modified Merill-Bassett type DAC used are seated into tungsten carbide backing plates that are then encased in a steel body to provide support for the cell. Stainless steel gaskets were pre-indented by the cell to a thickness between 0.11-0.18 mm before using an electrical discharge machine (commonly referred to as a spark eroder) to drill holes of either 0.3 or 0.4 mm diameter.

Crystals of suitable size and quality are selected and these are then fixed to the culet on top of one of the diamonds with the smallest amount of vacuum grease possible alongside the ruby pressure calibrant. The lower diamond and gasket are loaded with paraffin oil used as the PTM (in all studies within this thesis) before aligning and assembling the DAC. This is achieved by lowering the sample containing the second diamond face to close the cell.

Pressure inside the cell is commonly measured using ruby chips placed alongside the sample. These ruby chips display changes in their fluorescence spectrum that can be used to indirectly measure the pressure. The R1 line of the doublet is linearly dependant on pressure over a wide pressure range.[59] Therefore, comparison of ambient ruby chips with no load upon them and the ruby chip inside the cell allows for accurate calculation of the pressure the sample is under. It is important to make sure that the ruby for the ambient and pressure measurements come from the same source as minor variations in the composition impact the relative measurements in the fluorescence.

The use of DACs for single crystal X-ray diffraction experiments causes a variety of issues that are imposed by the physical constraints of the cell itself. These need to be carefully considered for any high-pressure experiment. The first of these is the large reflections caused by the diamonds that impact the data in two ways. The diamonds are single crystal themselves and therefore produce a diffraction pattern when exposed to X-ray radiation. Where these reflections are coincident with sample reflections the sample signal is swamped; further to this the strength of the interaction of the diamonds with the primary X-ray beam is such that it can reduce the beam sufficiently to impact on the intensity produced by the sample when they are both in diffracting conditions. Both of these effects cause issues with the scaling of the data, however the impact of these can be mitigated to a certain degree. To address these issues reflections from the diamonds, that are coincident with the sample reflections, are manually removed

from the integrated datasets before data scaling is conducted. The second, and more significant issue raised by the DAC, is the limited angles for the beam to pass through unhindered by the cell and gasket. This impacts the completeness of datasets that can be collected and in turn reduces the available data quality. To obtain the highest completeness and improved data quality, Ag-Kα radiation is the preferred choice for in-house single crystal X-ray high pressure data collections. The shorter wavelength of the radiation (λ = 0.5594 Å) allows for a greater amount of data to be collected from the limited opening angles to a given resolution. This is easily explained through the Ewald construction where the diameter of the sphere of data that is accessible is equal to 2/λ: the larger the diameter of the Ewald sphere the greater number of interactions with lattice points and therefore reflections present. The shorter wavelength also minimises absorption, a problem that is difficult to address and account for in a high pressure experiment due to the body of the DAC, that blocks a large number of X-rays due to being made from tungsten and steel.

1.2.4 Structure

Single crystal (SC) X-ray diffraction can be used to gain information on the structure of crystalline materials at an atomic resolution with data providing information of the foundations of structural properties. In particular, and most importantly for this work, the information gathered from the use of variable temperature SC X-ray diffraction experiments can be used to determine the spin state of central metal ions at the different temperatures of study through interpretation of the derived parameters within the structures and therefore, if the system displays spin crossover behaviour.

Some of these parameters derived from the data can be utilised in the determination of a change in spin state for an octahedral metal complex. These consist of the bond lengths between the metal centre and coordinating ligands and the volume of the octahedral sphere coordination (v_p) (see section 1.1). The parameters Σ and Θ relate to the distortion of the octahedral structure. The cause of variations in bond lengths for metal complexes has been described in section 1.1. For a Fe(II) metal complex with a 6 nitrogen coordination sphere, bond lengths increase by approximately 0.2 Å, from 1.9 Å to 2.1 Å on changing from LS to HS states. Changes in bond length are not reliable for each of the transition metal ions that display SCO behaviour. Manganese (III) complexes can display Jahn-Teller distortions involving the elongation and

compression of the axial bonds. Due to these changes in bond length, it can be unreliable for determining the spin state for Mn metal ions. Therefore, it is useful to utilise the other parameters described herein to determine if SCO behaviour is present. The other parameters found in octahedral metal complexes can also be calculated from the crystal structures.

The first parameter Σ is defined as the sum of deviations from 90˚ in the 12 cis φ angles within the coordination sphere.[18] A perfectly octahedral structure would consist of 12 90˚ angles, therefore Σ=0. The greater the value of Σ the greater the distortion of the octahedral environment. This distortion cannot come from individual contributions of bond length or volume changes. Σ must therefore be dependent on the spin state and can used to determine the spin state of the compound analysed. Another factor to consider is that Σ is dependent on the ligand coordinated. Therefore, values of Σ cannot be compared to structures containing different ligands. Higher values of Σ indicate HS and lower values are indicative of LS states, this variation is typically between 30-55%.[18]

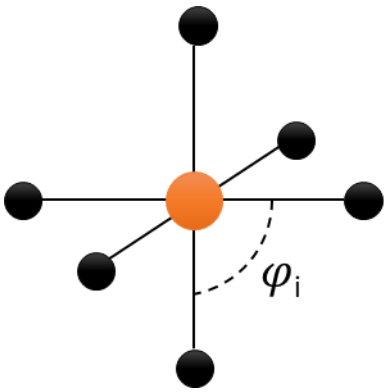

$$\sum = \sum_{i=1}^{12} (|\varphi - 90|)$$

Figure 1.15. Definition of the structural parameter Σ visualised and the equation used to calculate this parameter

The second parameter Θ is related to the 'trigonal twist' motion of the opposite trigonal faces of an ideal octahedron which should be equal to 60˚.[60] An investigation into this

parameter displayed using $[Fe(L)_n(NCS)_2]$ complexes displayed that with an increase in Θ the transition behaviour is more abrupt.[61] Θ is the sum of the deviation from 60˚ for the 24 unique θ angles in the octahedron and these angles are considered independent of orientation. Values of Θ, like Σ, are dependent on the ligands coordinated to the metal centre and comparisons between structures with different ligands are not particularly meaningful.

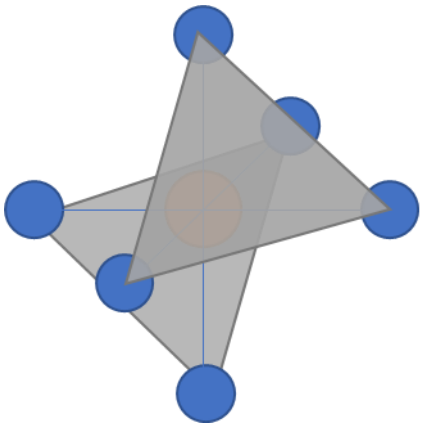

$$\Theta = \sum_{i=1}^{24} (|60 - \theta_i|)$$

Figure 1.16. Trigonal faces of an octahedral structure visualised for parameter Θ.

The structural parameters described can be obtained from standard variable temperature SC X-ray diffraction methods. The investigation of thermally induced SCO behaviour can be achieved with standard additions to a diffractometer, such as a temperature control unit *i.e.* Oxford Cryosystems Cryostream.[62] To investigate light irradiation and pressure induced SCO behaviour requires atypical and often custom equipment such as DACs for pressure induced transitions and high-powered laser sources for light irradiation studies. The parameters described above are just some of the changes associated with SCO. Other changes such as sample colour and changes in magnetism cannot be analysed by diffraction experiments and require separate equipment.

1.2.5 Methods For Detecting SCO

Considering the parameters discussed single crystal X-ray diffraction is a viable method for determining the spin state of SCO systems. However, there are various other properties that can be utilised to determine the spin state. These properties include the colour changes associated with a change in spin state and changes in magnetism of the central metal ion. As the name implies, single crystal X-ray diffraction requires a single crystal of good quality for analysis that can be arduous to obtain.

Other techniques can be accomplished using the bulk powder or are solution-based techniques.

The substantial difference in magnetic properties of $3d^6$ metal ions spin states are used to detect SCO behaviour. The LS state is diamagnetic with no unpaired electrons (S=0) and HS states with 2 unpaired electrons (S=2) are paramagnetic (see table 1.1). These changes in magnetism allow for methods other than XRD to analyse these systems. Magnetic susceptibility measurements record magnetic susceptibility (χ) as a function of temperature. This can be accomplished using traditional magnetometers or superconducting quantum interference device (SQUID) equipment. The transition from one spin state to another is mirrored by a change in the magnetic susceptibility, Curie law, the χ.T product is constant at any given temperature in a paramagnetic material, in a SCO material a change in a graph of χT vs T would allow for identification of a transition.

Mössbauer Spectroscopy is another technique that can be used to determine the magnetic state of a compound. Mössbauer Spectroscopy utilises recoilless nuclear resonance absorption of γ-radiation (Mössbauer effect), this technique has been used widely in the field of spin crossover. Measuring changes in isomer shift δ and quadrupole splitting ΔE_Q. These two parameters found in Mössbauer spectra can be used to identify HS and LS systems due to the large differences in values for Fe(II).[63] ^{57}Fe Mössbauer spectroscopy is advantageous for use with iron metal complexes with the ability to determine oxidation state of the metal ion, the spin state and the metal centre environment.[63] With the iron metal ions being the most common in terms of displaying SCO behaviour, means that Mössbauer spectroscopy has been an attractive method to analyse these compounds.

Vibrational Spectroscopy. Changes in metal-ligand bond lengths from HS-LS transitions causes changes in vibrational spectra, mainly in stretching frequencies.[64] IR and Raman spectroscopy measurements as a function of temperature can assign bands to LS and HS states.[64]

Optical Spectroscopy. Previously mentioned, changes in chromatic properties of the sample occur with LS-HS transitions and therefore optical spectra can be used to measure SCO during temperature changes. Observation of d-d transitions and MLCT (metal-to-ligand charge transfer) can be used to determine changes in spin state.[65]

1.3 Crystallography

Single-crystal X-ray diffraction has been utilised for almost a century to investigate the molecular structure of crystalline materials. It is one of the most valuable tools for structural analysis. SC-XRD experiments not only allow insight into the molecular structure but provides insight into parameters such as bond lengths, the unit cell parameters, symmetry and the discussed distortion parameters (section 1.2) of octahedral metal complexes. The fundamental details of crystallography and its experimental details from collection to refinement have all been widely discussed in detail.[66] Therefore, this section will only detail specifics for the non-standard equipment and techniques used at Newcastle University.

Temperature control, one of the most basic and widely used environmental controls for SC-XRD collections has been commonplace for in-house measurements for decades. To simply study basic thermal SCO behaviour, altering the sample temperature between collections. Standard techniques such as the use of a Cryostream allow samples to have their temperature controlled between ~100-500 K using a stream of nitrogen gas. The Oxford Cryosystems Cryostream uses liquid nitrogen supplied via a dewar to the cold head. The liquid nitrogen is then sent to a heater that converts it into its gaseous form. This gas is then passed through a heat exchanger and temperature controller before being dried. Finally, a gaseous stream of nitrogen is directed out of the nozzle onto the sample mounted to the diffractometer.[62]

To reach lower temperatures, a helium-based cooling system such as the Oxford Cryosystems HeliX can be employed to reach temperatures down to ~25 K. The HeliX utilises helium gas cooled through heat exchangers on a two-stage closed cycle refrigerator. The end nozzle of the HeliX is made of beryllium and envelops the sample operating much closer than a Cryostream. This ensures that the crystal is suspended in the flow of helium gas and achieving accurate sample temperature.[67] In some cases of SCO behaviour, the sample may require cooling lower than the 25 K available with the HeliX. To reach these temperatures, specialised equipment is required such as the specialist low temperature single crystal X-ray diffractometer XIPHOS I.

1.3.1 XIPHOS Suite

Single crystal X-ray diffraction at Newcastle University makes use of three diffractometers. The first is a Bruker D8 Venture single crystal X-ray diffractometer that can be used for standard experimentation with variable temperature available in the form of the previously discussed Cryostream (400-100 K) and the HeliX (>25 K). The Bruker D8 Venture has access to both copper and silver radiation sources.

The other two diffractometers are part of the XIPHOS suite that allow for single crystal X-ray diffraction experiments with several extreme conditions. The first XIPHOS I is a specialised ultra-low temperature diffractometer that can reach temperatures of ~2 K and is fitted with a molybdenum X-radiation source. XIPHOS II is a specialised high-pressure X-ray diffractometer that allows for easy mounting of samples in diamond anvil cells and uses a silver X-radiation source to optimise data completeness due to the limit angles available (see section 1.2.3).[68,69]

Figure 1.17. The single crystal X-ray diffractometer XIPHOS I, a specialised ultra-low temperature diffractometer with a modified displex cooling unit and sample containment system.

The single crystal X-ray diffractometer, XIPHOS I can achieve temperatures as low as ~2 K using a modified APD 202E displex cryogenic refrigerator with an additional Joule–Thompson stage. This combined with a high-pressure helium line and a vacuum allows for the ultra-low temperatures to be reached. A Lakeshore 340 controller is used to regulate temperature using an heating unit located in the sample environment.[68]

Recently improvements have been made to XIPHOS I by C. J. McMonagle and M.R. Probert. These improvements reduce the background noise caused by the beryllium

shielding can that created problems when attempting to collect data for weakly diffracting samples.[69] To combat this background changes were made to the materials used in the vacuum chamber and creating an internal collimator that can rotate alongside with changes in phi (ϕ) on the goniometer. The internal collimator removes powder rings created by the outer beryllium can. These powder rings were inconsistent and caused multiple issues when handling data. The changes visualised in figure 1.18, allow for ultra-low temperatures to still be obtained during experiments while increasing data quality and allowing for more complicated samples to be examined.

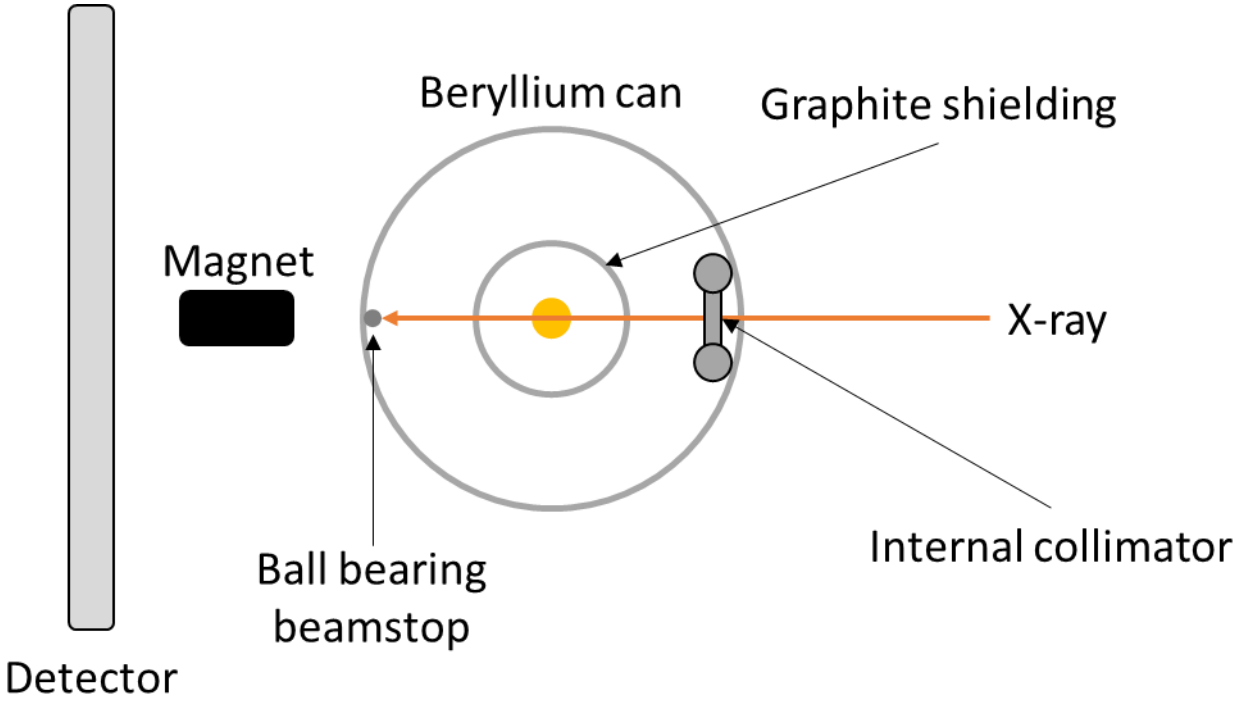

Figure 1.18. Schematic representation of the improved setup on the ultra-low temperature single crystal X-ray diffractometer XIPHOS I, including the internal collimator, beryllium can, metal ball bearing beamstop held in place by a magnet and graphite shielding.

1.4 Applications

An aim of the generation of new SCO systems is to be utilised as functional materials in switchable devices and Khan *et al* identified some of the requirements for a system to be used in the design of new applications.[70,71] The first, the transition from one spin state to another must be abrupt in both warming and cooling modes. Next, an easily detectable change in either the behaviour or appearance of the system alongside the transition including colour changes associated with SCO (thermochromism).

Information storage applications require a large thermal hysteresis for the bistability between the $T_{½}$ of heating and cooling modes. Finally, for general applications, the transition temperatures should be near room temperature and be operable between 0 – 100 °C. If a system was obtained that matched some of these requirements, there are three major potential applications in the form of display devices, data storage and sensors.

1.4.1 Display Devices

The intense colour change (thermochromism) associated with the changes in spin state could allow for SCO systems to be used as functional materials in new display devices technologies.[8,37] To realistically achieve this, the samples would be required to be operational at room temperature and be reproduceable with abrupt transitions. Fe(II) 1,2,4-triazoles have previously been studied for this reason in the hopes of tuning the temperature of the thermal transition. Metal dilution is one method explored in attempt to obtain desirable materials. Iron 1,2,4-triazole derivatives have been studied using metal dilutions, while temperatures were affected with dilution of the iron complexes with Zn(II) that does not undergo a spin transition the thermochromic effect was also hampered. The exploration of mixed ligand systems that contain various triazoles, these complexes were shown to have different temperature spin transitions were coordinated to a metal centre and another method that involved mixing counter ions in the same vein. This led to some unique systems being made that produced room temperature transitions with large hysteresis such as $[Fe(NH_2trz)_3](NO_3)_{1.7}(BF_4)_{0.3}$ (NH_2trz = 4-NH_2-1,2,4-triazole))with an associated hysteresis of 60 K.[37]

1.4.2 Data Storage

The observation of LIESST and reverse-LIESST phenomena displayed the potential of SCO materials to be used as molecular switches. Molecular switches have displayed the possibility to be used in the creation of new data storage technologies. To create these molecular switches would require the material to be in either an “on” or “off” state and remain in that state when the external stimulus is removed. At cryogenic temperatures both the LIESST and reverse-LIESST have been shown to have long lifetimes, but T_{LIESST} would need to be increased in order for such materials to be used in real world applications.

The photomagnetic effect within the hysteresis loop discussed previously allows for light induced transitions near room temperature. The sample would require a hysteresis ~100 K around room temperature to be desirable. With this effect being rarely observed, finding a material that fits these criteria is unlikely thus far.

Examples of thermally induced SCO materials that have been utilised in attempts to create new data storage technologies include the metal complex $[Fe(HB(pyrazoyl)_3)_2]$.[72] However, deterioration of this system after one thermal cycle could allow this system to be only read-only memory although it was a starting point for practical applications. Newer systems that have been shown to undergo room temperature transitions such as Real *et al* displaying guest induced transitions with electric voltage in an iron(II) coordination polymer.[73]

1.4.3 Sensors

Due to the ability of being both pressure and temperature induced SCO materials have been proposed as possible sensory materials. In a similar manner to potential uses as data storage, exposure to external stimuli causing an on/off response has possible uses for sensors in relation to temperature, pressure and light.

An example of this is the use of SCO behaviour as a pressure sensor from $[Fe(hyetrz)_3]I_2 \cdot 0.5EtOH$ (hyrtrz = 4-(2′- hydroxyethyl)-1,2,4-triazole). This material displays a pressure induced transition at 0.87 kbar that is accompanied by a colour change in the sample allowing for detection of the transition. [74]

The crossover between these three uses allows for materials to be designed with not one specific use in mind but serendipitously one material may fit one or more categories for future applications.

1.5 Notable Spin Crossover Systems

1.5.1 Background

The field of spin crossover is ever expanding - a great number of articles are published each year which aim to deepen the understanding of this phenomenon so that improved systems can be designed for practical applications. These complexes are studied in both the solid state and solution, widening the variety of functions they can theoretically achieve.[21] To further the progress of the field, a significant portion of current research into SCO complexes involves the adaptation of previously discovered

ligands. A variety of substituted ligands have been incorporated into complexes to produce the desired structural and magnetic behaviour.

The four metal ions (Fe(II), Fe(III), Co(II), Mn(III)) account for the majority of known SCO complexes, to date, dominated mainly by Fe(II) complexes.[75] While other metal ions such as Cr(II) display SCO behaviour, such reports are rarer because chromium is not a desirable material to work with due to its toxicity.[2] This is not to say that there is no further interest in using these metal centres, with new studies being conducted even on Cr(II).[76] Interestingly, the first Cr(II) SCO complex to be discovered in 1989 contained a P_4I_2 coordination sphere, vastly different from the coordination spheres observed in the majority of Fe(II) SCO complexes.[77,78]

There are several main routes to the synthesis of spin crossover complexes. The first of these; coincidence compounds synthesised with a desired purpose in mind with no intention of displaying SCO, however on further analysis of the structures the phenomenon is observed. Systems that display unusual behaviour in initial experimentation have further testing of magnetic or structural data that provides them with insight into spin transition. The second method is the adaption of the electronic effects of existing spin crossover compounds. Systems such as $[Fe(phen)_2(NCS)_2]$[15], $[Fe(bpp)_2](BF_4)_2$[79] and $[Fe(abpt)_2(NCS)_2]$[56,80–83] have been studied before in great depth for their SCO behaviour, ligands displayed in figure 1.19.

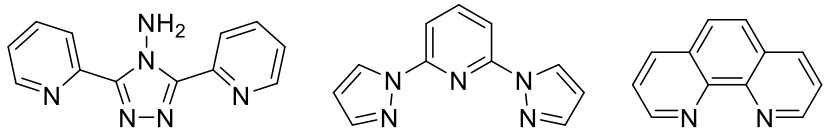

Figure 1.19. Molecular representation of the three ligands discussed A) abpt = 4-amino-3,5-bis(pyridin-2-yl)-1,2,4-triazole B) bpp = 2,6-di{pyrazol-3-yl}pyridine and C) phen = 1,10-phenthroline

With the archetypal system well studied, researchers have adapted these systems in attempts to understand SCO in greater detail. These changes can include adaptions to the ligands coordinated to the central metal ion, counter ion exchanges, solvent and polymorphic studies.[84] The archetypal system $[Fe(phen)_2(NCS)_2]$ has been studied extensively, the 1,10-phenanthroline ligand has a multitude of adaptions produced and

tested for any SCO behaviour.[85,86] $[Fe(bpp)_2](BF_4)_2$ has also been investigated extensively, specifically with research conducted by M. Halcrow *et al* to synthesise and analyse new derivities.[16,87–89] The metal complex $[Fe(abpt)_2(NCS)_2]$, a system with 4 polymorphs each displaying different SCO behaviour and three (polymorphs A, C and D) of these have been shown to display SCO behaviour at ambient pressures with studies completed on each of them.[56,80–83]

Exploration of the four polymorphs of $[Fe(abpt)_2(NCS)_2]$ are still producing new results years after the discovery of these systems and their initial analysis. Work by Sparkes *et al*[90] has shown that Polymorph B, previously believed to show no signs of a spin state transition, undergoes a transition during high pressure X-ray diffraction experiments alongside a structural transformation from $P2_1/n$ to P-1 with the transition occurring between 11.5-13.5 kbar. The loss of symmetry constraints in high pressure phases has been extensively documented, since losing symmetry constraints allows for more degrees of freedom.[91] The structure of polymorph D contains two crystallographically independent Fe(II) centres in the unit cell. Initially thermal experimentation displayed one Fe(II) centre exhibits SCO behaviour with a transition from HS to LS state upon on cooling. Further cooling of the sample does not cause the second Fe(II) centre change spin state.[83] It has been recently demonstrated that both metal centres in polymorph D can undergo spin transitions from HS to LS. The first at around ~9.6 kbar and the second centre at ~15 kbar.[90]

1.5.2 – Iron Spin Crossover Systems

Fe(II) accounts for the largest portion of spin crossover complexes, with $[Fe(Phen)_2(NCS)_2]$ being perhaps the most thoroughly studied in the field.[2] This system has lead to a range of new ligands belonging to the $[Fe(diimine)_2X_2]$ family, closely related to $[Fe(Phen)_2(NCS)_2]$ this includes ligands such as abpt and tzpy (tzpy = 3-(2-pyridyl)[1,2,3]triazolo[1,5-a]pyridine; figure 1.20).[92] A large number of studies on Fe(II) systems containing ligands based upon these are still being released with new results furthering the field and increasing the understanding of the phenomenon.

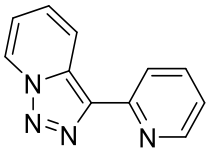

Figure 1.20. Molecular representation of tzpy = 3-(2-pyridyl)- [1,2,3]triazolo[1,5-a]pyridine

Modifications to ligands such as, 3-bpp (bis(pyrazol-3-yl)pyridine) coordinated to iron(II) have led to new room temperature SCO complexes in solution.[93] These systems also show interesting behaviour when studied by NMR spectroscopy in different solvents, the first complex $[Fe(L^{OH})_2](BF_4)_2$ (Figure 1.21) displays a small change in transition temperature, $T_{1/2}$ = 307 K in methanol-d_4 and 299 K in DMF-d_7. The second complex $[Fe(L^{t\text{-}Bu})_2](BF_4)_2$ also displays a small change in $T_{1/2}$, 214 K in acetonitrile-d_3, 201 K in DMF-d_7. Another noticeable factor is the large change in $T_{1/2}$ across the two systems with a small change in the substituent used. It is the first example of almost complete SCO which was achieved at near ambient conditions, which is one of the ultimate goals for the creation of functional SCO technologies.[71]

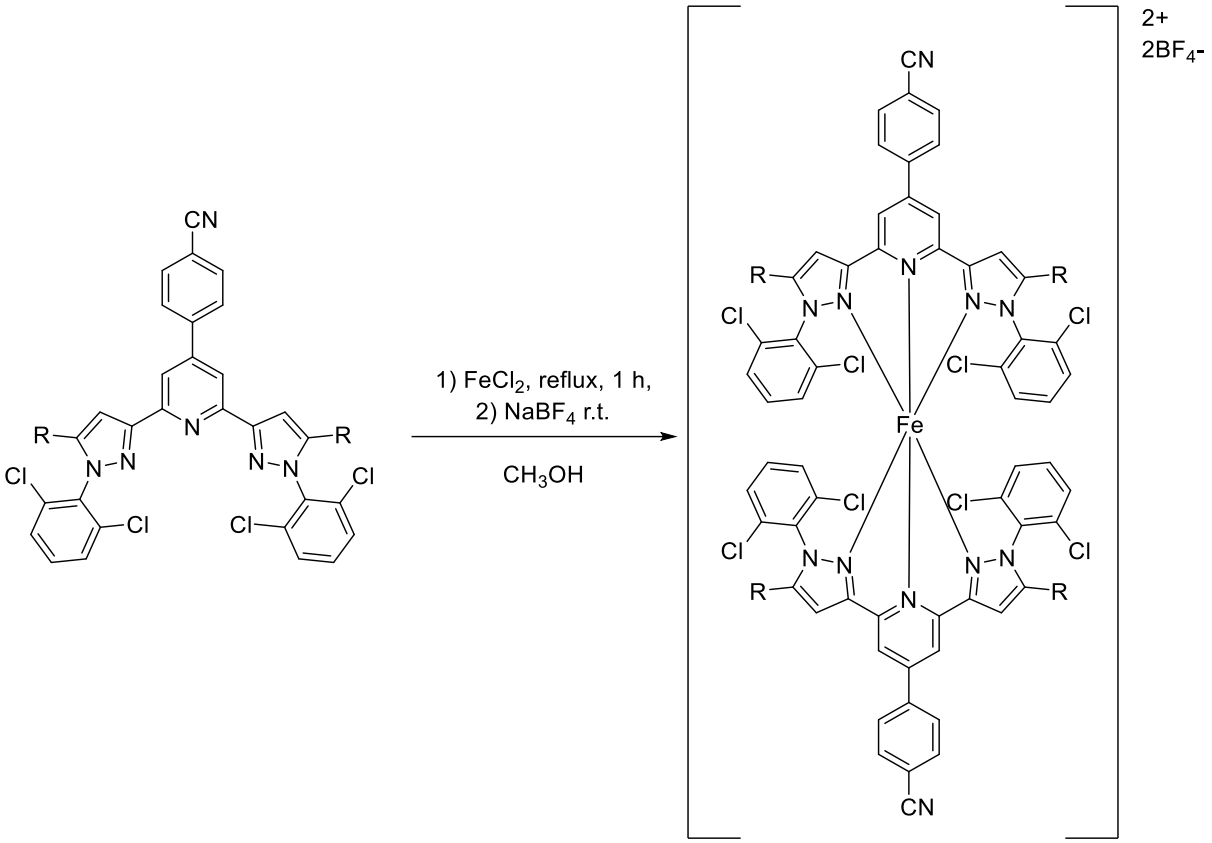

Figure 1.21. Molecular representation of the N,N′-disubstituted 3-bpp backbone (L^{OH}, R = OH, $L^{t\text{-}Bu}$ R = t-Bu) and complexes analysed in Y. V. Nelyubina *et al*.

Simple 1,2,4-triazoles have also been incorporated into SCO complexes, such as the iron(II) complex $[Fe(NH_2trz)_3](ns_2).2H_2O$ (NH_2trz = 4-amino-1,2,4-triazole, ns = 2-naphthalenesulfonate) reported by Lavrenova et al, which was studied both in solution and solid state.[94] The complex displayed sharp SCO behaviour in both the hydrate and dehydrated state in the solid state, as well as SCO behaviour in solutions of DMF. Upon heating, the $T_{1/2}$ between the hydrated and dehydrated analogues was similar (~13 K; Table 1.2), however, the transition temperatures on cooling were drastically different, creating a larger hysteresis in the dehydrated sample.

Table 1.2. SCO behaviour observed in $[Fe(NH_2trz)_3]$ complexes stuided by Lavrenoba et al.[94]

System	$T_{1/2}$ (heating)	$T_{1/2}$ (cooling)	$\Delta T_{1/2}$
$[Fe(NH_2trz)_3](ns_2).2H_2O$	333	322	11
$[Fe(NH_2trz)_3](ns_2)$	320	284	36
$[Fe(NH_2trz)_3](ns_2)$ in DMF	314	312	2

The incorporation of extended structures such as metal-organic frameworks (MOFs) into SCO systems has also led to new discoveries. A study of 2D porous single-crystal complexes containing prentrz (prentrz = (1E,2E)−3- phenyl-N-(4H-1,2,4-triazol-4-yl)prop-2-en-1-imine) was observed to display different SCO behaviour upon adsorption of water molecules into the framework.[95] The structural transformation, a change in conformation of the prentrz ligand causing a change in structure and causing large pores to appear in the crystal structure upon hydration. This transformation causes a shift in the SCO behaviour of the Fe(II) centres. The first structure $[Fe(prentrz)_2Pd^{II}(CN)_4].9/2H_2O$ displays a stepped transition at 150 K, with no plateau between the steps, whereas the second structure $[Fe(prentrz)_2Pd^{II}(CN)_4].4/3H_2O$ displays a stepped transition with two clears steps separated by a plateau.

Another example of the crossover between SCO and MOFs was reported by Brachňaková et al. Three MOFs containing *cis*-stillbene photoisomerizable guest molecules were synthesised and characterised by a variety of techniques, including single crystal XRD. The SCO properties of these systems were shown to be influenced by the steric hindrance of the bulky guest molecules - these steric effects also reduced the effectiveness of photoconversion of the guest molecules in question. While the authors confessed that the study did not have the anticipated outcome, the results were promising enough to warrant the continued study of guest molecules in these SCO-MOF blended systems.[96]

SCO complexes have even recently managed to extend into the field of supra-molecular chemistry. Layfield *et al* explored the SCO behaviour of the iron(II) complex $[Fe(bipy[9]CPP)(H_2B(pyz)_2)_2]$, which incorporated a bipyridyl-embedded cycloparaphenylene nanoloop (Bipy[9]CPP; figure 1.22).[97] The complex contained two molecules in the asymmetric unit, each of which exhibited identical SCO behaviour ($T_{1/2}$ = 130 K). Computational studies conducted on $[Fe(bipy[9]CPP)(H_2B(pyz)_2)_2]$ and

the structurally related acyclic variant [Fe(bipy)($H_2B(pyz)_2)_2$] suggested that the SCO behaviour could be tuned based on the size of nanoloop used in the complex.

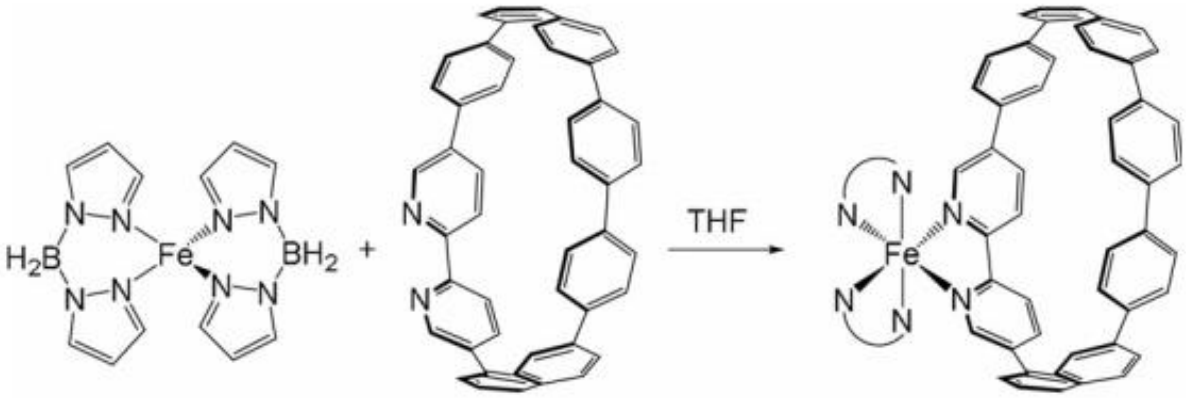

Figure 1.22. Structure of Bipy[9]CPP, $H_2B(pyz)_2)_2$ and the complex formed [Fe(bipy[9]CPP)($H_2B(pyz)_2)_2$].[97]

Although Fe(II) metal centres are dominate the majority of publications in the field, the first system to display the phenomenon was an iron(III) complex.[9] Fe(III) systems are of course still studied thoroughly today – recently, Jun Tao *et al* investigated the effects of halogen substitution of a hphsalpm ((5-X-(R,S)-((phenyl(2-pyridyl)methylimino)-methyl)phenolth)) ligand, where X = F, Cl, Br, I, on the resulting SCO behaviour of the complexes (Figure 1.23). Complexes containing Cl and Br substituted ligands displayed SCO behaviour with incomplete thermal transitions being observed. Contrastingly, the other complexes showed no signs of SCO behaviour. The authors noted this could be due to a change in electronics and intermolecular interactions - the chlorine and bromine analogues were, in fact, isomorphous. The fluorine analogue contained distinctly different electrostatic properties while being isostructural. The complex containing the iodine substituted ligand was not isomorphous, therefore, displayed different intermolecular interactions – this was believed to be a factor in disrupting the ability of the complex to display SCO behaviour. The complexes containing Cl and Br substituted ligands that underwent incomplete SCO displayed reversible LIESST effects when irradiated with 880 nm and 1064 nm light, respectively. The MeOH solvate of the iodine containing complex, that was thermally inert, surprisingly displayed a reverse-LIESST effect. By carefully tuning the photo-

responsive properties of structurally related systems, functional materials containing complexes that respond to a large array of wavelengths could one day be developed.[98]

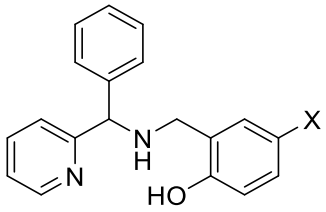

Figure 1.23. 5-X-(R,S)-((phenyl(2-pyridyl)methylimino)-methyl)phenol (hphsalpm)

1.5.3 – Cobalt Spin Crossover Systems

The synthesis of new ligands is just one factor to consider when designing new SCO complexes - the roles of counter ions and solvent molecules can also influence SCO behaviour. Cobalt(II) complexes containing modified terpyridine ligands displayed changes in behaviour when water molecules were present in the structure.[99] It was proposed that the increase in hydrogen bonding caused by addition of water played a vital role in the ability of the complex to undergo SCO. This study further highlights the impact of intermolecular interactions within the crystal structure and their effects on SCO behaviour and the need to study both hydrated and dehydrated analogues.

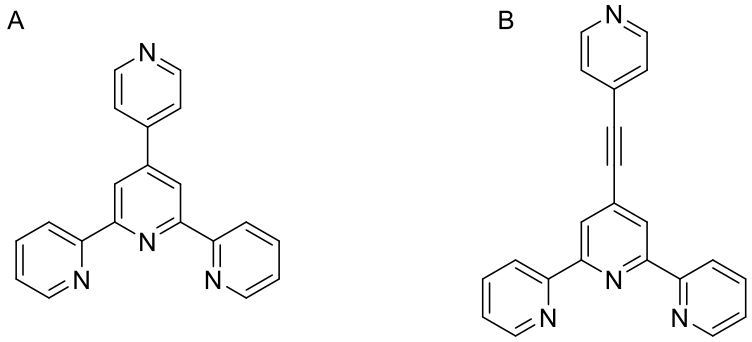

Figure 1.24. Molecular representation of A) pyterpy = 4'-(4'''-pyridyl)-2,2':6',2''-terpyridine, (B) pyethyterpy = 4'-((4'''-pyridyl)ethynyl)-2,2':6',2''-terpyridine studied in H. Zenno et al.[99]

The first instance of a cobalt(II) metal complex with a N_4S_2 ligand donor set was only recently discovered by Rentschler *et al*.[100] The complex contained two = 2,5-bis[(2-pyridylmethyl)thio]methyl-1,3,4-thiadiazole ligand coordinated in a tridentate facial manner and exhibited SCO behaviour centered about $T_{1/2}$ = 175 K (Figure 1.25). This

discovery shows that there is still a large amount of design space for metal ions other than iron(II) to be explored in the search for new SCO systems.

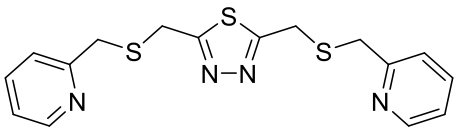

Figure 1.25. Molecular representation of = 2,5-bis[(2-pyridylmethyl)thio]methyl-1,3,4-thiadiazole.

1.5.4 – Manganese Spin Crossover Systems

Manganese(III) complexes have also been reported to exhibit SCO behaviour, however, examples are less common. Nevertheless, a number of studies have still been undertaken of complexes of manganese(III), with systems incorporating the Salen or Schiff base (2,2′-Ethylenebis(nitrilomethylidene)diphenol, Figure 1.26) ligand backbone making up a large proportion of these systems.[35] The ligand was originally coordinated to form an iron complex which displayed a change in magnetic moment at 180 K.[101]Since then the backbone of the salen ligand has been studied thoroughly in the field and still provides new complexes for study.

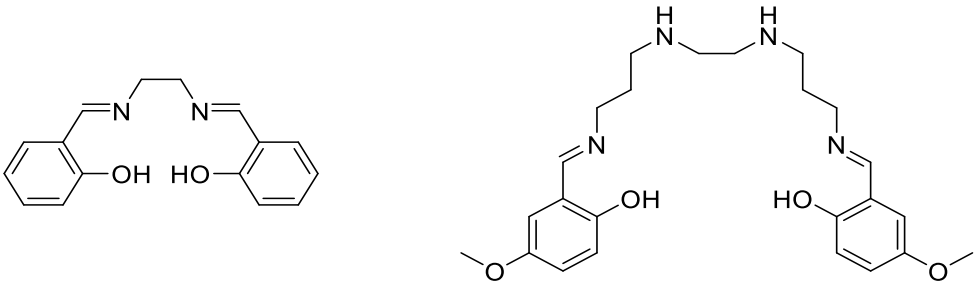

Figure 1.26. Molecular diagram of the ligand Salen (2,2′-Ethylenebis(nitrilomethylidene)diphenol) and the ligand 5-MeO-sal-N-1-5-8-12 discussed in M. Fuentealba et al.[102]

A manganese(III) complex containing 5-MeO-H2sal-N-(1-5-8-12) (Figure X) displayed SCO behaviour close to room temperature ($T_{1/2}$ = 281 K), which was accompanied by a pronounced thermochromic effect from dark purple at 400 K to bright pink at 90 K.[102] This study also discussed the effects of counter ion size on the temperature and abruptness of SCO behaviour, noting that a decrease in counter ion size increased

$T_{1/2}$. Noting that the choice of counter ion is another important factor to consider in the synthesis of new systems.

1.5.5 – Manipulating Spin Crossover.

Uncoordinated 1,2,4-Triazoles have been observed to be of great use in the medicinal field, they are also highly adaptable with various substituents that can be used in attempts to try and control the properties the researcher wishes to exploit.[103,104] Compared to some of the archetypal ligands such as 1,10-phenanthroline which have been studied extensively, exploration of new SCO systems with 1,2,4-triazoles has a wide range of experimental space available in the search for new functional materials. An example of the use of 1,2,4-triazoles in developing new materials, is the synthesis of one-dimensional SCO polymers. These systems garner considerable interest; early examples displayed abrupt thermal SCO behaviour near ambient temperatures with wide hysteresis loops, making them viable for potential applications.

Changes to SCO systems, that can completely remove SCO characteristics include: Changing counterions, different polymorphs and solvates.[84] In the case of counter-ions, the system $[Fe(bpp)_2](BF_4)_2$ shows an abrupt spin transition $T_{½}$ = 269 K and a metastable HS state when irradiated with a T(LIESST) = 110 K. On the other hand, other salts such as $[Fe(bpp)_2](PF_6)_2$ display different characteristics with $T_{½}$ = 170 K and T(LIESST) = 82 K.[16] This work also displays how free solvent molecules of crystallisation impact the transitions in these complexes with the compound $[Fe(bpp)_2](BF_4)_2{\cdot}3H_2O$ displaying effects to both thermal and light irradiated transitions with $T_{½}$ = 188 K and T(LIESST) = 70 K. As discussed above, $[Fe(abpt)_2(NCS)_2]$ displays the ability for different polymorphs of the same material to undergo different transitions or none. Polymorphism is a subject that is harder to investigate since it is not necessarily possible to design systems that will display polymorphism - crystal growth can be much more challenging to control than some of the other factors discussed above.

The field of spin crossover is ever expanding, with new discoveries forging the way towards readily tuneable systems for real-world applications. Whether this be through manipulation of the ligand, the metal centre, or via the blending of different disciplines, several methods have been used to design and promote SCO behaviour through

exposure to external stimuli. The aim of the work presented in the forthcoming chapters takes some of these ideas such as the modification of ligands and the application of high pressure to achieve SCO behaviour in a range of new complexes

1.6 Overview

This chapter has discussed the phenomenon spin crossover where exposure to external stimuli can cause spin state transitions in certain metal complexes. These external stimuli can be (but are not limited to) temperature, light and pressure. The potential applications of these systems have been discussed. The spin states of these systems can be investigated with single crystal X-ray diffraction among other techniques and it can also provide insight into the characteristics that make these transitions possible such as interactions in the crystal structure (hydrogen bonding and π-π stacking). Examples of these systems were discussed such as $[Fe(Phen)_2(NCS)_2]$, $[Fe(Bpp)_2](BF_4)_2$ and $[Fe(abpt)_2(NCS)_2]$ and the emerging results based upon the latter system. Finally, the other changes to these systems that can affect the transition behaviour of these complexes, such as polymorphism and the effects of counter ions.

Chapter 2 will discuss one of these results in the form of a high-pressure study on polymorph D of $[Fe(abpt)_2(NCS)_2]$, revealing new structures previously inaccessible. With these results in mind, Chapter 3 will discuss the synthesis of new novel ligands to be used in the creation of metal complexes to be explored for unusual behaviour such as SCO. Chapters 4-6 describe interesting outcomes from these coordination experiments in the form of Fe(II) systems each that display unique properties. Chapter 7 is a collection of various metal complexes formed during this work that has been analysed for their structure. These structures contain multiple metal centres such as Fe(II), Co(II) and Mn(III) but these systems did not display unique behaviour such as SCO and some require further experimentation. Chapter 8 discusses this requirement for further experimentation in terms of future work for these compounds and the final conclusions of the thesis. Finally, there is the inclusion of an experimental section detailing how the new compounds were synthesised and an appendix containing the crystallographic refinement details.

1.7 References

1 K. Senthil Kumar and M. Ruben, *Coord. Chem. Rev.*, 2017, **346**, 176–205.

2 P. Gütlich, *Eur. J. Inorg. Chem.*, 2013, 581–591.

3 S. Decurtins, P. Gutlich, C. P. Kohler, H. Spiering and A. Hauser, *Chem. Phys. Lett.*, 1984, **105**, 1.

4 J. F. Létard, *J. Mater. Chem.*, 2006, **16**, 2550–2559.

5 Hauser, Andreas, P. Gütlich and H. A. Goodwin, *Top. Curr. Chem.*, 2004, 158–198.

6 V. Ksenofontov, A. B. Gaspar, P. Gütlich and H. A. Goodwin, *Top. Curr. Chem.*, 2004, **235**, 23–64.

7 G. Molnár, T. Guillon, N. O. Moussa, L. Rechignat, T. Kitazawa, M. Nardone and A. Bousseksou, *Chem. Phys. Lett.*, 2006, **423**, 152–156.

8 J.-F. Létard, P. Guionneau and L. Goux-Capes, *Top. Curr. Chem.*, 2004, **235**, 221–249.

9 L. Cambi and L. Szegö, *Berichte der Dtsch. Chem. Gesellschaft*, 1931, **64**, 2591–2598.

10 P. Gütlich and H. A. Goodwin, *Top. Curr. Chem.*, 2012, **1**, 1–47.

11 A. H. Ewald, R. L. Martin, I. G. Ross and A. H. White, *Proc. R. Soc. Lond.*, 1963, **280**, 235–257.

12 O. G. Shakirova and L. G. Lavrenova, *Crystals*, 2020, **10**, 1–19.

13 A. Enriquez-Cabrera, A. Rapakousiou, M. Piedrahita Bello, G. Molnár, L. Salmon and A. Bousseksou, *Coord. Chem. Rev.*, 2020, **419**, 213396.

14 M. Nakaya, R. Ohtani, L. F. Lindoy and S. Hayami, *Inorg. Chem. Front.*, 2021, **8**, 484–498.

15 W. A. Baker and H. M. Bobonich, *Inorg. Chem.*, 1964, **3**, 1184–1188.

16 S. Marcén, L. Lecren, C. L., H. A. Goodwin and J.-F. Létard, 2002, **358**, 87–95.

17 A. Hauser, P. Gütlich and H. A. Goodwin, *Top. Curr. Chem.*, 2004, **233**, 49.

18 P. Guionneau, M. Marchivie, G. Bravic, J.-F. Létard and D. Chasseau, *Top. Curr. Chem.*, 2004, **234**, 97–128.

19 P. Gütlich, Y. Garcia and H. A. Goodwin, *Chem. Soc. Rev.*, 2000, **29**, 419–427.

20 P. Gutlich, S. Decurtins, K. M. Hasselbach, H. Spiering and A. Hauser, *Inorg. Chem.*, 1985, **24**, 2174–2178.

21 S. Brooker, *Chem. Soc. Rev.*, 2015, **44**, 2880–2892.

22 D. Unruh, P. Homenya, M. Kumar, R. Sindelar, Y. Garcia and F. Renz, *Dalt. Trans.*, 2016, **45**, 14008–14018.

23 P. Gütlich, *Top. Curr. Chem.*, 2004, **234**, 231.

24 M. Sorai, J. Ensling, K. M. Hasselbach and P. Gütlich, *Chem. Phys.*, 1977, **20**, 197–208.

25 Y. Qi, E. W. Müller, H. Spiering and P. Gütlich, *Chem. Phys. Lett.*, 1983, **101**, 503–505.

26 D. Collison, C. D. Garner, C. M. Mcgrath, J. F. W. Mosselmans, M. D. Roper, J. M. W. Seddon and N. A. Young, *Dalt. Trans.*, 1997, **2**, 4371–4376.

27 J. F. Létard, P. Guionneau, L. Rabardel, J. A. K. Howard, A. E. Goeta, D. Chasseau and O. Kahn, *Inorg. Chem.*, 1998, **37**, 4432–4441.

28 A. Desaix, O. Roubeau, J. Jeftic, J. G. Haasnoot, K. Boukheddaden, E. Codjovi, J. Linarès, M. Noguès and F. Varret, *Eur. Phys. J. B*, 1998, **6**, 183–193.

29 F. Renz, M. Hasegawa, T. Hoshi, U. El-Ayaan, W. Linert and Y. Fukuda, *Mol. Cryst. Liq. Cryst. Sci. Technol. Sect. A Mol. Cryst. Liq. Cryst.*, 1999, **335**, 1243–1252.

30 T. G. Gopakumar, F. Matino, H. Naggert, A. Bannwarth, F. Tuczek and R. Berndt, *Angew. Chemie - Int. Ed.*, 2012, **51**, 6262–6266.

31 L. Pauling and C. D. Coryell, *Proc. Natl. Acad. Sci.*, 1936, **22**, 210–216.

32 R. Claude, T. Granier, B. Gallois, J. Zarembowitch and C. Roux, *Inorg. Chem.*, 1994, **4**, 2273–2279.

33 S. Venkataramani, U. Jana, M. Dommaschk, F. D. Sonnichsen, F. Tuczek and R. Herges, *Science (80-.).*, 2011, **445**, 445–449.

34 P. Gütlich, A. Hauser and H. Spiering, *Angew. Chemie Int. Ed. Eng*, 1994, **33**, 2024–2054.

35 Y. Garcia and P. Gütlich, *Top. Curr. Chem.*, 2004, **234**, 49–62.

36 H. Spiering and N. Willenbacher, *J. Phys. Condens. Matter*, 1989, **1**, 10089–10105.

37 O. Kahn and C. J. Martinez, *Science (80-.).*, 1998, **279**, 44–48.

38 B. Gallois, C. Hauw, J. A. Real and J. Zarembowitch, *Inorg. Chem.*, 1990, **29**, 1152–1158.

39 Z. J. Zhong, J. Q. Tao, Y. Zhi, C. Y. Dun, Y. J. Liu and X. Z. You, *Dalt. Trans.*, 1998, **2**, 327–328.

40 J. A. Real, B. Gallois, T. Granier, S. P. Franz and J. Zarembowitch, *Inorg. Chem.*, 1992, **31**, 4972–4979.

41 A. Hauser, *Chem. Phys. Lett.*, 1986, **124**, 543–548.

42 P. Guionneau, F. Le Gac, A. Kaiba, J. S. Costa, D. Chasseau and J. F. Létard, *Chem. Commun.*, 2007, 3723–3725.

43 M. L. Boillot, J. Zarembowitch and A. Sour, *Top. Curr. Chem.*, 2004, **234**, 261–275.

44 K. Takahashi, Y. Hasegawa, R. Sakamoto, M. Nishikawa, S. Kume, E. Nishibori and H. Nishihara, *Inorg. Chem.*, 2012, **51**, 5188–5198.

45 B. Rösner, M. Milek, A. Witt, B. Gobaut, P. Torelli, R. H. Fink and M. M. Khusniyarov, *Angew. Chemie - Int. Ed.*, 2015, **54**, 12976–12980.

46 J. F. Létard, P. Guionneau, O. Nguyen, J. S. Costa, S. Marcén, G. Chastanet, M. Marchivie and L. Goux-Capes, *Chem. - A Eur. J.*, 2005, **11**, 4582–4589.

47 H. Liu, A. Fujishima and O. Sato, *Appl. Phys. Lett.*, 2005, **86**, 1–3.

48 S. Bonhommeau, G. Molnár, S. Cobo, D. Ostrovskii and A. Bousseksou, *Polyhedron*, 2009, **28**, 1610–1613.

49 S. Bonhommeau, G. Molnár, A. Galet, A. Zwick, J. A. Real, J. J. McGarvey and A. Bousseksou, *Angew. Chemie - Int. Ed.*, 2005, **44**, 4069–4073.

50 E. Freysz, S. Montant, S. Létard and J. F. Létard, *Chem. Phys. Lett.*, 2004, **394**, 318–323.

51 S. Speziale, A. Milner, V. E. Lee, S. M. Clark, M. P. Pasternak and R. Jeanloz, *Proc. Natl. Acad. Sci. U. S. A.*, 2005, **102**, 17918–17922.

52 A. B. Gaspar, G. Molnár, A. Rotaru and H. J. Shepherd, *Comptes Rendus Chim.*, 2018, **21**, 1095–1120.

53 A. Bouseksou, G. Molnár and G. Matouzenko, *Eur. J. Inorg. Chem.*, 2004, 4353–4369.

54 V. Legrand, S. Pechev, J. F. Létard and P. Guionneau, *Phys. Chem. Chem. Phys.*, 2013, **15**, 13872–13880.

55 P. Gütlich, A. B. Gaspar, Y. Garcia and V. Ksenofontov, *Comptes Rendus Chim.*, 2007, **10**, 21–36.

56 H. E. Mason, W. Li, M. A. Carpenter, M. L. Hamilton, J. A. K. Howard and H. A. Sparkes, *New J. Chem.*, 2016, **40**, 2466–2478.

57 A. B. Gaspar, M. C. Muñoz, N. Moliner, V. Ksenofontov, G. Levchenko, P. Gütlich and J. A. Real, *Monatsh. Chem.*, 2003, **134**, 285–294.

58 C. E. Weir, E. R. Lippincott, A. Van Valkenburg and E. N. Bunting, *J. Res. Natl. Bur. Stand. Sect. A Phys. Chem.*, 1959, **63A**, 55.

59 G. J. Piermarini, S. Block, J. D. Barnett and R. A. Forman, *J. Appl. Phys.*, 1975, **46**, 2774–2780.

60 J. K. McCusker, A. L. Rheingold and D. N. Hendrickson, *Inorg. Chem.*, 1996, **35**, 2100–2112.

61 M. Marchivie, P. Guionneau, J.-F. Létard and D. Chasseau, *Acta Crystallogr. Sect. B Struct. Sci. Cryst. Eng. Mater.*, 2003, **B59**, 479–486.

62 B. J. Cosier and A. M. Glazer, *J. Appl. Crystallogr.*, 1986, **19**, 105–107.

63 E. Kuzmann, Z. Homonnay, Z. Klenscar and R. Szalay, *Molecules*, 2021, **26**,

1062.

64 J.-P. Tuchagues, A. Bousseksou, G. Molnár, J. J. McGarvey and F. Varret, *Top. Curr. Chem.*, 2004, **235**, 84–103.

65 P. Gütlich, A. B. Gaspar and Y. Garcia, *Beilstein J. Org. Chem.*, 2013, **9**, 342–391.

66 W. Clegg, A. J. Blake, R. O. Gould and P. Main, *Crystal Structure Analysis: Principles and Practice*, Oxford University Press, 2nd edn., 2009.

67 A. E. Goeta, L. K. Thompson, C. L. Sheppard, S. S. Tandon, C. W. Lehmann, J. Cosier, C. Webster and J. A. K. Howard, *Acta Crystallogr. Sect. C Cryst. Struct. Commun.*, 1999, **55**, 1243–1246.

68 M. R. Probert, C. M. Robertson, J. A. Coome, J. A. K. Howard, B. C. Michell and A. E. Goeta, *J. Appl. Crystallogr.*, 2010, **43**, 1415–1418.

69 C. J. McMonagle and M. R. Probert, *J. Appl. Crystallogr.*, 2019, **52**, 445–450.

70 O. Kahn and E. Codjovi, *Phil. Trans. R. Soc.*, 1996, **354**, 359–379.

71 O. Kahn, J. Kröber and C. Jay, *Adv. Mater.*, 1992, **4**, 718–728.

72 L. Salmon, G. Molnár, S. Cobo, P. Oulié, M. Etienne, T. Mahfoud, P. Demont, A. Eguchi, H. Watanabe, K. Tanaka and A. Bousseksou, *New J. Chem.*, 2009, **33**, 1283–1289.

73 G. Levchenko, G. Bukin, H. Fylymonov, Q. Li, A. B. Gaspar and J. A. Real, *J. Phys. Chem. C*, 2019, **123**, 5642–5646.

74 K. Boukheddaden, M. H. Ritti, G. Bouchez, M. Sy, M. M. Dîrtu, M. Parlier, J. Linares and Y. Garcia, *J. Phys. Chem. C*, 2018, **122**, 7597–7604.

75 R. W. Hogue, S. Singh and S. Brooker, *Chem. Soc. Rev.*, 2018, **47**, 7303–7338.

76 J. Olguín, *Coord. Chem. Rev.*, , DOI:10.1016/j.ccr.2019.213148.

77 D. M. Halepoto, D. G. L. Holt, L. F. Larkworthy, G. J. Leigh, D. C. Povey and G. W. Smith, *J. Chem. Soc. Chem. Commun.*, 1989, 1322–1323.

78 D. M. Halepoto, D. G. L. Holt, L. F. Larkworthy, D. C. Povey, G. W. Smith and

G. J. Leigh, *Polyhedron*, 1989, **8**, 1821–1822.

79 H. A. Goodwin and K. H. Sugiyarto, *Chem. Phys. Lett.*, 1987, **139**, 470–474.

80 N. Moliner, M. C. Muñoz, S. Létard, J. F. Létard, X. Solans, R. Burriel, M. Castro, O. Kahn and J. A. Real, *Inorganica Chim. Acta*, 1999, **291**, 279–288.

81 C. F. Sheu, S. M. Chen, S. C. Wang, G. H. Lee, Y. H. Liu and Y. Wang, *Chem. Commun.*, 2009, **2**, 7512–7514.

82 K. Sugimoto, C.-H. Shih, J. Kim, C.-F. Sheu, M. Takata, Y. Wang and K. Kato, *Dalt. Trans.*, 2010, **39**, 9794.

83 C.-H. Shih, Y. Wang, B.-M. Cheng, K. Sugimoto, M. Takata and C.-F. Sheu, *Chem. Commun.*, 2012, **48**, 5715.

84 W. Zhang, F. Zhao, T. Liu, M. Yuan, Z. M. Wang and S. Gao, *Inorg. Chem.*, 2007, **46**, 2541–2555.

85 R. Kulmaczewski and M. A. Halcrow, *CrystEngComm*, 2016, **18**, 2570–2578.

86 M. Mörtel, T. Lindner, A. Scheurer, F. W. Heinemann and M. M. Khusniyarov, *Inorg. Chem.*, 2020, **59**, 2659–2666.

87 M. A. Halcrow and G. Chastanet, *Polyhedron*, 2017, **136**, 5–12.

88 Y. Jiao, J. Zhu, Y. Guo, W. He and Z. Guo, *J. Mater. Chem. C*, 2017, **5**, 5214–5222.

89 K. S. Kumar, I. Šalitroš, E. Moreno-Pineda and M. Ruben, *Dalt. Trans.*, 2017, **46**, 9765–9768.

90 H. E. Mason, J. R. C. Musselle-Sexton, M. L. Hamilton, J. A. K. Howard, M. R. Probert and H. A. Sparkes, *New J. Chem.*, 2021, **45**, 14014–14023.

91 R. M. Hazen, T. C. Hoering and A. M. Hofmeister, *J. Phys. Chem.*, 1987, **91**, 5042–5045.

92 V. Niel, A. B. Gaspar, M. C. Muñoz, B. Abarca, R. Ballesteros and J. A. Real, *Inorg. Chem.*, 2003, **42**, 4782–4788.

93 D. Y. Aleshin, I. Nikovskiy, V. V. Novikov, A. V. Polezhaev, E. K. Melnikova and Y. V. Nelyubina, *ACS Omega*, 2021, **6**, 33111–33121.

94 V. V. Kokovkin, E. V. Korotaev, I. V. Mironov and L. G. Lavrenova, *J. Struct. Chem.*, 2021, **62**, 1191–1199.

95 J. P. Xue, Y. Hu, B. Zhao, Z. K. Liu, J. Xie, Z. S. Yao and J. Tao, *Nat. Commun.*, 2022, **13**, 1–10.

96 B. Brachňaková, J. Moncoľ, J. Pavlik, I. Šalitroš, S. Bonhommeau, F. J. Valverde-Muñoz, L. Salmon, G. Molnár, L. Routaboul and A. Bousseksou, *Dalt. Trans.*, 2021, **50**, 8877–8888.

97 M. J. Heras Ojea, J. M. Van Raden, S. Louie, R. Collins, D. Pividori, J. Cirera, K. Meyer, R. Jasti and R. A. Layfield, *Angew. Chemie - Int. Ed.*, 2021, **60**, 3515–3518.

98 Z. K. Liu, Z. S. Yao and J. Tao, *Inorg. Chem.*, 2021, **60**, 10291–10301.

99 H. Zenno, F. Kobayashi, M. Nakamura, Y. Sekine, L. F. Lindoy and S. Hayami, *Dalt. Trans.*, 2021, **50**, 7843–7853.

100 F. Fürmeyer, D. Münzberg, L. M. Carrella and E. Rentschler, *Molecules*, 2020, **25**, 1–10.

101 A. Earnshaw, E. A. King and L. F. Larkworthy, *Chem. Commun.*, 1965, 180.

102 D. Villaman, C. J. McMonagle, M. R. Probert, O. Peña, Y. Moreno and M. Fuentealba, *CrystEngComm*, 2020, **22**, 3221–3233.

103 D. Fry and A. Lamble, *Brit Pat.*, 1955, **50**, 736–768.

104 V. Sharma, S. Birendra, R. Bhatia, M. Bachwani, R. Khandelwal and J. Ameta, *Pharmacol. Online*, 2011, **1222**, 1192–1222.

Chapter 2 – Pressure induced spin crossover of $[Fe(abpt)_2(NCS)_2]$ polymorph D

2.1 Introduction

This chapter will discuss a detailed high-pressure study revealing new results for the polymorph D of $[Fe(abpt)_2(NCS)_2]$ (abpt = 4-amino-3,5-bis(pyridin-2-yl)-1,2,4-triazole), a well-studied and characterized iron(II) abpt complex. A single crystal of polymorph D of $[Fe(abpt)_2(NCS)_2]$ was studied by SC-X-ray diffraction at elevated pressures utilising a diamond anvil cell.

The polymorphs A – D of $[Fe(abpt)_2(NCS)_2]$ have previously been extensively studied and reported in the literature. All four polymorphs are known to display slightly different spin crossover (SCO) behaviour.[1–6] The crystal structure of polymorph A contains a single iron(II) centre in the asymmetric unit. This iron(II) centre undergoes a thermal transition centred at $T_{½}$ = 188 K.[1] This polymorph has also been shown to display the LIESST phenomenon, at low temperature when the sample is exposed to red light, with a T_{LIESST} = 40 K.[1] It also displays SCO behaviour when the pressure is increased to 5.1(2) kbar.[2] Polymorph B originally was thought to display no SCO behaviour, with no thermal transition being observed under ambient pressure. However, experiments with increased pressure (>4.4 kbar) showed that, at increased pressure, the system can indeed undergo a spin state transition with cooling.[6] A high pressure transition at room temperature has also been observed with a change in spin state occurring between 11.5(2) and 13.5(2) kbar.[7] Polymorph C displays SCO behaviour with a thermal transition in one of the crystallographically independent iron centres based around $T_{½}$ = 86 K.[4] Crystals of polymorph C at low temperature when irradiated with a green light induce the LIESST phenomenon to be observed with a metastable HS state.[3] The discovery of the previously inaccessible structure of polymorph B led to a renewed interest into the unexplored experimental regions for further experimentations on the polymorphs of $[Fe(abpt)_2(NCS)_2]$, in particular polymorph D.

The asymmetric unit of polymorph D displayed in figure 2.1 contains two crystallographically independent Fe(II) centres, *i.e* the Fe centres that are unrelated by symmetry. One of these Fe(II) centres undergoes a thermal spin transition, $T_{½}$ = 162 K. Upon further cooling, the second Fe(II) centre does not change spin state.[3] The Light Induced Excited Spin State Trapping (LIESST) phenomenon is witnessed upon photo-irradiation of a crystal at 20 K with a 532 nm laser when the iron centre which

undergoes a thermal transition to the LS state upon cooling is promoted to a metastable HS* state.[5]

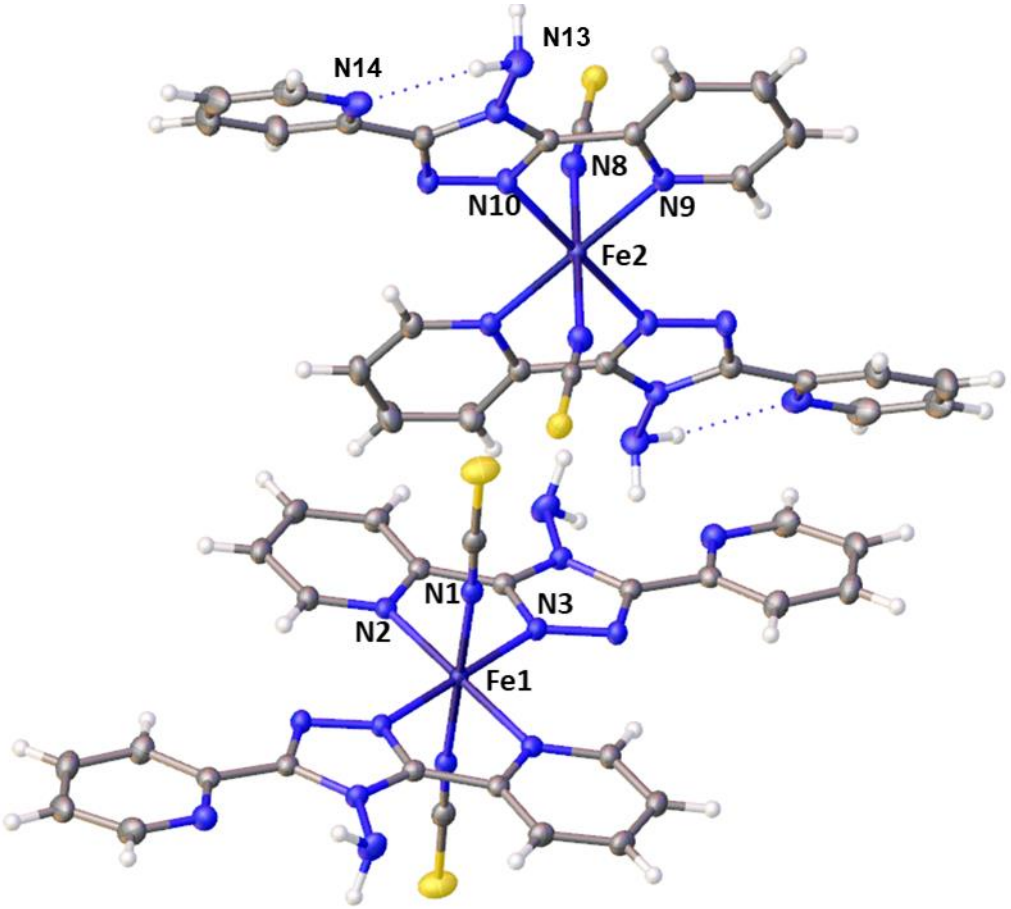

Figure 2.1. A symmetry expanded view of the crystallographic model of polymorph **D** of $[Fe(abpt)_2(NCS)_2]$ at 100 K, showing the 2 independent metal sites (Fe1 and Fe2). The anisotropic displacement parameters of all non-hydrogen atoms are shown at 50% probability.

2.2 Polymorph D high pressure study

Crystals used in this study were provided by Dr. H. Sparkes (Bristol University) have been grown over several weeks *via* slow diffusion layered technique. A methanol:water 1:1 solution containing iron(II) bis-isothiocyanate was slowly injected via a microlance needle under a methanol solution containing abpt and an interface formed between the two solutions where slow diffusion occurs. Due to the inability to separate crystals visually, SC-X-ray diffraction was used to separate single crystals into their respective polymorphic groups. A minimal data collection was performed on a Bruker D8 Venture single crystal X-ray diffractometer to obtain unit cell parameters of single crystals to identify each crystal's polymorphic form. Once a single crystal of polymorph D that

displayed high quality in the reflections present in the data collection was found, it was set aside for loading into the DAC. A high-quality crystal was required due to the challenging nature of high-pressure experiments in which the quantity of data that can be collected is limited due to the small opening angles of the DAC. A single crystal of polymorph D was mounted alongside two ruby chips in a modified Merill-Bassett type diamond anvil cell (DAC) custom built at Durham University using tungsten carbide backing plates (Easy Lab Ltd) with a nominal opening angle of 85˚ and type IA Boehler–Almax diamond anvils with 0.8 mm cutlets. Stainless steel gaskets were pre-indented and drilled to give a gasket chamber of ~0.3 mm and 0.15 mm depth and paraffin oil was used as the pressure transmitting medium (PTM) Paraffin oil is an inert oil which will not dissolve the sample and still allows suitable pressures, unlike some other PTMs such as methanol which would likely dissolve the sample. The Ruby R_1 fluorescence method was used to determine pressure inside the DAC.[8] Pressure measurements were taken before and after data collection to ensure the pressure did not change and had equilibrated before collection. The DAC was mounted onto the specialised high-pressure SC-X-ray diffractometer XIPHOS II fitted with a microfocus Ag-Kα (λ = 0.56086 Å) source.

The initial measurement for the crystal of polymorph D was completed at ambient pressure at room temperature (293 K), inside the DAC. This measurement is vital for ensuring data quality were appropriate for completion of the high-pressure experiments. The ambient data set is used to determine if the completeness of the data set will be sufficient or if it is reduced further due to the alignment of crystallographic axes with the diffractometer axes. This situation can only be resolved by reorientating the crystal within the DAC. After data collection all diffraction images were processed using the SAINT integration algorithms within the APEX3 suite[9], utilising a least squares profile fitting approach with optimised reflection box sizes and pre-scan optimisation of the unit cell and sample orientation. The DAC opening angle width was set to 38˚ for integration and further processing purposes and diamond peaks were systematically removed from the data prior to scaling and correction for absorption. SADABS[10] was utilised for interframe scaling and for the multi-scan absorption correction.

Initial structure solution was performed using SHELXT[11] via intrinsic phasing utilising the Olex2 interface.[12] This initial solution was able to locate positions for all of the non-hydrogen atoms within the asymmetric unit. A subset of the atoms in the solution were

determined to have the incorrect elemental assignment and these were corrected manually prior to refinement. Peaks in the residual electron density maps (F_o^2-F_c^2) indicated there were no further non-hydrogen atoms present with a max peak of 0.5 eÅ^{-3} located close to the iron centre and a minimum peak of -0.4 eÅ^{-3}. The positions and anisotropic displacement parameters of non-hydrogen atoms were refined freely with hydrogens added to the model geometrically and refined using a riding model. The structure was refined using the SHELXL[13] least squares minimisation algorithm in Olex2 with weighting parameters (see Table 2.3 for final refinement values) applied until the structure reached convergence with a shift/ESD of 0.000. The completeness of the dataset was calculated to be 50% to a resolution of 0.84 Å with an R_1 factor of 8.21% and wR_2: 22.31%, indicating the data were of high quality, especially considering the low completeness due to the physical constraints of the DAC.

The structural solution matched the published ambient pressure and temperature crystal structure shown in figure 2.1, consisting of two unique iron centres which are in approximately octahedral Fe-N_6 coordination geometry. The nitrogen atoms are provided from the isothiocyanate groups and two from each abpt ligand.

The packing exhibited by molecules of the metal complexes in the crystal structure of polymorph D is shown in figure 2.2, stacks form in the 010 crystallographic direction of alternating iron molecules with metal centre distances of Fe1 – Fe2 = 8.725(3) Å. The structure contains intramolecular NH-N hydrogen bonding interactions between the NH_2 (N13) group on the triazole and the nitrogen (N14) of the free 2-pyridyl displayed in figure 2.1. The Fe2 complex is involved in weak π-π interactions between the centroid of the 2-pyridyl ring and the centroid of the 2-pyridyl ring (figure 2.3).

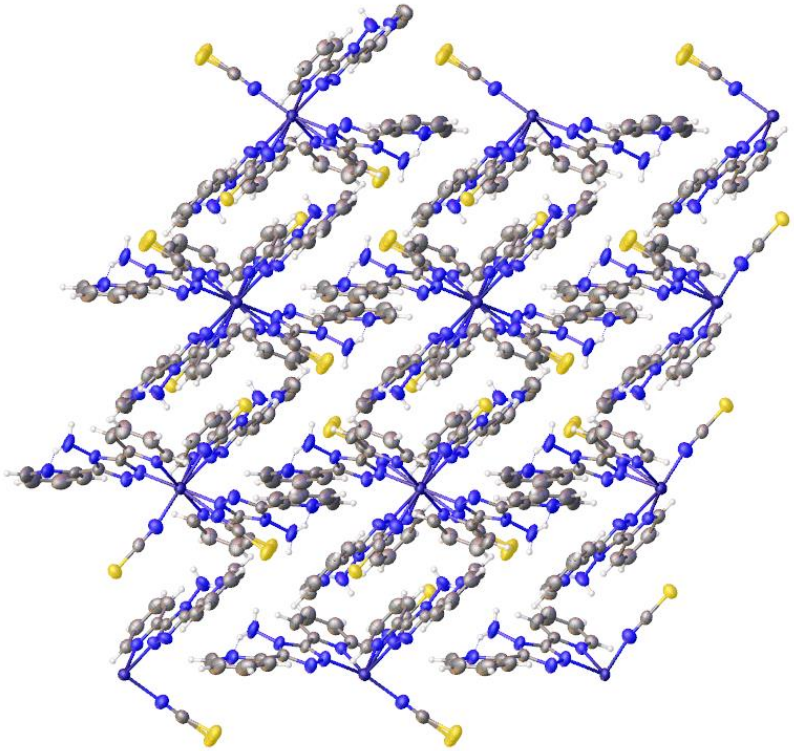

Figure 2.2. Image representing the packing of polymorph D of $[Fe(abpt)_2(NCS)_2]$ viewed down the *b* axis.

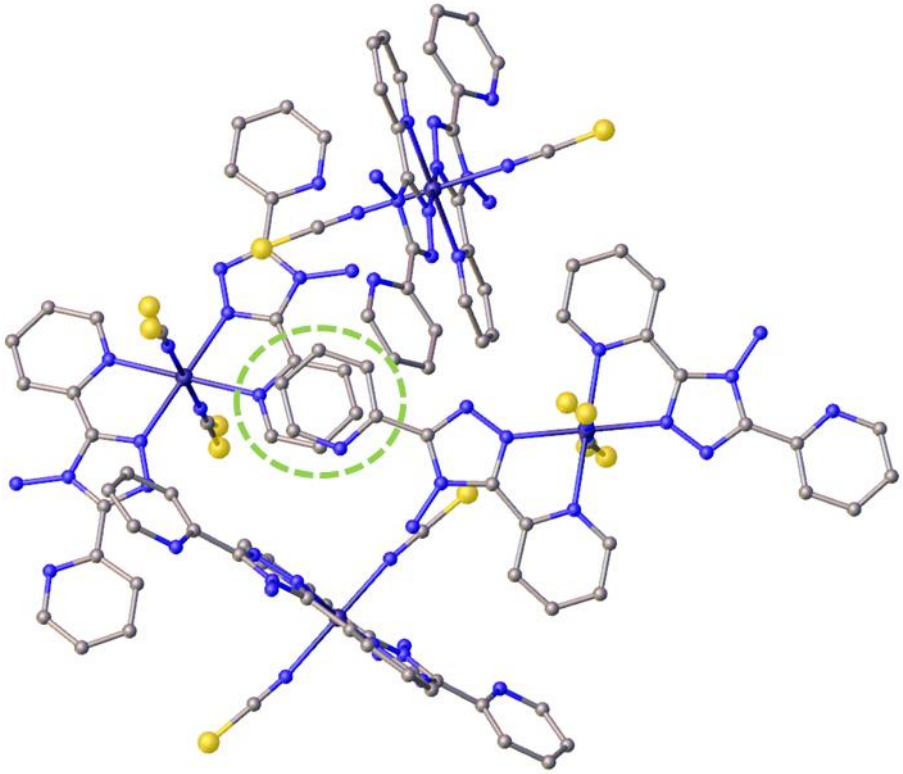

Figure 2.3. Image representing the π-π interactions between 2-pyridyl rings on separate iron complexes.

The Fe – N bond lengths of the ambient data set ranged from 2.118(5) – 2.212(4) Å for Fe1 and 2.129(5) – 2.180(5) Å for Fe2 in line with literature values and a fully HS system. The distortion parameters and octahedron volumes calculated were also consistent with HS iron(II) centres, $\Sigma = 72^{\circ}$ and 65° for Fe1 and Fe2 respectively and $v_p = 12.954$ Å^3 and 12.952 Å^3.

After completion of the refinement of the crystal structure model, it was determined that the data accessible from the crystal and it's loading into a DAC were suitable and provided high quality results, therefore, it was decided to use this crystal for the extended high-pressure measurements.

Further data collections were then performed at 1.8(2), 7.5(2), 9.6(2) 12.0(2) and 15.0(2) kbar. Ruby chip fluorescence measurements were employed for pressure monitoring throughout and repeated again after 30 mins to ensure the pressure was stable, additionally these measurements were performed once more after the data collection. The data were processed in the same manner as for the ambient dataset. However, the structure solution stage was bypassed by importing the model from the previous pressure point into the refinement starting by using the ambient model. The imported models were then refined against the appropriate dataset until convergence was achieved.

The data set at 1.8(2) kbar remained consistent with the ambient structure with a small change of unit cell parameters uniformly with increasing pressure and Fe – N bond lengths ranging from 2.116(4) – 2.210(4) Å and 2.127(4) – 2.2176(5) Å for Fe1 and Fe2 respectively both occupying a HS state.

The second pressure measurement at 7.5(2) kbar contained the first spin state switch, Fe2 – N bond lengths, Σ and v_p decreased substantially, Fe2 – N bond lengths now ranged from 1.985(4) – 2.026(6) Å indicating that the Fe2 iron centre had undergone almost complete SCO and now occupied a LS state. The Fe1 iron centre remained in a high spin state with Fe – N bond lengths consistent with the previous collections at 2.100(5) – 2.179(5) Å. This 7.5(2) kbar dataset is comparable to the low temperature structures presented in the literature where one iron centre switches spin state around $T_{½} = 162$ K.

The structural solution at 9.6(2) kbar shows the complete transition of Fe2. In addition to this the bond lengths, $\Sigma = 68^{\circ}$ and $v_p = 12.127$ Å^3 for Fe1 have also started to

decrease substantially. Fe1 – N bond lengths have decreased to 2.069(5) – 2.144(6) Å

This decrease in properties continues into the 12.0(2) kbar structure with the Fe1 – N bond lengths now at 2.045(5) – 2.117(5) Å.

Finally, the 15.0(2) kbar structure has completed the transition with Fe1 – N bond lengths now indicating a fully LS state ranging from 1.984(9) – 2.012(10) Å. Both iron centres are now occupying LS states, *i.e.* a fully low spin structure of polymorph D that was previously inaccessible by means of temperature induced transitions. Table 2.1 and Figure 2.4 show the relationship of the coordination spheres properties for each Fe(II) metal centre with changes in pressure.

Table 2.1. Fe - N bond lengths for polymorph D alongside distortion parameter Σ and volume of octahedron V_p.

	Ambient	1.8(2) kbar	7.5(2) kbar	9.6(2) kbar	12(2) kbar	15(2) kbar	Ambient pressure released
Fe1–N1 (Å)	2.118(5)	2.116(4)	2.100(5)	2.069(5)	2.045(5)	1.984(9)	2.106(10)
Fe1–N2 (Å)	2.212(4)	2.210(4)	2.179(5)	2.144(6)	2.117(5)	2.012(10)	2.203(11)
Fe1–N3 (Å)	2.150(4)	2.149(3)	2.135(4)	2.110(5)	2.084(4)	1.988(8)	2.147(8)
Fe2–N8 (Å)	2.129(5)	2.127(4)	1.985(4)	1.956(5)	1.949(4)	1.947(8)	2.144(11)
Fe2–N9 (Å)	2.180(5)	2.176(5)	2.026(6)	1.993(6)	1.984(5)	1.969(10)	2.188(13)
Fe2–N10 (Å)	2.161(4)	2.147(4)	2.007(5)	1.983(5)	1.976(5)	1.983(10)	2.165(10)
Σ Fe1 (˚)	72(1)	71(1)	70(1)	68(2)	67(1)	56(3)	73(3)
V_p Fe1 (Å^3)	12.954(15)	12.953(15)	12.61(2)	12.127(6)	11.707(19)	10.40(3)	12.82(4)
Σ Fe2 (˚)	65(1)	63(1)	52(2)	49(2)	50(1)	52(3)	61(3)
V_p Fe2 (Å^3)	12.952(18)	12.881(15)	10.594(17)	10.174(17)	10.056(16)	10.00(3)	13.16(4)

A dataset was collected at 17.0 kbar to try and investigate any further impact of pressure on the system, but the data quality had significantly decreased and, due to this the results were not used since they would be unreliable. A final dataset was

collected on the sample inside the DAC after the pressure had been released to obtain a second ambient structure, to aid determination of the reversibility of the process.

With the reduction in pressure both Fe centres returned to their natural HS state with Fe1 – N and Fe2 – N bond lengths ranging from 2.106(10) – 2.203(11) Å and 2.144(11) – 2.188(13) Å respectively. This means the pressure induced transitions are fully reversible, a quality which is sought-after in SCO materials. There is a small amount of deterioration of the sample quality after the highest-pressure measurement had been completed therefore there is the expected increase in errors for this final ambient pressure dataset.

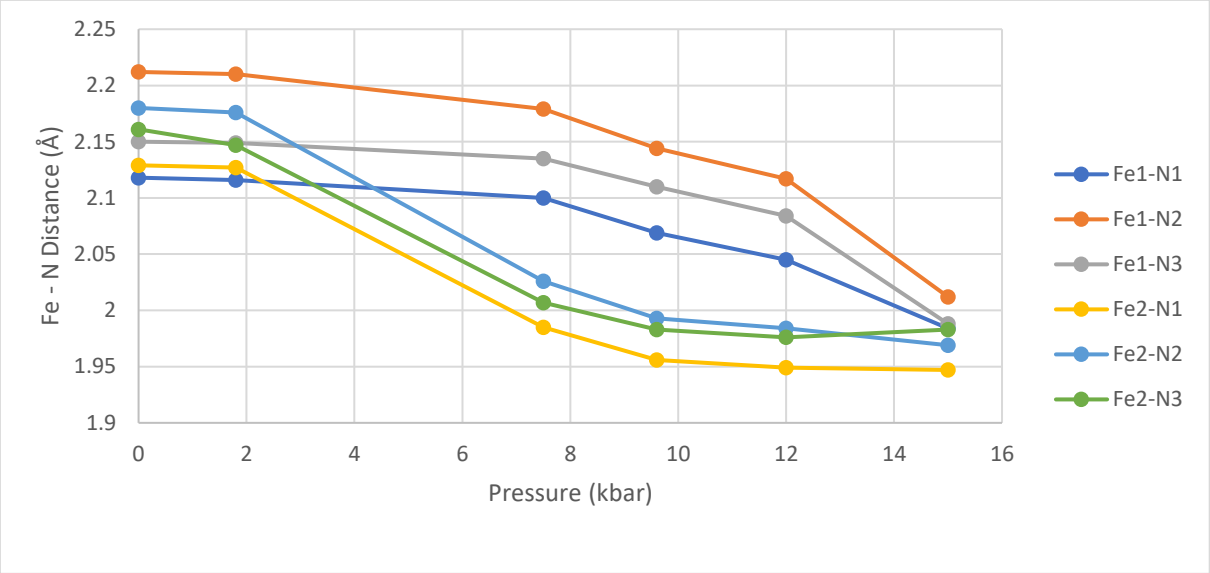

Figure 2.4. Fe – N bond lengths as pressure increases

Alongside the analysis of structural properties of the iron coordination sphere, an analysis of changes in unit cell parameters was completed between ambient and 15 kbar. The first parameters are axis length *a* which showed a total contraction of ~0.1 Å and axis *b* and *c* increased by ~0.6 and ~1 Å. A small increase in *β* angle of ~1˚ is observed with increasing pressure till 9.6(2) kbar before decreasing to ~1˚ below the ambient *β* angle in further increases of pressure. The final unit cell parameter volume, a decrease of ~12.5%, is witnessed between ambient and 15.0(2) kbar before returning to roughly the same volume when the cell is depressurised. These changes are displayed in figure 2.5 below.

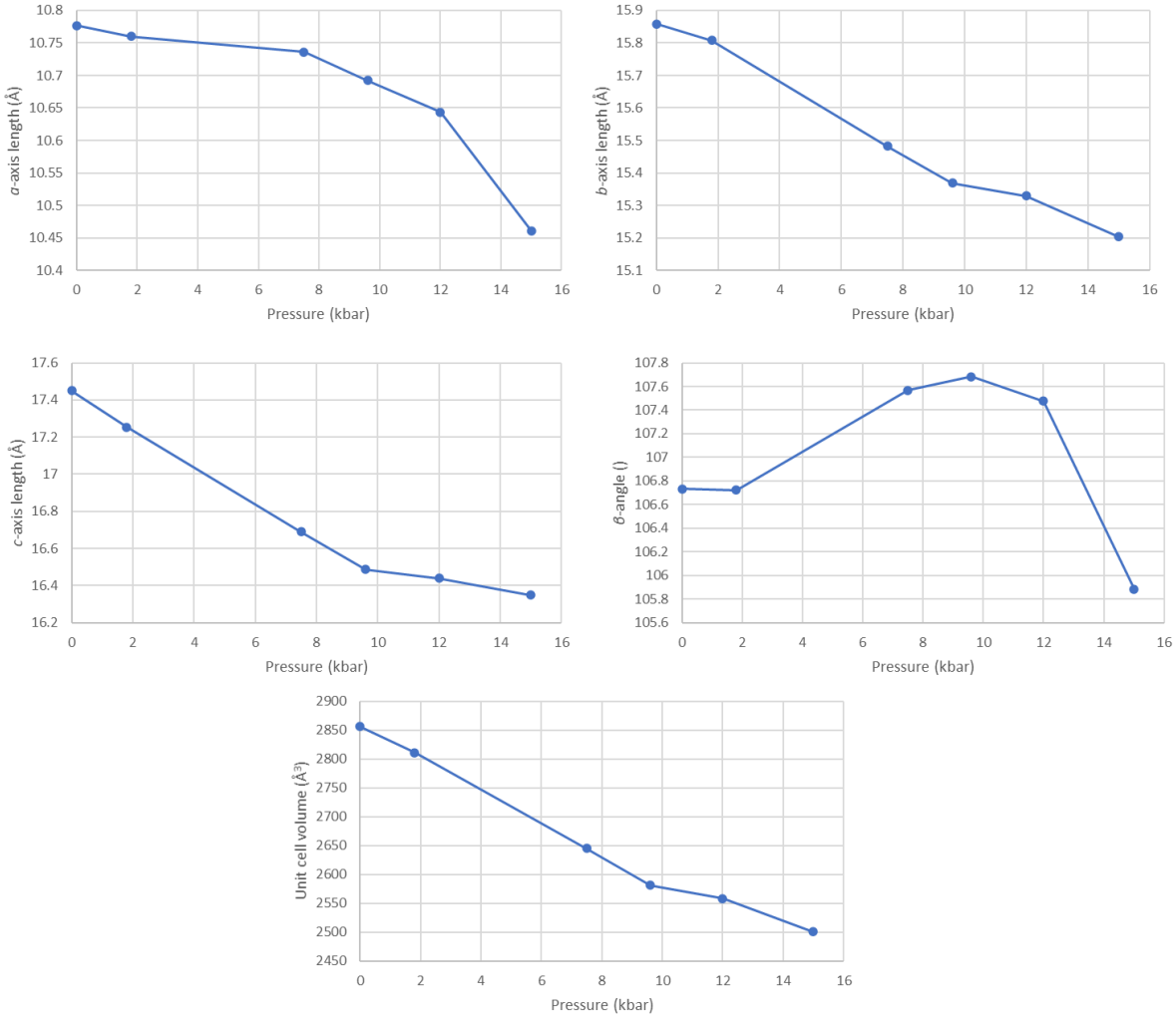

Figure 2.5. Changes in unit cell parameters with increasing pressure.

2.3 4-amino-3,5-bis(pyridin-2-yl)-1,2,4-triazole overview

This result is exceptional for multiple reasons. The first is that with the application of pressure, access to a LS-LS structure of polymorph D was enabled which was previously inaccessible with thermal experiments. Both metal centres revert to the HS state on the relaxation of pressure with only a small drop in data quality. To the author's knowledge, this is the first display of a reversible two-stepped transition induced by high-pressure. In the literature there are multinuclear species which undergo stepped transitions with temperature and could be good candidates for high pressure experiment in attempts to access states previously not observed. Combined with the discovery of a pressured induced transition in polymorph B which undergoes no thermal transitions indicates there could be other systems which show no signs of thermal SCO but could have pressure induced transitions.

Alongside the four reported polymorphs of $[Fe(abpt)_2(NCS)_2]$ which show interesting properties by displaying rather different SCO behaviour, there are other reported compounds containing abpt which exhibit SCO: these are literature compounds available in the Cambridge Structural Database (CSD). These compounds are listed in table 2.2 below, alongside properties such as the $T_{1/2}$ for these systems and if π-π interactions are present in the crystal structure to show the relationship between π-π interactions in the structure and the ability to display SCO behaviour. Suggesting some correlation between the inclusion of π-π interactions and the occurrence of SCO.

Table 2.2. Summary of abpt containing systems which display spin crossover.

Structure	Thermal Spin crossover	$T_{1/2}$	π-π
Polymorph A[1–3]	Y	188	Y
Polymorph B[6]	N	-	Y
Polymorph C[3,4]	Fe1=Y Fe2=N	86	Fe1=Y Fe2=N
Polymorph D[3,5]	Fe1=N Fe2=Y	162	Fe1=N Fe2=Y
$Fe(abpt)_2(C(CN)_3)_2$ [14]	Y	336	Y
$Fe(abpt)_2((NC)_2CC(OCH_3)C(CN)_2)_2$ [14]	N	-	N
$Fe(abpt)_2((NC)_2CC(OC_2H_5)C(CN)_2)_2$ [14]	Partial	377	Y
$Fe(abpt)_2((NC)_2CC(OC_2H_5)C(CN)_2)_2$ [14]	Fe1=Y Fe2=N	383	Fe1=Y Fe2=Y
$Fe(abpt)_2[N(CN)_2]_2$ [15]	Fe1=Y Fe2=Y	~86 stepped	Fe1=Y Fe2=Y
$Fe(abpt)_2(C_{16}SO_3)_2$ [16]	Y	-	Y
$Fe(abpt)_2Cl_2$ [17]	N	-	-
$Fe(abpt)_2(NCSe)_2$ A [1,7]	Y	-	Y
$Fe(abpt)_2(NCSe)_2$ B [6]	N	-	Y

The large number of systems generated from one ligand with different spin crossover behaviours with new results such as the pressure induced transition represented here, lead to great interest into the structural impacts that other substituted 1,2,4-triazoles could produce. The synthesis of new 1,2,4-triazoles and complexation to various metal salts to synthesise and characterise new compounds with the potential to display spin crossover behaviour. There are substituted 1,2,4-triazoles in the literature but there is

room for the synthesis of new compounds with different substituents to change the electronics of the ligand.

2.4 Conclusions

In summary, the spin crossover behaviour of polymorph D under the effects of pressure has been characterised. Previously reported to undergo a thermal transition in only one of the iron centres, the second iron centre remains HS with further cooling. The cell and structural parameters of polymorph D were monitored from ambient to 15.0(2) kbar. The first iron centre underwent a pressure induced transition at ~9.6(2) kbar, the second iron centre began to undergo a transition at higher pressures and was almost completely LS by 15.0(2) kbar. Both iron centres reverted to the HS state upon depressurisation of the diamond anvil cell.

The ligand abpt has been shown to create a large amount of iron-based metal complexes, a number of these display spin crossover behaviour. There is further room for study with the use of high pressure on these systems and the study of new substituted 1,2,4-triazoles and the potential new metal complexes that can be synthesised for further study in the aims of creating new systems which display SCO behaviour.

2.5 References

1 N. Moliner, M. C. Muñoz, S. Létard, J. F. Létard, X. Solans, R. Burriel, M. Castro, O. Kahn and J. A. Real, *Inorganica Chim. Acta*, 1999, **291**, 279–288.

2 H. E. Mason, W. Li, M. A. Carpenter, M. L. Hamilton, J. A. K. Howard and H. A. Sparkes, *New J. Chem.*, 2016, **40**, 2466–2478.

3 C. F. Sheu, S. M. Chen, S. C. Wang, G. H. Lee, Y. H. Liu and Y. Wang, *Chem. Commun.*, 2009, **2**, 7512–7514.

4 K. Sugimoto, C.-H. Shih, J. Kim, C.-F. Sheu, M. Takata, Y. Wang and K. Kato, *Dalt. Trans.*, 2010, **39**, 9794.

5 C.-H. Shih, Y. Wang, B.-M. Cheng, K. Sugimoto, M. Takata and C.-F. Sheu, *Chem. Commun.*, 2012, **48**, 5715.

6 A. B. Gaspar, M. C. Muñoz, N. Moliner, V. Ksenofontov, G. Levchenko, P. Gütlich and J. A. Real, *Monatsh. Chem.*, 2003, **134**, 285–294.

7 H. E. Mason, J. R. C. Musselle-Sexton, M. L. Hamilton, J. A. K. Howard, M. R. Probert and H. A. Sparkes, *New J. Chem.*, 2021, **45**, 14014–14023.

8 G. J. Piermarini, S. Block, J. D. Barnett and R. A. Forman, *J. Appl. Phys.*, 1975, **46**, 2774–2780.

9 *Bruker AXS Inc., Apex3, Bruker AXS Inc., Madison, Wisconsin, USA, 2015*.

10 L. Krause, R. Herbst-Irmer, G. M. Sheldrick and D. Stalke, *J. Appl. Crystallogr.*, 2015, **48**, 3–10.

11 G. M. Sheldrick, *Acta Crystallogr. Sect. A Found. Crystallogr.*, 2015, **71**, 3–8.

12 O. V Dolomanov, L. J. Bourhis, R. J. Gildea, J. A. K. Howard and H. Puschmann, *J. Appl. Crystallogr.*, 2009, **42**, 339–341.

13 G. M. Sheldrick, *Acta Crystallogr. Sect. C Struct. Chem.*, 2015, **71**, 3–8.

14 G. Dupouy, M. Marchivie, S. Triki, J. Sala-Pala, J. Y. Salaün, C. J. Gómez-García and P. Guionneau, *Inorg. Chem.*, 2008, **47**, 8921–8931.

15 C. F. Sheu, S. Pillet, Y. C. Lin, S. M. Chen, I. J. Hsu, C. Lecomte and Y. Wang, *Inorg. Chem.*, 2008, **47**, 10866–10874.

16 N. G. White, H. L. C. Feltham, C. Gandolfi, M. Albrecht and S. Brooker, *Dalt. Trans.*, 2010, **39**, 3751–3758.

17 J. A. Kitchen, A. Noble, C. D. Brandt, B. Moubaraki, K. S. Murray and S. Brooker, *Inorg. Chem.*, 2008, **47**, 9450–9458.

Chapter 3 – Synthesis of a library of 3,5-substituted-1,2,4-triazoles.

3.1 Background

Heterocycles have been widely used in the generation of metal complexes, particularly those that undergo phenomena such as spin crossover (SCO) which involves a change in spin state at the metal centre when exposed to an external stimulus such as temperature, pressure or light (*cf.* Chapter 1.2). Heterocycles such as 1,10-phenanthroline (phen), 2,6-dipyrazolyl pyridine (bpp) and 4-amino-3,5-bis(pyridin-2-yl)-1,2,4-triazole (abpt) and their derivatives have been used to create new complexes to study SCO (*cf.* Chapter 1.5).[1–4] Accordingly, the aim here was to synthesise a range of new heterocyclic compounds, that when complexed to a metal, had an effect on Δ_o and ultimately create new metal complexes that display SCO behaviour.

The success of the high-pressure study on polymorph D of $[Fe(abpt)_2(NCS)_2]$, (*cf.* Chapter 2), led to interest in the use of 4-amino-3,5-bis(pyridin-2-yl)-1,2,4-triazole (abpt) as a starting heterocyclic species. After thorough review of the literature, it was apparent there was a scarcity of substituted 1,2,4-triazoles utilised in the study of metal complexes as SCO's. Therefore, it was believed that new substituents could be introduced to the 1,2,4-triazole to induce electronic changes to the corresponding metal complex that may enable SCO behaviour. Through the introduction of substituted aromatic systems with electron donating and electron withdrawing groups, an inductive effect (+ve or -ve) through the σ and/or π network would be possible.

The abpt backbone lends itself well to this possibility, with substitution possible in the 3- and 4- position of the triazole ring, whilst maintaining the pyridine required for metal binding in the 5- position (Figure 3.1).

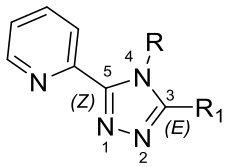

Figure 3.1. The 1,2,4-triazole backbone containing a 2-pyridyl ring to allow for bidentate coordinating motiffs and two substituents R and R_1 which will allow for different electronic effects.

It is believed that aromatic groups containing electron donating groups, such as methoxy or methyl and/or electron donating groups, such as fluoride, nitro, cyano could be introduced at the R and R_1 positions to provide a heterocyclic compound that may allow the subsequent metal complex to possess SCO properties.

To identify a synthetic route that would be capable of introducing the substitutions required, an extensive literature search was conducted.[5–7] Understandably, the synthesis of substituted 1,2,4-triazoles has been explored extensively, however, a selection of synthetic routes were investigated to find a synthesis that could be used to produce both symmetrical and unsymmetrical substituted 1,2,4-triazoles. The number of steps, yields and time taken to complete these synthetic routes were considered before selection of a safe and repeatable method was chosen.

The first syntheses investigated were those that could produce unsymmetrical substituted 1,2,4-triazoles (Scheme 3.1). Of the many routes available, those highlighted, include a one pot synthesis of 1,2,4-triazoles from isothiocyanates, monosubstituted hydrazines and sodium hydrogencyanamide.[8] In the presence of 1-(3-dimethylaminopropyl)-3-ethylcarbodiimide hydrochloride (EDC), two unsymmetrical substituted 1,2,4-triazoles were produced in medium to high yields, (40-90 %), however as mixture of products in ratios ranging from almost 100:1 to 3:1. The dominant product in each case was the isomer **A1** with NH_2 and R_2 adjacent. However, the position of the substitutions on the central triazole was not in keeping with the proposal with substituents on N1 instead of the desired N4. The purification of the mixture could prove difficult and time consuming, therefore, other routes were considered.

The second synthetic route considered the reaction of cyanamide in the presence of acid with arylthiosemicarbazides to produce a 1,2,4-triazole and a 1,3,4-thiadiazole (Reaction B).[9] The yields of 1,2,4-triazoles from this synthetic route were relatively high (60-80 %), even though the thiadiazole product can also be formed. As before, separation of the products may be difficult and the substitution of the triazole was only possible at the N_4 position with introduction of other substitution requiring a much more advanced precursor that may not be stable under the reaction conditions.

A microwave assisted reaction in one synthetic step from substituted amine to produce a disubstituted 1,2,4-triazole with a different R group on C_3 and C_5.[10] This synthetic route was used to resynthesis some previous 1,2,4-triazoles and displayed increased yields compared to previously published methods. The reaction would allow for two substituents to be located at R_1 and R_2 but with hydrogen as the only substituent at N_4. The final synthetic route investigated for unsymmetrical products is the three step synthesis of a substituted 1,2,4-triazole closely related to abpt with a chlorophenyl replacing one of the 2-pyridyl rings[11], these products with electron withdrawing and donating groups as the substituents are what are desired in this study. The downsides of this synthetic route were the slightly lower yields (~47 %) for some of the 1,2,4-triazoles. However, this synthetic route was the closest thus far of providing access to the new 1,2,4-triazoles desired.

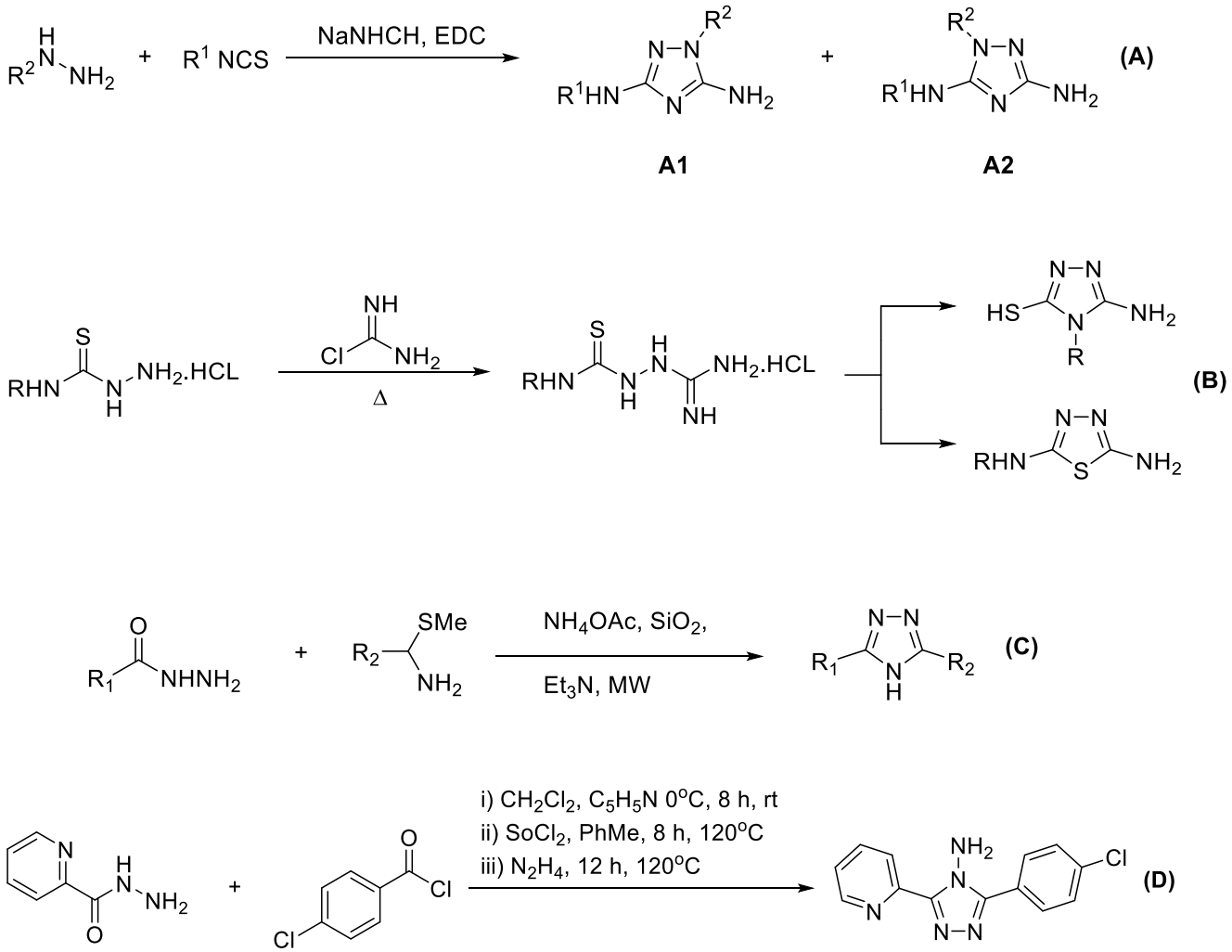

Scheme 3.1. Synthetic routes to unsymmetrical substituted triazoles A) Liu and Iwanowicz[8], B) Bondock *et al*[9], C) Daliang *et al*[10] and D) Xin *et al*[11]

Notwithstanding the synthesis of unsymmetrical triazoles, symmetrical 1,2,4-triazoles such as abpt can be produced through far fewer synthetic transformations (Scheme 3.2)

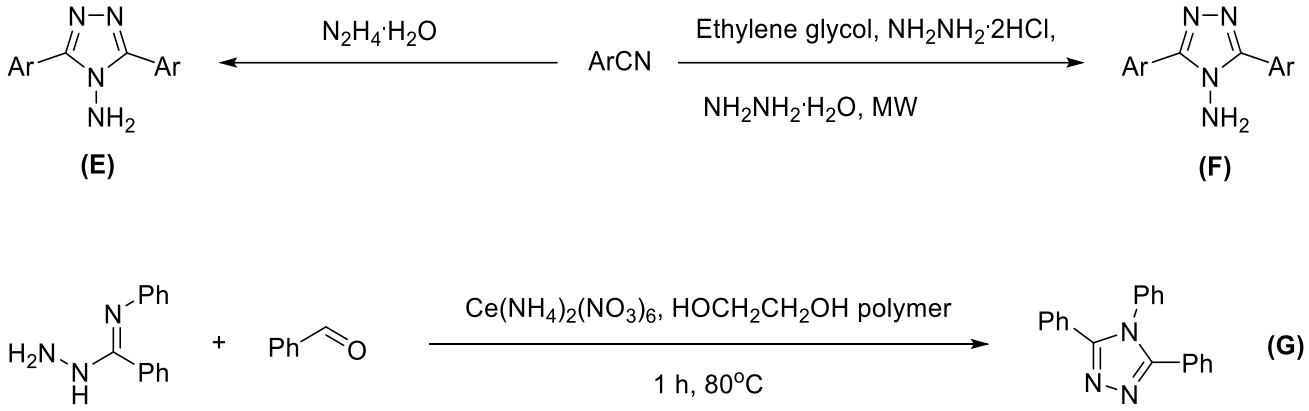

Scheme 3.2. Synthetic route to symmetrical substituted from E) Sharma *et al*[12], F) Bentiss *et al*[13] and G) Nakka *et al*[14].

One such synthesis utilises either aliphatic nitriles and hydrazines or prepared from aromatic aldehydes via nitriles using microwave irradiation.[12,13] The yields obtained were moderate (58 %) with some of the yields reported using microwave irradiation being higher than the classical heating method used in previously published *e.g.* Ar = 2-pyridyl reported a 95 % yield compared to the 85 % previously published work. These two routes were providing methods appropriate for this study, with reasonable yields and only one product, except for the NH_2 group located at N_4. The final synthetic route in scheme 3.2 consists of the synthesis of 3,4,5-trisubstiutted 1,2,4-triazoles via the oxidative cyclization of amidrazones with aldehydes utilising polyethylene glycol as a solvent and a catalyst of ceric ammonium nitrate.[14] This route has been used to synthesise other substituted 1,2,4-triazoles with aromatic rings possessing halogens in high yields (~80 %). The outcome is a symmetrical product with three aromatic rings as the substituents, and provides access to an analogue closely aligned to our desired compounds

Nevertheless, a synthetic route that was chosen that allowed for the synthesis of both symmetrical and unsymmetrical substituted 1,2,4-triazoles and had been used to synthesise substituted 1,2,4-triazoles with aromatics at R and R_1.[15] The synthetic route was attractive as it would produce a wide variety of compounds with few substrate

modifications. The substituted amines used in the first step of the synthesis would dictate the R group and the hydrazines used in the final step would dictate the group at R_1 (Scheme 3.3).

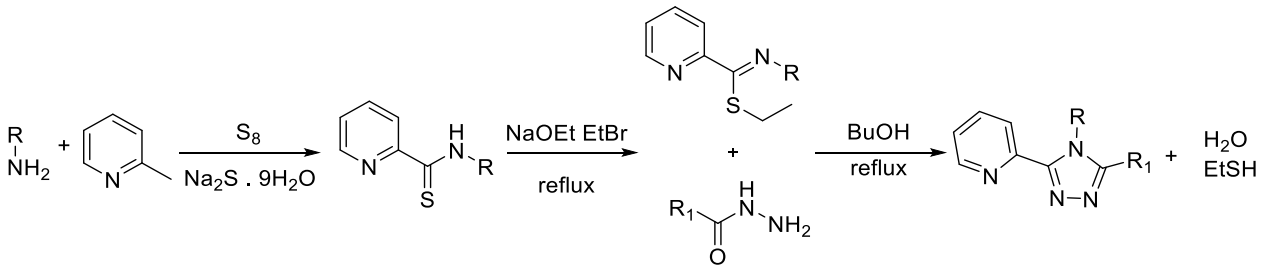

Scheme 3.3. General synthetic route used in this study.

The synthesis consists of three steps, the first is a combination of primary amine, sulphur, and 2-methylpyridine to create a carbothioamide. The carbothioamide is alkylated with bromoethane to form a carboximidothioic acid before refluxing in butanol with a hydrazide to form the substituted 1,2,4-triazoles.

Having chosen the synthetic route, it would be tested on substituted 1,2,4-triazoles present in the literature, allowing for modifications to be made to the synthesis before applying the synthesis to new compounds.[16–22]

3.2 Results

As previously described, the synthetic route comprises three main steps, the first being the reaction between primary amines, 2-methyl pyridine, and sulphur with sodium sulphide as a catalyst to synthesis a carbothioamide (Scheme 3.4).

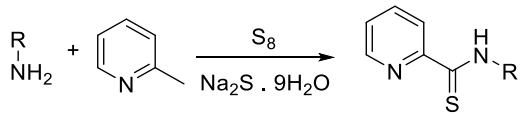

Scheme 3.4. Step 1 of the synthetic scheme to produce the carbothioamides.

The primary amines used in this first stage of this synthesis; each included an aromatic ring, either phenyl or pyridine based. Some of these aromatic rings contained substituents such as 4-fluorophenyl, 3,5-difluorophenyl and 4-methoxyphenyl in attempts to create a range of 1,2,4-triazoles that would display different electronic effects when coordinated to a metal ion.

During this first step of the synthesis, 2-methylpyridine was used as the solvent for this reaction and therefore was in large excess. Upon completion of the reaction, the sample was filtered through a silica plug and washed with DCM, solvent was then removed via rotary evaporation, this removed some of the excess 2-methylpyridine but not all of it. The sample was then washed with diethyl ether, rotary evaporation was used to extract the product from the remaining volatiles which was mostly excess 2-methylpyridine. This method was adequate for the smaller scale reactions that were attempted, however, when the reactions were scaled up the large amount of excess 2-methylpyridine was removed via vacuum distillation. This proved to be an effective method and was employed to all future reactions on a large scale.

The purification of the carbothioamides where R = 3- or 4-pyridyl was easier, as after 48 h of heating the sample was diluted with water and acidified slowly dropwise until a pH of ~5. A slightly yellow solid precipitated and were filtered and before being left to dry in the oven overnight (~16h). This was a more rapid process with no need to vacuum distil large amounts of excess 2-methyl pyridine as with other carbothioamide products.

A specific example of this synthesis is that of *N*-(pyridine-4-yl)-2-pyridine carbothioamide used to synthesise **4** (Table 3.1). Starting with a round bottom flask loaded with 4-aminopyridine, 2-methyl pyridine, sulphur and sodium sulphate, refluxed for 48 h, the sample was then diluted in a sodium hydroxide solution and acidified with conc. HCl drop wise to pH ~5 at which point the product dropped out of solution as a brown-yellow precipitate. The product *N*-(pyridine-4-yl)-2-pyridine carbothioamide has been previously synthesised in the literature and a ^{1}H NMR spectrum was obtained to confirm the correct product and that it was clean (Figure 4.2).(ref) The peaks of interest are those observed between 7.5 – 8.8 ppm a number of aromatic signals related to the two pyridyl rings. The NMR spectrum in question should contain two peaks split into triplets and the remaining split into doublets. The final peak located at ~12.25 ppm indicative of the proton environment located on the amine. Once the synthetic route was tested on previously published compounds, new substituents were tested.

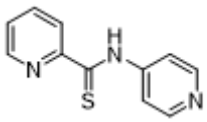

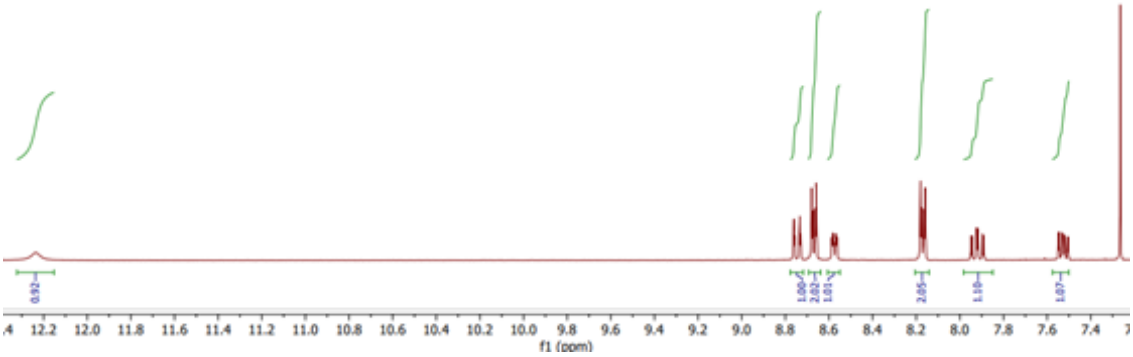

Figure 3.2. ^{1}H NMR of *N*-(pyridine-4-yl)-2-pyridine carbothioamide

Florine substituted rings such as 4-fluorophenyl and 3,5-difluorophenyl utilised to create new 1,2,4-triazoles proved to be largely successful with 8 new triazoles containing fluorinated aromatics. With this initial success of the fluorine substituents, there was an interest in using increasingly fluorinated aromatic substituents. To attempt these four amines were acquired for further synthesis of 1,2,4-triazoles. These included 2,4,6-trifluoro-benzenamine, 2,3,5,6-tetrafluoro-benzenamine, 2,3,4,5,6-pentafluoro-benzenamine and 2,3,5,6-tetrafluoro-4-pyridinamine. The four amines were tested in attempts to produce the corresponding carbothioamides, when analysed by ^{1}H NMR all of them appeared to have not reacted with the starting material as these were the primary peaks in the spectra. 2,3,4,5,6-pentafluoro-benzenamine did have a reasonable yield (>15% by NMR) present in the sample but attempts to extract it from the brown gum proved to be unsuccessful on multiple attempts.

With a procedure in place to produce the carbothioamide, the second stage required alkylation to produce a carboximidothioic acid (Scheme 3.5). This alkylation of the sulphur would hopefully increase its reactivity, becoming a better leaving group and in turn increasing yields for the final product.

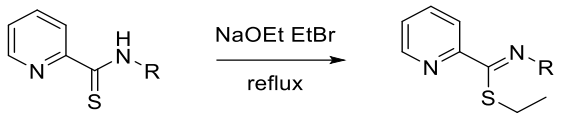

Scheme 3.5. Second stage of the synthetic route the alkylation of the carbothioamides to synthesis the intermediate.

The synthesis of **5** without this step had a reasonable yield of 71%. However, when this step was ignored, for example in the synthesis of **15**, the yield of the final 1,2,4-triazole was only 7%. The experiment was repeated this time including the ethylation step, which doubled the yield to 14%. Whilst this yield is not good it is an improvement, therefore, ethylation was included for synthesis of all compounds moving forward.

An example procedure saw excess 2-methylpyridine removed from the first stage of **4**, sodium ethoxide was prepared from adding sodium to an ethanol solution, *N*-(pyridine-4-yl)-2-pyridine carbothioamide in an ethanol solution was added to the sodium ethoxide, bromoethane was added dropwise and refluxed for 6 h. The solution was filtered to remove KBr, volatiles removed with rotary evaporation to yield *N*-(pyridine-4-yl)-ethyl ester-2-pyridinecarboximidothioic acid the intermediate for **4.**

The product had been previously synthesis in the literature and checked via ^{1}H NMR spectrum. (Ref) The two key identifier's for the successful synthesis were firstly the loss of the NH peak (12.2 ppm) from the first stage carbothioamide. Secondly, the observation of a triplet and doublet, integrating to ~2 and ~3 hydrogens respectively, located ~3.5 and 4.5ppm, indicating the presence of an ethyl group (Figure 3.3).

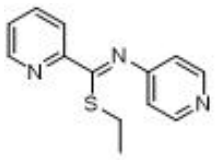

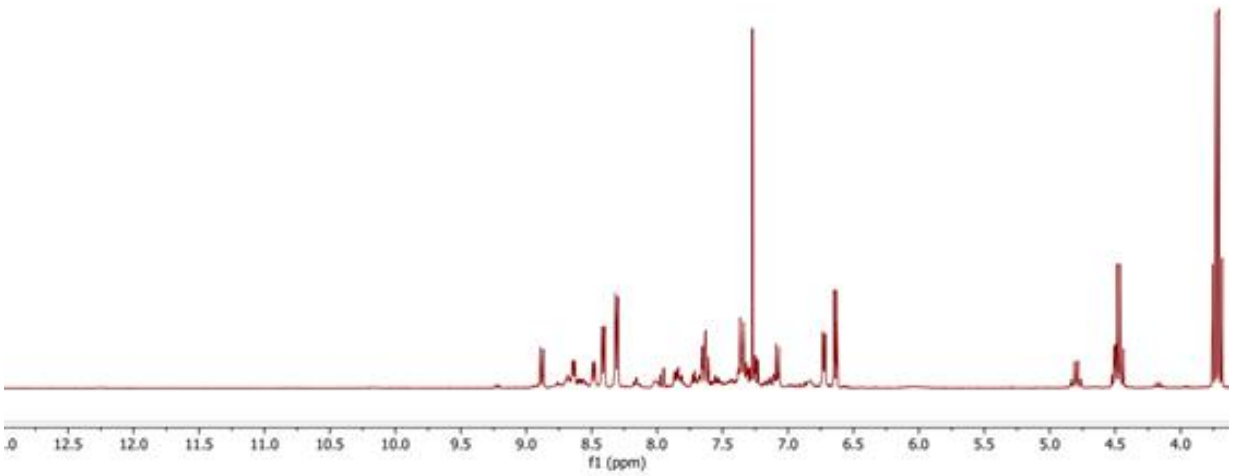

Figure 3.3. ^{1}H NMR of *N*-(pyridin-4-yl)-ethyl ester-2-pyridine carboximidothioic acid.

The final step of the synthesis for producing new 1,2,4-triazoles, involved the reflux of the carboximidothioic acid and hydrazides in n-BuOH (Scheme 4.6).

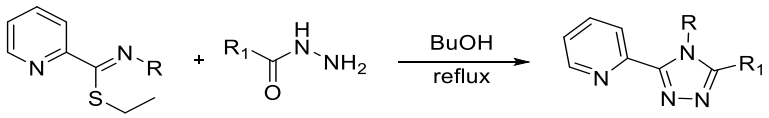

Scheme 3.6. Final stage of the synthesis taking the alkylated intermediate and hydrazide to synthesise the substituted 1,2,4-triazole.

This was the most consistent step of the route with virtually no changes needed to the reflux of the compounds. The variable for this step was the time required for the final compound to precipitate from the n-BuOH solution. Once reacted, the solutions were placed in a freezer at -4˚C, in some cases the compound precipitated in less than a day, for others the time before precipitation was 4 days. One exception to the consistency of this step was the synthesis of **9**, a substituted triazole which contained R = 4-fluorophenyl and R_1 = 4-methoxyphenyl, an unexpected result occurred. During the reflux of ethyl (Z)-*N*-(4-fluorophenyl)pyridine-2-carbothioate and 4-methoxybenzoic

acid hydrazide the 4-fluorophenyl (which was indicated as present in the starting material when analysed by ^{1}H NMR) had been removed and replaced by a hydrogen yielding **9** a literature compound which could and has been utilised for coordination experiments.[22]

Following from the previous examples**,** the synthesis of **4** was achieved from *N*-(pyridine-4-yl)-2-pyridine carbothioamide and 3-pyridine carboxylic acid hydrazide in BuOH refluxed for 48 h, the sample was cooled before placed in a freezer at -4˚C for ~2 days. A light brown powder precipitated from the solution, this precipitate was filtered and washed with diethyl ether. A ^{1}H NMR of the solid was acquired and compared to the literature. The loss of the ethyl peaks between 2 – 5 ppm and the increased number of peaks in the aromatic region 6 – 10 ppm, from 9 protons in the carbothioamide to 13 in the final 1,2,4-triazole (**4**) are used to confirm the successful synthesis (Figure 3.4).

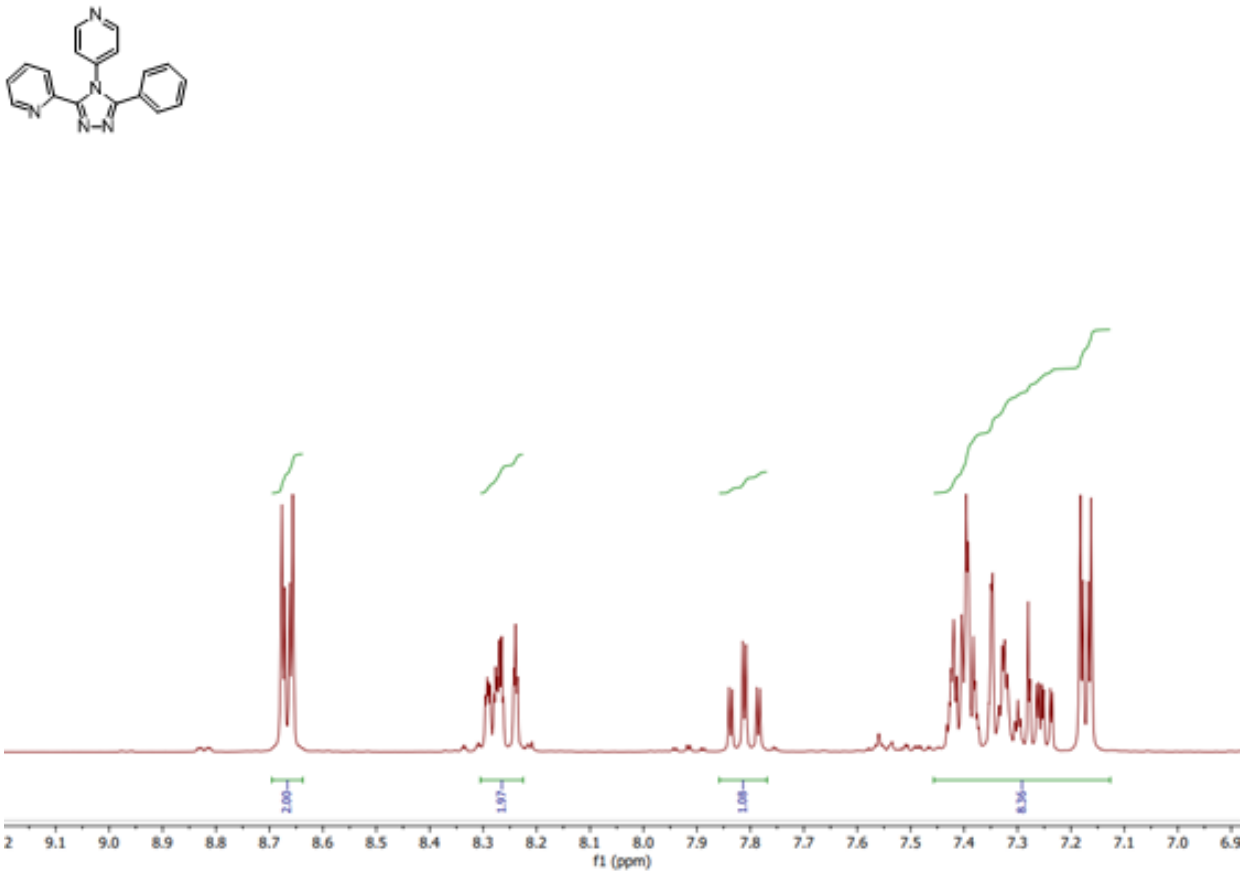

Figure 3.4. Peaks of interest in the ^{1}H NMR of the 1,2,4-triazole **4.**

Throughout this study, various other substituents were utilised in the attempts to create new substituted triazoles, the first of these attempts was to create a 1,2,4-triazole with 4-nitrophenyl at the R position, with R_1 = 2-pyridyl. The synthesis of this was attempted

twice following the general synthetic route, the outcome was the same each time producing a green-brown solid which did not match the intended compound by ^{1}H NMR.

Due to the successful synthesis of **22** a 1,2,4-triazole with 4-cyanophenyl at the R position, 4-cyanobenzoic acid hydrazide was purchased and used in attempts to synthesise new systems with 4-cyanophenyl at R_1. This was attempted with R = phenyl, 4-pyridyl and 4-fluorophenyl each experiment was undertaken twice, the first with the standard 48 h reflux in butanol, all three remained as starting material. This was repeated with a longer reflux period of ~ 100 h which did not drive the reaction forward.

This synthesis was utilised to produce 13 new substituted 1,2,4-triazoles and the synthesis of 9 literature triazoles that are of use in future studies. Table 1 shows the compounds synthesised with the substituents used at R and R_1 and their respective yields, compounds **10-22** are new compounds synthesised, compounds **1-9** are compounds which have been reported in the literature but were synthesised to both test the synthetic route and be used in complexation experiments.

Table 3.1. The 13 new triazoles and the 8 literature compounds prepared in this study and the substituents at R, R_1 and their respective yields.

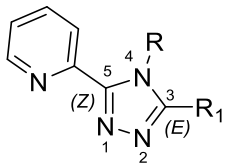

Compound No	R	R_1	Yield %(reference)
1	phenyl	phenyl	81[16]
2	phenyl	2-pyridyl	44[17]
3	phenyl	4-pyridyl	73[16]
4	4-pyridyl	phenyl	64[18]
5	4-pyridyl	2-pyridyl	71[18]
6	4-pyridyl	3-pyridyl	58[19]
7	4-pyridyl	4-pyridyl	45[20]
8	4-methoxyphenyl	2-pyridyl	76[21]
9	hydrogen	4-methoxyphenyl	38[22]
10	phenyl	3-pyridyl	32
11	phenyl	4-fluorophenyl	44
12	phenyl	4-methoxyphenyl	29
13	4-pyridyl	4-fluorophenyl	32
14	4-pyridyl	4-methoxyphenyl	30
15	3-pyridyl	2-pyridyl	14
16	4-fluorophenyl	2-pyridyl	53
17	4-fluorophenyl	phenyl	40
18	4-fluorophenyl	3-pyridyl	28
19	4-fluorophenyl	4-pyridyl	33
20	4-fluorophenyl	4-fluorophenyl	68
21	3,5-difluorophenyl	2-pyirdyl	39
22	4-Cyanophenyl	2-pyridyl	51

3.3 Crystal structures

During the ligand synthesis, we were fortunate enough to obtain crystalline material suitable for diffraction studies of **14-19** and **20-22**. The structures were collected in house on the Bruker D8 Venture or at Diamond Light Source (DLS) I19 remotely.

3.3.1 Crystal structure of 14

Suitable single crystals for SC-X-ray diffraction were grown from the slow evaporation of a methanol solution containing **14**. The sample vial was left for several weeks before nucleation was observed and a further week before single crystals of an appropriate size were present. Crystals were removed from the sample vial and placed into inert perfluoro poly ether oil, *Fomblin-YR 1800*, on a glass slide to allow manipulation and observation under a microscope.

A clear plate-shaped single crystal that displayed high visual quality under examination was selected, the crystal was mounted onto the Bruker D8 Venture diffractometer using a 50 µm Kapton loop using inert oil for adhesion and protection. A minimal data collection was performed at 150 K (laboratory standard), initial data collection showed the sample to be of high quality by quality of reflections present in diffraction frames, unit cell parameters were found and suggested a primitive monoclinic space group.

Full data collection was performed on the same crystal at 150 K without being removed from the diffractometer. Data was collected using Cu-Kα radiation (λ= 1.5406 Å). The required redundancy was set to 4 to a resolution limit of 0.84 Å. Diffraction images processed using the SAINT integration algorithms within the APEX3 suite[23] utilising a least squares profile fitting approach with the optimised reflection box sizes and pre-scan optimisation of the unit cell and sample orientation. An absorption correction was performed on the data using the SADABS multi-scan approach in XPREP.[24]

Structure solution was performed by SHELXT[25] via intrinsic phasing in the Olex2 GUI2 which confirmed a monoclinic space group setting of $P2_1/c$. The structure solution was able to locate all the non-hydrogen atoms present, some molecules required corrections to their assignments. No further peaks in the residual electron density maps (F_o^2-F_c^2) indicated there were no further atoms present in the asymmetric unit and therefore no solvent present. The positions and anisotropic displacement parameters of non-hydrogen atoms were refined freely with hydrogens added to the model geometrically and refined using a riding model. The structure was refined using SHELXL[26] least squares minimisation algorithm in the Olex2 GUI before application of a weighting parameter employed until the structure convergence as implied by a shift/ESD of 0.001. The minimum unaccounted electron density was -0.2 eÅ^{-3} and the maximum 0.2 eÅ^{-3} located along the C1 – C2 bond. The final refined structure was 99.4% complete to 0.84 Å, with an R_1 = 3.04% and wR_2 = 7.61% suggesting the data was of very high quality. The unit cell contains one unique molecule (Z' = 1) and 4 molecules of **14** in the unit cell. The final refinement results are shown in figure 3.5.

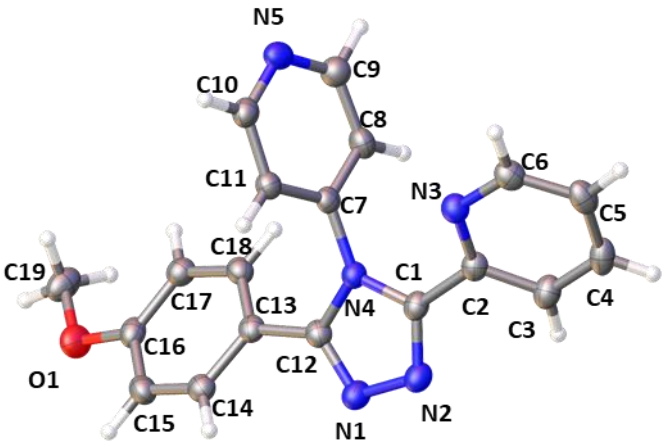

Figure 3.5. Crystal structure of **14**, anisotropic displacement parameters of all non-hydrogen atoms are shown at 50% probability.

The crystal packing of **14** is displayed in figure 3.6, there are layers of alternate facing molecules of **14.** There is no hydrogen bonding present between molecules and no π-π stacking.

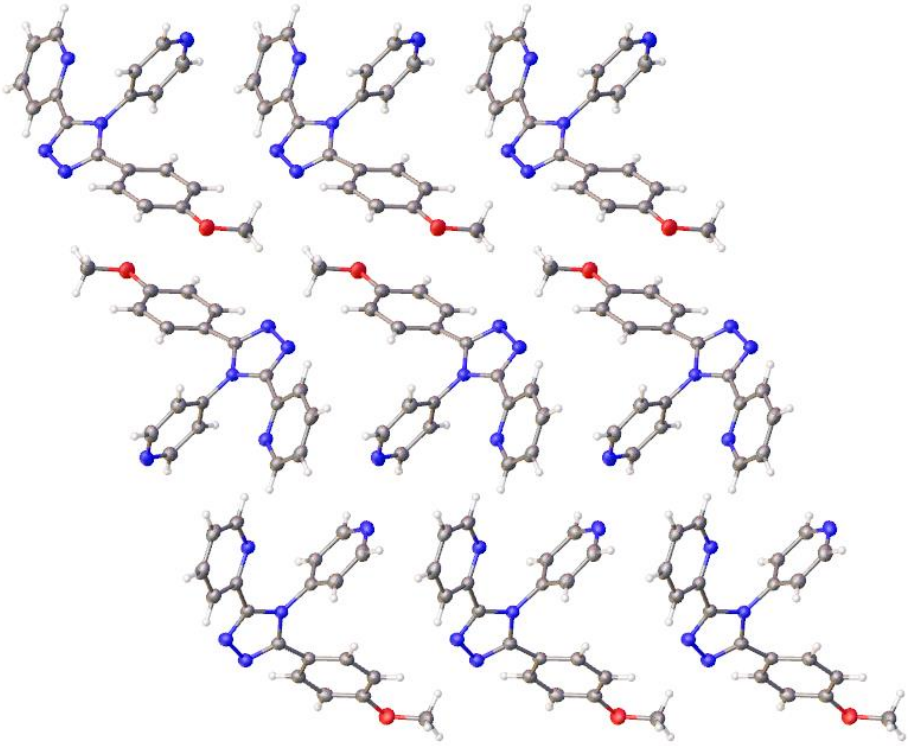

Figure 3.6. Image representing the packing of molecules of **14**, viewed along the *b* axis.

3.3.2. Crystal structure of 15 - Polymorph I

Compound **15** crystallised as two different, data on the first polymorph were collected at diamond light source. Suitable single crystals for SC-X-ray diffraction were grown from the slow evaporation of a methanol solution containing **15**. The sample vial was left for approximately one month before tiny needle shaped crystals were observed. Crystals were removed from the sample vial and placed into inert perfluoro poly ether oil, *Fomblin-YR 1800*, on a glass slide to allow manipulation and observation under a microscope.

A clear needle-shaped single crystal that displayed high visual quality under examination was selected, the crystal was mounted onto the Bruker D8 Venture diffractometer using a 50 µm Kapton loop using inert oil for adhesion and protection. A minimal data collection was performed at 150 K, initial data collection showed the sample to be of an okay quality on initial diffraction, the crystal size being exceptionally small meant the data quality collected in house might not be good. Therefore, two crystals were mounted onto 50 µm Kapton loop using inert oil for adhesion and protection. The samples were flash frozen in liquid nitrogen and placed into a sample puck to be transported to Diamond Light Source.

At DLS the first crystal of dimensions 0.196 × 0.031 × 0.016 mm was plucked from the puck by a robot and mounted onto the I-19 diffractometer. A Pre-scan was taken of the sample at 100 K to gauge its quality. A full data collection was conducted on the crystal with synchrotron radiation (λ = 0.6889). The data collected on I-19 is converted to files useable with APEX3 for inhouse structure solution using a cnf_to_sfrm python script.[27] Diffraction images processed using the SAINT integration algorithms within the APEX3 suite utilising a least squares profile fitting approach with the optimised reflection box sizes and pre-scan optimisation of the unit cell and sample orientation. An absorption correction was performed on the data using the SADABS multi-scan approach in XPREP.

Structure solution was performed by SHELXT via intrinsic phasing in the Olex2 GUI2 which confirmed a monoclinic space group setting of $P2_1/n$. Final structure contained shift/ESD of 0.001 suggesting convergence of the model. The minimum unaccounted electron density was -0.4 $eÅ^{-3}$ and the maximum 0.7 $eÅ^{-3}$. The final refined structure was 99.9% complete to 0.71 Å, with an R1 = 5.32% and wR2 = 15,11% suggesting the data were of high quality. The unit cell contains one unique molecule (Z' = 1) and 4 molecules of **6** in the unit cell. The final refinement results are shown in figure 3.7.

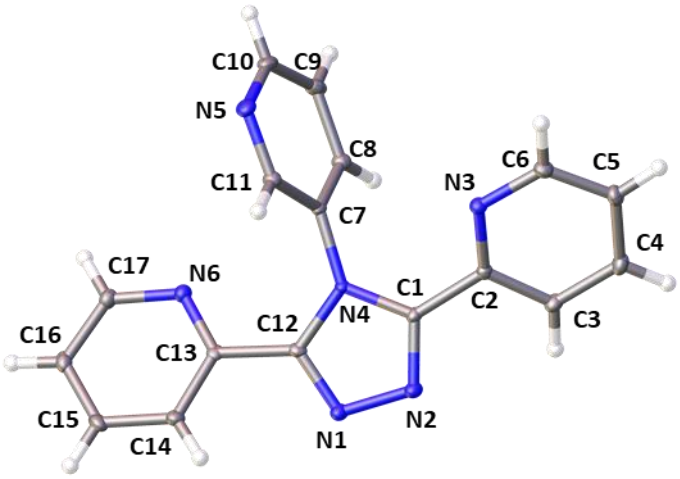

Figure 3.7. Crystal structure of **15**, anisotropic displacement parameters of all non-hydrogen atoms are shown at 50% probability.

Crystal packing of the structure is shown in figure 3.8, there are alternating pattern of molecules mirrored throughout the packing. There is no hydrogen bonding present in the structure and no π- π stacking.

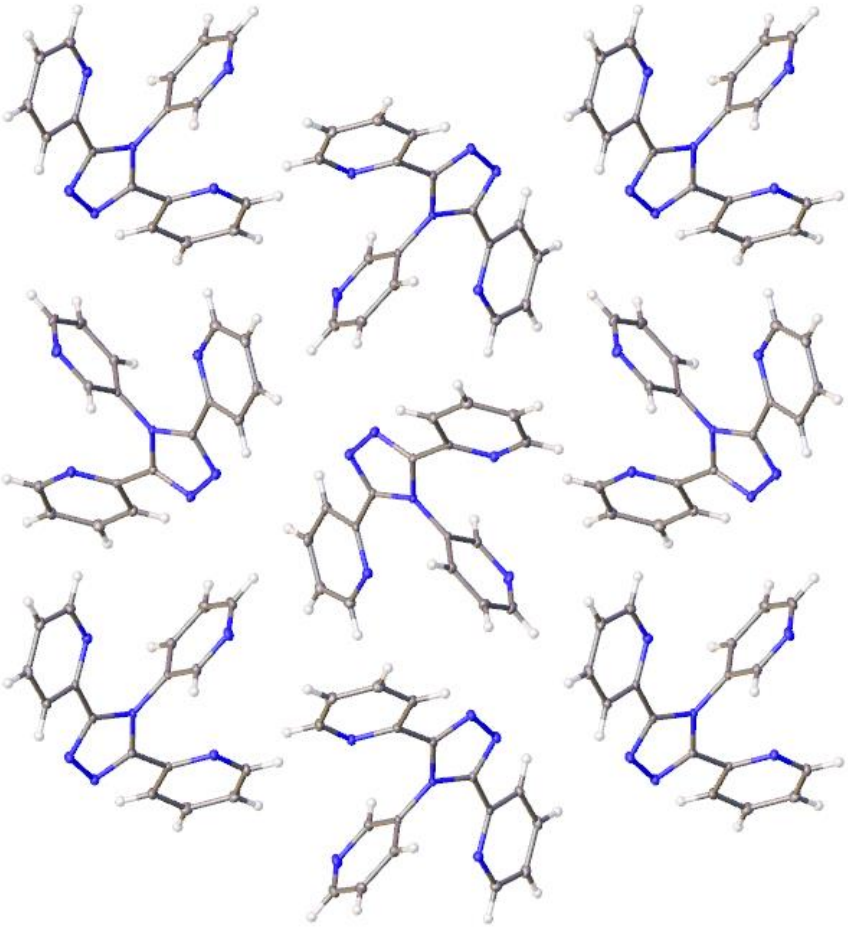

Figure 3.8. Image representing the packing of molecules of **15** polymorph I, viewed along the *a* axis.

3.3.3. Crystal structure of 15 – polymorph II

The second crystal structure for **15** was polymorph II collected in house, obtained from a crystallisation intended to produce a new metal complex, however while no crystals of a metal complex were obtained the new polymorph was discovered.. Suitable single crystals for SC-X-ray diffraction were grown from the slow evaporation of a methanol:water 3:1 mixture containing **15** and $FeCl_2$. A methanol:water 1:1 solution containing $FeCl_2$ was slowly injected under a methanol solution containing 6, careful to not disturb the interface, no colour change at the interface was noticed. After 1 month no nucleation had formed in the sample vial and the layers had diffused into one another. Venting holes were placed into the top of the sample vial to allow evaporation to occur. After 1 week nucleation had started in the bottom of the vial, after another 2 weeks small needle shaped crystals were present. Crystals were removed from the sample vial and placed into inert perfluoro poly ether oil, *Fomblin-YR 1800*, on a glass slide to allow manipulation and observation under a microscope.

A clear needle-shaped single crystal that displayed high visual quality under examination was selected. Structure solution was performed by SHELXT via intrinsic phasing in the Olex2 GUI2 which confirmed a monoclinic space group setting of P-1. Final structure contained shift/ESD of -0.001 suggesting convergence of the model. The minimum unaccounted electron density was -0.3 eÅ^{-3} and the maximum 0.4 eÅ^{-3} located near the centre of the triazole. The final refined structure was 98.5% complete to 0.81 Å, with an R_1 = 7.88% and wR_2 = 22.76% suggesting the data were of acceptable quality. The unit cell contains one unique molecule (Z' = 1) and 2 molecules of **15** in the unit cell. The final refinement results are shown in figure 3.9.

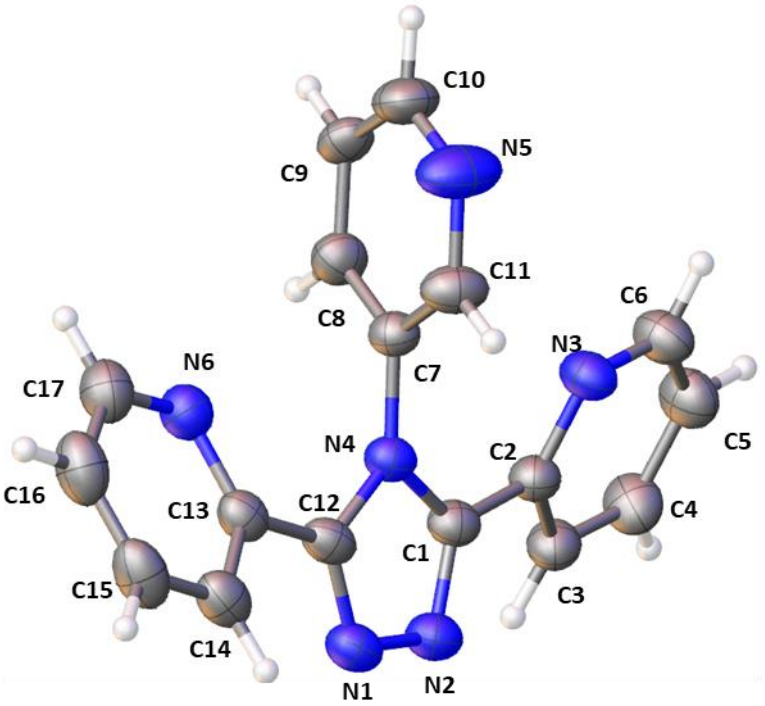

Figure 3.9. Crystal structure of **15** polymorph II, anisotropic displacement parameters of all non-hydrogen atoms are shown at 50% probability.

The packing of polymorph II (Figure 3.10) is starkly different from polymorph I, with the inversion centre present in the *P*-1 space group setting compared to the screw axis and glide plane symmetry elements present in the $P2_1/n$ space group setting. The structure contains a pattern of inverted compounds which build up to form layers.

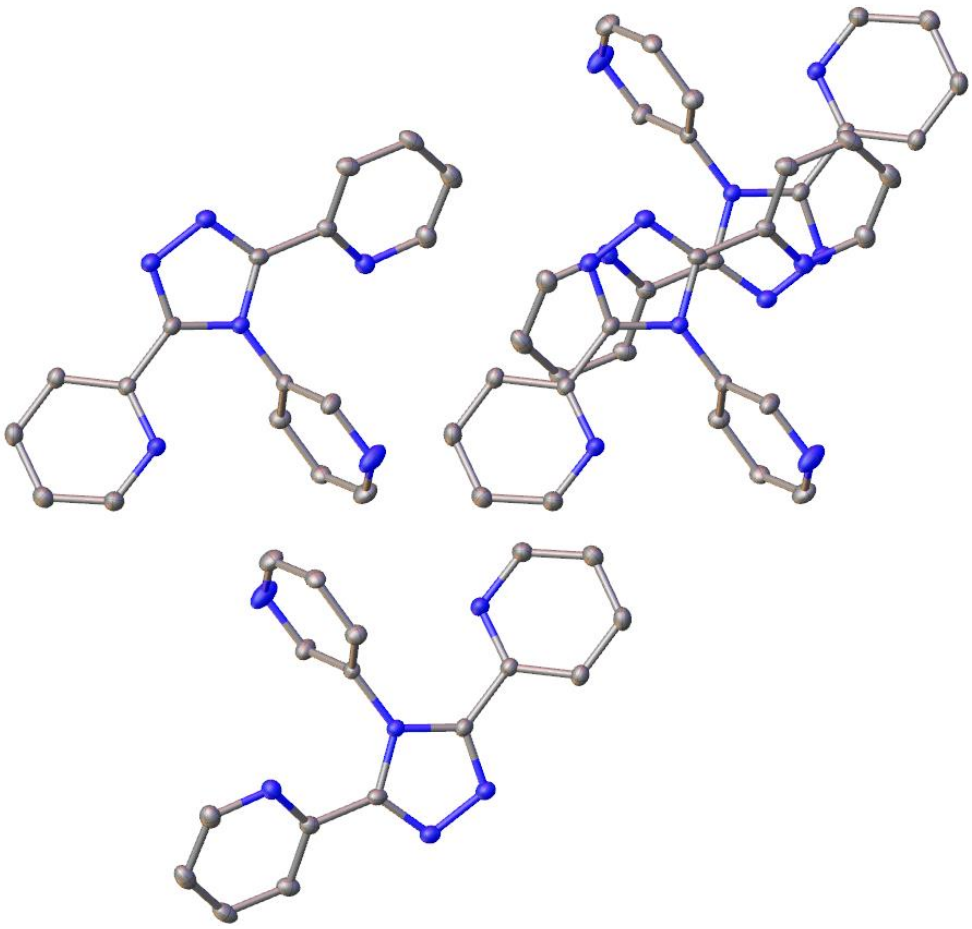

Figure 3.10. Image representing the packing of molecules of **15** polymorph II viewed along the *a* axis.

3.3.4. Crystal structure of 16

Suitable single crystals for SC-X-ray diffraction were grown from the slow evaporation of a methanol solution containing **16**. The sample vial was left for several days before nucleation was observed and a within week large rhomboid single crystals were present. Crystals were removed from the sample vial and placed into inert perfluoro poly ether oil, *Fomblin-YR 1800*, on a glass slide to allow manipulation and observation under a microscope.

A hay-brown plate-shaped single crystal that displayed high visual quality under examination was selected. Structure solution was performed by SHELXT via intrinsic phasing in the Olex2 GUI2 which confirmed a monoclinic space group setting of P-1 Final structure contained shift/ESD of 0.002 suggesting convergence of the model. Final structure is displayed in figure 3.11, the minimum unaccounted electron density was -0.4 eÅ^{-3} and the maximum 0.2 eÅ^{-3} located near C12'. The final refined structure was 98.7% complete to 0.81 Å, with an R1 = 4.17% and wR2 = 10.14% suggesting the

data were of high quality. The unit cell contains (Z' = 2) and 4 molecules of **16** in the unit cell.

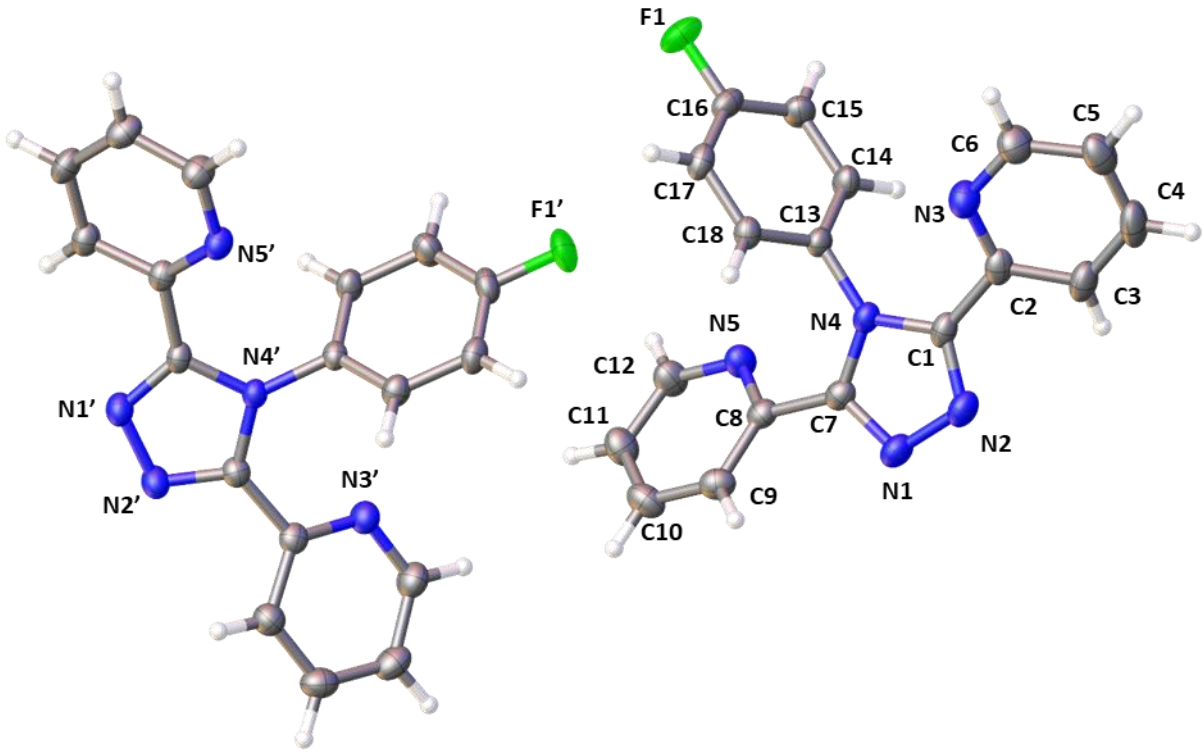

Figure 3.11. Crystal structure of **16**, anisotropic displacement parameters of all non-hydrogen atoms are shown at 50% probability.

The crystal packing of **16** is displayed in figure 3.12, the packing involves clusters of 4 molecules of **16** centred around an inversion point the larger crystal structure is built upon this with very little overlap. There is hydrogen bonding present through CH-N interactions between C14 and N1' at 2.4191(10) Å. There is no π-π stacking in the crystal structure.

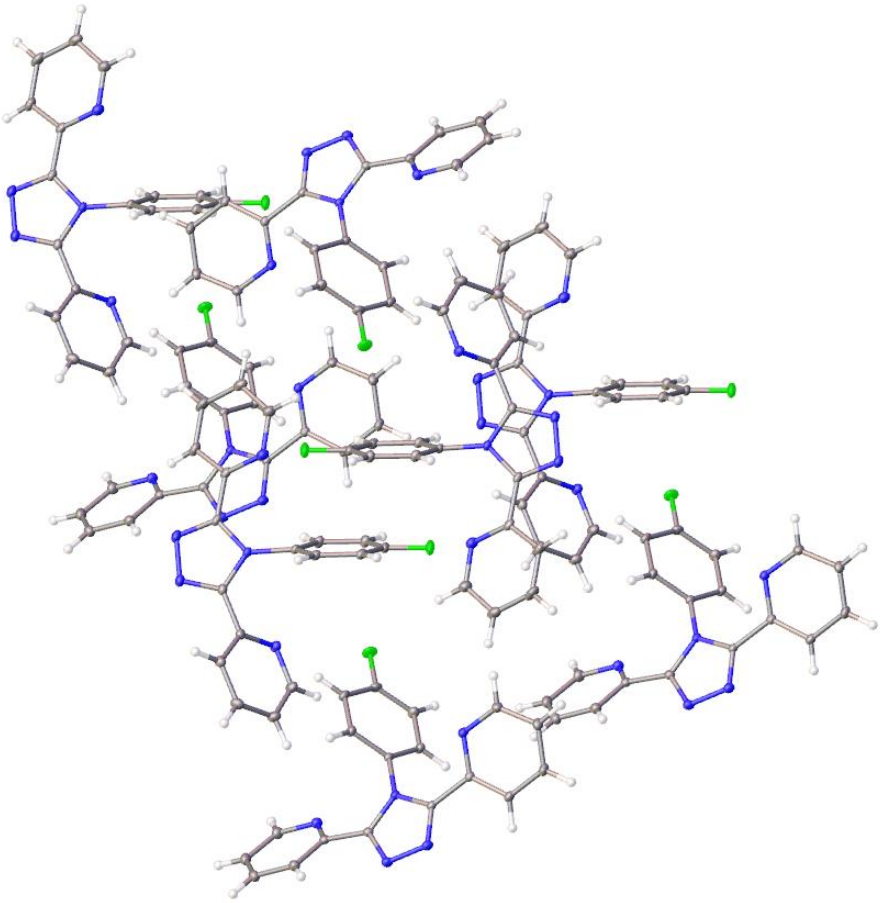

Figure 3.12. Image representing the packing of molecules of **16**, viewed along the *c* axis.

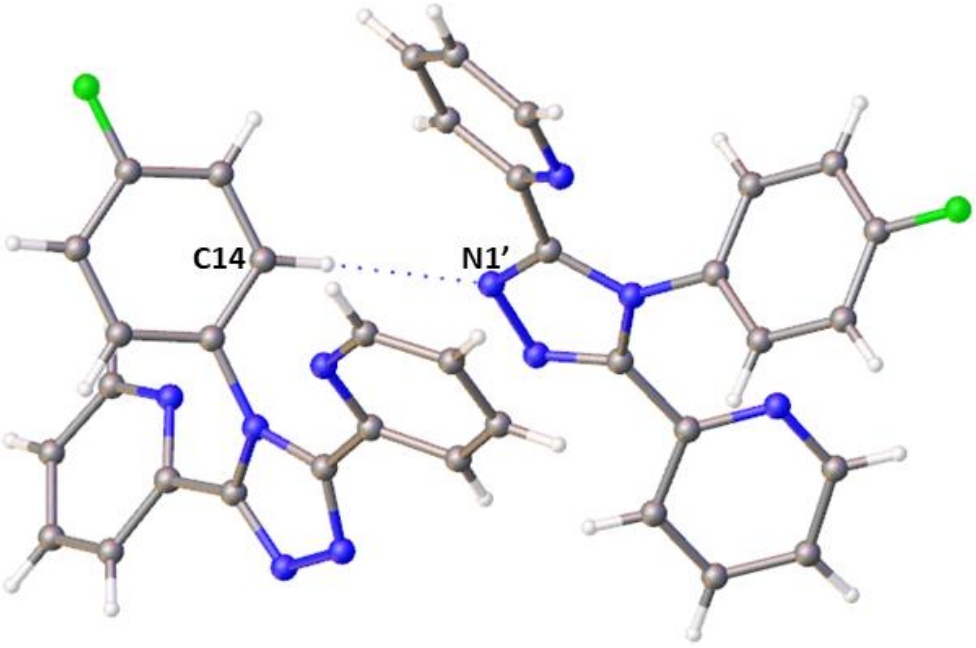

Figure 3.13. Image representing the hydrogen bonding interactions present in the crystal structure of **16**.

3.3.5 Crystal structure of 17

Suitable single crystals for SC-X-ray diffraction were grown from the slow evaporation of a methanol solution containing **17**. The sample vial was left for several days before nucleation was observed and a within week large rhomboid single crystals were present. Crystals were removed from the sample vial and placed into inert perfluoro poly ether oil, *Fomblin-YR 1800*, on a glass slide to allow manipulation and observation under a microscope.

A hay-brown plate-shaped single crystal of 0.103 x 0.105 x 0.167 mm dimensions that displayed high visual quality under examination was selected.Structure solution was performed by SHELXT via intrinsic phasing in the Olex2 GUI2 which confirmed a monoclinic space group setting of $P2_1/n$. Crystal structure contained shift/ESD of -0.001 suggesting convergence of the model. Final structure is displayed in figure 3.13, the minimum unaccounted electron density was -0.4 $eÅ^{-3}$ and the maximum 0.4 $eÅ^{-3}$ located near N3. The final refined structure was 99.3% complete to 0.81 Å, with an R1 = 4.11% and wR2 = 10.69% suggesting the data were of high quality. The unit cell contains one unique molecule (Z' = 1) and 4 molecules of **17** in the unit cell (Figure 3.14).

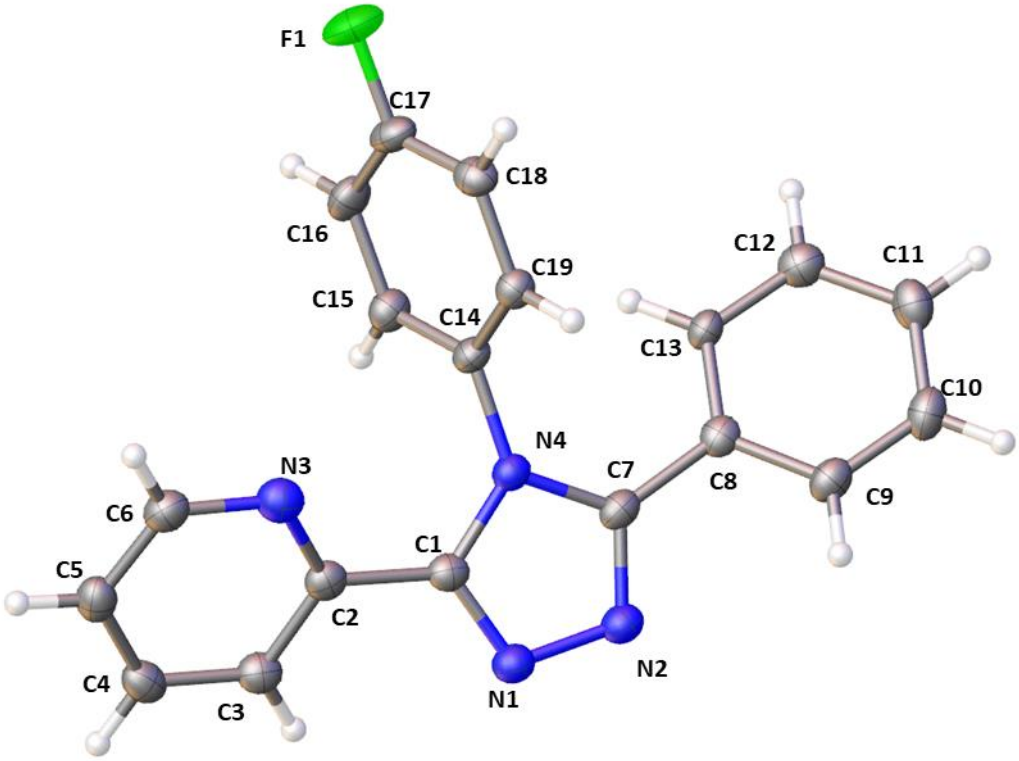

Figure 3.14. Crystal structure of **17**, anisotropic displacement parameters of all non-hydrogen atoms are shown at 50% probability.

The crystal packing contains alternating patterns of molecules mirrored throughout, stacks of **17** form and follow inverted patterns in the 010 and 001 crystallographic directions (Figure 3.15).

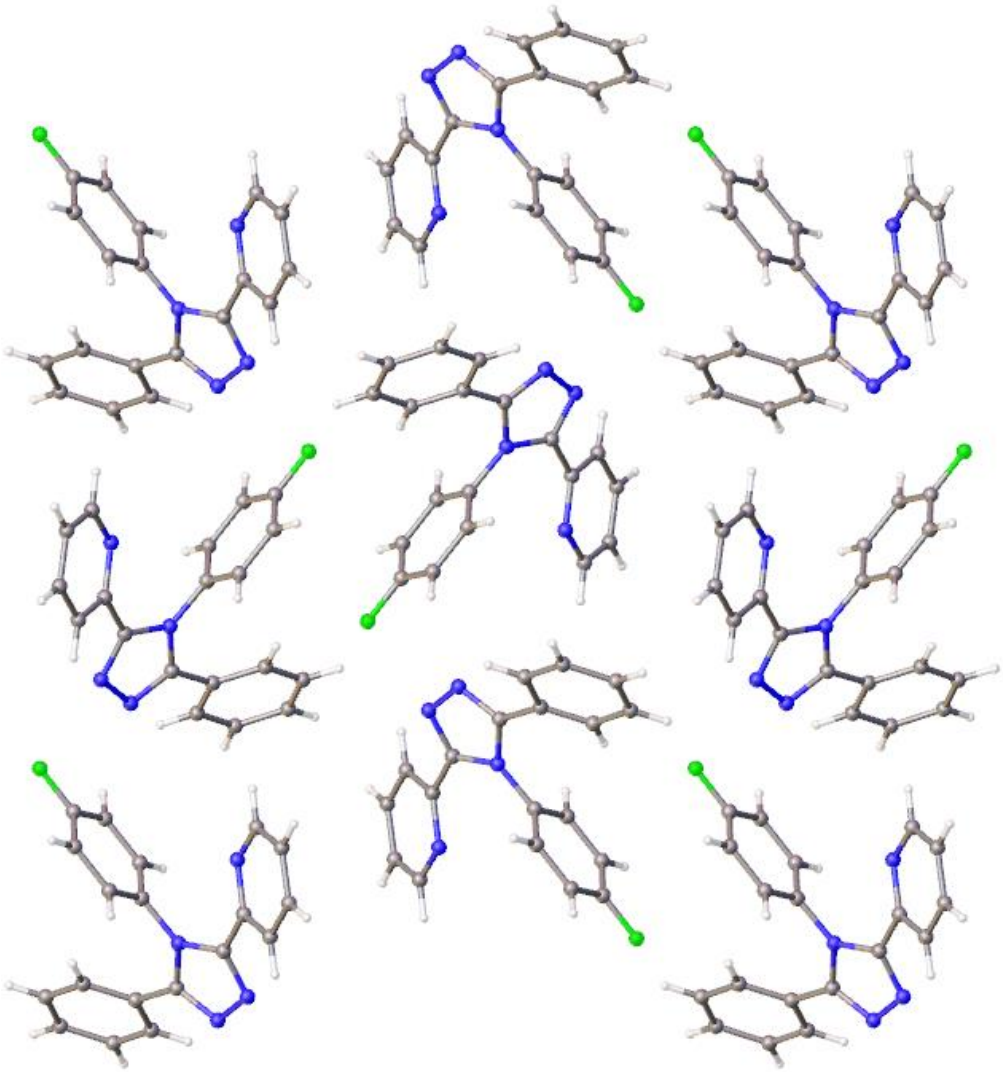

Figure 3.15. Crystal packing of **17** shown along the *a* axis.

Hydrogen bonding interactions are present in the crystal structure (Figure 3.15), the first interaction is from one of the nitrogens in the central triazole N2 which has hydrogen bonding with the hydrogen modelled to C18 at 2.5682(12) Å, the second interaction is between F1 and the hydrogen on C9 at 2.4688(9) Å. There are π-π interactions between the 2-pyridyl rings of separate compounds, centroid-centroid distance 3.963 Å at a shift/ESD of 2.250 Å (Figure 3.17).

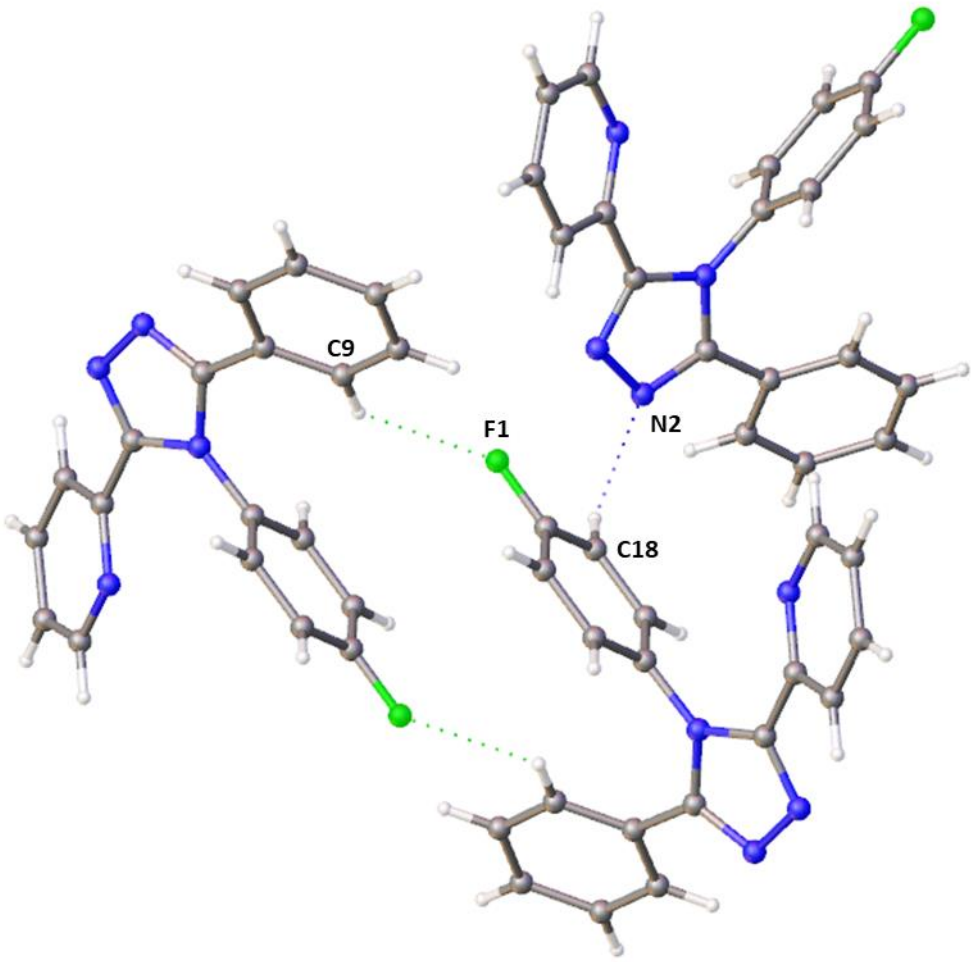

Figure 3.16. Image representing the hydrogen bonding interactions present in the crystal structure of **17**.

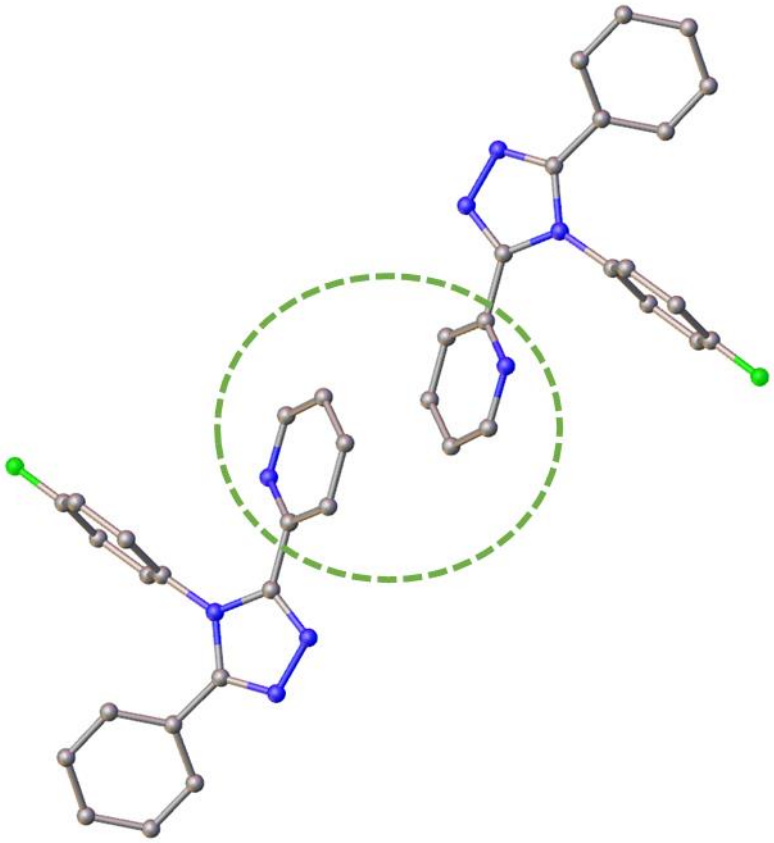

Figure 3.17. Image representing the π-π interactions between 2-pyridyl rings present in the crystal structure of **17**.

3.3.6. Crystal structure of 19

Suitable single crystals for SC-X-ray diffraction were grown from the slow evaporation of a saturated ethanol solution containing **19**. The sample vial was left for several weeks before nucleation was observed and a further 2 week before single crystals of an appropriate size were present. Crystals were removed from the sample vial and placed into inert perfluoro poly ether oil, *Fomblin-YR 1800*, on a glass slide to allow manipulation and observation under a microscope.

A clear plate-shaped single crystal that displayed good visual quality under examination was selected. Structure solution was performed by SHELXT via intrinsic phasing in the Olex2 GUI2 which confirmed a monoclinic space group setting of $P2_1/n$. Final structure contained shift/ESD of 0.001 suggesting convergence of the model. The minimum unaccounted electron density was -0.2 $eÅ^{-3}$ and the maximum 0.2 $eÅ^{-3}$ located near nitrogen atom N3. The final refined structure was 99.4% complete to 0.84 Å, with an R1 = 3.41% and wR2 = 9.42% suggesting the data were of a high quality. The unit cell contains one unique molecule (Z' = 1) and 4 molecules of **18** in the unit cell. The final refinement results are shown in figure 3.18.

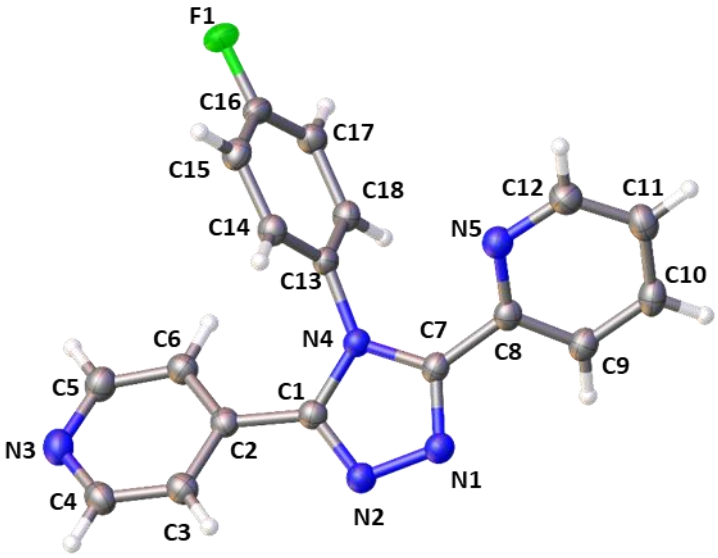

Figure 3.18. Crystal structure of **19**. anisotropic displacement parameters of all non-hydrogen atoms are shown at 50% probability.

Crystal packing of **19** is extremely similar to that displayed in **14**, **15-I** and **17**, with layers of inverted molecules forming stacks in the 010 and 001 crystallographic directions (figure 3.19).

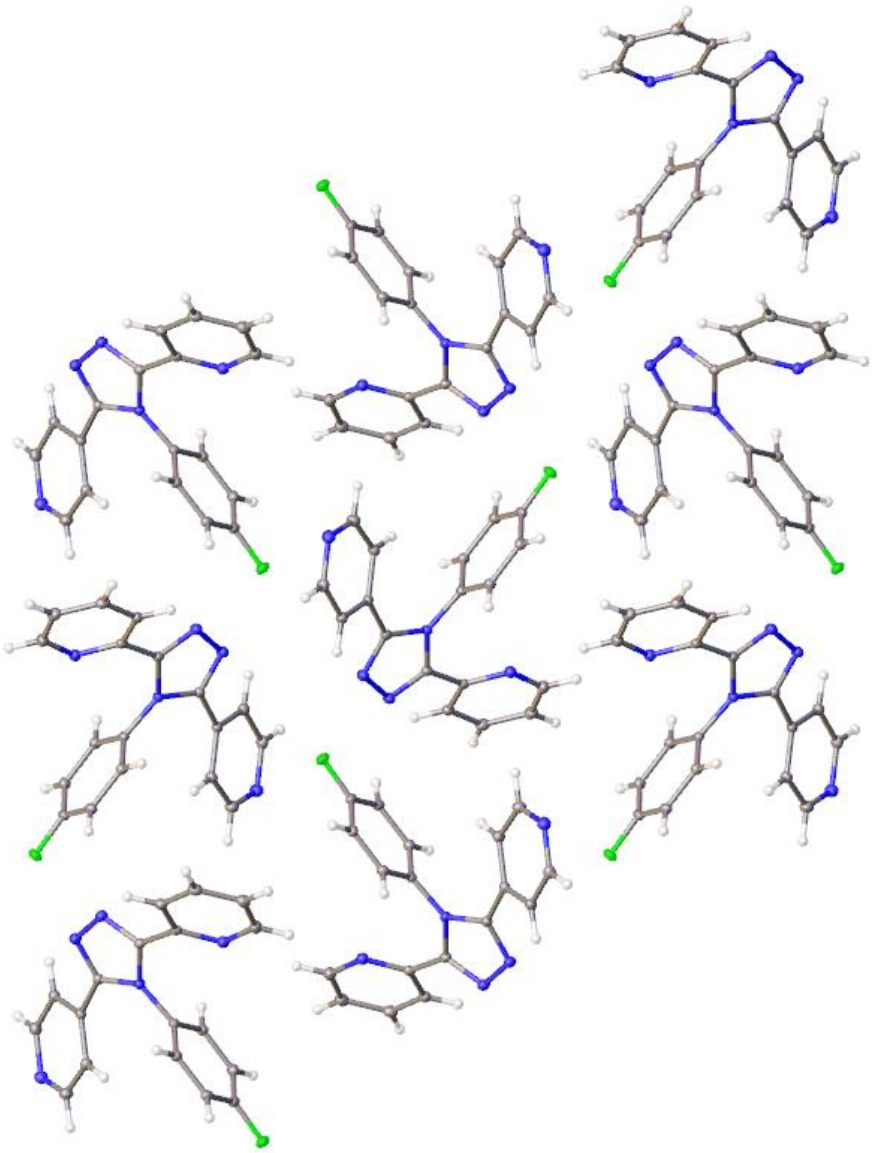

Figure 3.19. Image representing the packing of molecules of **19**, viewed along the *a* axis.

Hydrogen bonding interactions are observed in this crystal structure. Hydrogen bonding between the hydrogen located on C14 and N1 at a distance of 2.4191(10) Å (Figure 3.20). There are no π-π interactions observed in the crystal structure.

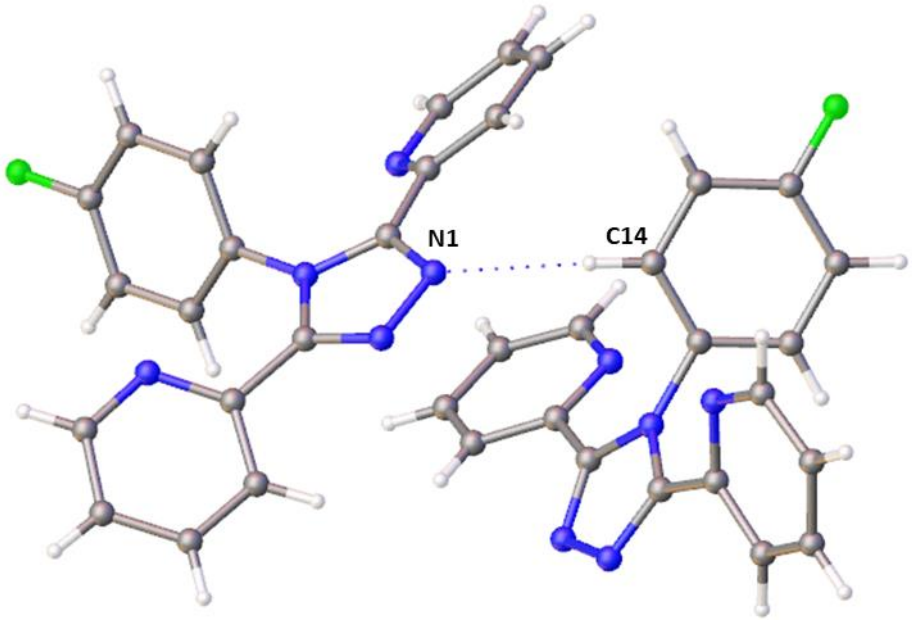

Figure 3.20. Image representing the hydrogen bonding interactions in the crystal structure of **19**.

3.3.7. Crystal structure of 20

Suitable single crystals for SC-X-ray diffraction were grown from the slow evaporation of a methanol solution containing **20**. The sample vial was left for several weeks before nucleation was observed and a further week before single crystals of an appropriate size were present. Crystals were removed from the sample vial and placed into inert perfluoro poly ether oil, *Fomblin-YR 1800*, on a glass slide to allow manipulation and observation under a microscope.

A clear needle-shaped single crystal that displayed good visual quality under examination was selected

Structure solution was performed by SHELXT via intrinsic phasing in the Olex2 GUI2 which confirmed a monoclinic space group setting of $P2_1/n$. Final structure contained shift/ESD of 0.000 suggesting convergence of the model. The minimum unaccounted electron density was -0.3 $eÅ^{-3}$ and the maximum 0.2 $eÅ^{-3}$ near the centre of 2-pyridyl ring. The final refined structure was 99% complete to 0.81 Å, with an R1 = 6.67% and wR2 =17.31% suggesting the data were of high quality. The unit cell contains one unique molecule (Z' = 1) and 4 molecules of **20** in the unit cell. The final refinement results are shown in figure 3.21.

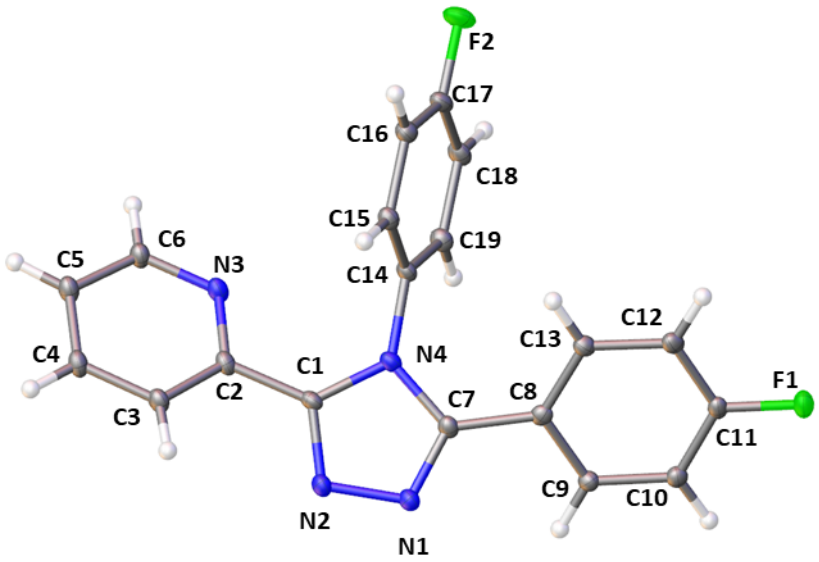

Figure 3.21. Crystal structure of **20**, anisotropic displacement parameters of all non-hydrogen atoms are shown at 50% probability, disorder omitted for clarity.

The packing of **20** shown in figure 3.22, displays familiar patterns to those seen in the crystal structures of **14**, **15** and **19**. There are no hydrogen bonding or π-π interactions observed in this structure.

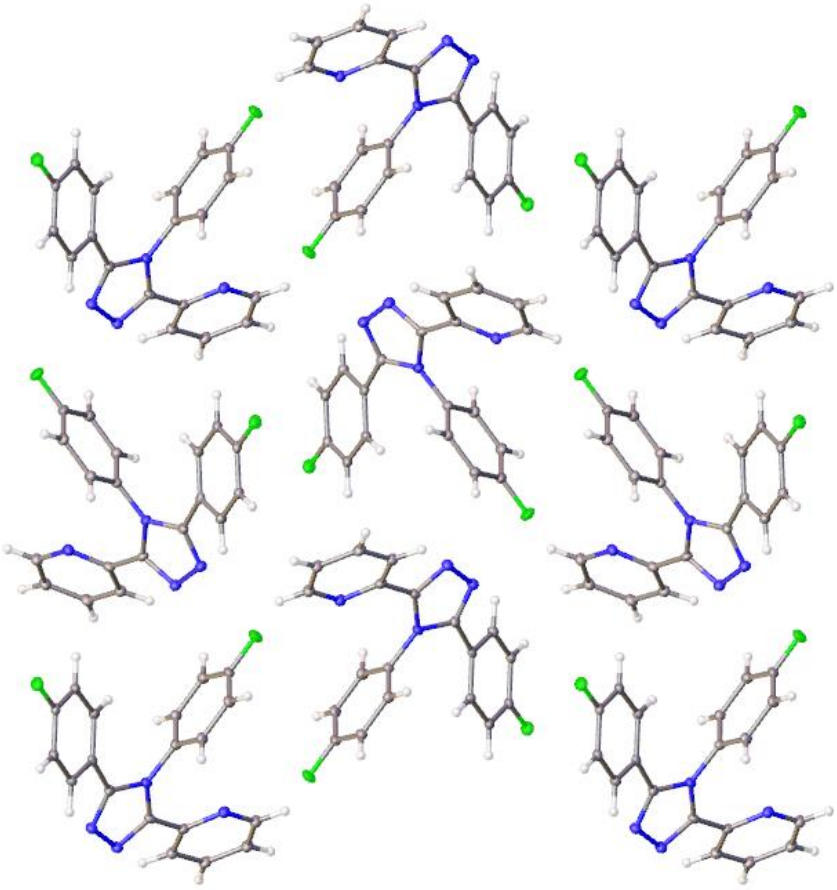

Figure 3.22. Image representing the packing of molecules in the crystal structure of **20**, viewed the *a* axis.

3.3.8 Crystal Structure of 21

Suitable single crystals for SC-X-ray diffraction were grown using the ENAcT method at Newcastle University.[28] The technique uses a “liquid-handing robot” to place a nanodrop of selected oils in a 96 well plate, a saturated solution containing the compound is then injected by the robot into the centre of each oil droplet. The 96 well plate it then sealed with a glass cover and left to crystallise. The crystals used to collect the structure of **21** were grown from a saturated droplet of DMF with FC40 oil. Crystals present in the wells are examined under microscope and the glass cover cut away from crystals that are required. The crystal is then transferred from the well into an inert perfluoro poly ether oil, *Fomblin-YR 1800*, on a glass slide to allow manipulation.

A clear plate-shaped single crystal was the only crystal grown from the 96 well plate, the crystal was mounted onto the Bruker D8 Venture diffractometer using a 50 µm Kapton loop using inert oil for adhesion and protection. A minimal data collection was performed at 150 K, initial data collection showed the sample to be of high quality by

quality of reflections present in diffraction frames, unit cell parameters were found and suggested a primitive orthorhombic space group.

Structure solution was performed by SHELXT via intrinsic phasing in the Olex2 GUI2 which confirmed an orthorhombic space group setting of $P2_12_12_1$. Final structure contained shift/ESD of 0.000 suggesting convergence of the model. The minimum unaccounted electron density was -0.3 eÅ^{-3} and the maximum 0.6 eÅ^{-3} located near nitrogen N2. The final refined structure was 99.6% complete to 0.81 Å, with an R1 = 7.51% and wR2 = 22.09% suggesting the data was of acceptable quality. The unit cell contains one unique molecule (Z' = 1) and 4 molecules of **21** in the unit cell. The final refinement results are shown in figure 3.23.

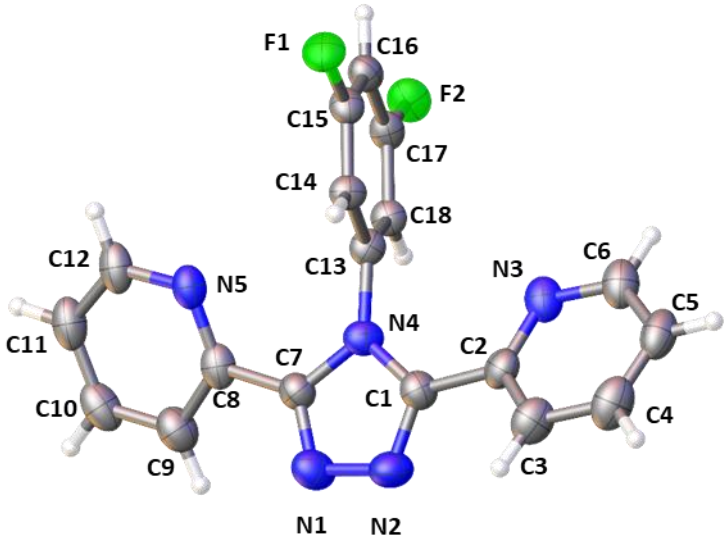

Figure 3.23. Crystal structure of **21**. anisotropic displacement parameters of all non-hydrogen atoms are shown at 50% probability.

Crystal packing of **21** shown in figure 3.24, shows the same cross stitch pattern seen previously. There are hydrogen bonding interactions observed in the crystal structure, in the form of CH-N hydrogen bonding between the hydrogen on C16 and N2 which is 2.272(8) Å. There are no π-π interactions observed in the crystal structure.

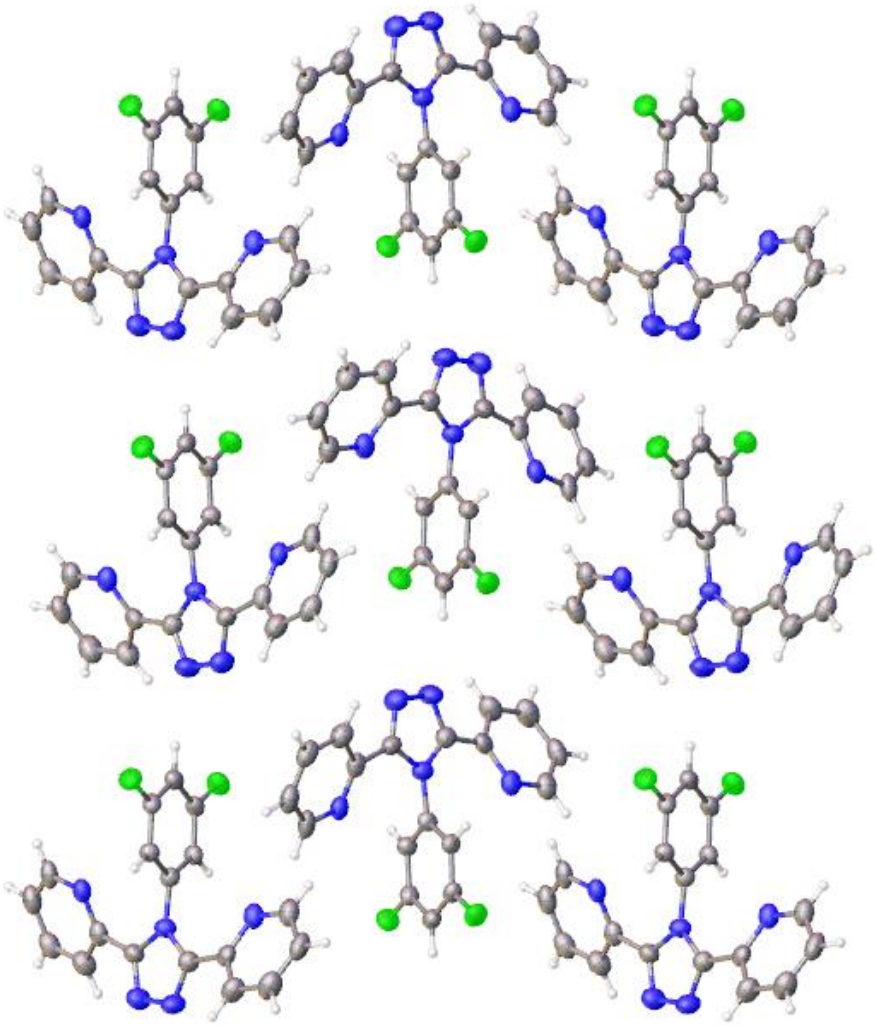

Figure 3.24. Image representing the packing of molecules in the crystal structure of **21**, viewed along the *b* axis.

3.3.9. Crystal structure of 22

Suitable single crystals for SC-X-ray diffraction were grown from the evaporation of a saturated acetone wash solution containing **22** and excess 2-Pyridinecarboxylic acid hydrazide. The sample vial was left for several hours before small needle-shaped crystals were observed. Crystals were removed from the sample tube and placed into inert perfluoro poly ether oil, *Fomblin-YR 1800*, on a glass slide to allow manipulation and observation under a microscope.

A clear small needle-shaped single crystal of that displayed high visual quality under examination was selected.,

Structure solution was performed by SHELXT via intrinsic phasing in the Olex2 GUI2 which confirmed a monoclinic space group setting of *P*-1. Final structure contained shift/ESD of 0.000 suggesting convergence of the model. The minimum unaccounted

electron density was -0.5 eÅ^{-3} and the maximum 0.6 eÅ^{-3} located near the oxygen O1. The final refined structure was 98.1% complete to 0.81 Å, with an R1 = 9.66% and wR_2 = 30.69% suggesting the data was of low quality, this could be due to the very small crystal size and therefore, weak diffraction pattern the Rint was 11.75%. The unit cell contains one unique molecule (Z' = 2) and 2 molecules of **22** and 2 2-pyridinecarboxylic acid, 2-(1-methylethylidene)hydrazide in the unit cell indicating the structure to be a co-crystal. The final refinement results are shown in figure 3.25.

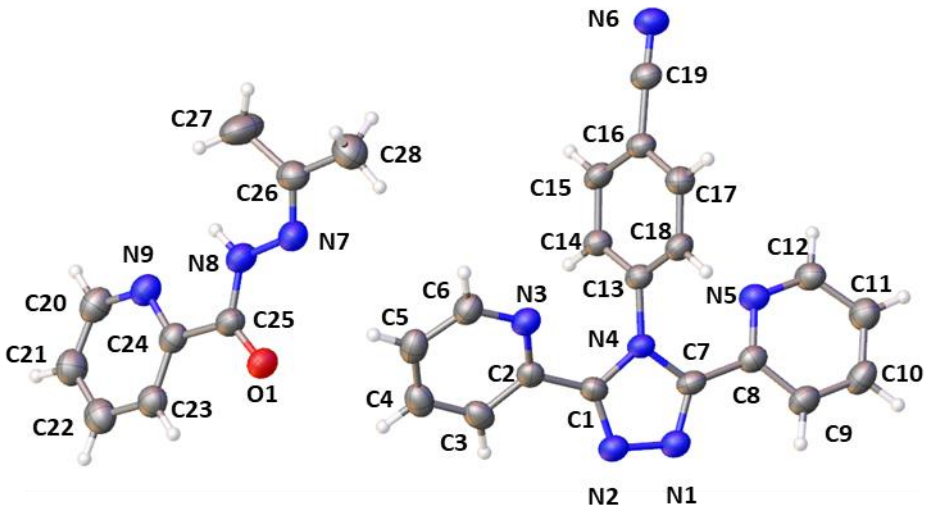

Figure 3.25. Crystal structure of **22**, anisotropic displacement parameters of all non-hydrogen atoms are shown at 50% probability.

The crystal packing of **22** is displayed in figure 3.25, stacks of molecules of **22** formed in the 100 crystallographic directions Molecules of 2-pyridinecarboxylic acid, 2-(1-methylethylidene)hydrazide forming separate stacks at 90˚ in the 010 crystallographic direction. Hydrogen bonding interactions are observed in the structure between the hydrogen on C5 and O1 at 2.395(3) Å. There are no π-π interactions observed in the crystal structure.

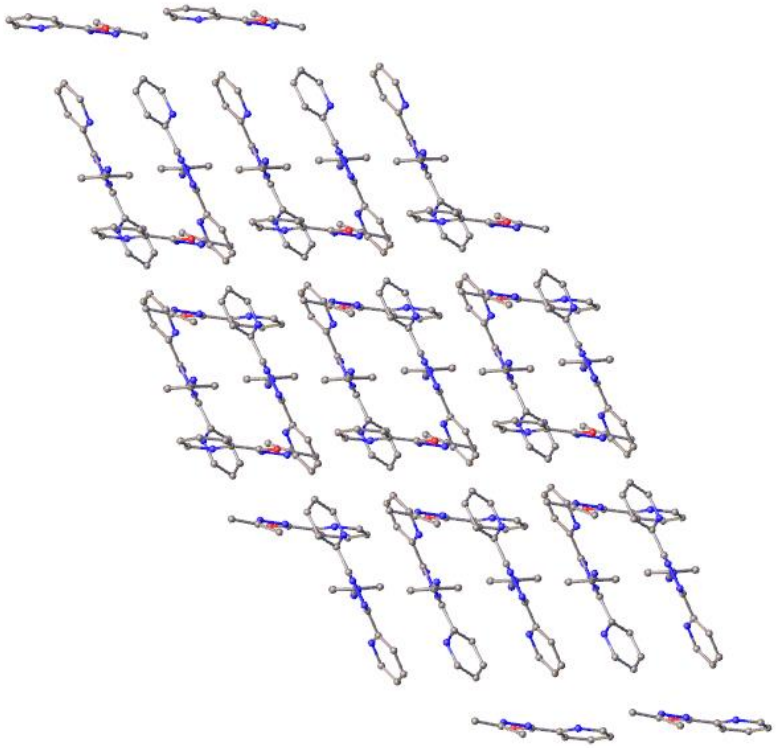

Figure 3.26. Image representing the packing of molecules in the crystal structure of **22**, viewed along the *c* axis.

3.4 Coordination & Crystallisation

The primary purpose for these new triazoles is to be coordinated to various metal salts to produce new complexes. These complexes will be studied for their structural properties in the hopes of discovering new systems that display spin crossover behaviour or other interesting structural phenomena. To achieve this each of the ligands synthesised in this study once successfully synthesised and were coordinated to metal salts in situ to the crystallisation of the metal complexes.

Due to the abundance of SCO complexes containing iron(II) metal centres, the ligands will primarily be coordinated to iron(II) metal salts to form. Other metals have been used such as iron(III), cobalt(II/III) and manganese(III) these metals belong to the d^4-d^7 transition metals and can display the phenomenon and will provide direct comparisons if isomorphous structures can be crystallised.

This was accomplished with various methods of crystallisation, the three main methods were layering, evaporation from saturated solutions and vapour diffusion.

The layered crystallisation method utilises the miscibility between different solvents, this creates a layer between the two solvents and an interface where ligand and metal

salts can interact slowly and produce crystals. A metal salt is dissolved into one solvent and slowly injected via a microlance needle under another solution containing the ligand, a layer forms between the two solutions where they slowly mix and a change of colour is often noted.

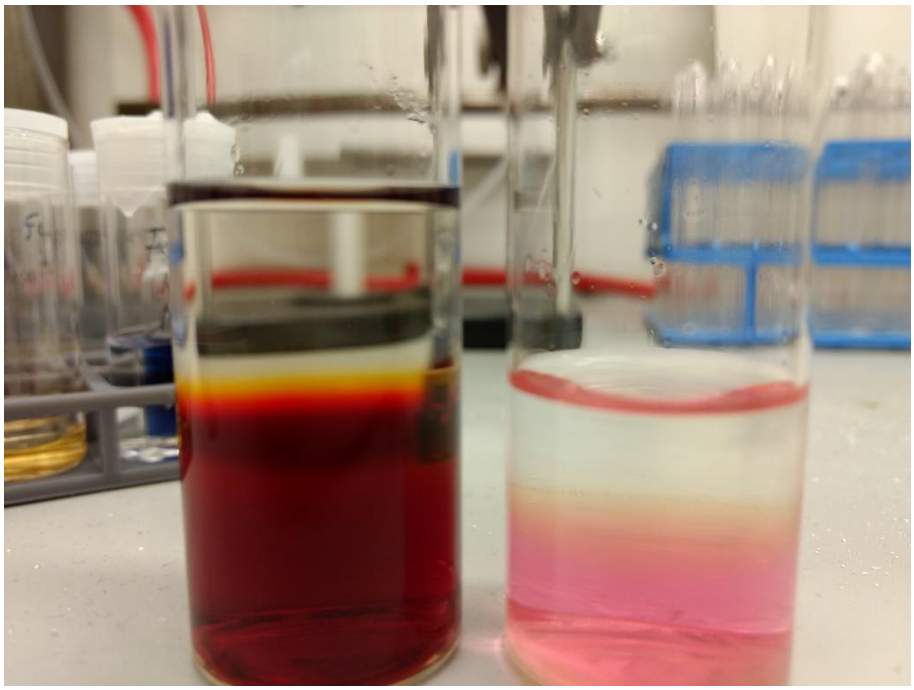

Figure 3.27. Two layered crystallisations, the left shows the characteristic red colour of the iron bis-isothiocyanate solution, the right the pink of a cobalt bis-isothiocyanate.

Evaporation is perhaps the simplest method of producing crystals, solvent is saturated with both metal and ligand, this solution can be heated or simply left to stir for some time. The sample vial has ventilation holes in the lid which allow solvent to evaporate, increasing the concentration of the sample, as the concentration increases the sample will start to crystallise inside the sample vial.

Vapour diffusion pictured below (figure 3.28) involves a central chamber where the compound is in a saturated solution, an antisolvent which is more volatile is then placed in the outer chamber. As this antisolvent evaporates the vapours enter the central chamber and mix with the compound containing solution forcing the compound out of solution.

Figure 3.28. Example of a vapour diffusion crystallisation, the outside chamber contains diethyl ether which will diffuse into the inner chamber containing a methanol solution of a cobalt metal complex.

3.5 Conclusion

This study has produced 13 new substituted 1,2,4-triazoles using a single synthetic route, 8 literature triazoles have also been synthesised creating a library of compounds to be used in complexation studies with metal salts in attempts to create new systems for structural study by single crystal X-ray diffraction.

3.6 References

1 R. Kulmaczewski and M. A. Halcrow, *CrystEngComm*, 2016, **18**, 2570–2578.

2 M. Mörtel, T. Lindner, A. Scheurer, F. W. Heinemann and M. M. Khusniyarov, *Inorg. Chem.*, 2020, **59**, 2659–2666.

3 M. A. Halcrow and G. Chastanet, *Polyhedron*, 2017, **136**, 5–12.

4 J. A. Kitchen, A. Noble, C. D. Brandt, B. Moubaraki, K. S. Murray and S. Brooker, *Inorg. Chem.*, 2008, **47**, 9450–9458.

5 S. Maddila, R. Pagadala and S. Jonnalagadda, *Lett. Org. Chem.*, 2013, **10**, 693–714.

6 K. T. Potts, *Chem. Rev.*, 1961, **61**, 87–127.

7 P. Kaur and A. Chawla, *Int. Res. J. Pharm.*, 2017, **8**, 10–29.

8 C. Liu and E. J. Iwanowicz, *Tetrahedron Lett.*, 2003, **44**, 1409–1411.

9 S. Bondock, A. El-Gaber Tarhoni and A. A. Fadda, *Monatshefte fur Chemie*, 2008, **139**, 153–159.

10 D. Li, H. Bao and T. You, *Heterocycles*, 2005, **65**, 1957–1962.

11 X. He, B. Li, L. Chen, X. Shen and D. R. Zhu, *Heterocycl. Commun.*, 2014, **20**, 201–206.

12 V. Sharma, S. Birendra, R. Bhatia, M. Bachwani, R. Khandelwal and J. Ameta, *Pharmacol. Online*, 2011, **1222**, 1192–1222.

13 F. Bentiss, M. Lagrenée and D. Barbry, *Tetrahedron Lett.*, 2000, **41**, 1539–1541.

14 M. Nakka, R. Tadikonda, S. Rayavarapu, P. Sarakula and S. Vidavalur, *Synth.*, 2015, **47**, 517–525.

15 J. A. Kitchen, N. G. White, M. Boyd, B. Moubaraki, K. S. Murray, P. D. W. Boyd and S. Brooker, *Inorg. Chem.*, 2009, **48**, 6670–6679.

16 M. Santus, *Liebigs Ann. Chem.*, 1988, 179–182.

17 M. Santus, *Acta Pol. Pharm.*, 1976, **33**, 557–83.

18 M. H. Klingele and S. Brooker, *European J. Org. Chem.*, 2004, 3422–3434.

19 J. H. Guo, W. Guo, X. Wang and M. Du, *Inorg. Chem. Commun.*, 2012, **22**, 77–81.

20 W. Guo, Y. Y. Yang and M. Du, *Inorg. Chem. Commun.*, 2010, **13**, 863–866.

21 H. K. Fun, K. Chinnakali, S. Shao, D. Zhu and X. Z. You, *Acta Crystallogr. Sect. C Cryst. Struct. Commun.*, 1999, **55**, 770–772.

22 E. Orselli, G. S. Kottas, A. E. Konradsson, P. Coppo, R. Fröhlich, L. De Cola, A. Van Dijken, M. Büchel and H. Börner, *Inorg. Chem.*, 2007, **46**, 11082–11093.

23 *Bruker AXS Inc., Apex3, Bruker AXS Inc., Madison, Wisconsin, USA, 2015*.

24 L. Krause, R. Herbst-Irmer, G. M. Sheldrick and D. Stalke, *J. Appl. Crystallogr.*, 2015, **48**, 3–10.

25 G. M. Sheldrick, *Acta Crystallogr. Sect. A Found. Crystallogr.*, 2015, **71**, 3–8.

26 G. M. Sheldrick, *Acta Crystallogr. Sect. C Struct. Chem.*, 2015, **71**, 3–8.

27 N. T. Johnson and M. R. Probert, *Priv. Commun.*

28 A. R. Tyler, R. Ragbirsingh, C. J. McMonagle, P. G. Waddell, S. E. Heaps, J. W. Steed, P. Thaw, M. J. Hall and M. R. Probert, *Chem*, 2020, **6**, 1755–1765.

Chapter 4: Structural analysis of [Fe(2-(4,5-bis(4-fluorophenyl)-4H-1,2,4-triazol-3-yl)pyridine)$_2$(NCS)$_2$] complexes

4.1 Introduction

This chapter will detail the generation and variable temperature structural analysis of [Fe(2-(4,5-bis(4-fluorophenyl)-4H-1,2,4-triazol-3-yl)pyridine)$_2$(NCS)$_2$]·MeOH or [Fe(**20**)$_2$(NCS)$_2$]·MeOH (**23a**) and [Fe(2-(4,5-bis(4-fluorophenyl)-4H-1,2,4-triazol-3-yl)pyridine)$_2$(NCS)$_2$] or [Fe(**20**)$_2$(NCS)$_2$] (**23b**), two complexes synthesised from the ligand 2-(4,5-bis(4-fluorophenyl)-4H-1,2,4-triazol-3-yl)pyridine (**20)** and iron bis-isothiocyanate using the layering crystallisation method previously used for the four polymorphs of [Fe(abpt)$_2$(NCS)$_2$][1–6] (see chapter 3.5). The two systems described herein are almost identical apart from the inclusion of a methanol solvent of crystallisation. This minor change in the components of the crystal is found to significantly impact the structural parameters. Ligand **20** was a new substituted 1,2,4-triazole prepared for this work and the synthesis of this ligand was discussed in Chapter 3.

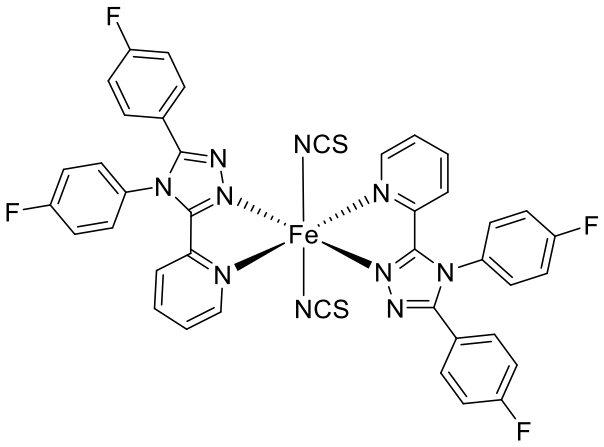

Figure 4.1. Molecular representation of the [Fe(2-(4,5-bis(4-fluorophenyl)-4H-1,2,4-triazol-3-yl)pyridine)$_2$(NCS)$_2$] demonstrating the connectivity of the iron centred moiety

4.2 [Fe(2-(4,5-bis(4-fluorophenyl)-4H-1,2,4-triazol-3-yl)pyridine)$_2$(NCS)$_2$].MeOH – 23a

Single crystals suitable for analysis by single crystal X–ray diffraction (SC-XRD) were generated by preparing a 0.006 mmol methanol (0.5 ml) solution containing 2-(4,5-

bis(4-fluorophenyl)-4H-1,2,4-triazol-3-yl)pyridine (**20**) and a 0.003 mmol iron(II) bis-isothiocyanate solution of water and methanol in a 1:1 ratio (0.5 ml). The orange iron-containing solution was slowly injected using a microlance hypodermic needle and 2 ml syringe under the clear ligand containing solution to avoid disruption of the interface. The interface turned to a dark red colour immediately after injection of the iron-containing solution, the injection was conducted slowly to ensure layering had formed and mixing of the two solutions only occurred at the interface (figure 4.2).

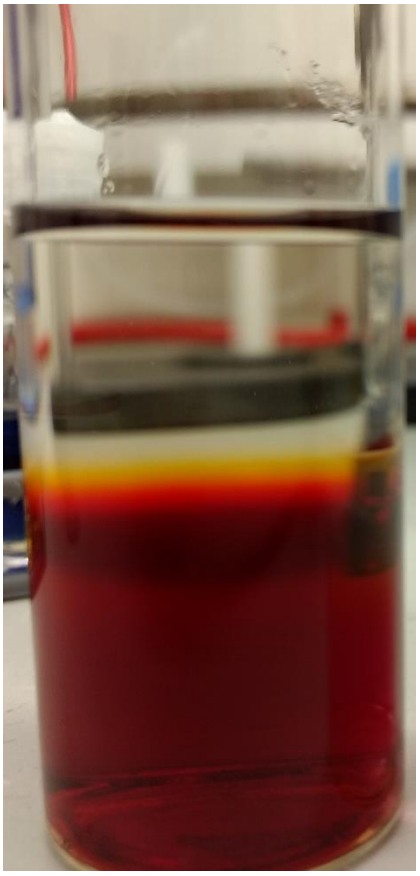

Figure 4.2. The solution of a layered crystallisation to grow crystals of **23a**.

On leaving the solution undisturbed for several days, nucleation of crystalline material was observed at the interface and, after two weeks, large red-orange single crystals were present. Crystals were then carefully removed from the solution and placed under an inert perfluoro poly ether oil, *Fomblin-YR 1800,* on a clear glass microscope slide for ease of manipulation and observation.

A high-quality red crystal with dimensions 0.072 x 0.103 x 0.163 mm^3 was selected for analysis by SC-XRD.

Initial structure solution was performed using SHELXT [7] *via* intrinsic phasing in the Olex2 interface[8] confirmed the space group setting of *C2/c*. Structure reached convergence as implied by a shift/ESD of 0.000. The minimum unaccounted electron density was -1.3 eÅ^{-3} and the maximum peak of 0.9 eÅ^{-3} located near S1 on the isothiocyanate indicating a low amount of disorder. The completeness of the dataset was measured to 99.6 % to a resolution of 0.81 Å with a R_1 factor of 8.39 % and wR_2 of 20.07 % indicating the sample was of generally good quality.

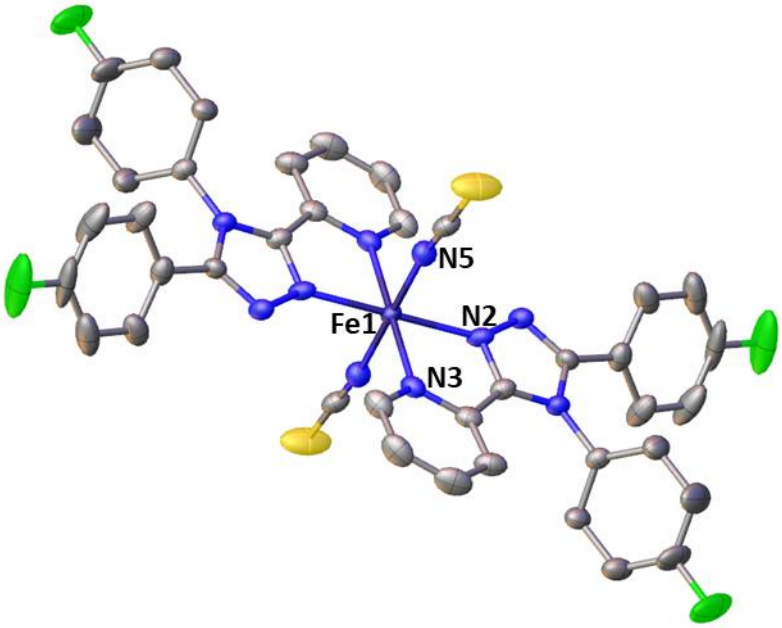

Figure 4.3. A symmetry expanded view of the crystallographic model of **23a** at 150 K. The anisotropic displacement parameters of all non-hydrogen atoms are shown at 50% probability. Hydrogen atoms have been removed for clarity.

The final refinement results yielded a structure with the monomeric unit that contained a complex with an iron(II) metal centre that is coordinated to 2-(4,5-bis(4-fluorophenyl)-4H-1,2,4-triazol-3-yl)pyridine ligands, two negatively charged isothiocyanate ligands and one uncoordinated methanol molecule. Coordination of **20** occurs through nitrogen atoms N2 and N3, a common coordination motif in previous results of 1,2,4-triazoles.[9,10]. The coordination sphere of six nitrogen atoms coordinated to the metal centre is predicted to be optimal for iron(II) spin crossover systems.

The packing exhibited by the metal complexes in **23a** is shown in figure 4.4 with discrete layers of complexes separated by a layer of methanol solvent molecules.

These layers are co-planar to the crystallographic (100) plane with the fluorine atoms directed towards the layer boundaries. There are edge to face hydrogen – π interactions between molecules in the stacks. These stacks are linked to each other via π-π interactions. The Fe – Fe distance between molecules in the same stack (crystallographic [010] direction) is 8.997(7) Å. These layers contain interactions between one another in the form of extensive hydrogen bonding between metal complexes and the uncoordinated methanol molecules shown in figure 4.5. Hydrogen bonding interactions are witnessed in the form of CH-S between S1 and C4 of distance 2.876(2) Å and CH-N intramolecular hydrogen bonding between C6 and N1 of distance 2.494(4) Å, CH-F between C19 and F1 molecules from separate metal complexes at 2.445(6) Å, finally CH-O hydrogen bonding between C10 and O1 at 2.386(18) Å.

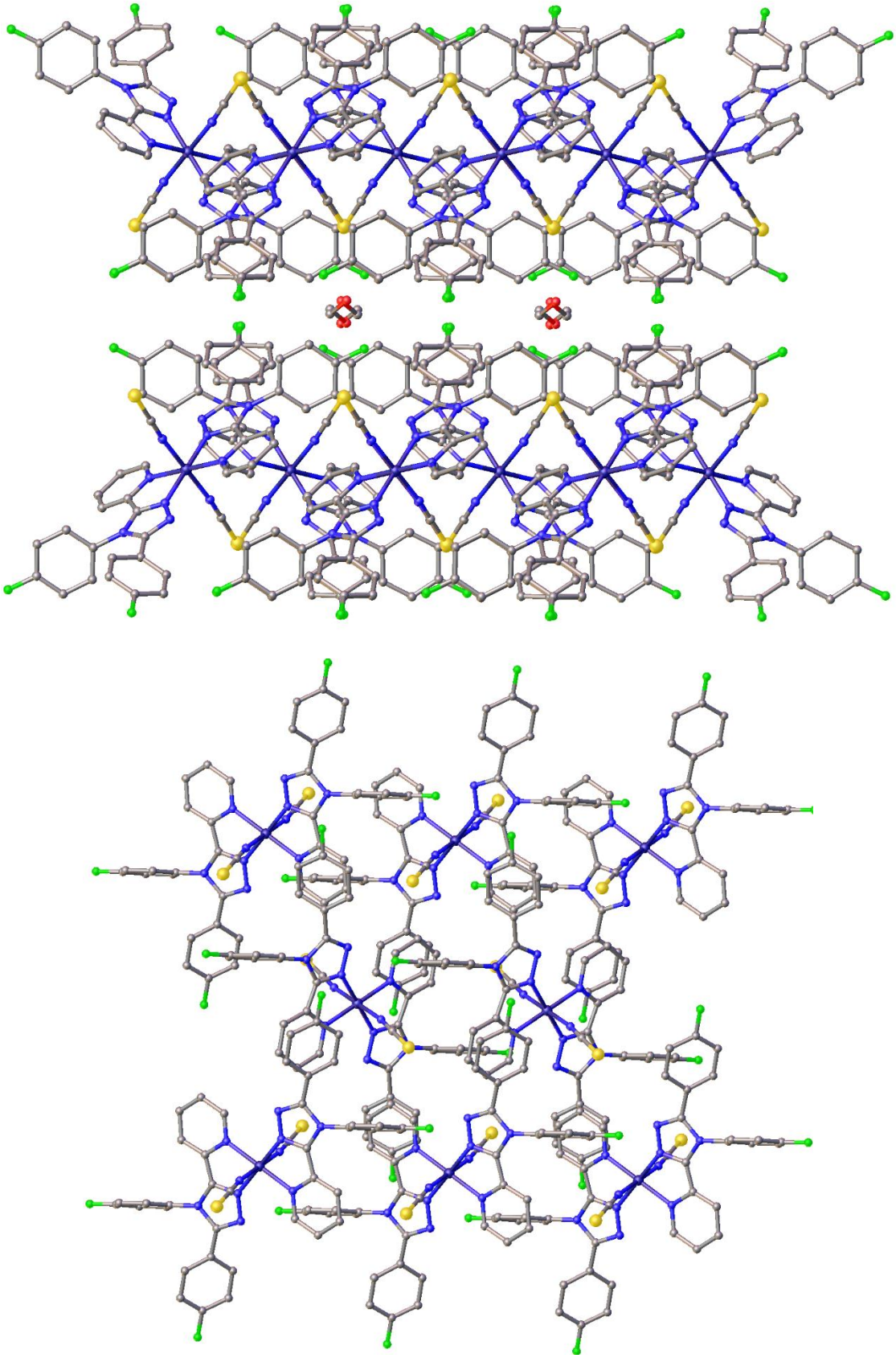

Figure 4.4. Image representing the packing of metal complexes of **23a** along the 001 direction (top) and the 100 plane (bottom).

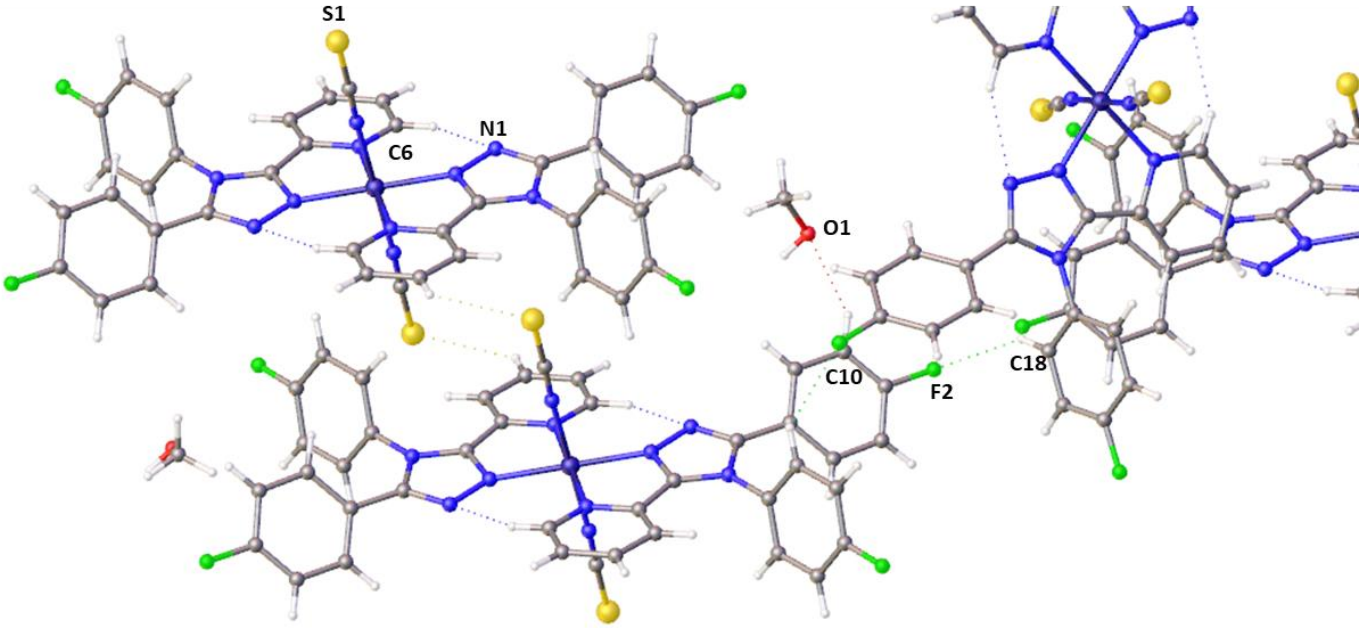

Figure 4.5. Image representing the extensive hydrogen bonding displayed between metal complexes and the free methanol solvent molecules present in crystalline model of **23a**

After final refinement convergence the structure was interrogated for its structural properties. The Fe – N bond lengths were in the range of ~2.01 – 2.08 Å, suggesting that the structure could contain a mixture of HS (2.1 – 2.2 Å) and LS (1.9 – 2.0 Å) spine states, therefore, the complex is mid transition. The observation of the Fe – N bond distances indicated that single crystals of this sample need to be analysed at a range of temperatures to observe any transitions. The calculated value of the octahedron volume (v_p) = 11.142(14) was another indicator that the system was in caught between spin states. Therefore, XIPHOS I – a single crystal diffractometer optimised for low temperature collections – was used to collect full diffraction datasets at various temperatures.[11,12] To optimise data quality a new single crystal was selected as the first crystal had undergone stress due to the transition in the first data collection. The sample was mounted to a sharpened graphite rod using a minimal amount of epoxy resin glue (Loctite™ double bubble), known to be a good thermal conductor to hold the crystal in place while mounted vertically in the cold head, see chapter 1.3.

Full data collections were conducted at 2.2, 100 and 293 K using Mo – Kα (λ=0.71073Å) radiation. These temperatures were chosen as 2.2 K is the lowest temperature that XIPHOS I holds temperature steadily, 100 K as the cryostream on

the Bruker D8 is reliable to this temperature and 293 K the ambient temperature on XIPHOS I in the instrument room. An ambient dataset would be collected at 293 K with the sample not placed under the vacuum and the shielding cans not attached. This measurement served two purposes. The first is an ambient set to probe if the structure is in a fully HS state at room temperature, the second to ensure the crystal is of high quality and the data collection strategies that are limited on XIPHOS I would allow for good quality data to be collected. Once this ambient data had been collected and processed in the same manner as the 150 K dataset, the shielding cans were attached to XIPHOS I and a vacuum applied until it reached 10^{-6} mbar. After the system reached stability, the sample was cooled to 100 K at 5 K/min, the sample was centred by diffraction since the shielding cans block all vision of the sample. The same strategy was used to conduct a full data collection. Finally, the sample was cooled at 1 K/min until 2.25 K the lowest temperature where stability can be guaranteed. The sample was again recentred by diffraction before the strategy was applied to collect the final dataset.

Table 4.1. Structural parameters at various temperature in **23a.**

	2.2 K	**100 K**	**150 K**	**293 K**
Fe – N2 (Å)	1.9761(19)	1.979(2)	2.043(5)	2.161(2)
Fe – N3 (Å)	2.0109(19)	2.014(3)	2.083(5)	2.207(3)
Fe – N5 (Å)	1.9437(19)	1.945(3)	2.008(5)	2.115(3)
Σ (˚)	55.0(1)	54.5(2)	61.6(2)	71.2(2)
v_p (Å^3)	10.128(6)	10.156(7)	11.142(14)	12.987(10)

The twist and fold angles of the 1,2,4-triazole and 2-pyridyl ring at 293 K are 9.93(10) and 5.04(11)˚ of the coordinated ligand. As the temperature is decreased the twist angle decreases and the fold angle increases as shown in table 4.2 alongside the twist and fold angles of the crystal structure of **20**.

Table 4.2. Twist and fold angles of **23a**.

	Free ligand	**293 K**	**150 K**	**100 K**	**2 K**

Twist	29.4(14)	9.93(10)	7.2(2)	4.96(9)	5.11(8)
Fold	2.3(12)	5.04(11)	6.5(2)	8.02(9)	7.97(8)

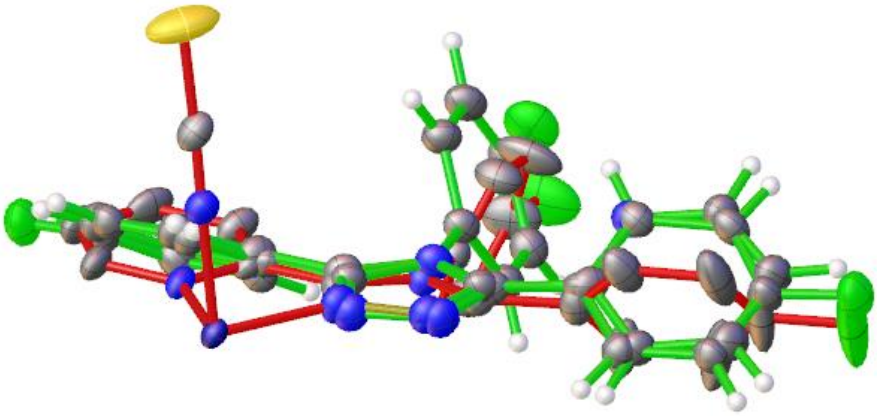

Figure 4.6. The overlayed crystal structures of uncoordinated **20** at 150 K (Green), **23a** at 150 K (red)

The processing of diffraction data was carried out in the same fashion as for the first crystal at 150 K. The full structure determination at 293 K yielded the same asymmetric unit as figure 2 in the same space group setting with solvent molecules present. Inspection of the Fe – N bond distances ranging from 2.11 – 2.21 Å shown in Table 4.1 indicate the iron centre is in a fully HS state.

Structure determination of the 100 K data yielded the same asymmetric unit in the same space group setting. The interrogation of the Fe – N bond distances ranging from 1.98 – 2.01 Å, a contraction of ca. 10%, indicative of full transition of metal centres to the LS state. The parameter Σ was calculated for each crystal structure showing the change in octahedral distortion from high spin 71˚ to 55˚ for the low spin state. This contraction and change in spin states shows the sample undergoes thermal spin crossover and must be further analysed.

No wider structural phase transition was observed beyond the change in spin state upon cooling to 2.2 K, with the structure remaining in the *C2/c* space group setting throughout. This final dataset indicates that the crystals could be used in potential future photoirradiation experiments. Light induced excited spin state trapping (LIESST) described (see Chapter 1.2.2), where a spin crossover material at low

temperature is irradiated with a specific wavelength to promote the LS crystal structure to a metastable HS* state.

These results show that a thermal transition has occurred between 293 and 100 K with the iron centre presumably fully converting from the HS to LS state between these temperatures. The first data set at 150 K indicated the transition was happening around this temperature with the structure trapped between spin states. To further investigate the type of transition and the temperatures SCO occurs an additional study was proposed to investigate the unit cell parameters of the system as a function of temperature. This study would allow for a rough estimate of $T_{½}$ the temperature the structure is halfway through a thermal transition and the crystal is 50% HS and 50% LS.

A new crystal was selected to ensure high data quality was conducted using the Bruker D8 Venture with Cu-Kα radiation. The choice to return to this diffractometer was determined due to the speed that collections could be conducted with modern nitrogen flow cooling system that could be automated and the higher quality X-ray detector, to obtain the best quality data in a timely manner. An automated set of minimal data collections of 3 omega scans with 40 frames with a 0.50˚ scan width at 10 second X-ray exposure time that would allow for ample data to determine unit cell parameters. The cryostream was automated to change temperature and stabilise for 20 minutes before the next data set was collected. The first collection was conducted at 250 K before cooling stepwise to 100 K in increments of 5, 10 and 25 K. Once the data collection at 100 K was completed, the same sample was then heated back to 250 K following the reverse of the cooling steps. Analysing both the cooling and heating of the same crystal allows for the observation of any potential hysteresis present during the transition.

Unit cell parameters were determined and refined for each of the data collections in the APEX3 GUI. These parameters were interrogated as a function of temperature and plotted as graphs to visualise changes.

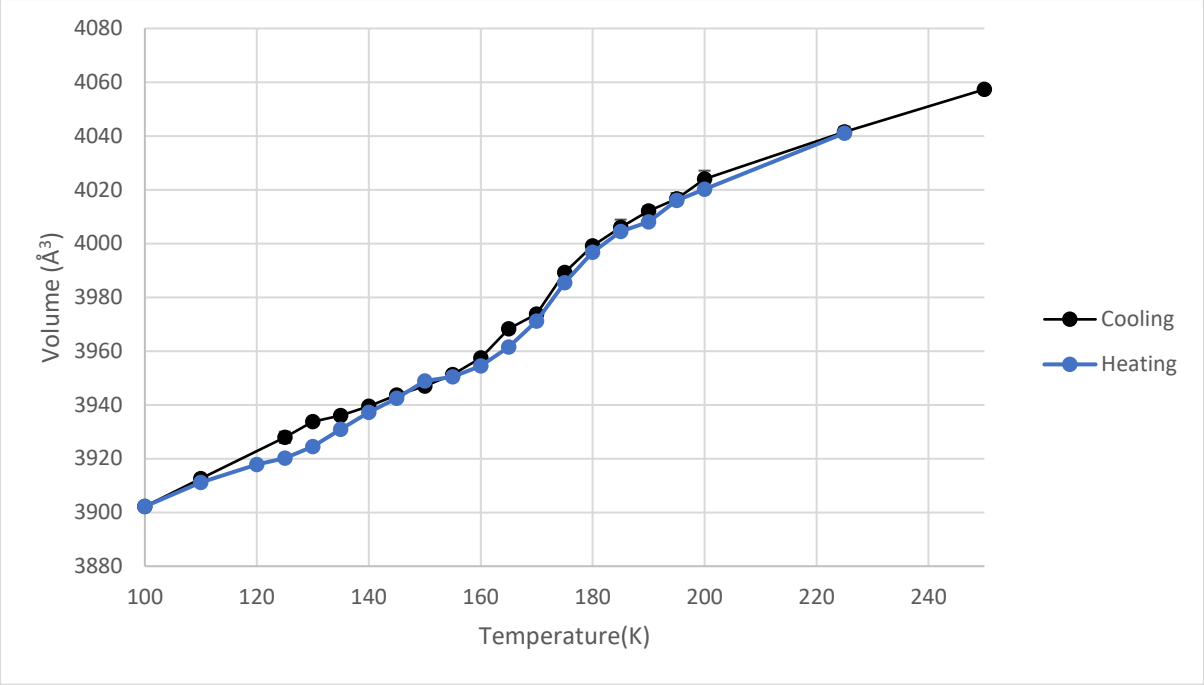

Figure 4.7. Unit cell volume between 250-100 K while cooling (black) and heating (Blue).

The first parameter analysed was the unit cell volume. Naturally cooling the sample would cause contractions of the volume so a sample that displays no thermal transition should have a straight line, theoretically. **23a** shows a steeper decrease in volume between 185 and 165 K and this validates that a thermal spin transition is occurring between the room temperature and 100 K measurement. Using these values, the $T_{½}$ appears to be around 175 K. The total unit cell volume decreases between 250 and 100 K by ~3.8% and is mirrored in the heating of the sample. No hysteresis is witnessed in the sample with the transitions occurring roughly in the same location in the heating and cooling. The return of the sample to the HS state confirms the transition is reversible.

This does not 100% align with the initial result that the 150 K measurement indicated that this was trapped between spin states. However, that crystal was flash frozen at 150 K rather than slowly cooled down that could have influenced the transition. This effect of the flash freezing alongside potential damage to crystal quality is one of the reasons the sample was cooled from room temperature to 250 K before measurements began.

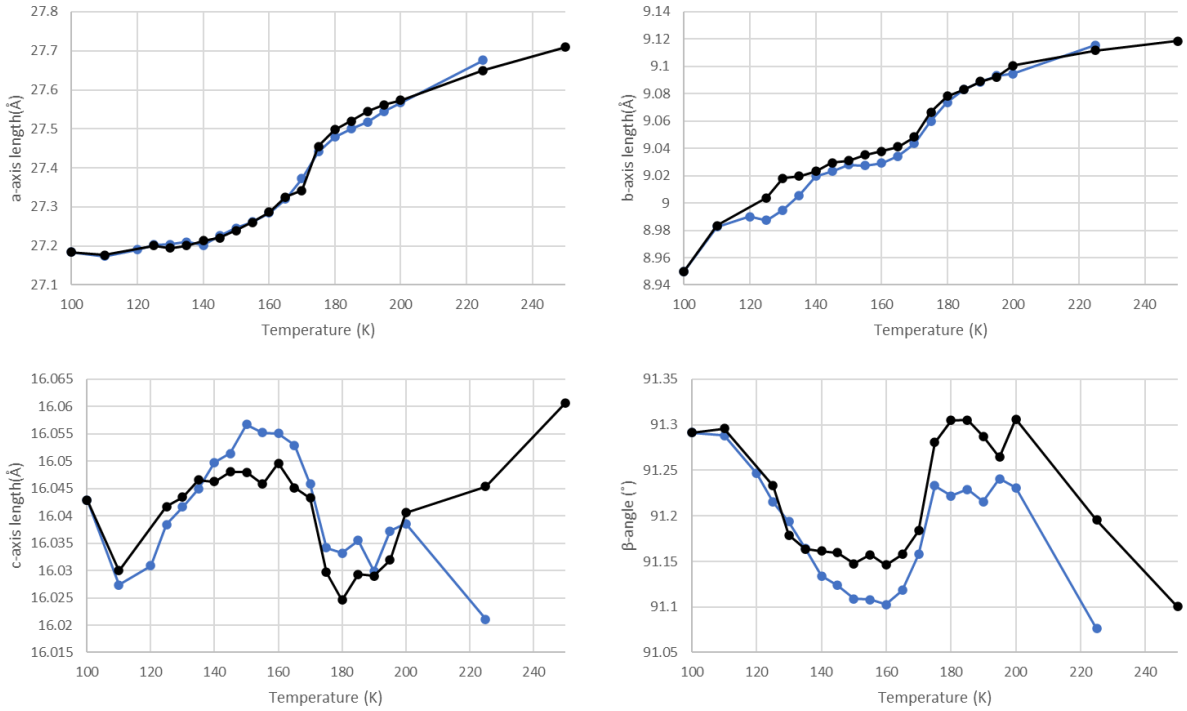

Figure 4.8. Unit cell parameters a, b, c and Beta with changing temperature (Black = cooling, Blue = heating)

Unit cell parameters *a, b, c* and the *β*-angle changes upon heating and cooling are displayed in figure 4.8. Both *a* and *b* follow a similar trend to the unit cell volume with steady decreases in length before a large drop between 175 and 170 K. These parameters see a ~1.9% decrease in length between 250 and 100 K. These results further strength the hypothesis of the thermal transition being ~170-5 K.

The third unit cell axis length *c* and the *β*-angle follower similar trends to one another. Unlike the steady decreases witnessed previously, both parameters change back and forth with changes in temperature. Axis length c contracts until 185 K before stretching until 165 K and this trend is seen again between 150 and 100 K. Due to this, the overall change in axis length between 250 and 100 K is only ~0.2 %. This pattern is largely repeated with the heating of the sample apart from the datapoint at 225 K. The *β*-angle increases until 200 K before remaining largely steady before decreasing 175 and 170 K before holding steady again. At 145 K the angle increases again and remains this way till 100 K and the pattern is repeated with heating of the sample. Each of the unit cell parameters analysed are in line with the $T_{1/2}$= ~175 K.

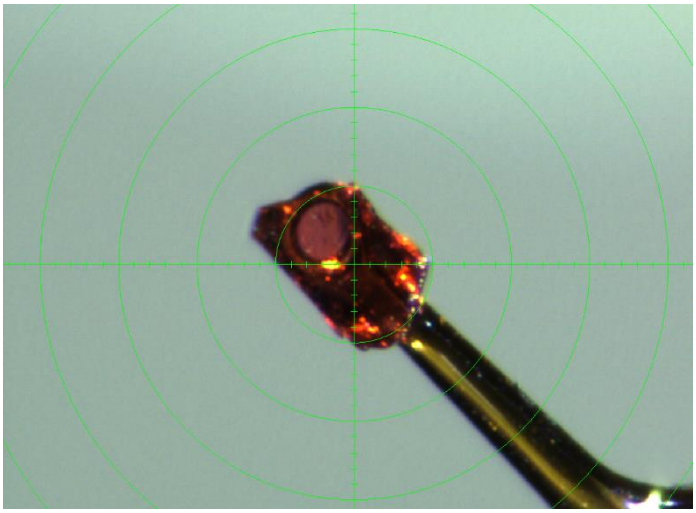

Figure 4.9. A reddish-orange single crystal of **23a** via the Bruker D8 Venture camera at 250 K.

Crystals of spin crossover are often associated with a distinct colour change as the metal centre changes spin state.[13] Images of **23a** were captured on the Bruker D8 Venture while conducting the unit cell experiments with changing temperature. The first image in figure 4.9 displays the crystal as reddish-orange at 250K.

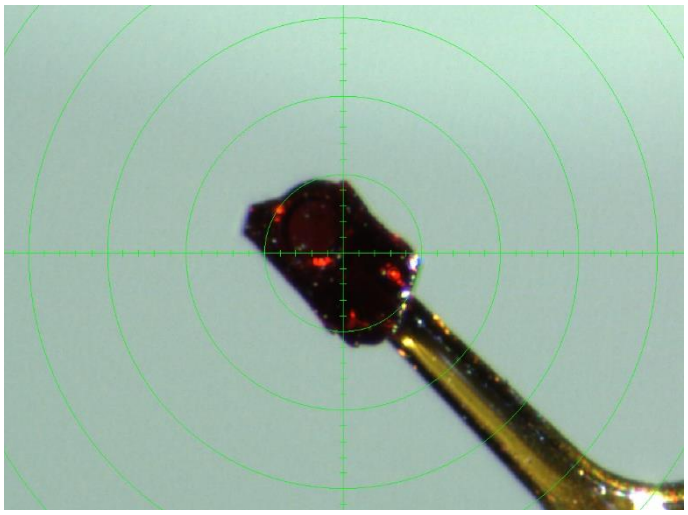

Figure 4.10. The same single crystal of **23a** via the Bruker D8 Venture camera at 135 K, now displaying a dark red colour.

The sample was slowly cooled through the transition and the crystal darkened until it reached the dark red shown in figure 4.10. Further cooling of the sample did not alter the colour. The colour change, while not as distinct as many examples that change from red to yellow, is further confirmation of the thermal transition.

With the successful high-pressure study conducted on polymorph D of $[Fe(abpt)_2(NCS)_2]$ in chapter 2 and the other studies on the other polymorphs[14], an investigation of the effects of pressure on **23a** was proposed. A single crystal was loaded into a modified Merrill-Bassett diamond anvil cell containing a stainless-steel gasket with a 0.4 mm hole, ruby spheres and paraffin oil. The specialised high-pressure diffractometer XIPHOS II with a Mo-Ka source was used for data collection. The unit cell was collected using 4 Phi scans with 0.5˚ scan width at 20 second exposure time. Measurements were performed from ambient pressure until ~6.3 kbar before the sample degraded and no longer gave high quality diffraction. No large changes in unit cell parameters were witnessed in this period. The crystals of **23a** grew as thin plates meaning they were unsuitable for the high-pressure cell this could be a factor into the quick deterioration of sample quality.

4.3 [Fe(2-(4,5-bis(4-fluorophenyl)-4H-1,2,4-triazol-3-yl)pyridine)$_2$(NCS)$_2$]– 23b

Single crystals of **23b** were grown from a layered crystallisation method, methanol solution (0.5 ml) containing a 1:1 mixture of **20** and **7** 0.003 mmol each. A second solution of water:methanol in a 1:1 ratio (0.5 ml)containing 0.006 mmol iron(II) bis-isothiocyanate was made. The orange iron-containing solution, as to not disturb the interface that forms was slowly injected via a needle under light yellow ligand solution. The interface turned to a dark red immediately. This crystallisation was originally a basic attempt to create a mixed ligand system containing one of each ligand with two isothiocyanates.

The solution was left undisturbed for several days and in this time very thin orange plate-like single crystals began to nucleate at the interface. The sample was left for a further week by that time single crystals had formed at the interface. Crystals were then carefully removed from the solution and placed under an inert perfluoro poly ether oil, *Fomblin-YR 1800,* on a clear glass microscope slide to allow easy manipulation and observation.

Initial structure solution was performed with SHELXT revealing a space group setting of *P21/c.* Structure reached convergence implied by a shift/ESD of 0.000. The structure was 99.6% complete to 0.84 Å with an R_1 of 5.09 % and wR_2 of 13.24 % indicating the crystal was of high quality. The maximum electron density map peak was of 0.5 eÅ^{-3} located near the metal centre and a minimum peak of -0.7 eÅ^{-3}.

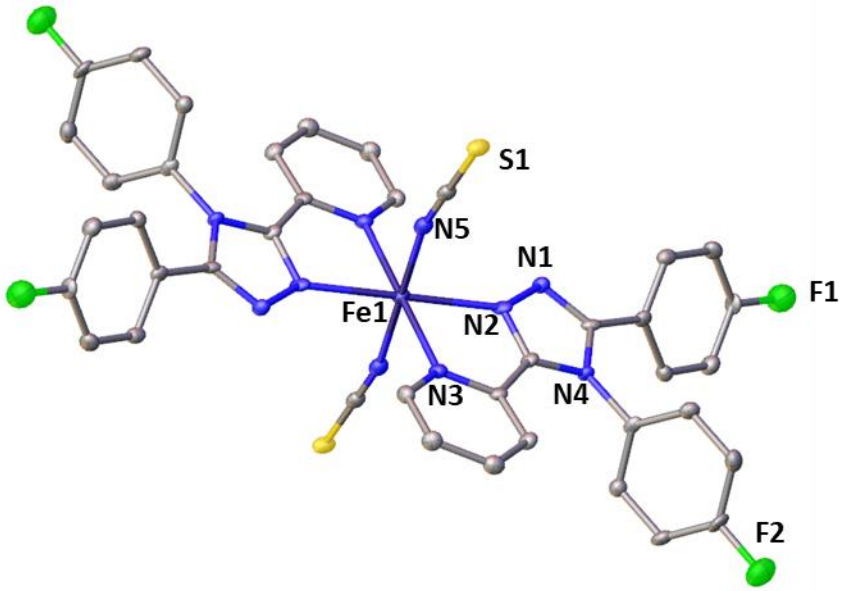

Figure 4.11. A symmetry expanded view of the crystallographic model of **23b** at 30 K. The anisotropic displacement parameters of all non-hydrogen atoms are shown at 50% probability. Hydrogen atoms omitted for clarity.

The final refinement results are shown in figure 4.11, a monomeric unit almost identical to **23a** except for no solvent molecules present in the cell. An iron(II) centre is coordinated to two **20** ligands and two isothiocyanates. Coordination to the metal centre occurs through nitrogen atoms 2 and 3 in **20**. The metal centre is located on an inversion centre and has a 6-nitrogen coordination sphere.

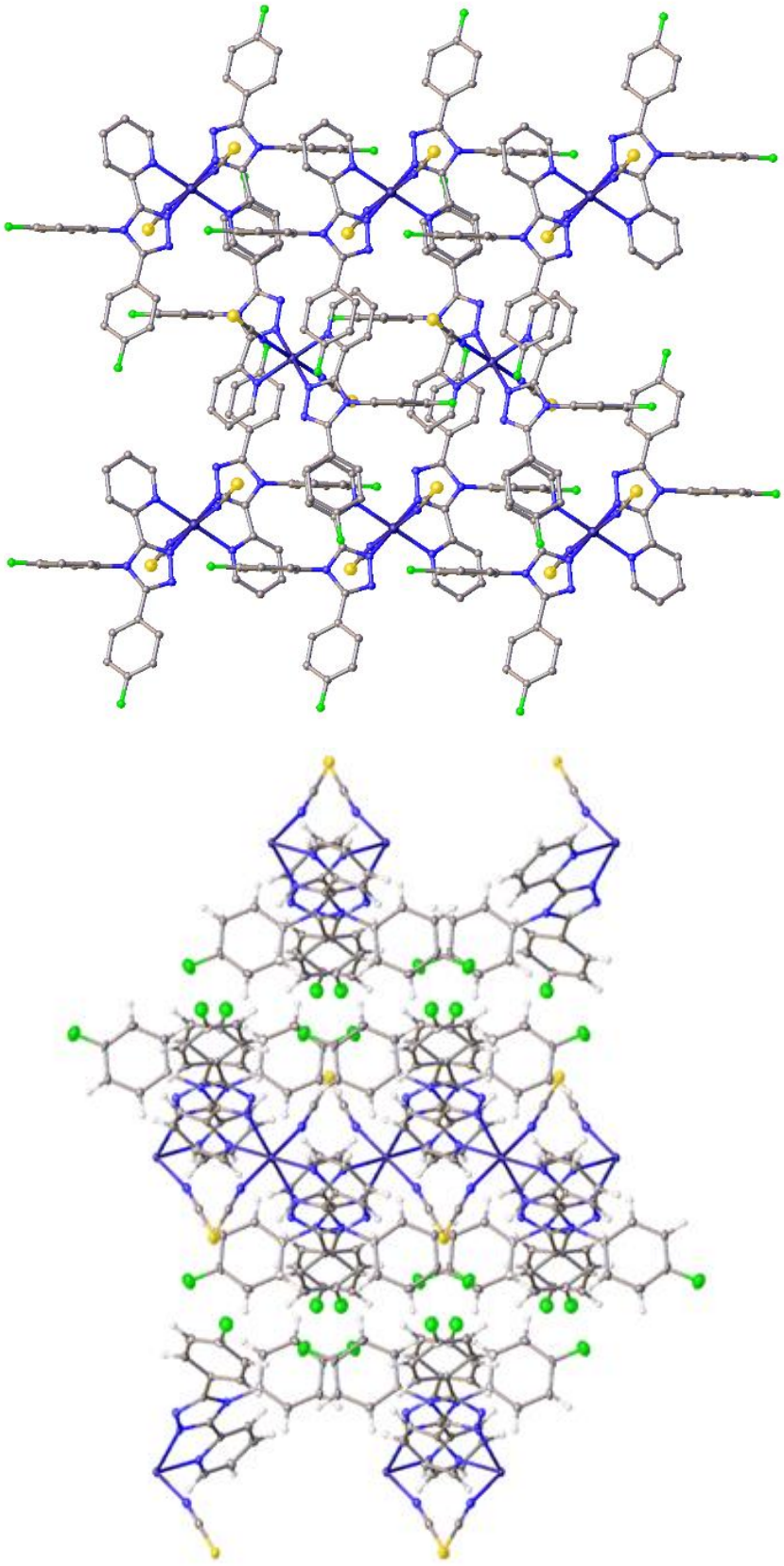

Figure 4.12. Image representing the iron centre packing of **23b** along the 001 (top) and along the 100 (bottom) axis showing the now empty pockets where methanol molecules were present in **23a**.

Crystals of **23b** pack in a similar manner to **23a** with layers of metal complex co-planar to the crystallographic (100) plane (figure 4.12), with no layers of solvent molecules separating them. This changes the packing slightly as fluorine atoms are angled differently to **23a,** no longer forming the same channels that the methanol occupied. The fluorine atoms are once again directed towards the layer boundaries. The Fe – Fe distance between iron atoms in the same stack (010) is 9.136 Å. There is π-π stacking present in 23b that was not present in 23a between a 4-fluorophenyl and the coordinated 2-pyridyl ring at 3.833 Å with a shift of 1.340 Å. Hydrogen bonding is also displayed in this system in the form of CH-S, first between S1 and C4 at 2.8449(12) Å, second between S1 and C12 at 2.8899(12) Å. The final hydrogen bonding observed is between F1 and C15, distance 2.372(3) Å.

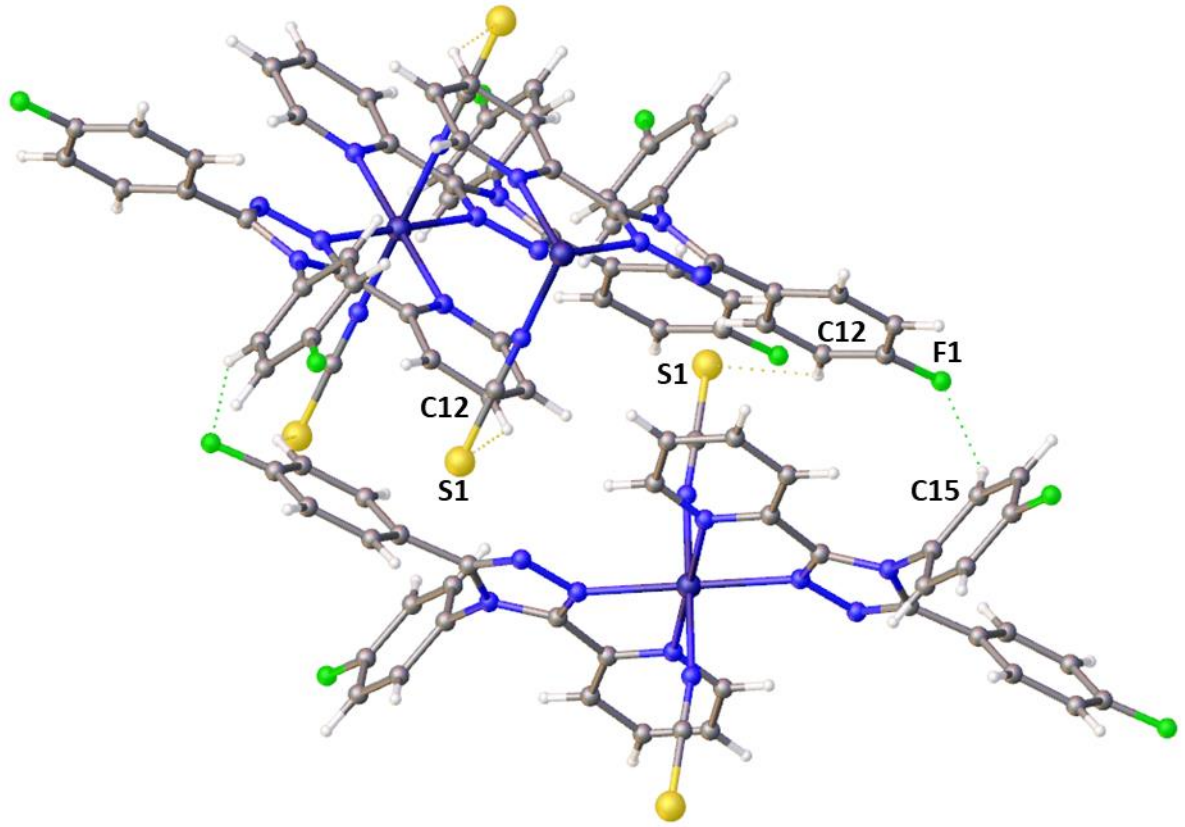

Figure 4.13. Image representing the hydrogen bonding interactions displayed in the crystalline model of **23b**.

Structural properties were investigated once the refinement had reached convergence. The analysis of Fe – N bond lengths that appeared in the range of 2.1 – 2.2 Å indicated the system was occupying a fully HS state and the Σ parameter was 74.3˚ and v_p = 12.859(13) Å^3. This indicated that the sample would need to be analysed

at a lower temperature to observe any electronic transitions. To achieve this the cooling apparatus on the diffractometer was swapped to the N-helix, capable of cooling to 20 K. The same crystal was used for this study and the sample was cooled at 5 K/min until it reached 30 K. Unlike XIPHOS I, the sample can be observed during the cooling process and no change in colour was observed.

Full data collection was performed at 30 K using the same strategy as the 250 K dataset. Data processing was carried out in the same manner as the 250 K dataset. Full structural determination of the 30 K data yielded the same structure as previously found with no change in space group any minor changes in unit cell parameters less than 1% average between the *a,b,c* and *β*. The structure was interrogated to observe any change in Fe – N bond lengths and these remained similar to the higher temperature measurement ranging from 2.1-2.22 Å and structural parameter $\Sigma = 73.3^{\circ}$, indicating the structure had not undergone a spin state transition while cooling the sample. v_p also remained consistent with a high spin state at 12.688(13) $Å^3$

This result was reminiscent of the four polymorphs of $[Fe(abpt)_2(NCS)_2]$, each displaying different spin crossover behaviour. Yet, there is a solvent molecule present in **23a, 23b** contains no solvent, meaning one is a solvate of the other instead of being polymorphs.

It was later found that during attempts to screen crystals of **23a** for the high-pressure experiments, the original crystals that had been left in oil between two glass slides in the instrument room had lost solvent. Unit cell matrix were matching the P21/c structure after the solvent loss. With this discovery further investigations into the crystal structures of **23a** and **23b** were conducted.

The crystal packing between the two systems is almost identical with small changes in Fe – Fe bond distances. The lack of π-π stacking in **23a** seems to be overcome by other structural characteristics of the system. A hypothesis for the difference in behaviour for these systems is a form of solvent mediated transition occurring in **23a** and the vast hydrogen bonding displayed in the crystal structure, this warrants further investigation into these systems with future work in using different solvents to test for further transitions.

One other explanation could be the void space and compressibility of the two structures. Void space analysis of **23a** indicates the complex occupies 66.25% of the

unit cell. Compared to an increased volume in **23b** at 66.95%. It is believed this is difference is not significant enough to cause large changes in thermal transitions, however.

4.4 Conclusion

Two new complexes have been discovered and their crystals analysed by SC-X-ray diffraction. The structures of these two systems are extremely similar with the same monomeric unit present, the key difference being a methanol solvent molecule present in **23a** this solvent molecule changes the space group of the system and the presence of this drastically changes the structural parameters upon cooling. **23a** displays the spin crossover phenomenon with a $T_{1/2}$=~175 K as indicated by a series of collections allowing for the unit cell parameters to be analysed. During this study it was noted that there was no thermal hysteresis present in the sample. Crystals of **23b** were cooled down to 30 K in attempts to discover similar results but the structure remained in the high spin state, indicating the transition could occur through a solvent mediation mechanism.

This hypothesis becomes clearer when analysing the crystal packing of these structures in that the difference in the hydrogen bonding displayed in **23a** (figure 4.4) allows for better communication between metal complexes in the structure. It was also found that crystals of **23a** that occupy the *C2/c* space group when left in the presence of air desolvate with the loss of this solvent molecule changing the structure into **23b** and now occupying a $P2_1/c$ space group. These $P2_1/c$ crystals can also be grown through other standard crystallisation methods.

This is the first structure of this study that contained one of the new 1,2,4-triazoles synthesised to display the spin crossover behaviour. Further investigation of this sample with magnetic techniques such as SQUID could allow for a more detailed view of transition. Crystals of **23a** were used in high pressure experiments whereby samples were loaded into a diamond anvil cell and tested at various pressures before sample quality degraded and no longer caused diffraction to a significant resolution. The samples were plate-like in morphology and not ideal for high pressure experimentation. Large crystals could be grown in the future in an attempt to collect a more in detail study of any pressure induced transition. Finally, crystals of **23a**

displayed no further change in structure with further cooling to 2.2 K. Therefore, crystals could be used in LIESST studies to determine if a light induced transition is possible.

4.5 References

1 N. Moliner, M. C. Muñoz, S. Létard, J. F. Létard, X. Solans, R. Burriel, M. Castro, O. Kahn and J. A. Real, *Inorganica Chim. Acta*, 1999, **291**, 279–288.

2 H. E. Mason, W. Li, M. A. Carpenter, M. L. Hamilton, J. A. K. Howard and H. A. Sparkes, *New J. Chem.*, 2016, **40**, 2466–2478.

3 C. F. Sheu, S. M. Chen, S. C. Wang, G. H. Lee, Y. H. Liu and Y. Wang, *Chem. Commun.*, 2009, **2**, 7512–7514.

4 K. Sugimoto, C.-H. Shih, J. Kim, C.-F. Sheu, M. Takata, Y. Wang and K. Kato, *Dalt. Trans.*, 2010, **39**, 9794.

5 C.-H. Shih, Y. Wang, B.-M. Cheng, K. Sugimoto, M. Takata and C.-F. Sheu, *Chem. Commun.*, 2012, **48**, 5715.

6 A. B. Gaspar, M. C. Muñoz, N. Moliner, V. Ksenofontov, G. Levchenko, P. Gütlich and J. A. Real, *Monatsh. Chem.*, 2003, **134**, 285–294.

7 G. M. Sheldrick, *Acta Crystallogr. Sect. A Found. Crystallogr.*, 2015, **71**, 3–8.

8 O. V Dolomanov, L. J. Bourhis, R. J. Gildea, J. A. K. Howard and H. Puschmann, *J. Appl. Crystallogr.*, 2009, **42**, 339–341.

9 J. A. Kitchen, N. G. White, M. Boyd, B. Moubaraki, K. S. Murray, P. D. W. Boyd and S. Brooker, *Inorg. Chem.*, 2009, **48**, 6670–6679.

10 N. Moliner, M. C. Muñoz, P. J. Van Koningsbruggen and J. A. Real, *Inorganica Chim. Acta*, 1998, **274**, 1–6.

11 M. R. Probert, C. M. Robertson, J. A. Coome, J. A. K. Howard, B. C. Michell and A. E. Goeta, *J. Appl. Crystallogr.*, 2010, **43**, 1415–1418.

12 C. J. McMonagle and M. R. Probert, *J. Appl. Crystallogr.*, 2019, **52**, 445–450.

13 P. Gütlich, Y. Garcia and H. A. Goodwin, *Chem. Soc. Rev.*, 2000, **29**, 419–427.

14 H. E. Mason, J. R. C. Musselle-Sexton, M. L. Hamilton, J. A. K. Howard, M. R. Probert and H. A. Sparkes, *New J. Chem.*, 2021, **45**, 14014–14023.

Chapter 5: Structural analysis of [Fe(2,2'-(1-(pyridine-4-yl)-1H-1,2,4-triazole-3,5-diyl)dipryrdine)$_2$(NCS)$_2$] complexes

5.1 [Fe(2,2'-(1-(pyridine-4-yl)-1H-1,2,4-triazole-3,5-diyl)dipryrdine)$_2$(NCS)$_2$].6H$_2$O – 24a

This chapter will discuss the generation and structural analysis of the complexes **24a** and **24b**, these system were generated from the literature compound N4-(4-Pyridyl)-3,5-di(2-pyridyl-1,2,4-triazole) (**5**) and iron bis-isothiocyanate.[1–3] A mixture of layering crystallisation method used to generate the four polymorphs of [Fe(abpt)$_2$(NCS)$_2$][4–9] and evaporation was used previously discussed in chapter 3.4. This method produced two new compounds that displayed some unique properties.

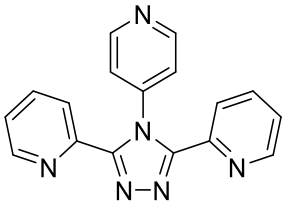

Figure 5.1. Molecular representation of N4-(4-Pyridyl)-3,5-di(2-pyridyl)-1,2,4-triazole

N4-(4-Pyridyl)-3,5-di(2-pyridyl)-1,2,4-triazole is a previously studied compound within the literature. From these studies the compound has been used as a ligand with various transition metals such as Cu, Ag and Fe.[10–13] In the literature there was no result for iron(II) bis-isothiocyanate among other metal salts.

Suitable single crystals for SC-XRD were grown by preparing a (20 mg 0.006 mmol) methanol solution (2 ml) containing N4-(4-Pyridyl)-3,5-di(2-pyridyl-1,2,4-triazole (**5**) and a 0.003 mmol methanol:water solution (1 ml) in a 1:1 ratio containing iron(II) bis-isothiocyanate. The orange iron solution was injected slowly via a needle under the ligand solution as to avoid disturbing the interface that formed, this interface turned to a deep red upon initial mixture of the solutions.

After several weeks no crystals had formed and the two solutions had mixed, ventilation holes were added to the lid of the sample tube vial and the solution was left to slowly evaporate. After a week nucleation started and after a further week, two sets of single crystals were present, the first were small red platelike crystals, secondly larger yellow platelike crystals were deposited. Crystals were extracted to a

microscope slide and place into an inert perfluoro poly ether oil, *Fomblin-YR 1800,* allowing for sample manipulation.

A yellow single crystal that displayed visual high quality under examination by microscope with dimensions 0.102 x 0.154 x 0.167 mm was selected for analysis by single crystal X-ray diffraction.

The final refinement had a shift/ESD of 0.001, with residual electron density peaks of min = -1.0 eÅ^{-3} and max = 1.2 eÅ^{-3} located near the iron metal centre, the completeness to 0.84 A was 99% with an R_1 factor of 5.60% and wR_2 of 16.43%. Indicating the sample was of high quality.

The final refinement results displayed in figure 5.2, a complex with an iron(II) metal centre coordinated to two 2,2'-(1-(pyridine-4-yl)-1H-1,2,4-triazole-3,5-diyl)dipyridine through nitrogen atoms N3 and N4 and two negatively charged isothiocyanates to form a octahedral complex. The coordination sphere of 6 nitrogen is considered to be optimal for the possibility of SCO being present in iron(II) systems. There are 6 uncoordinated water molecules present in the crystal structure for every metal complex.

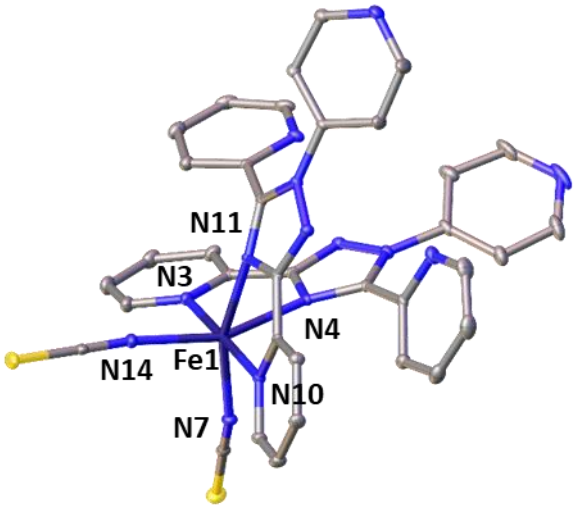

Figure 5.2. Asymmetric unit of **24a** at 150 K, anisotropic displacement parameters of all non-hydrogen atoms are shown at 50% probability. Hydrogen atoms omitted for clarity.

The crystal packing of **24a** displayed in figure 5.3, layers of metal complexes stack to with metal – metal distances of 8.863(4) Å between centres in the same layer and 12.365(5) Å between different layers of metal complexes. The packing forms channels in between layers of metal complexes that are occupied by the high number of water molecules, these water molecules allow for hydrogen bonding (figure 5.4) to occur between different layers of metal complexes, potentially improving communication in the structure.

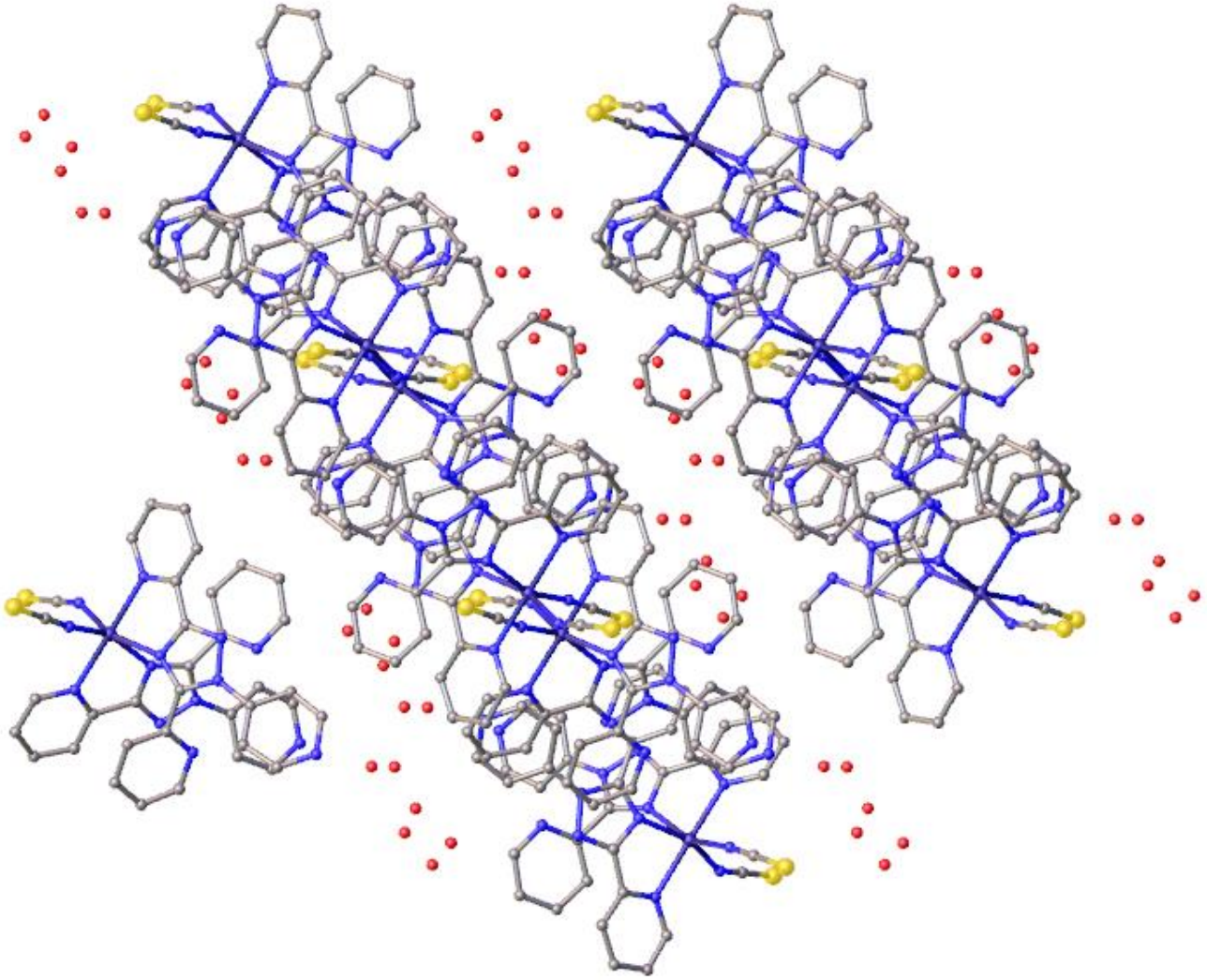

Figure 5.3. Image representing the packing of metal complex and solvent molecules in the crystal structure of **24a**, viewed along the *b* axis.

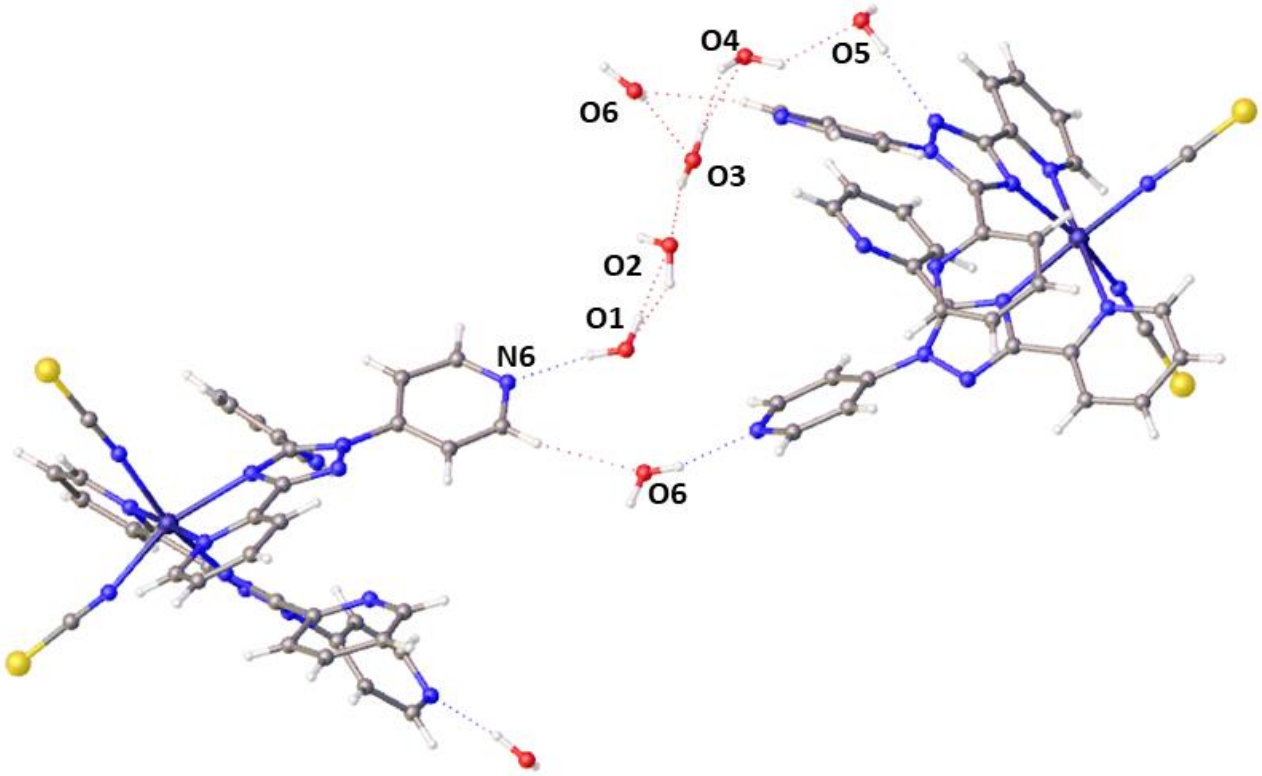

Figure 5.4. Image representing the hydrogen bonding interactions between two metal complex moieties and the water molecules present in **24a**.

The key aspect of this new crystal structure is the change in the triazole coordinated to the metal centre. The original ligand shown in figure 1 is a literature compound and previously coordinated to various metals. However, in the crystal structure discovered the ligand has undergone a form of migration during the coordination process (figure 5.5). To confirm this the NMR of the starting material was investigated reconducted to ensure it was clean and in line with the literature results, a crystal structure of the starting material had also been obtained that matched the known crystal structure accessible on the CSD (Cambridge structural database). A literature search was conducted to discover experiments that induce a similar migration had been discovered by Sally Brooker et al.[3] Utilising 1,2,4-triazoles migrations are forced to occur by adapting the aromatic ring located at nitrogen 4. These migrations were also found to occur with certain solvents and heating of the sample. The serendipitous result found is unique due to the migration occurring during the coordination process and no change in structure to the aromatic ring that migrates, the result also occurs at room temperature while not completely unique is a rare occurrence.

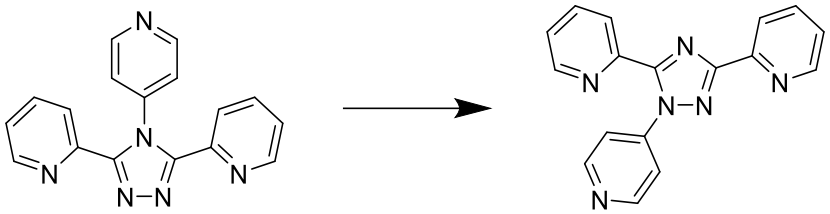

Figure 5.5. Molecular representation of the ligand rearrangement observed

While this result was unexpected, the structure was still a candidate for potentially thermal transitions. Once the refinement reached convergence the structure was interrogated for its structural parameters. Analysis of Fe – N bond lengths that ranged from 2.07 – 2.24 Å indicated the system occupied a fully high spin state, the distortion parameters Σ = 98.723(2) ˚ and v_p = 13.097(12) Å^3. Cooling of the sample would be required to observe any potential thermal transitions.

These yellow crystals were left exposed to air for weeks prior to initial data collection, during this time they were observed to appear cloudy and cracked. Multiple crystals were analysed briefly by X-ray diffraction. The quality of these crystals had dropped significantly, it this is likely due to a loss of solvent over time.

Due to the sample quality decreasing over time with the loss of solvent a new crystal was selected. Another crystal was selected for use on the ultra-low temperature diffractometer XIPHOS I.[14,15] The crystal was mounted to sharpened graphite using a two-part epoxy resin (Loctite double bubble) that is a known good thermal conductor. The graphite rod was attached the sample holder on XIPHOS I before the two vacuum cans were attached. The sample was exposed to vacuum of 10^{-6} and cooled to 2 K at 5 K/min. Samples on XIPHOS I must be centred by diffraction, when exposed to X-rays for this purpose the sample quality had dropped significantly, and the sample was deemed unsuitable for further study. The quick loss of solvent in the sample unfortunately proved to be a large obstacle in further studies.

5.2 [Fe(2,2'-(1-(pyridine-4-yl)-1H-1,2,4-triazole-3,5-diyl)dipryrdine)$_2$(NCS)$_2$].MeOH 24b

The small red plate shaped crystals found in the same sample vial as the yellow crystals, were also analysed by X-ray diffraction. Red crystals were extracted from the sample vial alongside the yellow and placed into the inert oil on a glass slide.

A red platelike crystal of 0.077 x 0.108 x 0.113 mm, was selected for analysis by single crystal X-ray diffraction. Structure solution was performed using SHELXT[16] via intrinsic

phasing in Olex2[17] confirming the *Pnma* space group originally predicted by XPREP, the majority non-hydrogen atoms in the asymmetric unit were successfully located with some corrections in elemental assignment.

The final refinement had a shift/ESD of 0.000, with residual electron density peaks of min = -0.4 eÅ^{-3} and max = 0.4 eÅ^{-3} located near the iron metal centre, the completeness to 0.84 Å was 100% with an R_1 factor of 6.89% and wR_2 of 21.73%. These refinement results are after a solvent mask had been applied, this is because a more severe case of desolvation occurs during the collection. The refinement before the mask was applied would not reach convergence due to the inability to model solvent molecules that were lost during the collection, a recollection was attempted to resolve this issue but results did not change for the better.

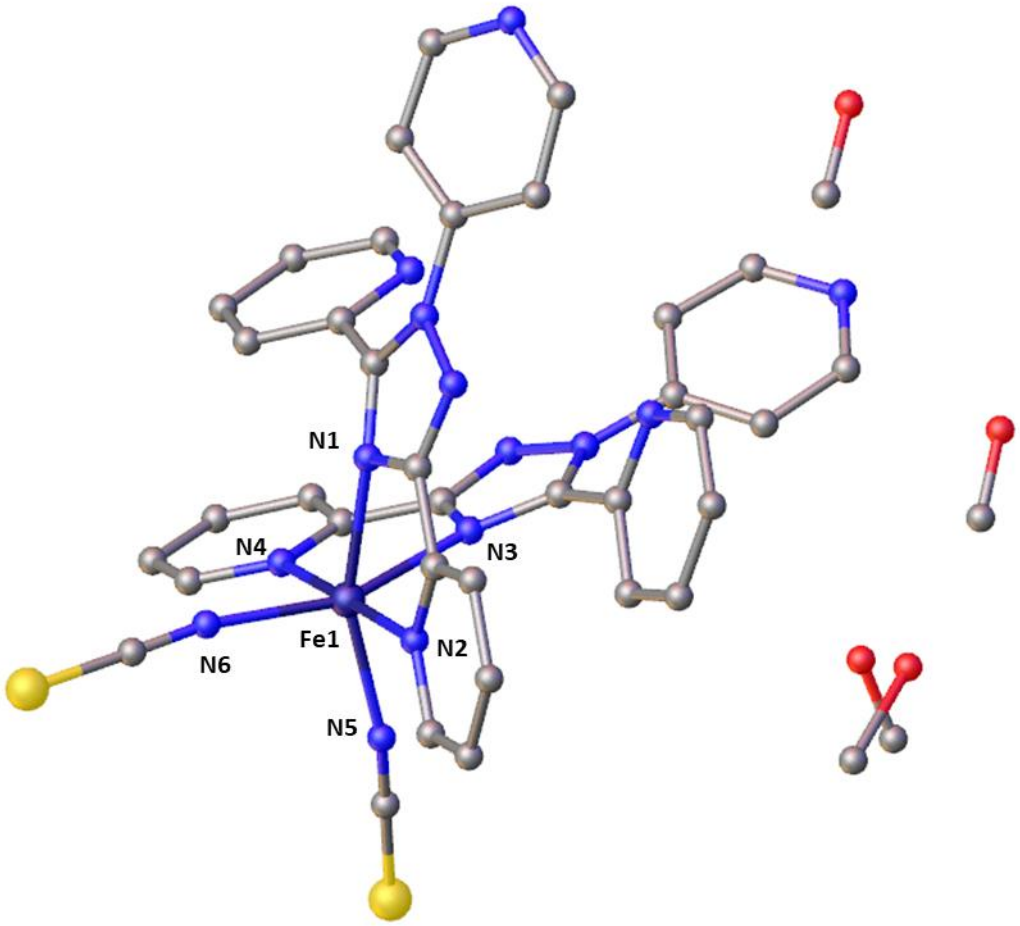

Figure 5.6. Asymmetric unit of **24b** at 150 K, anisotropic displacement parameters of all non-hydrogen atoms are shown at 50% probability. Hydrogen atoms omitted for clarity.

Final refinement results yielded the structure in figure 5.5, consisting of the same metal complex found in **24a**, an iron(II) metal centre coordinated to two migrated 2,2'-(1-(pyridine-4-yl)-1H-1,2,4-triazole-3,5-diyl)dipryrdine ligands and two isothiocyanates. The repeating unit also contained 4 uncoordinated methanol molecules (2 methanol molecules removed using SQUEEZE algorithm. The coordination sphere of 6 nitrogen atoms is consistent with **24a** and remains optimal for potential SCO.

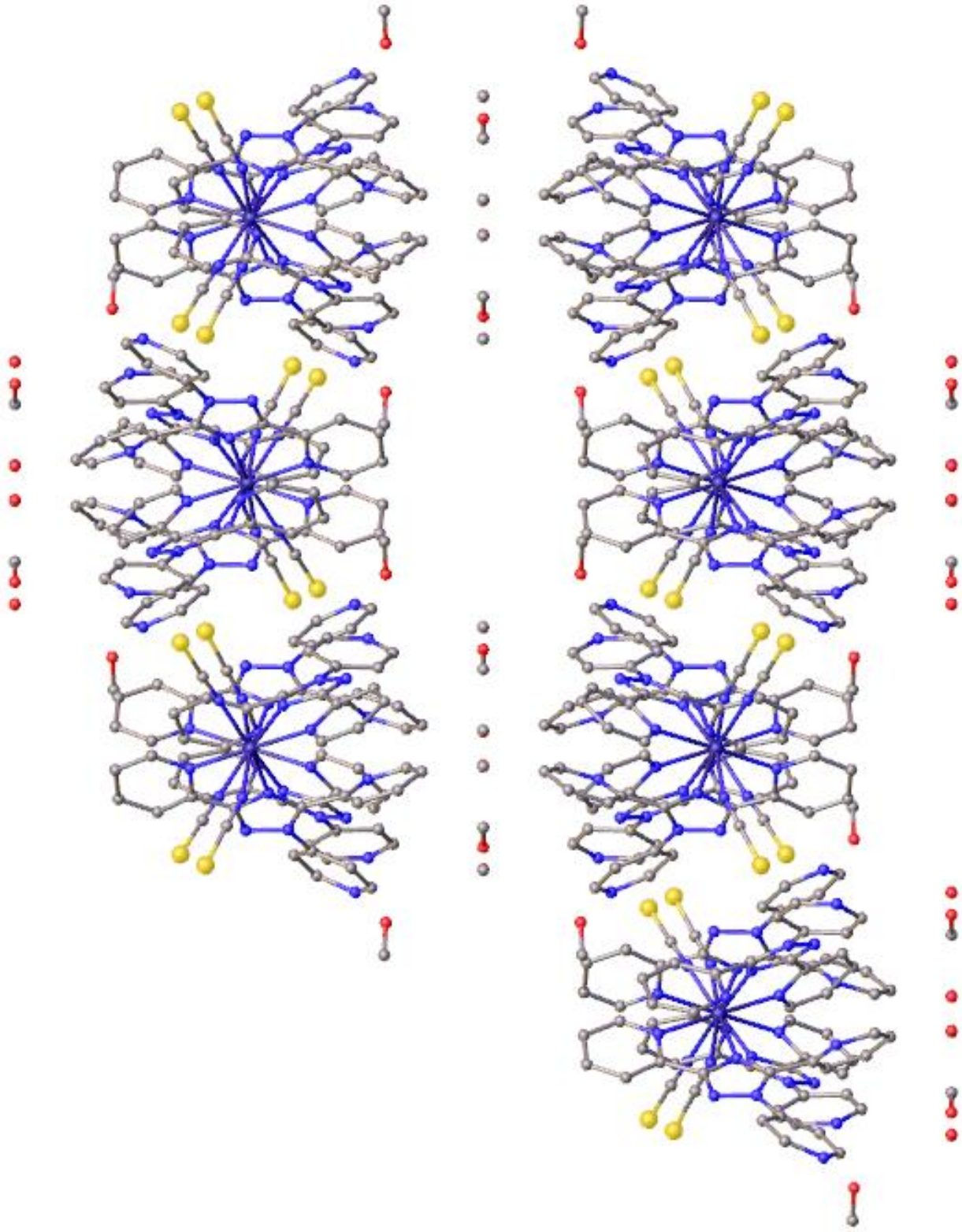

Figure 5.7. Image representing the packing of metal complexes and solvent in **24b** viewed along the *a* axis.

Crystal packing of **24b** displayed in figure 5.7 is similar to **24a** with layers of metal complex separated by the various methanol molecules. The distance between moieties in the same layer = 8.676(3) Å and between layers = 14.8339(6) Å. The hydrogen

bonding of the system could not be investigated due to the large disorder across methanol molecules present in the cell.

Thus, the structures are different solvates, the yellow hydrate and red methanol solvate. There was a hypothesis that this red crystal could have been the unmigrated ligand coordinating but this result dispels that.

Interrogation of the structural parameters revealed the Fe – N bond lengths to range from 2.07 – 2.26 Å, distortion parameters Σ = 101.345(3)˚ and v_p = 13.1643(3) Å^3, indicating the system occupied a fully HS state.

The data quality for **24b** was significantly hampered by the loss of solvent molecules during collection, this resulting in low quality data. Therefore, a solvent mask was applied to allow a stable refinement that could be interrogated and as previously mentioned a structure that does not converge before the application of a solvent mask. Due to the exact positions of methanol molecules are unreliable since they are leaving the crystal during collection. A new single crystal was selected, mounted on a Kapton loop with an excess of *Fomblin-YR 180 0*oil used to shield the sample from air and hopefully stop solvent leaving the crystal structure. The crystal was monitored by diffraction, the reflections displayed reductions in quality within 2 hours. Recrystallisations were attempted with small red platelike crystals being grown again, these crystals also lost solvent and quality quickly.

With all these factors taken into account further measurements of crystals of **24b** were not pursued.

5.3 Investigation Of The Structural Rearrangement

Unfortunately, further analysis of **24a** and **24b** was hampered by the loss of free solvent molecules from the crystal structure. This meant that investigations into potential spin crossover phenomenon in these systems could not be complete. Fortunately, the results of these crystal structures provided interesting results that were not originally expected, the rearrangement of the 4-pyridyl being the key result.

As mentioned previously the literature investigation of these migrations yielded a body of work conducted over years and published as various papers prominently by *Sally Brooker et al*.[18,19] The work they conducted involved causing these rearrangements to occur via adapting the ring that migrates and in some cases coordinating the already migrated ring to a metal centre.

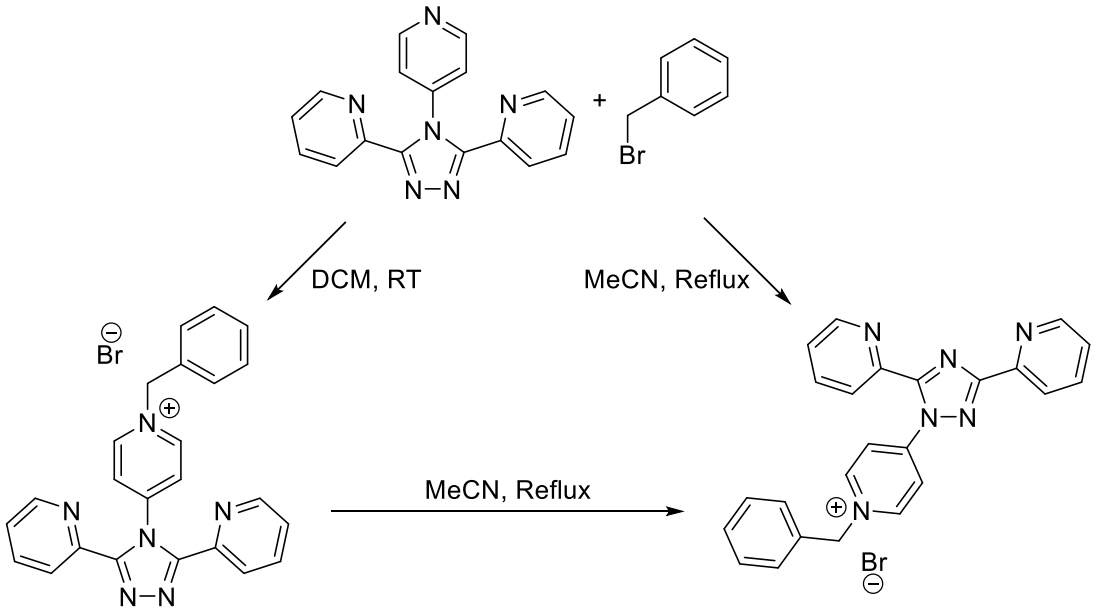

Figure 5.8. Image adapted from Sally Brooker et al (2010)[3], displaying the effects of changing experimental conditions on **5**.

Figure 5.8 displays some of their results starting with the same compound (N4-(4-Pyridyl)-3,5-di(2-pyridyl-1,2,4-triazole - **5**) where they induce a rearrangement with the (bromomethyl)benzene, in the presence of MeCN and under reflux conditions, this changed the structure of the 4-pyridyl ring. The addition of (bromomethyl)benzene in the presence of DCM at room temperature reacted at the same position on the 4-pyridyl but did not cause a rearrangement of the ring. This is an example of one result in their studies, it stated that temperature and the solvent used were crucial to causing these rearrangements to occur.

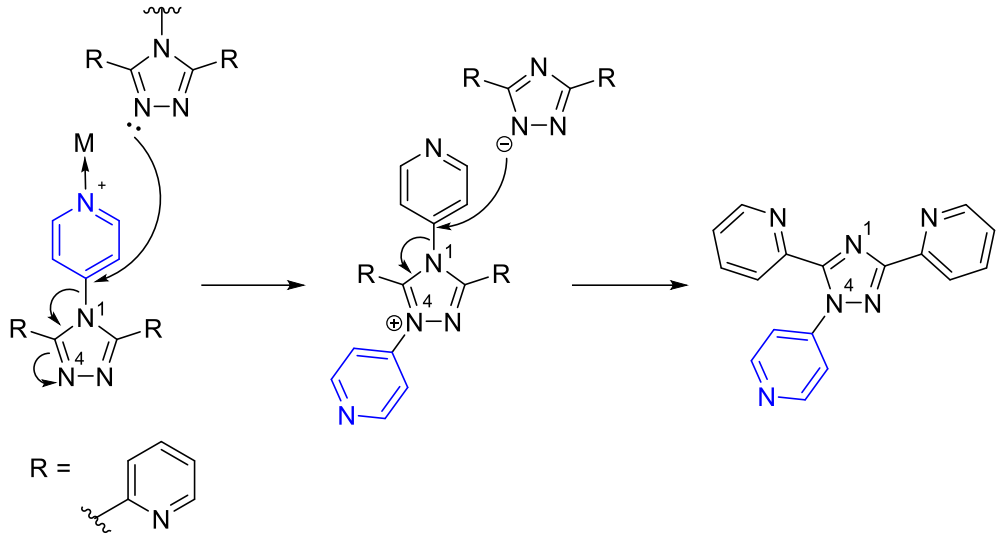

Figure 5.9. Proposed mechanism based upon the mechanism discussed in S. Brooker et al.[3]

A proposed mechanism (figure 5.9) has been discussed in S. Brooker *et al* [3]. In this study it is proposed that acidic conditions could be one of the driving forces for the reaction of this rearrangement. The experiments that produced crystals of **24a** and **24b** contained no acid, one hypothesis is that the metal ion could be acting as a weak acid driving forward the migration.

The results observed in **24a** and **24b** are unique in the aspect that while this rearrangement occurred there was no change in the structure of the 4-pyridyl ring. Secondly, to the authors knowledge none of the rearrangements previously discovered have occurred during the coordination to a metal ion. The result also occurred at room temperature, while not unheard of, is uncommon in these migrations. The combination of these three factors making the two structures prepared and analysed extremely interesting. With these results presented in this work and the information in the literature it was vital that a new range of experiments be undertaken. These experiments incorporated the factors of different solvents and heating of the sample being crucial to the rearrangements. Therefore, new crystallisations containing the ligands with a 4-pyridyl ring (**4-7** and **13-14**) with a wide range of solvents and heating of the samples were set up in order to discover any other migrations that may have been missed.

These crystallisations produced new crystal structures that will be discussed, the first in chapter 6, in that the use of new experimental parameters proved crucial to its discovery.

5.4 Conclusion

Two new complexes have been synthesised and crystals grown from a singular crystallisation vial using the layered crystallisation method. These crystals analysed by SC-X-ray diffraction yielding two new crystal structures **24a** and **24b**. During the coordination process a rearrangement of the 4-pyridyl ring from atom nitrogen-4 to nitrogen-1 of the triazole ring. These two structures contained the same monomeric unit with different solvents present in the structure, **24a** = water, **24b** = methanol. The interrogation of Fe – N bond lengths revealed both structures to be in the fully high spin states. Crystals of **24a** were mounted onto ultra-low temperature diffractometer XIPHOS I to collect a 2.2 K dataset, however, the sample deteriorated with the loss of solvent under the strong vacuum used in this set up. Crystals of **24b** suffered from a loss of solvent and sample quality during the initial data collect, the crystals were monitored and lost solvent within 2 hours while mounted on the Bruker D8 Venture diffractometer, the loss of solvent during data collection meant the crystal structure had a large amount of disorder associated with the methanol solvent molecules. With these problems both samples could not be investigated at lower temperatures and have their ability to undergo SCO probed.

The rearrangement observed in these structures has been studied in the literature with proposed mechanisms and insights into temperature and solvents that can induce these migrations. The results presented here are interesting in that they occur while coordination to iron(II) bis-isothiocyanate, do not change the structure of the 4-pyridyl ring other than it’s position on the triazole and they occur at room temperature These results changed the way coordination experiments were conducted on ligands containing a 4-pyridyl ring, leading to new results discussed in chapter 6.

5.5 References

1 M. H. Klingele and S. Brooker, *European J. Org. Chem.*, 2004, 3422–3434.

2 J. A. Kitchen, N. G. White, M. Boyd, B. Moubaraki, K. S. Murray, P. D. W. Boyd and S. Brooker, *Inorg. Chem.*, 2009, **48**, 6670–6679.

3 J. A. Kitchen, D. S. Larsen and S. Brooker, *Chem. - An Asian J.*, 2010, **5**, 910–918.

4 N. Moliner, M. C. Muñoz, S. Létard, J. F. Létard, X. Solans, R. Burriel, M. Castro, O. Kahn and J. A. Real, *Inorganica Chim. Acta*, 1999, **291**, 279–288.

5 H. E. Mason, W. Li, M. A. Carpenter, M. L. Hamilton, J. A. K. Howard and H. A. Sparkes, *New J. Chem.*, 2016, **40**, 2466–2478.

6 C. F. Sheu, S. M. Chen, S. C. Wang, G. H. Lee, Y. H. Liu and Y. Wang, *Chem. Commun.*, 2009, **2**, 7512–7514.

7 K. Sugimoto, C.-H. Shih, J. Kim, C.-F. Sheu, M. Takata, Y. Wang and K. Kato, *Dalt. Trans.*, 2010, **39**, 9794.

8 C.-H. Shih, Y. Wang, B.-M. Cheng, K. Sugimoto, M. Takata and C.-F. Sheu, *Chem. Commun.*, 2012, **48**, 5715.

9 A. B. Gaspar, M. C. Muñoz, N. Moliner, V. Ksenofontov, G. Levchenko, P. Gütlich and J. A. Real, *Monatsh. Chem.*, 2003, **134**, 285–294.

10 J. Klingele, H. Scherer and M. H. Klingele, *Zeitschrift fur Anorg. und Allg. Chemie*, 2009, **635**, 2279–2287.

11 C. P. Li, J. Guo and M. Du, *Inorg. Chem. Commun.*, 2013, **38**, 70–73.

12 X. Wang and Y. M. Guo, *Inorg. Chem. Commun.*, 2015, **60**, 115–118.

13 L. H. Xiao and X. W. He, *Inorg. Nano-Metal Chem.*, 2020, **50**, 361–367.

14 M. R. Probert, C. M. Robertson, J. A. Coome, J. A. K. Howard, B. C. Michell and A. E. Goeta, *J. Appl. Crystallogr.*, 2010, **43**, 1415–1418.

15 C. J. McMonagle and M. R. Probert, *J. Appl. Crystallogr.*, 2019, **52**, 445–450.

16 G. M. Sheldrick, *Acta Crystallogr. Sect. A Found. Crystallogr.*, 2015, **71**, 3–8.

17 O. V Dolomanov, L. J. Bourhis, R. J. Gildea, J. A. K. Howard and H. Puschmann, *J. Appl. Crystallogr.*, 2009, **42**, 339–341.

18 H. L. C. Feltham, A. S. Barltrop and S. Brooker, *Coord. Chem. Rev.*, 2017, **344**, 26–53.

19 S. Brooker, *Chem. Soc. Rev.*, 2015, **44**, 2880–2892.

Chapter 6: Structural analysis of spin crossover system [Fe(2-(3-(4-methoxyphenyl)-1-(pyridine-4-yl)-1H-1,2,4-triazol-5-yl)pyridine)$_2$(NCS)$_2$]

6.1 Synthesis and crystal structure analysis of system [Fe(2-(3-(4-methoxyphenyl)-1-(pyridine-4-yl)-1H-1,2,4-triazol-5-yl)pyridine)$_2$(NCS)$_2$]

This chapter will detail the generation and structural analysis of **25**, an organometallic species synthesised from **14** and iron(II) bis-isothiocyanate using a modified version of the layering technique used to create the four polymorphs of [Fe(abpt)$_2$(NCS)$_2$].[1–6] The synthesis of this structure comes as a direct result of the discoveries made in chapter 5 where a rearrangement of a 4-pyridyl ring from nitrogen 4 to nitrogen 1 on the 1,2,4-triazole **5** occurs during the coordination to the metal centre. This result, in combination with literature studies that suggested solvent and heating of the sample were important factors to getting these rearrangements to occur, meant new experiments were set up with different solvents and heating of samples prior to crystallisation.[7]

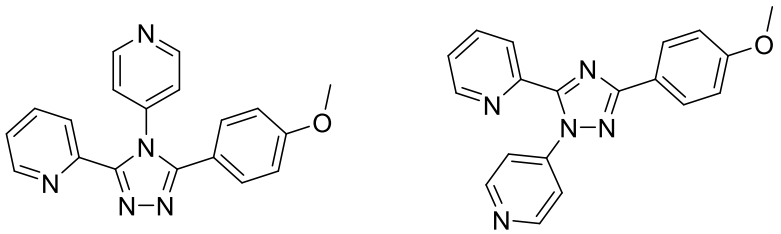

Figure 6.1. Molecular representation of **14** (left) and its rearranged structure (right).

Single crystals suitable for SC-XRD were grown from a methanol and water solution in a 1:1 ratio containing iron(II) bis-isothiocyanate that was injected slowly via a needle under a methanol solution containing **14**. The layered vial was then heated at 50˚C for 1 hour before cooled to room temperature and left to allow for crystallisation. After several days no crystals formed at the interface and ventilation holes were added to the sample tube lid. After 1 week nucleation appeared on the side of the vial and within 2 weeks fully formed single crystals of an appropriate size were present. Crystals were removed from the sample tube and placed into inert perfluoro poly ether oil, *Fomblin-YR 1800*, on a glass slide and observed under a microscope.

A brown-yellow needle single crystal of 0.088 x 0.092 x 0.336 mm^3 dimensions was selected that displayed high quality under observation by microscope. Structure solution was performed by SHELXT[8] via intrinsic phasing in the Olex2 GUI[9] that confirmed a orthorhombic space group setting of *Pbcn*. Final structure solution reached convergence as implied by a shift/ESD of -0.001. The minimum unaccounted electron density of -0.8 $eÅ^{-3}$ and the maximum of 0.6 $eÅ^{-3}$ located along the Fe1 – N11 bond. The final structure was refined against data that were 99.9% complete to 0.83 Å with R_1 factor of 4.43% and wR_2 of 13.55% indicating the sample dataset was of high quality.

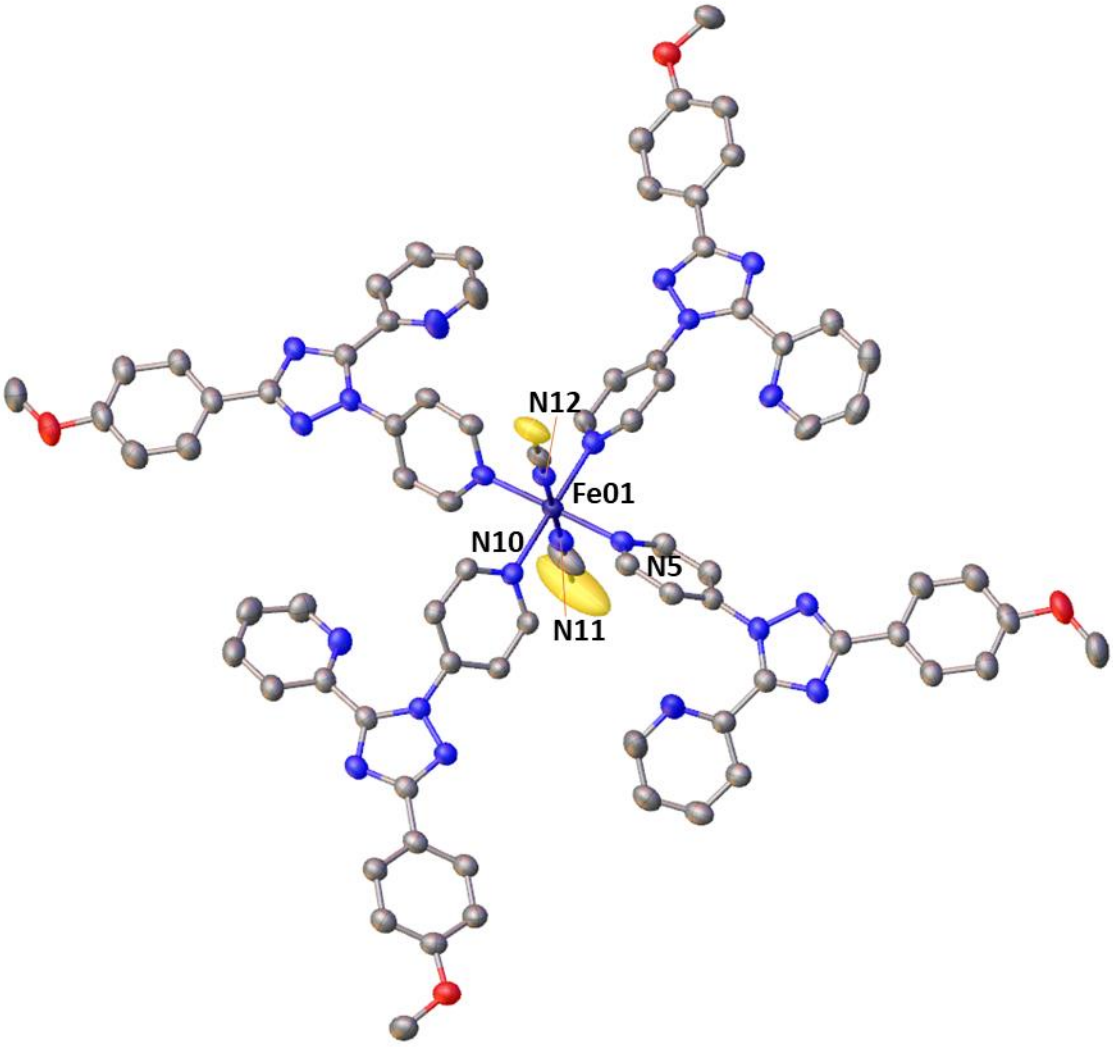

Figure 6.2. A symmetry expanded view of the crystallographic model of **25** at 150 K, anisotropic displacement parameters of all non-hydrogen atoms are shown at 50% probability. Hydrogen atoms have been removed for clarity.

The final refinement results yielded the structure presented in figure 6.2, a monomeric unit containing a organometallic complex consisting of an iron(II) centre, two isothiocyanates coordinated and four 2-(3-(4-methoxyphenyl)-1-(pyridine-4-yl)-1H-1,2,4-triazol-5-yl)pyridine ligands that had undergone a similar migration to that witnessed in **24a** and **24b**. While a similar migration had occurred, the coordination was now occurring solely through nitrogen atom 5 in the 4-pyridyl fragment. The ligands are now binding in a monodentate mode due to the restrictions imposed by the rearrangement, which was unexpected, and a change to previous results that all contained ligands displaying bidentate coordination. This change to coordination behaviour is due to the inability for the ligand to coordinate in a bidentate fashion without causing a large amount of strain on the structure. Coordinating in a monodentate fashion allows for less steric hinderance and bond angels closer to the optimal for a octahedral structure.

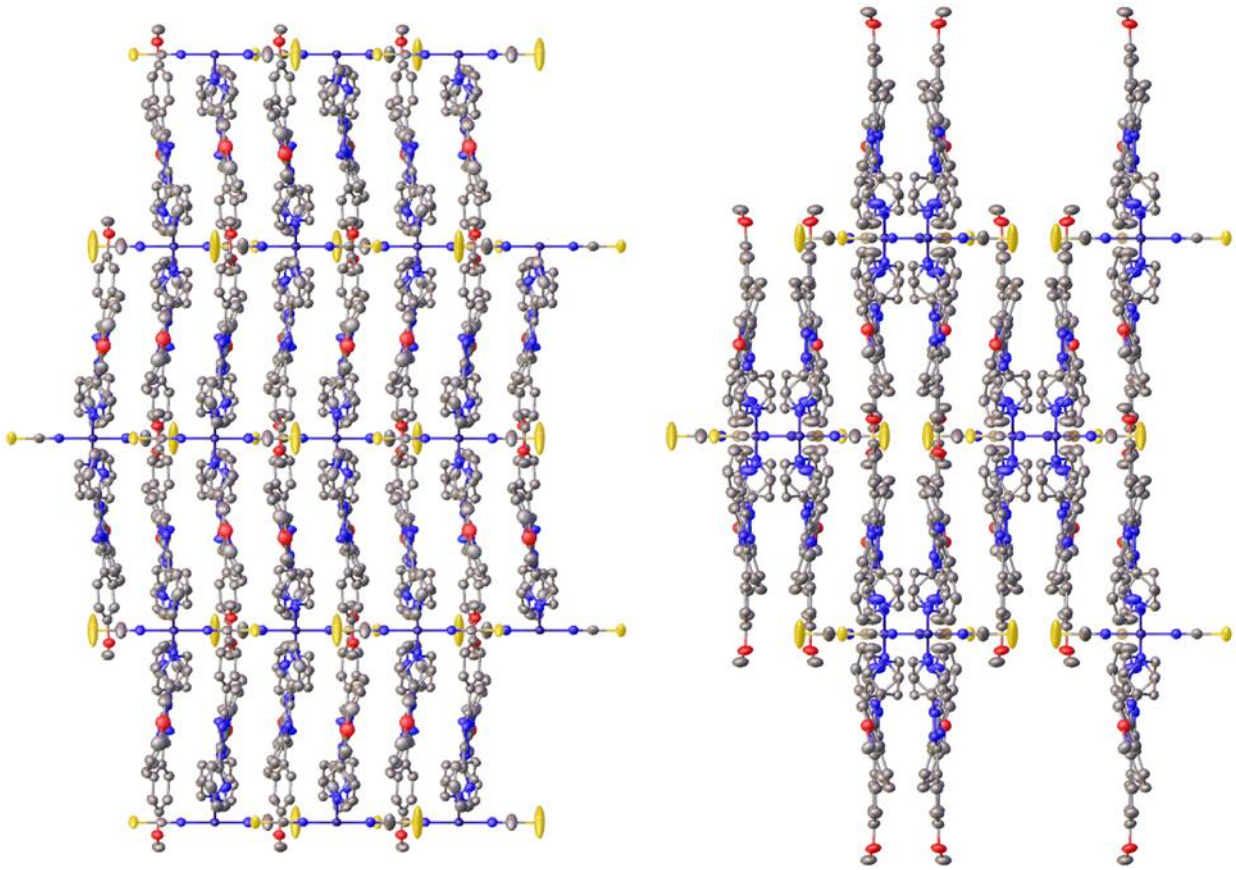

Figure 6.3. Image representing the packing of metal complexes in the crystal structure of **25** along the *a* (left) and *c* (right) axis.

The crystal packing of the structure is shown in figure 6.3 and shows the heavy overlapping of ligands in the packing present in the structure. Stacking is observed in

the structure with stacks of metal complexes forming in the 010 crystallographic direction. (Fe – Fe atom distances = 11.5452(4) Å.) Hydrogen bonding in the system is observed in the strucute and these interactions are shown in figure 6.4. On each metal complex one of the sulphur atoms has two sets of hydrogen bonds: CH-S between S2 and C4 at 2.9784(5), CH-N, between N6 and C19 at 2.5452(14) Å. Finally, the methoxy group on each rearranged ligand displays hydrogen bonding through both the oxygen and carbon, CH-O, O1 to C22 and CH-N, C14 to N9 at 2.5504(15) Å and 2.5627(14) Å respectively.

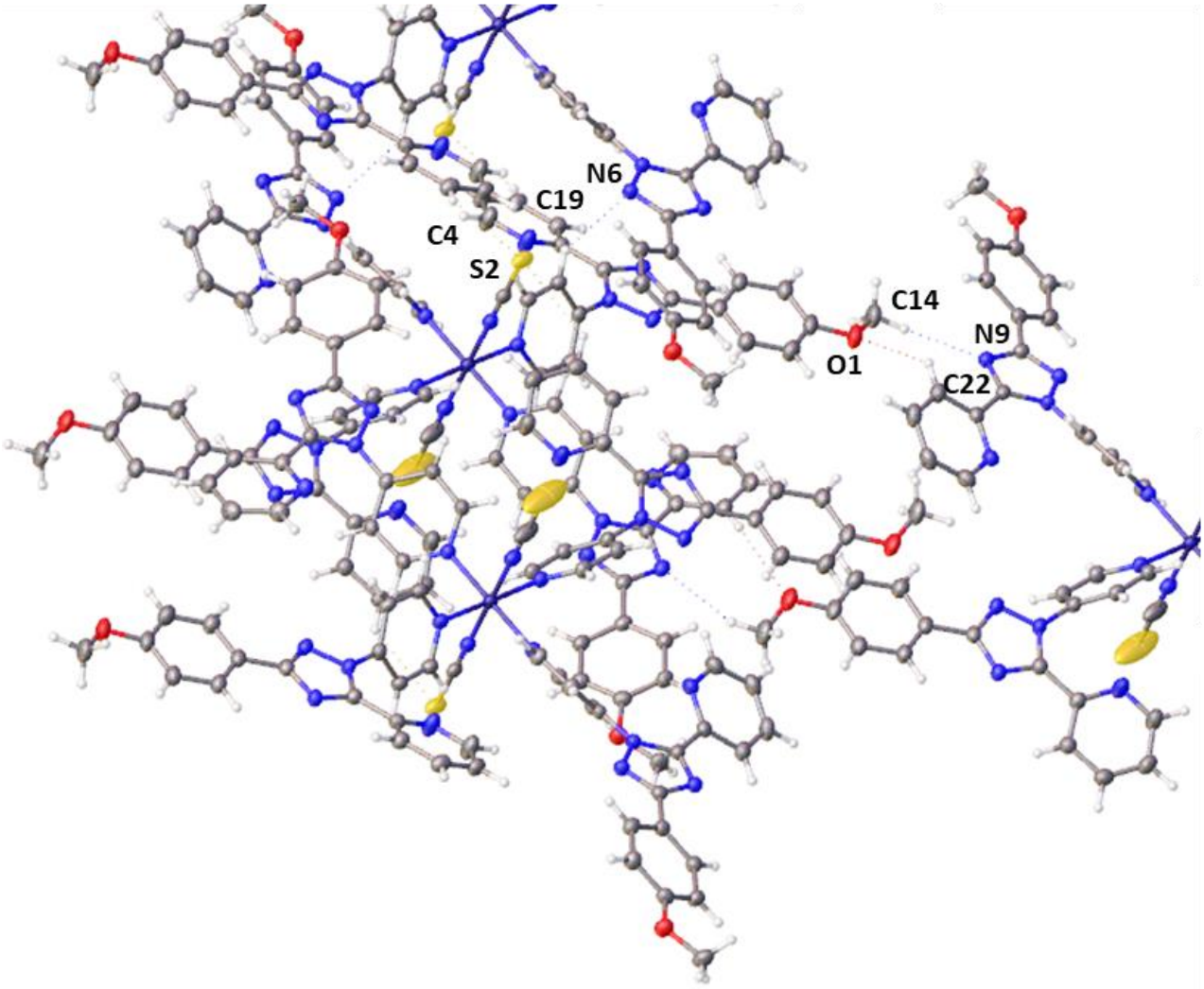

Figure 6.4. Image displaying the hydrogen bonding interactions in the crystal structure of **25**.

π-π stacking is observed in the structure between the coordinated 4-pyridyl ring and the uncoordinated 2-pyridyl, distance 3.9134(15) Å with a shift of 1.662(4) Å (figure 6.5).

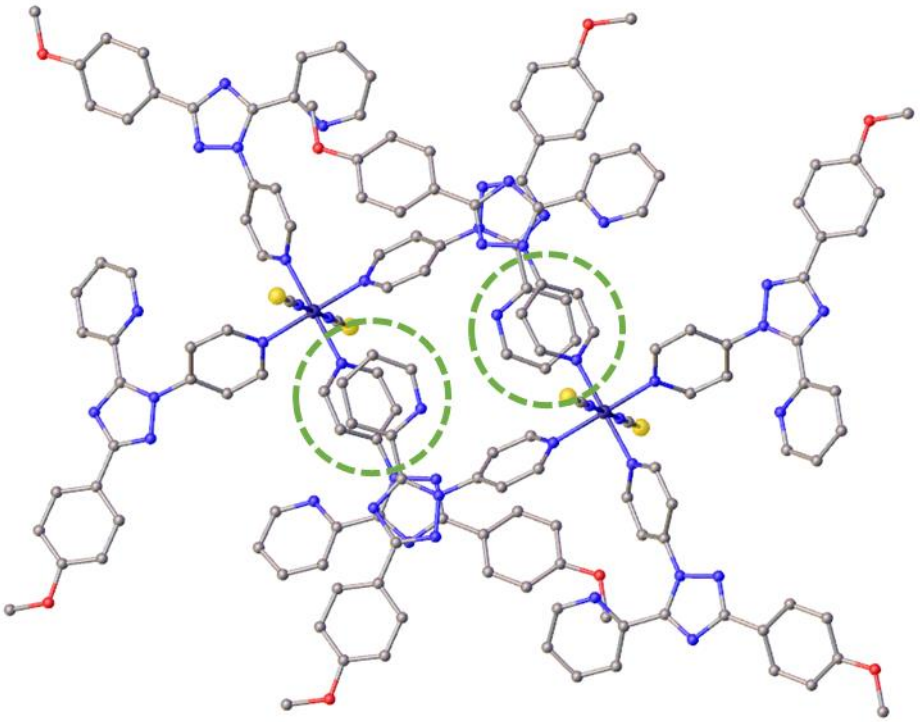

Figure 6.5. Image displaying the π-π interactions in the crystal structure of in **25**.

The structure of the final refinement was interrogated for its structural parameters. The Fe – N bond lengths ranged from 1.97 – 2.03 Å. These bond lengths were not representative of an iron(II) metal centre fully occupying either a HS or LS state. This result suggests that the sample is in between spin states and warrants further investigation with variable temperature studies.

A new single crystal was selected for new diffraction experiments at 250 and 90 K. This was due the crystal previously measured being left exposed to air for 4 months (during an enforced laboratory closure for the Covid19 national lockdown) and it was potentially damaged by being flash frozen through a transition. The crystal of 0.138 x 0.138 x 0.244 mm was mounted onto the Bruker D8 Venture SC-X-ray diffractometer at room temperature and cooled to 250 K at 5 K/min.

Full data collection was performed at 250 K and processing of data was conducted in the same manner as the 150 K data. Full structural determination at 250 K yielded the same cell contents as at 150 K, Fe – N bond lengths were investigated, ranging from 2.10 – 2.20 Å indicating the system now occupied a fully HS state, a distortion parameter Σ of 9.840(4)˚.

Table 6.1. Fe – N bond lengths for **25** at various temperatures.

	90 K	**150 K**	**250 K**
Fe – N5 (Å)	1.9937(16)	2.018(2)	2.19763(5)
Fe – N10 (Å)	1.9978(15)	2.027(2)	2.18874(4)
Fe – N11 (Å)	1.950(3)	1.972(3)	2.10466(6)
Fe – N12 (Å)	1.959(3)	1.978(3)	2.10988(6)
Σ (˚)	7.476(3)	7.332(3)	9.840(4)
v_p (Å^3)	10.383(6)	10.770(8)	13.511(9)

The twist and fold angles of the central 1,2,4-triazole and coordinated 4-pyridyl in each ligand were analysed to observe any major changes as temperature was decreased. Due to the rearrangement occurring, these could not be compared directly to the free ligand. Small changes are noted in the twist angles of the second ligand that decreases with temperature. The most dramatic change is witnessed in the fold of ligand 1 that drops significantly from 3.47 – 1.87˚ as the temperature is decreased.

Table 6.2. Twist and fold angles of coordinated ligands in **25.**

	250 K		**150 K**		**90 K**	
Ligand	1	2	1	2	1	2
Twist (˚)	39.80(8	56.56(8)	40.82(9)	55.71(9)	40.35(6)	55.35(6
Fold (˚)	3.47(8)	2.09(18)	2.16(9)	1.34(10)	1.87(6)	1.43(7)

The crystal was cooled to 90 K at 5 K/min before full data collection. Structure determination at 90 K yielded the same cell contents. The Fe – N bond lengths were investigated once more, this time ranging from 1.95-1.99 Å and a distortion parameter Σ of 7.476(3)˚ indicating the system was now in a fully LS state. These results show that **25** has undergone a thermal spin transition somewhere between 90 and 250 K. Cell parameters remained roughly consistent throughout measurements and no further structural changes occurred. The original data set at 150 K might be located around the $T_{½}$ where the system is undergoing transition and at 50% HS and 50% LS. To investigate the $T_{½}$ of the structure, an examination of unit cell parameters as a function of temperature was performed.

A new crystal was selected to ensure high data quality, mounted onto the Bruker D8 Venture, employing Cu-Kα radiation and a nitrogen flow cryostream allowing for

automated temperature changes. An automated set of minimal data collections of 3 omega scans with 40 frames with a 0.50˚ scan width, 10 second exposure time would allow for ample data for determination of unit cell parameters. The cryostream was automated to change temperature and stabilise for 20 minutes before data collection. First data collection was performed at 250 K before cooling step-wise to 100 K in 5, 10 and 25 K steps. Once a data collection was completed at 100 K, the crystal was heated back up following the same steps up to 250 K. The analysis of unit cell parameters across these temperatures would allow for potential determination of $T_{½}$ and any hysteresis present in the transition.

Unit cell parameters were determined and refined for each data collection in the APEX3 GUI.[10] The parameters were interrogated as a function of temperature and plotted as graphs for visualisation.

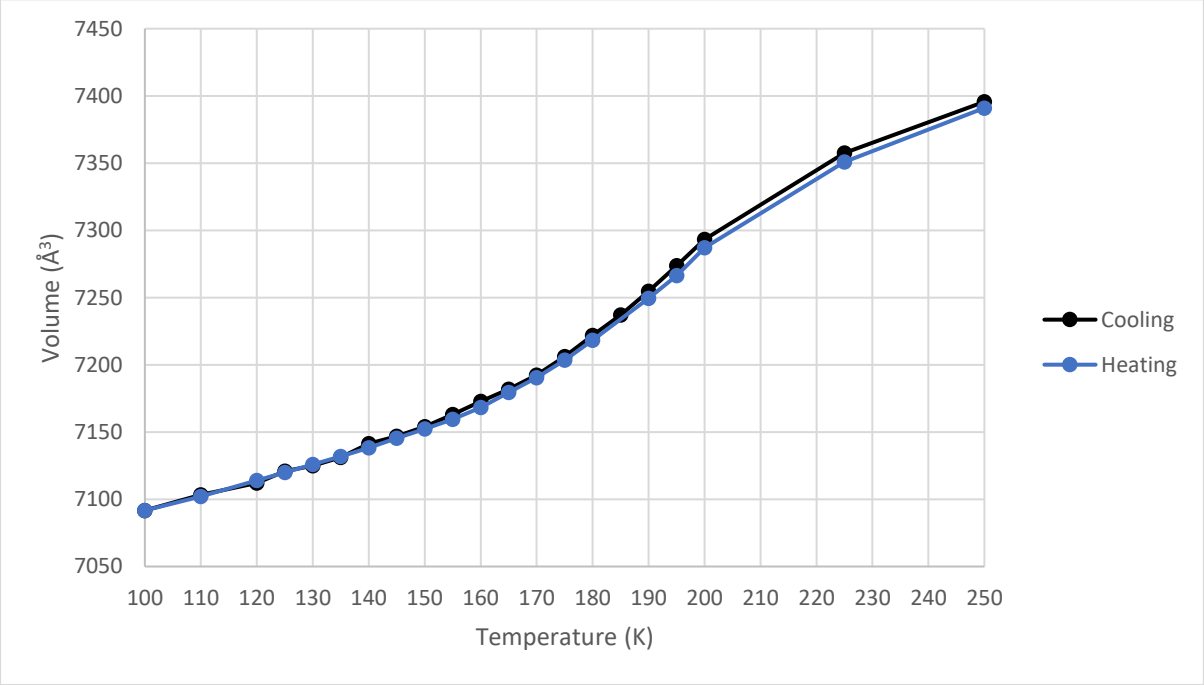

Figure 6.6. Unit cell volume of **25** between 250 – 100 K while cooling (black) and heating (blue)

The first unit cell parameter analysed was the unit cell volume. Cooling the sample would cause the volume to decrease even if the sample displayed no thermal transition. However, the rate of these changes allows for a rough estimate of $T_{½}$. The gradient is steepest between 200 and 170 K before levelling off until 100 K. The total unit cell volume decreases between 250 and 100 K by ~4.11% and is mirrored in the heating of the sample. The results displayed for both cooling and increasing

temperature are almost identical, initially suggests there is no thermal hysteresis present in the structure. The analysis of the unit cell volume suggests a gradual spin transition occurring in the sample and investigation of the other parameters *a*, *b* and *c* is required for a more accurate estimate of $T_{½}$. The system is orthorhombic meaning all angles are equal to 90˚ and therefore do not change with temperature.

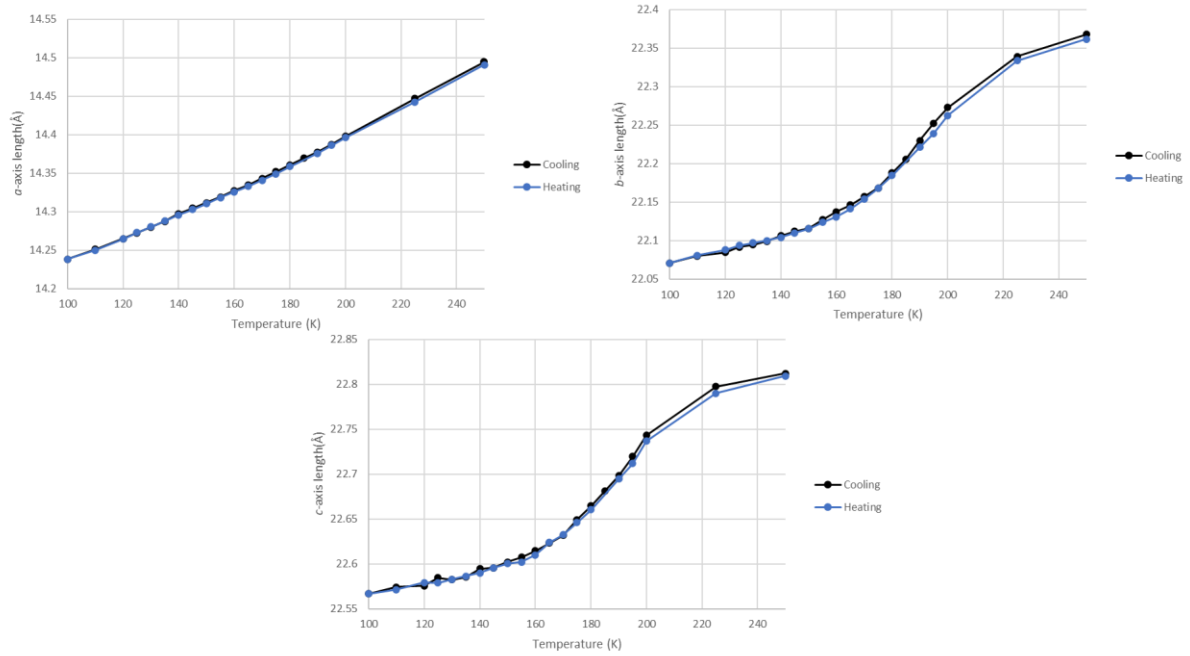

Figure 6.7. Unit cell parameters *a*, *b* and *c* as a function of temperature.

The *a*-axis length remains remarkably consistent through the cooling and heating cycle offering little indication of where the transition might be occurring. The total contraction in the *a* axis is ~1.8%. This data provides little detail into the $T_{½}$ of the structure but could be an indication of the spin transition being very gradual in nature.

Axis lengths *b* and *c* are more informative, following a more prominent trend than that displayed in the unit cell volume. Each of these parameters start off with a gradual decrease with cooling until the 200 K data point after this the rate of contraction is increased until 170 K in *b* and 165 K in *c*. The total contraction in b and c are 1.32% and 1.08 % respectively. With these two parameters we can estimate the $T_{½}$ to be located around 185-190 K. The trends witnessed in the cooling are almost identical to the trends displayed by the heating of the sample with no hysteresis observed. The gradual nature of the transition could explain why the flash frozen sample at 150 K displayed bond lengths between the two spin states.

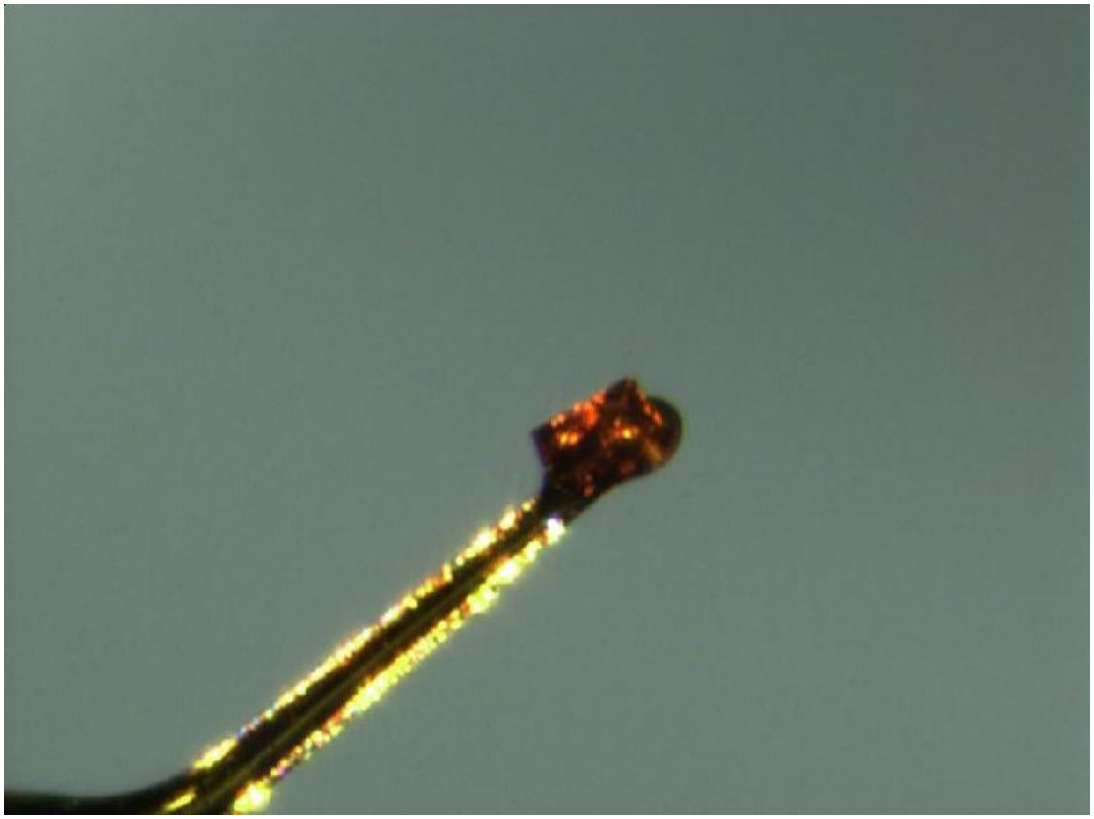

Figure 6.8. Colour of a single crystal of **25** at 250 K mounted on the Bruker D8 Venture

Crystals of spin crossover systems are often associated with a colour change as they pass through the transition.[11] Images of **25** were captured on the Bruker D8 Venture at 250 K displaying a light reddish-orange colour.

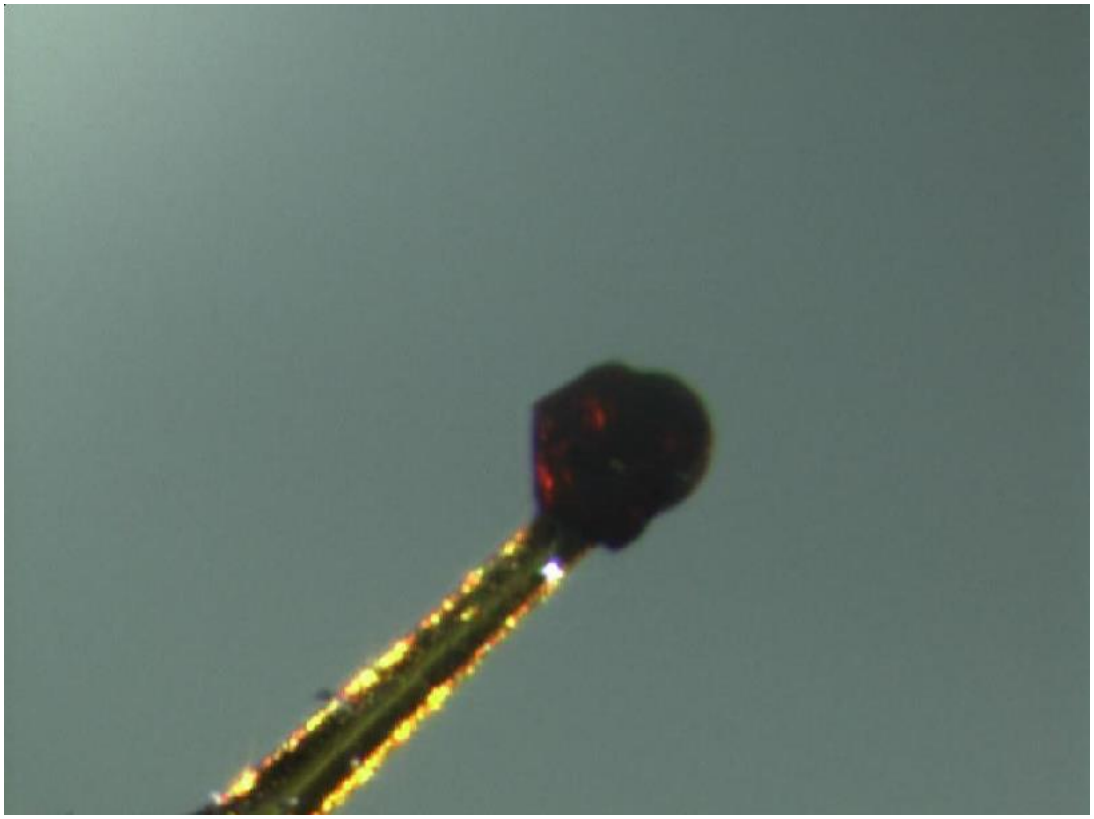

Figure 6.9. The same single crystal of **25** at 90 K mounted on the Bruker D8 Venture demonstrating the darkening of the colour upon cooling.

An image of the sample was taken on the Bruker D8 Venture at 90 K. The sample had undergone its thermal transition and the colour had deepened to a dark red. The colour change is not as distinct as some in the literature but it still provides further proof of SCO.

The success of the polymorph D discussed in chapter 2 alongside the literature high pressure studies on the other polymorphs of $[Fe(abpt)_2(NCS)_2]$ prompted a high-pressure study of **25**. A single crystal was loaded into a modified Merill-Bassett diamond anvil cell (DAC), containing a stainless steel gasket with a wide 0.4 mm hole, containing ruby spheres for pressure determination and paraffin oil as the pressure transmitting media. The DAC was mounted onto the specialised high-pressure diffractometer XIPHOS II with a Ag-Kα (λ = 0.56086 Å) source.[12] Data collections were performed at ambient temperature and stepwise until ~5.7 kbar before the sample degraded and there were no longer high-quality reflections present in the frames. This experiment was repeated using another crystal that displayed similar results. There was no indication with unit cell parameters that a pressure induced transition had occurred.

6.2 Conclusion

A new complex **25** has been synthesised and crystals successfully grown from the heating of a layered solution. The crystals were analysed by SC-X-ray diffraction at 150 K. Full structural determination revealed a species that had undergone a migration similar to the one discussed in chapter 5. The structure consisted of four rearranged versions of ligand 5, coordinating to the iron(II) centre in a monodentate fashion, alongside two isothiocyanates coordinated.

The Fe – N bond lengths were interrogated at 150 K, ranging from 1.97 to 2.02 Å indicating the system contained metal centres that were a mixture of HS and LS spin states. Full data collections were performed at 250 and 90 K on a new crystal to investigate if **25** undergoes the spin crossover phenomenon. The structure at 250 K was solved and analysed revealing the fully high spin structure with Fe – N bond lengths ranging from 2.10 to 2.19 Å. The 90 K data was solved and analysed that displayed Fe – N bond lengths range from 1.95 to 1.99 Å that indicated the system was fully low spin and that the structure had undergone SCO. Unit cell parameters for a series of data points between 250 and 100 K were investigated to reveal a gradual spin transition with a midpoint between 165-170 K. A high-pressure study was attempted on crystals of **25** but did not succeed due to sample deterioration with increasing pressure.

The system displayed a large number of weak interactions such as hydrogen bonding and π-π interactions that could have increased communication between metal complexes helping with the ability to display SCO behaviour.

The discovery of this structure was only possible due to the previous work in chapter 5 that alongside an investigation into the literature, changed the experimental variables on crystallisations of ligand 5. Layered crystallisations with no heating provided no crystals whereas heating of the sample prior being left to crystalise provided crystals that had undergone the rearrangement.

6.3 References

1 N. Moliner, M. C. Muñoz, S. Létard, J. F. Létard, X. Solans, R. Burriel, M. Castro, O. Kahn and J. A. Real, *Inorganica Chim. Acta*, 1999, **291**, 279–288.

2 H. E. Mason, W. Li, M. A. Carpenter, M. L. Hamilton, J. A. K. Howard and H. A. Sparkes, *New J. Chem.*, 2016, **40**, 2466–2478.

3 C. F. Sheu, S. M. Chen, S. C. Wang, G. H. Lee, Y. H. Liu and Y. Wang, *Chem. Commun.*, 2009, **2**, 7512–7514.

4 K. Sugimoto, C.-H. Shih, J. Kim, C.-F. Sheu, M. Takata, Y. Wang and K. Kato, *Dalt. Trans.*, 2010, **39**, 9794.

5 C.-H. Shih, Y. Wang, B.-M. Cheng, K. Sugimoto, M. Takata and C.-F. Sheu, *Chem. Commun.*, 2012, **48**, 5715.

6 A. B. Gaspar, M. C. Muñoz, N. Moliner, V. Ksenofontov, G. Levchenko, P. Gütlich and J. A. Real, *Monatsh. Chem.*, 2003, **134**, 285–294.

7 J. A. Kitchen, D. S. Larsen and S. Brooker, *Chem. - An Asian J.*, 2010, **5**, 910–918.

8 G. M. Sheldrick, *Acta Crystallogr. Sect. A Found. Crystallogr.*, 2015, **71**, 3–8.

9 O. V Dolomanov, L. J. Bourhis, R. J. Gildea, J. A. K. Howard and H. Puschmann, *J. Appl. Crystallogr.*, 2009, **42**, 339–341.

10 *Bruker AXS Inc., Apex3, Bruker AXS Inc., Madison, Wisconsin, USA, 2015*.

11 P. Gütlich, Y. Garcia and H. A. Goodwin, *Chem. Soc. Rev.*, 2000, **29**, 419–427.

12 M. R. Probert, C. M. Robertson, J. A. Coome, J. A. K. Howard, B. C. Michell and A. E. Goeta, *J. Appl. Crystallogr.*, 2010, **43**, 1415–1418.

7.Chapter 7 – A collection of metal complex crystal structures.

7.1 Introduction

This chapter focuses on the crystal structures collected for many complexes generated in this work over the course of this project, these systems either did not display any signs of thermal transitions or were not investigated further. There are many new crystal structures in this chapter displaying the large quantity of work undertaken in the search for metal complexes that display properties such as SCO behaviour. To the author's knowledge each of these structures were novel and previously unpublished structures at the time of writing. Compared to the previous results discussed in chapters 4-6, the metal complexes discussed herein contain metal other than Fe(II), such as Co(II) and Mn(III), These structures also contain counterions other than isothiocyanate. The first system discussed have been split into separate categories based on the unique structural traits they display. Several trends were observed in the generation these novel systems, they will be discussed at the end of the chapter.

The general procedure for the collection of new samples consisted of removing crystals from the sample vial and placing them into an inert oil for manipulation and allow observation of the visual quality of the crystal. Crystals were mounted on the Bruker D8 Venture single crystal X-ray diffractometer via a 50 µm Kapton loop. A minimal data collection was conducted to enable determination of unit cell parameters to allow for comparison to know structures in the literature or determine if the structure has been collected in house before. A full data collection performed at 150 K which is the laboratory standard, data was collected using Cu-Kα radiation (λ = 1.5406 Å). Resolution limit set to a minimum or 0.84 Å which is the suggested IUCr standard for publication, redundancy was based upon the suggested space group setting and crystal quality. Diffraction images processed using the SAINT integration algorithms within the APEX3 suite[1] utilising a least squares profile fitting approach with the optimised reflection box sizes and pre-scan optimisation of the unit cell and sample orientation. An absorption correction was performed on the data using the SADABS multi-scan approach in XPREP, a multi-faceted crystal face indexing absorption method was used for those which displayed very high absorption or crystals were particularly large. Structure solution was performed by SHELXT[2] via intrinsic phasing in the Olex2 interface[3] which confirmed a space group setting for the crystal structure.

The structures were refined using SHELXL[4] least squares minimisation algorithm in the Olex2 interface with weighting parameters employed.

Once the structure solution had been performed, an interrogation of the structural properties was conducted. This interrogation involved the analysis of bond lengths of the coordination sphere, analysis of the coordination of the ligand and the crystal packing of the system including hydrogen bonding and π-π stacking. If the structure showed promise of potential to display any interesting phenomenon the structure was analysed with variable temperature. A select few structures were analysed with increased pressure using a diamond anvil cell (DAC).

Once a structure had their initial collection analysed, the structural properties such as coordination sphere bond lengths were interrogated to determine the spin state of the system. The samples were given a priority listing for further experiments based upon these structural properties. As seen in Chapters 4 and 6 if the bond lengths do not conform with a fully HS or LS state for the metal ion it is given the greatest priority for variable temperature experiments using either the Bruker D8 Venture or XIPHOS I. Having a six-nitrogen coordination sphere promoted a higher priority. Unique features such the rearrangements seen previously also provided increased priority to the sample.

7.2 Crystal Structures Of Double-Bridged Metal Complexes

The first group of systems, **26**, **28** and **29**, contain two metal ions bridged by two trisubstituted 1,2,4-triazoles creating the binuclear species. Crystals of system **26** were grown from a methanol solution containing iron(II) perchlorate and **8** stirred at room temperature for 2 hours. The solution was left to evaporate undisturbed for 2 weeks before nucleation occurred on the sample vial, 3 weeks later after the majority solvent had evaporated. A high-quality brown-yellow crystal was selected for analysis by SC-XRD.

Structural solution revealed a $P2_1/c$ space group convergence as implied by a shift/ESD of -0.001. The minimum unaccounted electron density was -0.5 $eÅ^{-3}$ and the maximum 0.9 $eÅ^{-3}$ located around one of the perchlorate counter ions. The final refined structure was 100% complete to 0.81 Å, with an R_1 = 3.31% and wR_2 = 9.05% suggesting the data was of very high quality, Z' = 1 and Z = 4. The final refinement results are shown in figure 7.1.

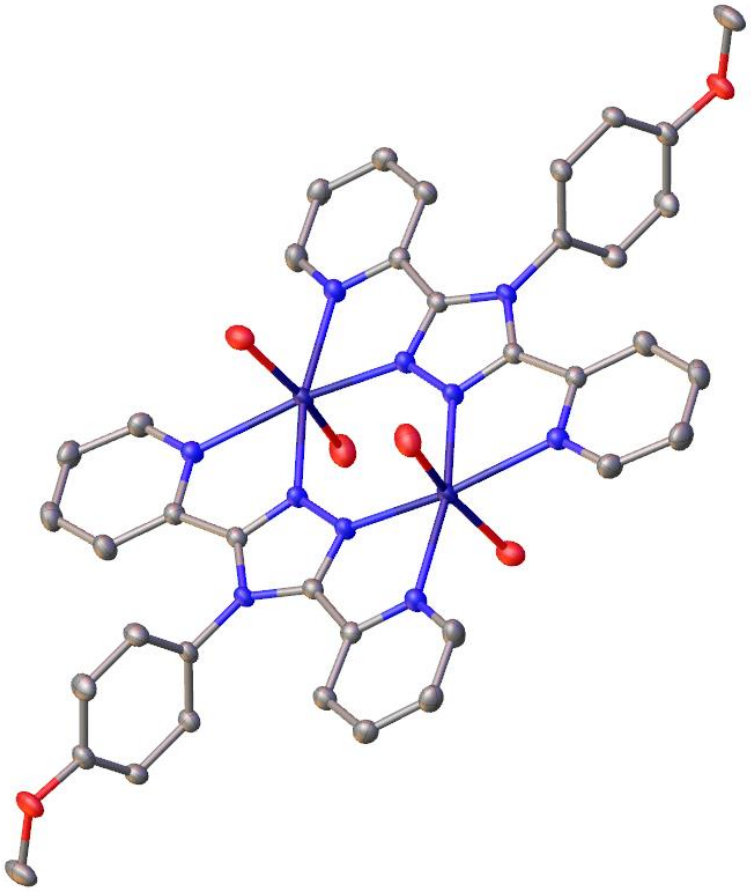

Figure 7.1. A symmetry expanded view of the crystallographic model of **26**, anisotropic displacement parameters of all non-hydrogen atoms are shown at 50% probability. Hydrogens and counter ions omitted for clarity.

The final refinement yielded a complex with two iron(II) metal centres, these metal centres are double bridged by two **8** which are coordinating through 4 nitrogen atoms each N1, N2, N3 and N5. Each metal each has two water molecules coordinated in a trans position, the iron has a N_4O_2 coordination sphere which is not considered to be optimal for iron(II) spin crossover systems there are four ClO_4^- counter ions present in the structure. The iron(II) centre sits on an inversion centre. The shape of the molecule forms a shallow bowl structure.

Crystal packing show in figure 7.2. the individual metal complexes separated from one another by the large number of perchlorate counter ions. The flat structure leads to each molecule facing the same direction with little twist and a lack of overlap between molecules. Analysis of the Fe – N and Fe – O bond lengths which ranged from 2.08-2.27 Å, indicating the system full occupied HS state. The N2 – Fe1 – N3 bite angle of the ligand was 73.23(6)˚, the angle O2 – Fe1 – O3 bond is distorted to 165.12(7)˚. OH

– O Hydrogen bonding is observed between two coordinated water molecules and the one of the perchlorate counters (O2H – O9, 2.0725(16) Å and O3H – O8, 2.0291(17) Å). The sample displaying HS state bond lengths at 150 K and the coordinated water molecules creating a coordination sphere of N_4O_2, these factors meant the sample for low priority for low temperature measurements. However, with the unique bridged structure a high-pressure experiment was conducted on a crystal.

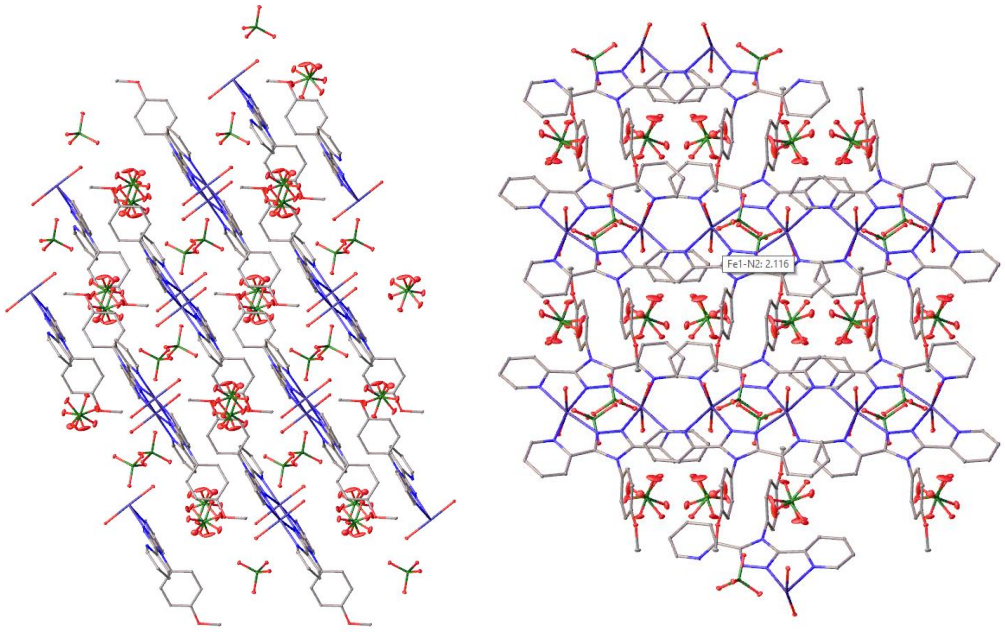

Figure 7.2. Image representing the packing of metal complexes and counter ions in the crystal structure of **26**, viewed along the *b* (left) and *c* (right) axis.

A single crystal was mounted onto a diamond face alongside 2 ruby spheres on a modified Merill-Bassett type diamond anvil cell. Paraffin oil was used as the PTM and pressure determination was conducted with the Ruby R1 fluorescence method.[5] Pressure measurements were conducted before and after collections. The first measurement was an ambient collection which closely matched the 150 K data set. The pressure was increased to 3.6 and 5.5, 12.9 kbar, structures solved with bond lengths indicating it was still in a HS state and data quality was still high. The pressure was increased further to 15.9 kbar, the data quality had dropped significantly, and the structure could no longer be solved, the crystal was removed from the cell and was damaged.

The discovery of this bridged structure led to crystallisation experiments with a increased amount of ligand, A methanol solution containing iron(II) perchlorate and 4

equivalents **8** was stirred for 2 h, ventilation holes were added to the sample vial and left to evaporate for 2 weeks before nucleation was observed and a further week before single crystals of an appropriate size were present. These crystals were removed from the solution placed into an inert perfluoro poly ether oil, Fomblin-YR 1800, on a clear glass microscope for easy manipulation and observation. A high-quality red crystal was selected for analysis by SC-XRD.

Structure solution was performed by SHELXT (Ref) via intrinsic phasing in the Olex2 GUI2 which confirmed a rhombohedral space group setting of R-3. The structure reached convergence as implied by a shift/ESD of 0.001. The minimum unaccounted electron density was -0.4 $eÅ^{-3}$ and the maximum 3.0 $eÅ^{-3}$ located between two ligands. The final refined structure was 68.1% complete to 0.88 Å, with an R1 = 11.08% and wR_2 = 35.57% suggesting the data was of suboptimal quality, Z' = 1.33 and Z = 24. The final refinement results are shown in figure 7.3.

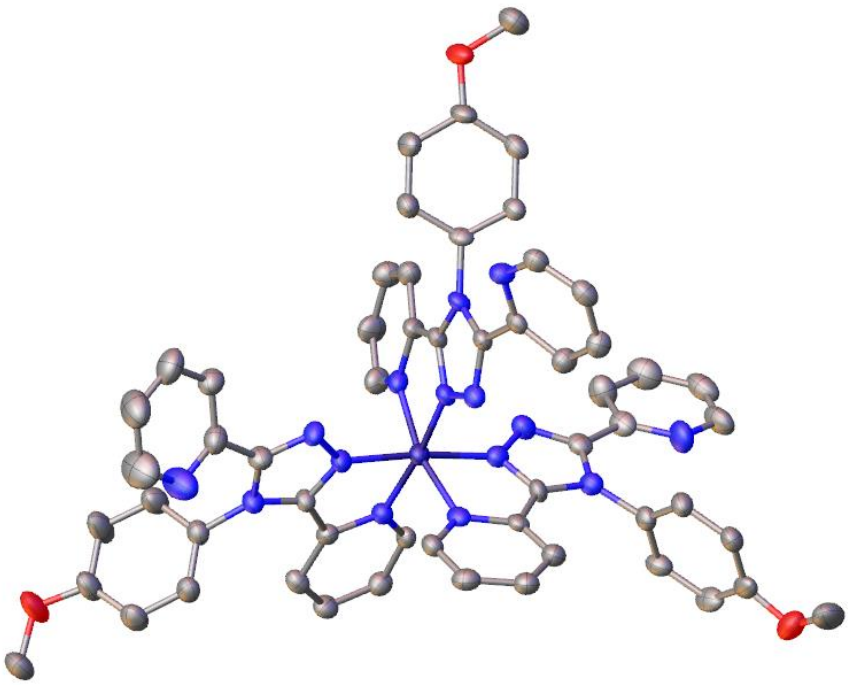

Figure 7.3. A symmetry expanded view of the crystallographic model of **27**, anisotropic displacement parameters of all non-hydrogen atoms are shown at 50% probability. Hydrogens and counter ions omitted for clarity.

The final refinement yielded a complex with an iron(II) metal centre coordinated to 3 bidentate **21** ligands via nitrogen atoms N2 and N3. There are two perchlorate counter ions present and 6 methanol molecules which were extremely disordered and an extinction correction used for the structure. An interrogation of the structural indicated the system was in a fully LS state with Fe – N bond lengths ranging from 1.90-2.00 Å, N2 – Fe1 – N3 bite angle of 80.7(2), N7 – Fe1 – N8 = 79.9(2) and N12 – Fe1 – N13 = 80.7(2).

The packing metal complex and counter ions are displayed in figure 7.4, the packing is arranged with one of the coordinated ligands on the each metal complex pointing towards the gap between two ligands on another metal complex. Hydrogen bonding interactions are observed in the crystal structure of 27 (C43H-O4, 2.355(8) Å)

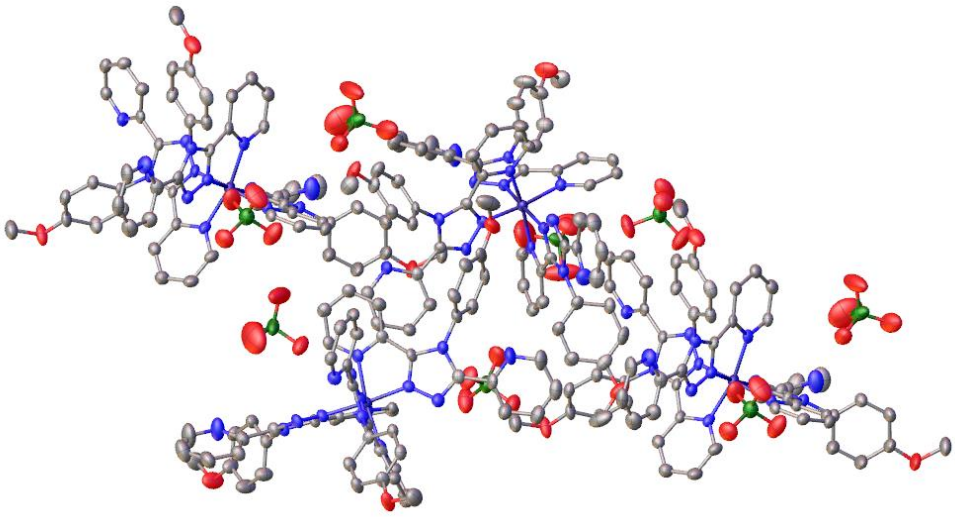

Figure 7.4. Image representing the packing of metal complexes and counter ions in the crystal structure of **27**, viewed along the *a* axis.

A data collection of the sample was attempted at 293 K to investigate if the sample was HS at room temperature, the data quality was worse than previous and structure solution could not be obtained. Attempts to regrow crystals of this sample and collect a better data set were unsuccessful, the poor quality of the sample did not improve, this could be due to the large amount of methanol solvent molecules in the structure which could cause the sample to desolvate during collection.

Single crystals of **28** were grown from a layered crystallisation, a methanol:water 1:1 solution containing cobalt(II) bromide was slowly injected via microlance needle careful

not to disturb the boundary that forms under a methanol solution containing 3 equivalents of **8**. No colour change was observed at the interface. After 2 days single crystals of an appropriate size had formed at the interface, these crystals were removed from the sample and and placed into inert perfluoro poly ether oil, *Fomblin-YR 1800*, on a glass slide to allow manipulation and observation under a microscope.

Structure solution was performed by SHELXT via intrinsic phasing in the Olex2 GUI2 which confirmed a triclinic space group setting of *P*-1. The structure reached convergence as implied by a shift/ESD of -0.001. The minimum unaccounted electron density was -0.7 $eÅ^{-3}$ and the maximum 0.9 $eÅ^{-3}$ located near Br1. The final refined structure was 98.5% complete to 0.81 Å, with an R1 = 2.61% and wR_2 = 6.96% suggesting the data was of very high quality. The final refinement results are shown in figure 7.5.

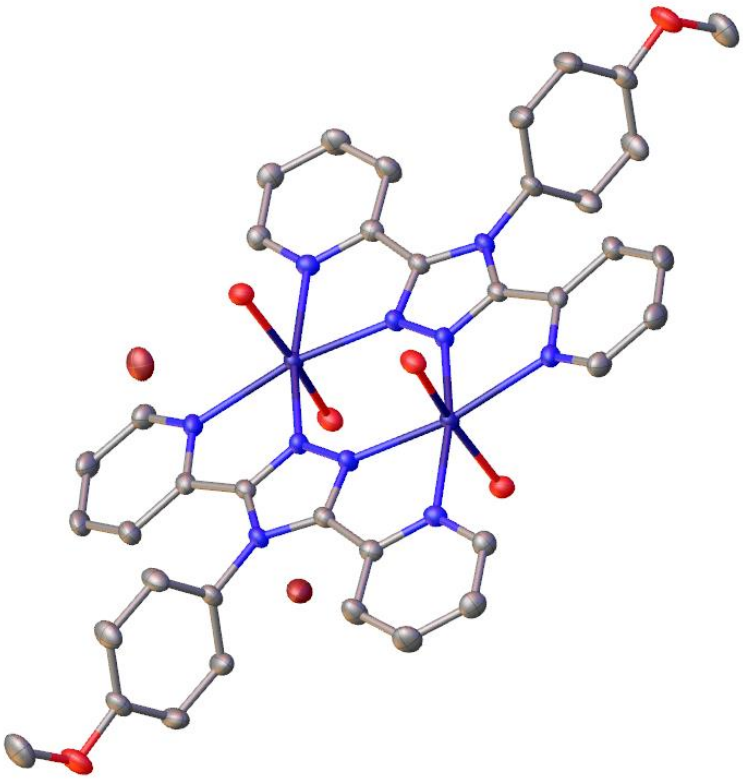

Figure 7.5. A symmetry expanded view of the crystallographic model of **28**, anisotropic displacement parameters of all non-hydrogen atoms are shown at 50% probability. Hydrogens omitted for clarity.

The final refinement yielded a second binuclear double bridged species. Two cobalt(II) metal centres are bridged by two molecules of 21 coordinated via nitrogen atoms N1,2,3 and 5, each metal is coordinated to two water molecules and there are 4 uncoordinated bromines acting as counter ions. 6 Uncoordinated water molecules of

crystallisation are present. The coordination sphere is N4O2 which is not optimal for SCO systems, the Co – N and Co – O bond lengths range from 2.04 – 2.23 Å indicating the system is in a HS state. The N2 – Co1 – N3 bite angle = 74.35(6)˚ and trans angle for water molecules O2 - Co1 – O3 is distorted to 167.21(6)˚.

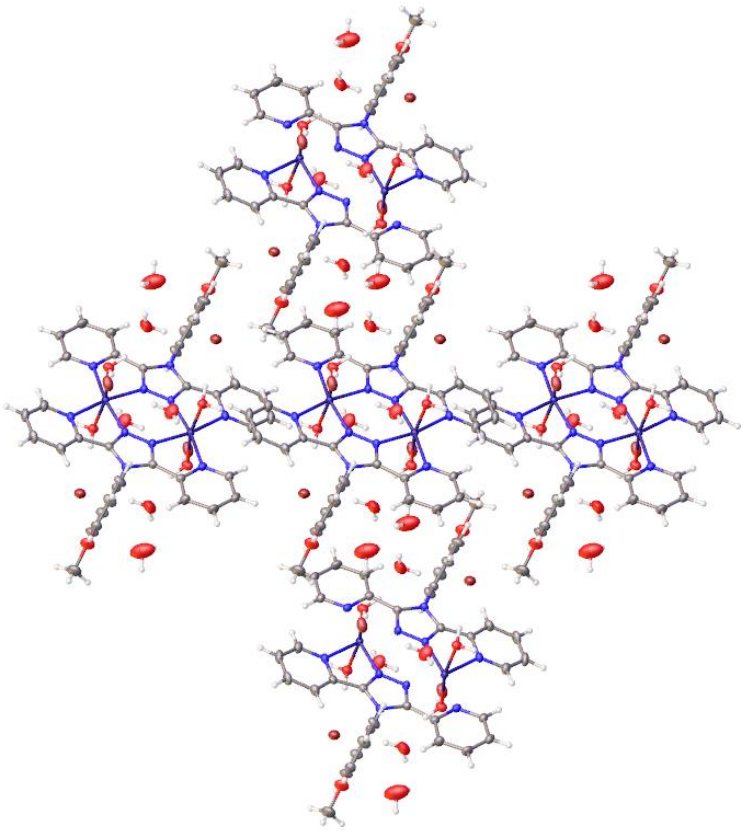

Figure 7.6. Image representing the packing of metal complexes, solvent and counter ions in the crystal structure of **28** viewed along the *b* axis.

The crystal packing shows the separation of metal complexes with stacks of metal complexes forming along the *a* axis, these stacks are separated by the uncoordinated counter ions and free solvent molecules, there very little overlap between metal complexes. There is an extensive hydrogen bonding system observed in this structure as shown in figure 7.7.

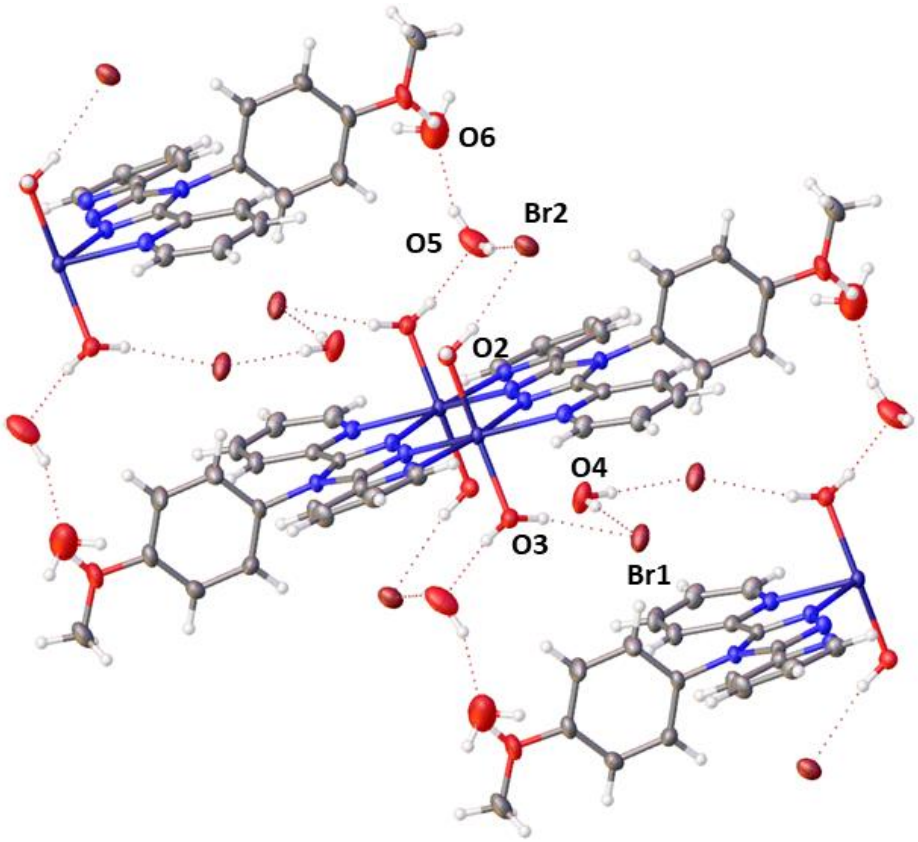

Figure 7.7. Image representing the extensive hydrogen bonding observed in the crystal structure of **28**.

Hydrogen bonding originating from coordinated water molecules forms a network of hydrogen bonds between uncoordinated solvent molecules and bromine counter ions. This hydrogen bonding extends between multiple atoms before reaching another metal complex in the same stack. O2H – Br2, 2.3093(2) Å, O3H – Br1, 2.3823(2) Å, O3H – O5, 1.7846(19) Å, O5H – O6, 1.938(4) Å.

A new single crystal of **28** was selected for low temperature experimentation on XIPHOS I. The sample was mounted to a sharpened graphite rod using a minimal amount of epoxy resin glue (Loctite^{TM} double bubble), known to be a good thermal conductor to hold the crystal in place while mounted vertically in the cold head. Full data collection was performed at 2 K, data integration and structure solution performed in the same manner as the 150 K data set. The structure solution yielded the same asymmetric unit, interrogation of the bond lengths revealed they were almost identical ranging from 2.04-2.23 Å remaining in a HS state.

A third double bridged species was discovered, single crystals of **29** were grown from a layered crystallisation, a methanol:water 1:1 solution containing cobalt(II) bis-

isothiocyanate was slowly injected via microlance needle careful not to disturb the boundary that forms under a methanol solution containing 3 equivalents of **16**. No colour change was observed at the interface. After 5 days single crystals of an appropriate size had formed at the interface, these crystals were removed from the sample and placed into inert perfluoro poly ether oil, *Fomblin-YR 1800*, on a glass slide to allow manipulation and observation under a microscope. Crystal was glued with double bubble two-part epoxy which is known to be a good thermal conductor to a sharpened graphite rod, the sample was mounted on the cold head of XIPHOS I. Full data collection performed at 2 K.

Structure solution was performed by SHELXT via intrinsic phasing in the Olex2 GUI2 which confirmed a triclinic space group setting of *P*-1. The structure reached convergence as implied by a shift/ESD of -0.001. The minimum unaccounted electron density was -0.8 $eÅ^{-3}$ and the maximum 1.0 $eÅ^{-3}$located near Cl1. The final refined structure was 91.9% complete to 0.80 Å, with an R_1 = 3.93% and wR_2 = 11.44% suggesting the data was of high quality. The final refinement results are shown in figure 7.8.

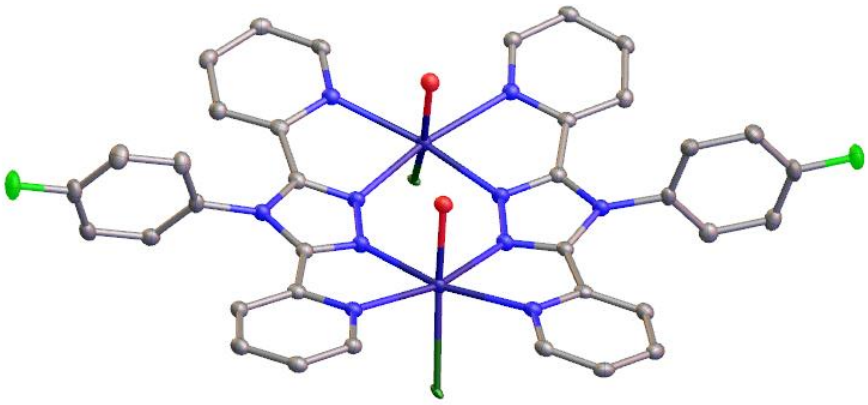

Figure 7.8. A symmetry expanded view of the crystallographic model of **29**, anisotropic displacement parameters of all non-hydrogen atoms are shown at 50% probability. Hydrogens and counter ions omitted for clarity.

The final refinement yielded a double bridged structure containing two cobalt(II) metal centres, bridged by two copies of 7 coordinating via nitrogen atoms N1, N2, N3 and N5. Each cobalt is coordinated to a water molecule and a chloride in a trans fashion. There are two uncoordinated chloride counter ions present in the structure. The N2 – Co1 – N3 bite angle = 74.1(1)˚ and the N1 – Co1 – N5 bite angle = 74.64(10)˚, the trans oxygen and chloride angle has been distorted to 162.24(7) ˚. The coordination sphere of N4Cl1O1 is not common for SCO in cobalt(II) spin crossover systems. The

coordination sphere bond lengths range from 2.11 – 2.37 Å indicating a fully HS system at 2 K.

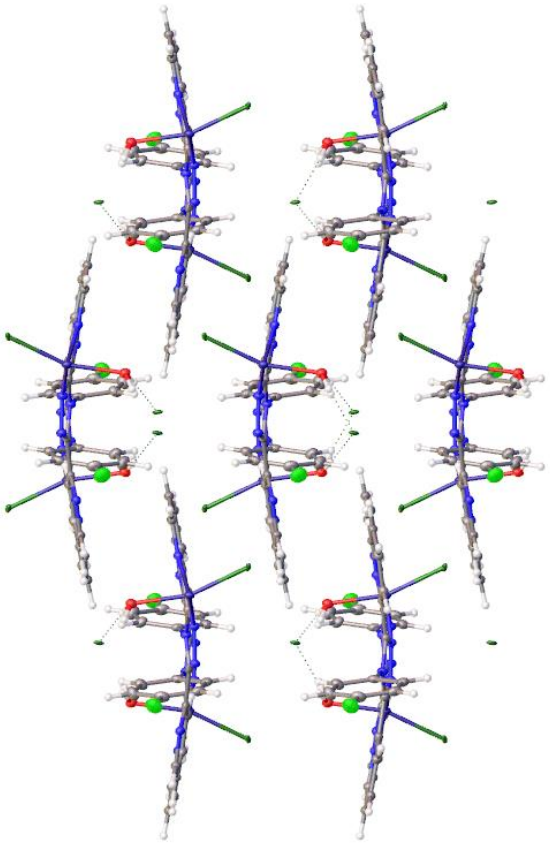

Figure 7.9. Image representing the packing of metal complexes and counter ions in the crystal structure of **29** viewed along the *a* axis.

Figure 7.9 displays the bowl like structure of 29 and the large distortion of the trans oxygen and chloride atoms. The packing forms distinct inverted layers with significant overlap between molecules occurring. Hydrogen bonding occurs between the coordinated water molecules and the free chloride counter ions (O1H – Cl2, 2.130-2.17(6) Å, O1H – Cl2, 2.13(7) Å). There is further interactions observed between this chloride and the 4-fluorophenyl (C13H – Cl2, 2.7094(7) Å). The final interaction is observed between a coordinated chlorine and the 4-fluorophenyl located on another metal complex (C14H – Cl1, 2.6506 Å).

A 150 K temperature collection was performed on this structure originally however the data quality was subpar and not included, new crystals were grown and used on XIPHOS to test the structure at the lowest temperature possible. The structure remained in a HS state at 2K indicates there will be no change in spin state with changing temperature.

7.3 Crystal Structures Of Coordination Polymers

The next interesting results came in the form of some coordination polymer crystal structures which were collected.

Suitable single crystals of **30** were grown from a layered crystallisation, a methanol:water 1:1 solution containing cobalt bis-isothiocyanate was injected slowly with a microlance needle under a methanol solution containing **3**. After several days crystals of an appropriate size had formed on the interface, these crystals were removed from the sample and placed into inert perfluoro poly ether oil, *Fomblin-YR 1800*, on a glass slide to allow manipulation and observation under a microscope. A pink block-shaped single crystal was selected for analysis by SC-XRD.

Structure solution was performed by SHELXT via intrinsic phasing in the Olex2 GUI2 which confirmed a triclinic space group setting of *P*-1. The structure reached convergence as implied by a shift/ESD of 0.000. The minimum unaccounted electron density was -1.2 $eÅ^{-3}$ and the maximum 0.6 $eÅ^{-3}$ located along the Co1 – N2 bond. The final refined structure was 98% complete to 0.81 Å, with an R_1 = 7.41% and wR_2 = 23.36% suggesting the data was of average quality. The final refinement results are shown in figure 7.10.

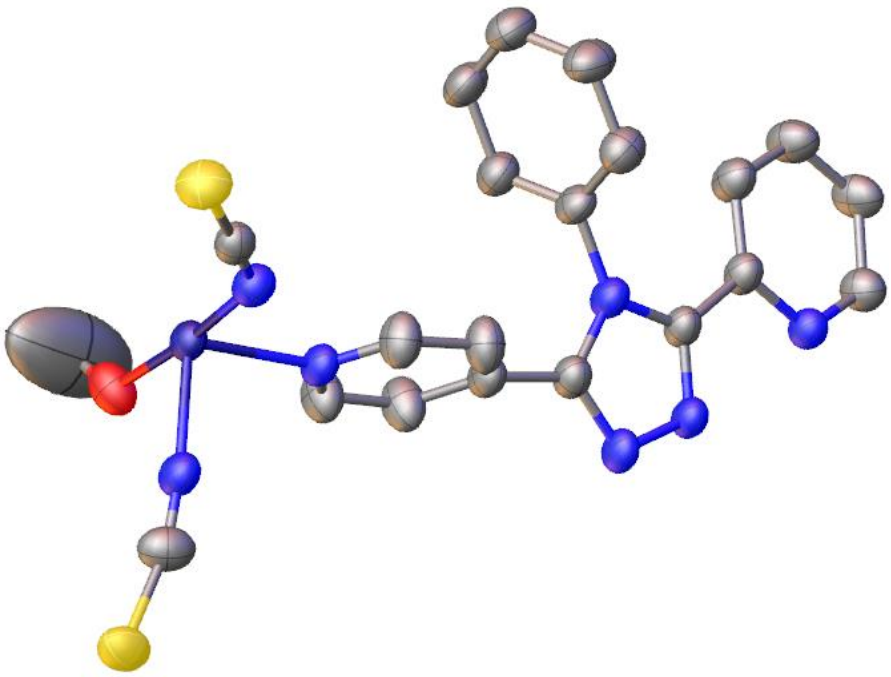

Figure 7.10. Asymmetric unit of the crystal structure of **30**, anisotropic displacement parameters of all non-hydrogen atoms are shown at 50% probability. Hydrogens omitted for clarity.

The final refinement consists of a cobalt (II) metal centre coordinated to two ligands of **3**, one of these ligands are bidentate coordination through atoms N2 and N3. The second ligands are monodentate and coordinated through nitrogen atom N5. Each of these ligands is then coordinated to another metal centre forming a coordination polymer. These different bonding motifs are displayed in figure 7.11. There are two coordinated isothiocyanates and a methanol molecule coordinated to each metal centre.

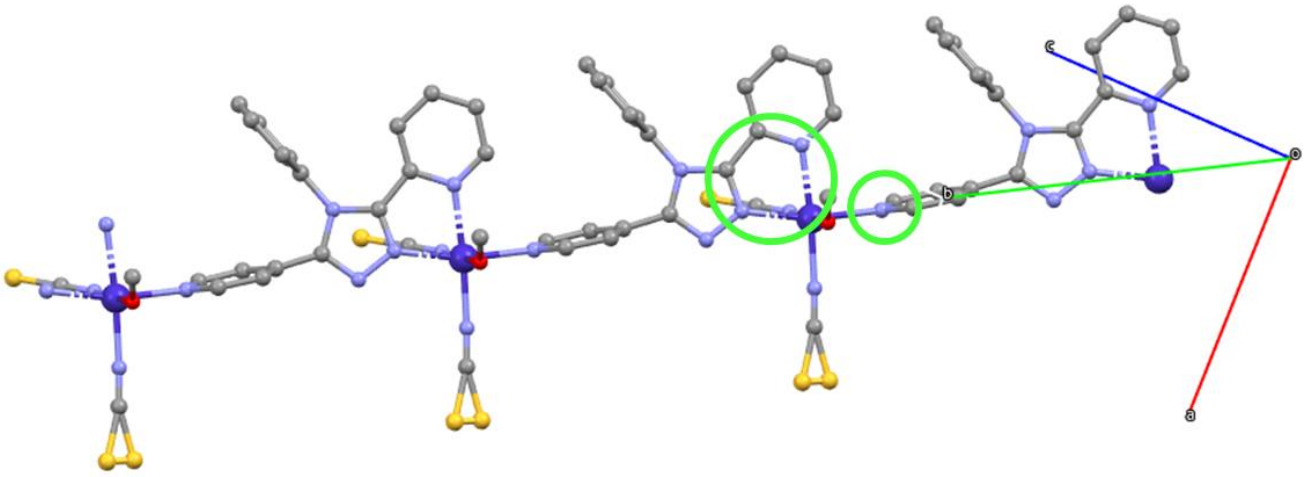

Figure 7.11. Image representing the coordination motifs present in the crystal structure of **30**.

The extended structure consists of long coordination polymer chains, these pack as shown in figure 7.12, with stacks of chains in along the *a* axisand inverted stacks forming layers.

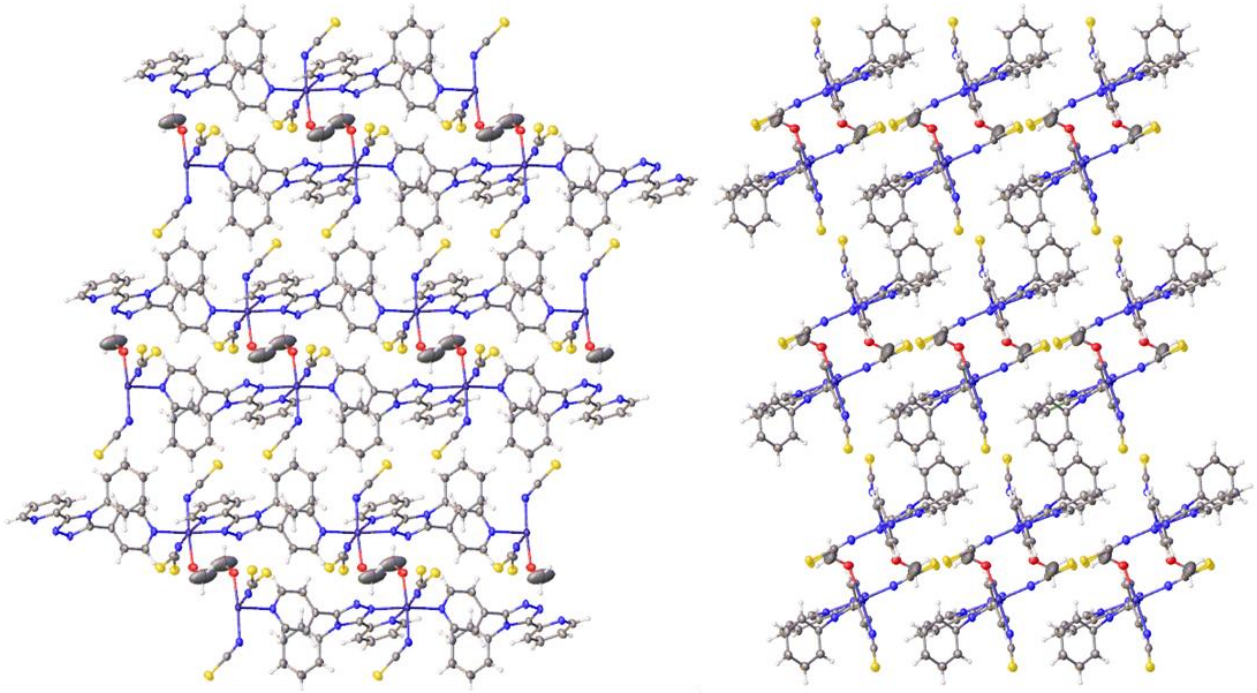

Figure 7.12. Image representing the packing of molecules in the crystal structure of **30** viewed along the *a* axis (left) and *b* axis(right).

Interrogation of the structure revealed the Co – N bond lengths ranged from 2.06 – 2.20 Å and the Co – O bond length was 2.142(3) Å, indicating the system was in a HS state. The N2 – Co1 – N3 bite angle = 75.63(12)˚, the cis isothiocyanates had distorted to an angle of 95.25(15)˚.

A new single crystal of this sample was selected for low temperature experimentation on XIPHOS I. The sample was mounted to a sharpened graphite rod using a minimal amount of epoxy resin glue (Loctite™ double bubble), known to be a good thermal conductor to hold the crystal in place while mounted vertically in the cold head. Full data collection was performed at 3 K, data integration and structure solution performed in the same manner as the 150 K data set. The structure solution yielded the same asymmetric unit, interrogation of the bond lengths revealed they were almost identical ranging from 2.06-2.20 Å remaining in a HS state.

An isomorphous iron(II) crystal structure (**31**) was discovered, Suitable single crystals were grown from a layered crystallisation, a methanol:water 1:1 solution containing iron bis-isothiocyanate was injected slowly with a microlance needle under a methanol

solution containing **16**. After several weeks crystals of an appropriate size had formed on the interface, these crystals were removed from the sample and placed into inert perfluoro poly ether oil, *Fomblin-YR 1800*, on a glass slide to allow manipulation and observation under a microscope. A red block-shaped single crystal was selected for analysis by SC-XRD.

Structure solution was performed by SHELXT via intrinsic phasing in the Olex2 GUI2 which confirmed a triclinic space group setting of *P*-1. The structure reached convergence as implied by a shift/ESD of 0.000. The minimum unaccounted electron density was -0.8 $eÅ^{-3}$ and the maximum 0.5 $eÅ^{-3}$ located near S1. The final refined structure was 98.8% complete to 0.81 Å, with an R_1 = 5.22% and wR_2 = 14.03% suggesting the data was of average quality. The final refinement results are shown in figure 7.13.

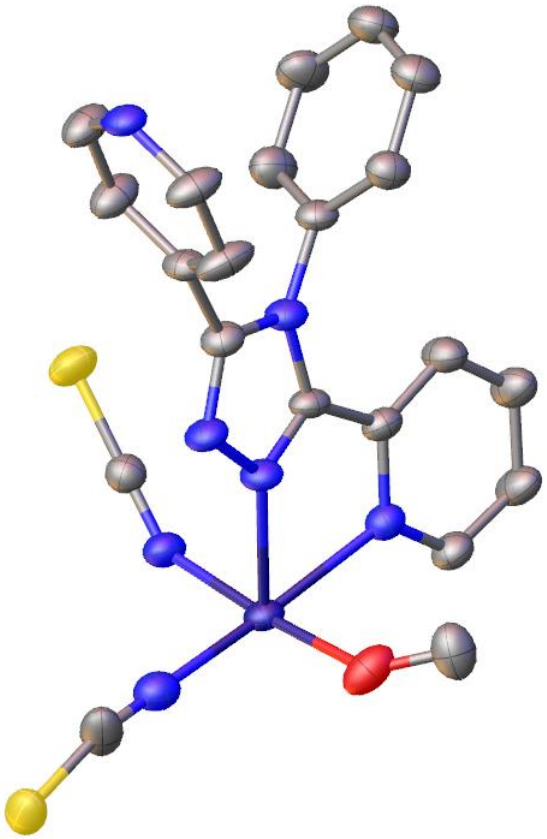

Figure 7.13. Asymmetric unit of the crystal structure of **31**, the anisotropic displacement parameters of all non-hydrogen atoms are shown at 50% probability.

The final refinement displayed in figure 7.13, consists of an iron (II) metal centre coordinated to two ligands of **16**, one of these ligand is bidentate coordination through atoms N2 and N3. The second ligands are monodentate and coordinated through nitrogen atom N5. Each of these ligands is then coordinated to another metal centre

forming a coordination polymer. The two coordinated isothiocyanate counter ions are in a cis fashion, there is a coordinated methanol molecule trans to one of the isothiocyanates, the structure is isomorphous to the previous cobalt structure. The N2 – Fe1 – N3 bite angle is 74.17(10) ˚. The packing of molecules in this structure is almost identical to **30**.

A low temperature experiment of this structure was awaiting collection, however, XIPHOS I was out of commission and the experiment could not be completed. A high-pressure experiment was instead conducted on XIPHOS II.

A single crystal was mounted onto a diamond face alongside 2 ruby spheres on a modified Merill-Bassett type diamond anvil cell. Paraffin oil was used as the PTM and pressure determination was conducted with the Ruby R1 fluorescence method. Pressure measurements were conducted before and after collections. An ambient data set was collected to determine data quality, due to the triclinic nature of the structure the completeness was low ~25%. The low completeness impacted the data quality of, therefore, the unit cell parameters would be analysed as the pressure increased, minimal data collections were performed at ambient, 6.25, 8.5 and 24 kbar. The unit cell parameters did not diverge far from the ambient structure for collections at 6.25 and 8.5 kbar, the crystals integrity was compromised on the final increase in pressure resulting in very few reflections at 24 kbar. In the future a more in-depth study of this system was set to be investigated, however, with the N_5O_1 coordination sphere it is of a low priority and time available to conduct these studies ran out.

7.4 Crystal Structures Of Novel Mononuclear Metal Complex

Suitable single crystals were grown from a layered crystallisation, a methanol:water 1:1 solution containing cobalt bis-isothiocyanate was injected slowly with a microlance needle under a methanol solution containing **20**. After a week, crystals of an appropriate size had formed on the interface, these crystals were removed from the sample and placed into inert perfluoro poly ether oil, *Fomblin-YR 1800*, on a glass slide to allow manipulation and observation under a microscope. A red plate-shaped single was selected for analysis by SC-XRD.

Structure solution was performed by SHELXT via intrinsic phasing in the Olex2 GUI2 which confirmed a C-centred monoclinic space group setting of *C*2/*c*. The structure reached convergence as implied by a shift/ESD of -0.002. The minimum unaccounted electron density was -0.5 $eÅ^{-3}$ and the maximum 0.5 $eÅ^{-3}$ located near S1. The final

refined structure was 98.4% complete to 0.88 Å, with an R_1 = 5.90% and wR_2 = 15.90% suggesting the data was of okay quality. The final refinement results are shown in figure 7.14.

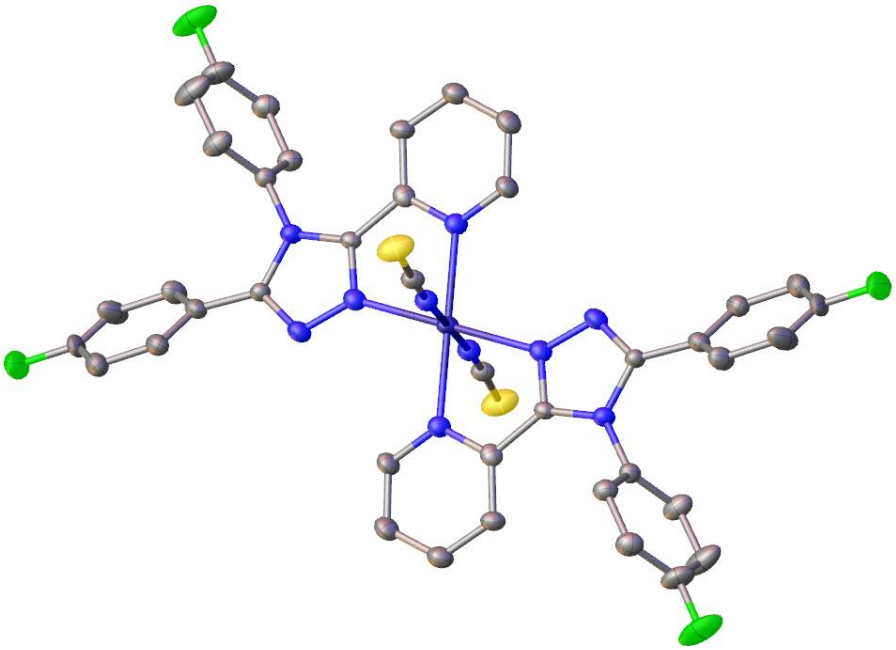

Figure 7.14. A symmetry expanded view of the crystallographic model **32** anisotropic displacement parameters of all non-hydrogen atoms are shown at 50% probability. Hydrogens and solvent omitted for clarity.

Final refinement yielded a structure containing a cobalt(II) metal centre, coordinated to two **20** ligands in a bidentate motif and two isothiocyanate counterions in a trans fashion. There is one uncoordinated methanol molecule present in the structure. This structure is isomorphous to the solvate structure **23a** reported in chapter 4. The unit cell is almost identical and the cell contents the same apart from the iron(II) being replaced by cobalt(II). The structure was interrogated for its structural properties, Co – N bond lengths ranged from 2.08 – 2.16 Å indicating the system was in a HS state. The N2 – Co1 – N3 bite angle is 76.39(13) Å, slightly lower than that observed in **23a** at 79.98(8) Å.

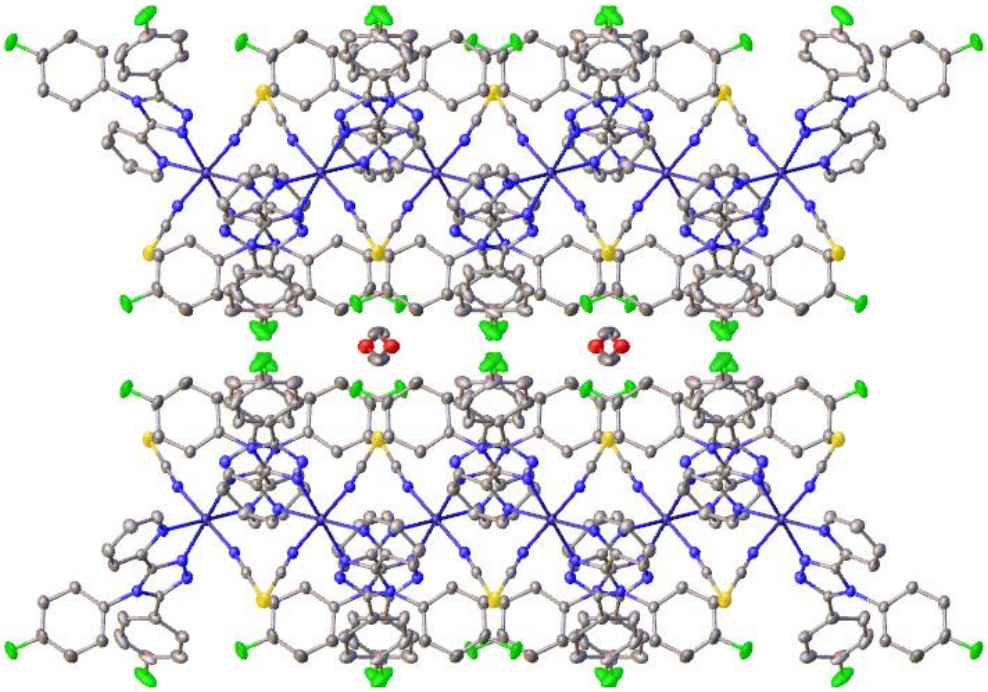

Figure 7.15. Image representing the packing of metal complexes and solvent molecules in the crystal structure of **32** viewed along the *c* axis.

The packing of this structure is almost identical to **23a** discussed in Chapter 4 with channels between layers of molecules which contain pockets of solvent molecules. Due to the similarities in this complex and **23a**, being isomorphous and containing a methanol solvent molecule, the crystal structure was cooled to 100 K and minimum data collection performed to observe any changes in structure. No changes were observed, and the structure was a candidate for XIPHOS I, however the machine was out of commission towards the end of the time available and the sample could not be tested down to ~2 K. In this future this experiment should be conducted to see if this sample also undergoes a thermal transition, and how large the change in $T_{1/2}$ is compared to the iron analogue.

The final metal complex containing ligand **20**, suitable single crystals were grown from a layered crystallisation, a methanol:water 1:1 solution containing manganese bis-isothiocyanate was injected slowly with a microlance needle under a methanol solution containing **20**. After 2 weeks crystals of an appropriate size had formed on the interface, these crystals were removed from the sample and placed into inert perfluoro poly ether oil, *Fomblin-YR 1800*, on a glass slide to allow manipulation and observation under a microscope. Alight pink block-shaped single was selected for analysis by SC-XRD.

Structure solution was performed by SHELXT via intrinsic phasing in the Olex2 GUI2 which confirmed a monoclinic space group setting of $P2_1/c$. The structure reached convergence as implied by a shift/ESD of 0.000. The minimum unaccounted electron density was -0.2 eÅ^{-3} and the maximum 0.2 eÅ^{-3} located along the C7 – C8 bond. The final refined structure was 100% complete to 0.81 Å, with an R_1 = 2.32% and wR_2 = 6.60% suggesting the data was of extremely good quality. The final refinement results are shown in figure 7.16.

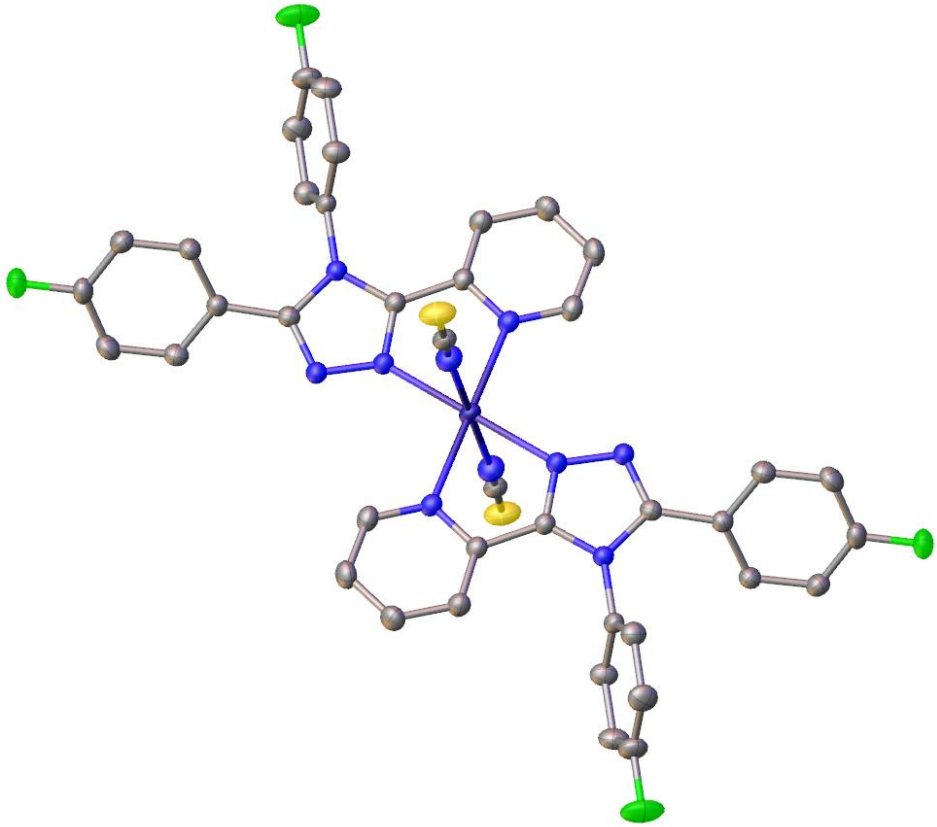

Figure 7.16. A symmetry expanded view of the crystallographic model **33** anisotropic displacement parameters of all non-hydrogen atoms are shown at 50% probability. Hydrogens and solvent omitted for clarity.

Final refinement yielded a structure containing a manganese(II) metal centre, coordinated to two **20** ligands in a bidentate motif and two isothiocyanate counterions in a trans fashion. This structure is isomorphous to the solventless structure **23b** reported in chapter 4. The unit cell is almost identical and the cell contents the same apart from the Fe(II) being replaced by Mn(II). The structure was interrogated for its

structural properties, Mn – N bond lengths ranged from 2.18 – 2.27 Å indicating the system was in a HS state. The N2 – Mn1 – N3 bite angle is 73.24(4) Å. The crystal packing displayed in figure 7.17, is the same as discussed in chapter 4 for the solventless structure **23b**.

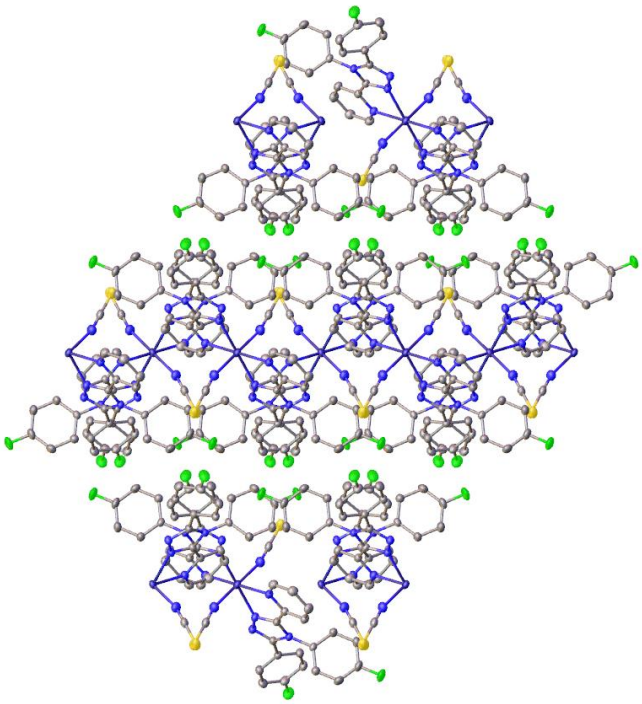

Figure 7.17. Image representing the packing of metal complexes and solvent molecules in the crystal structure of **33** viewed along the *c* axis.

The structure being fully high spin at 150 K and containing an optimal 6 nitrogen coordination sphere made it a candidate for use in a low temperature study. A new single crystal of this sample was selected for low temperature experimentation on XIPHOS I. The sample was mounted to a sharpened graphite rod using a minimal amount of epoxy resin glue (Loctite^{TM} double bubble), known to be a good thermal conductor to hold the crystal in place while mounted vertically in the cold head. Full data collection was performed at 3 K, data integration and structure solution performed in the same manner as the 150 K data set. The structure solution yielded the same asymmetric unit, interrogation of the Mn – N bond lengths revealed they were almost identical ranging from 2.19-2.27 Å remaining in a HS state. Similar to structure **23b** displays no signs of spin crossover. Attempts to regrow the solvate *C*2/*c* structure were attempted with different crystallisation techniques such as evaporation from a

methanol solution and reattempting the layered crystallisation, however, no crystals of the solvate were obtained.

Suitable single crystals of **34** were grown from a layered crystallisation, a methanol:water 1:1 solution containing cobalt(II) bis-isothiocyanate was injected slowly with a microlance needle under a methanol solution containing **16**. After a 1-week crystals of an appropriate size had formed on the interface, these crystals were removed from the sample and placed into inert perfluoro poly ether oil, *Fomblin-YR 1800*, on a glass slide to allow manipulation and observation under a microscope. A pink block-shaped single was selected for analysis by SC-XRD.

Structure solution was performed by SHELXT via intrinsic phasing in the Olex2 GUI2 which confirmed a triclinic space group setting of *P*-1. The structure reached convergence as implied by a shift/ESD of 0.000. The minimum unaccounted electron density was -0.6 $eÅ^{-3}$ and the maximum 0.3 $eÅ^{-3}$ located near S1. The final refined structure was 98.5% complete to 0.81 Å, with an R_1 = 3.29% and wR_2 = 9.59% suggesting the data was of good quality. The final refinement results are shown in figure 7.18.

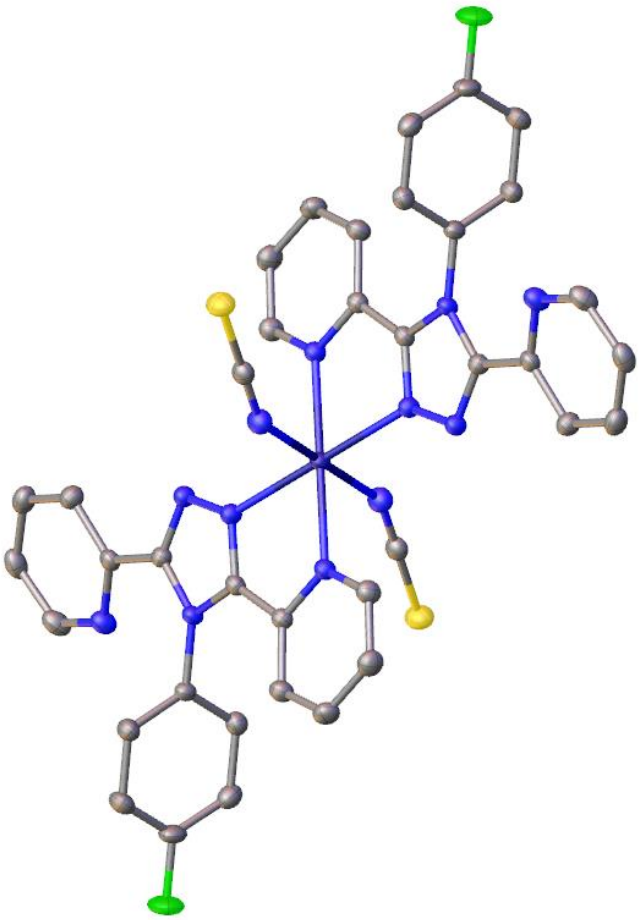

Figure 7.18. A symmetry expanded view of the crystallographic model of **34**. The anisotropic displacement parameters of all non-hydrogen atoms are shown at 50% probability. Hydrogens omitted for clarity.

The final refinement yielded a structure containing a cobalt(II) metal centre, coordinated two **16** ligands in a bidentate motif and 2 coordinated trans isothiocyanates. The structure has a N6 coordination sphere, the bond lengths investigated, ranging from 2.08 – 2.15 Å indicating the metal centre occupied a HS state.

The crystal packing of **34** displayed in figure 7.19, stacks of metal complex form along the 100 crystallographic direction with overlap between metal complexes from different layers. There is π-π stacking present between metal complexes with the overlap present from the uncoordinated 2-pyridyl rings displayed in figure 7.20, a centroid – centroid distance of 3.687 Å. This close stacking of the complexes leads to hydrogen bonding in the structure, CH-N hydrogen bonding is present between the H18 and N1 distance of 2.450 Å.

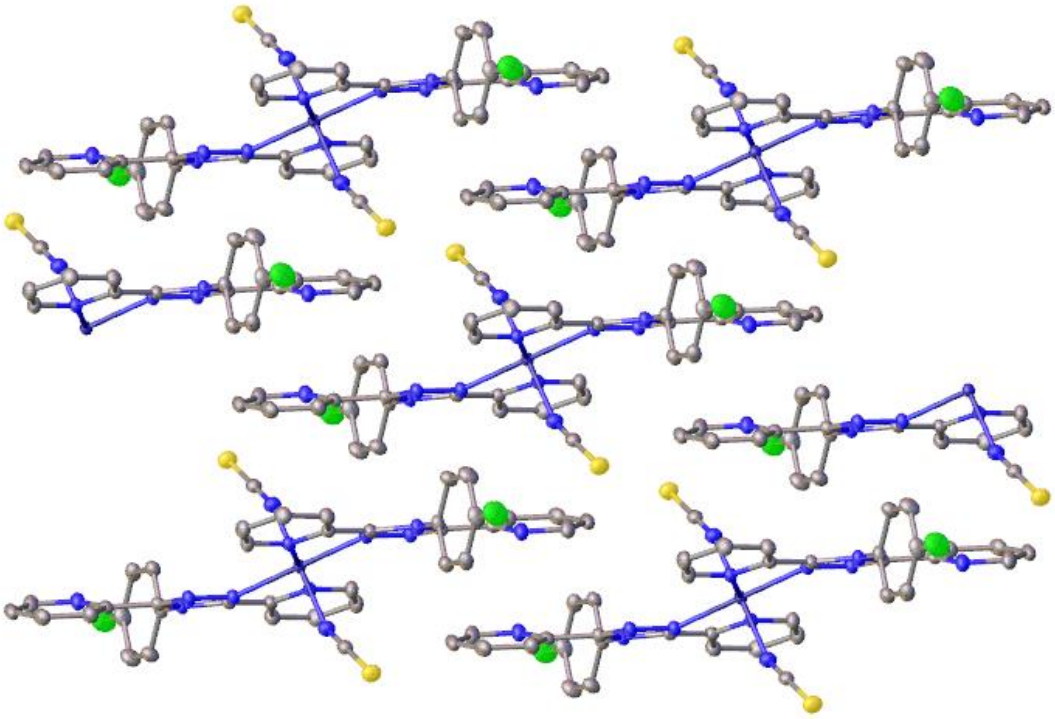

Figure 7.19. Image representing the packing of metal complexes in the crystal structure of **34** viewed along the *c* axis.

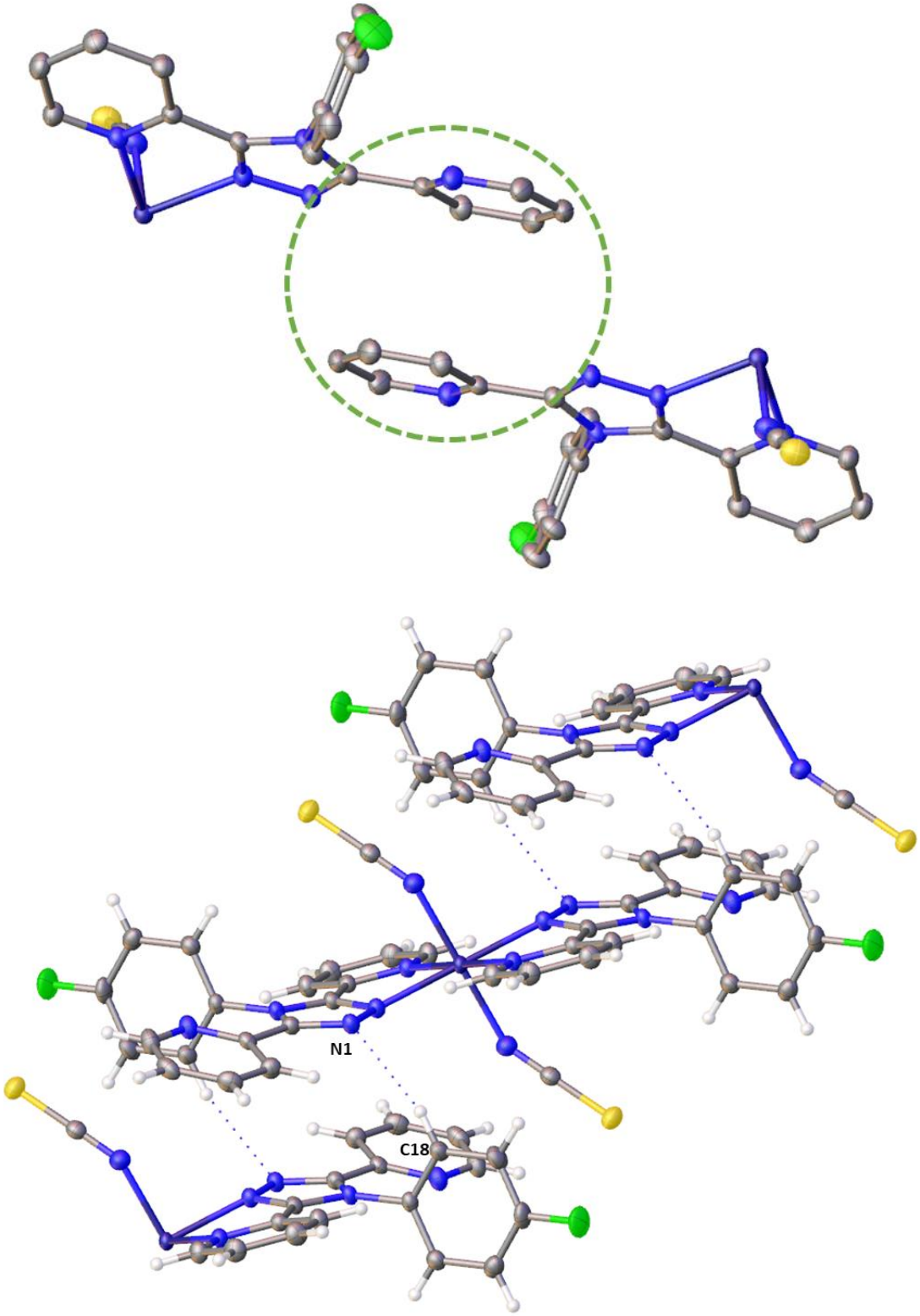

Figure 7.20. Weak interactions in **34** in the form of π-π interactions (top) and hydrogen bonding interactions (bottom).

The increased communication in the system from both the π-π stacking and hydrogen bonding lends itself to be a being a candidate for low temperature studies with XIPHOS I. Unfortunately, this crystal structure was found late on in this work and with XIPHOS

I being out of commission time was not available to conduct the low temperature study required.

Suitable single crystals of **35** were grown from a layered crystallisation, a methanol:water 1:1 solution containing manganese bis-isothiocyanate was injected slowly with a microlance needle under a methanol solution containing **16**. After a 1-week crystals of an appropriate size had formed on the interface, these crystals were removed from the sample and placed into inert perfluoro poly ether oil, *Fomblin-YR 1800*, on a glass slide to allow manipulation and observation under a microscope. A large yellow block-shaped single was selected for analysis by SC-XRD.

Structure solution was performed by SHELXT via intrinsic phasing in the Olex2 GUI2 which confirmed a triclinic space group setting of *P*-1. The structure reached convergence as implied by a shift/ESD of 0.000. The minimum unaccounted electron density was -0.6 eÅ^{-3} and the maximum 0.2 eÅ^{-3} located near C17 and C16. The final refined structure was 97.8% complete to 0.81 Å, with an R_1 = 2.66% and wR_2 = 7.46% suggesting the data was very high quality. The final refinement results are shown in figure 7.21.

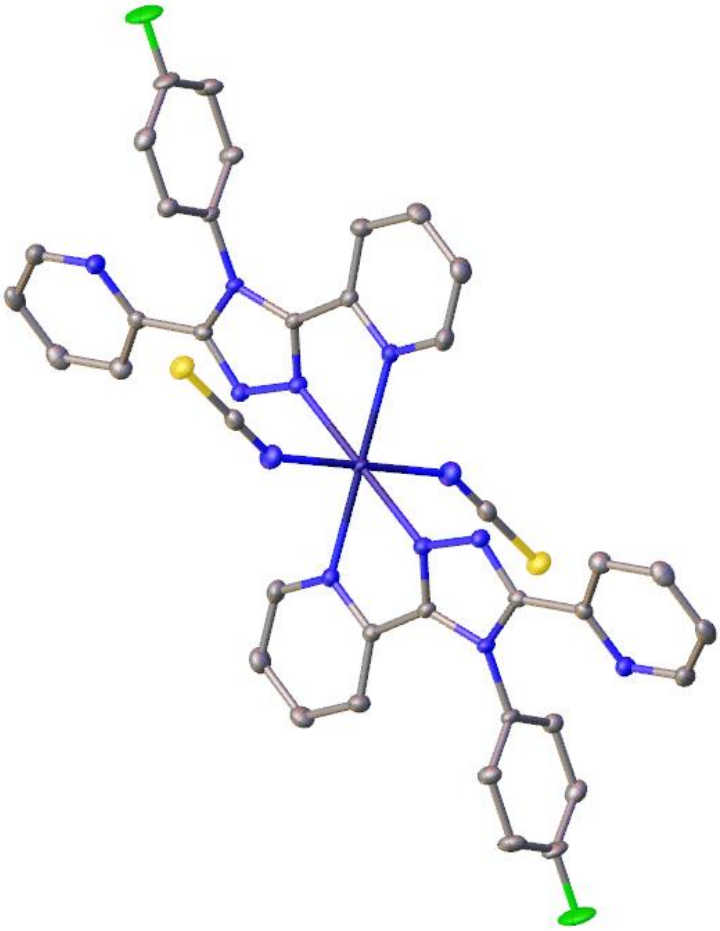

Figure 7.21. A symmetry expanded view of the crystallographic model of **35**. The anisotropic displacement parameters of all non-hydrogen atoms are shown at 50% probability. Hydrogens omitted for clarity.

The final refinement yielded a manganese complex, with a Mn(II) metal centre coordinated to two **16** ligands in bidentate fashion through nitrogen atoms N2 and N3. There are two coordinated trans isothiocyanates and no solvent present in the structure. The structure was isomorphous to the previous cobalt structure **34** with a N_6 coordination sphere. The bond lengths of this structure were interrogated and ranged from 2.16-2.28 Å.

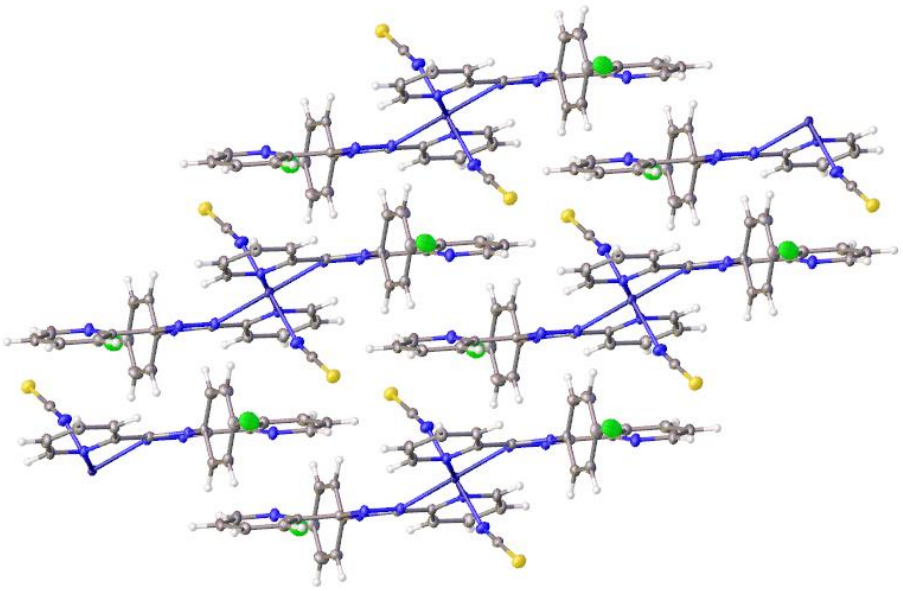

Figure 7.22. Image representing the packing of metal complexes in the crystal structure of **35** viewed along the *a* axis.

As the structure is isomorphous the packing is the same as the cobalt isomorph. Once again there are π-π stacking present between metal complexes with the overlap present from the uncoordinated 2-pyridyl rings as shown in figure 7.23, a centroid – centroid distance of 3.715 Å shift/ESD ed = 1.453 Å. The same hydrogen bonding interactions are observed between metal complexes, CH-N hydrogen bonding between the H18 and N1 distance of 2.474 Å.

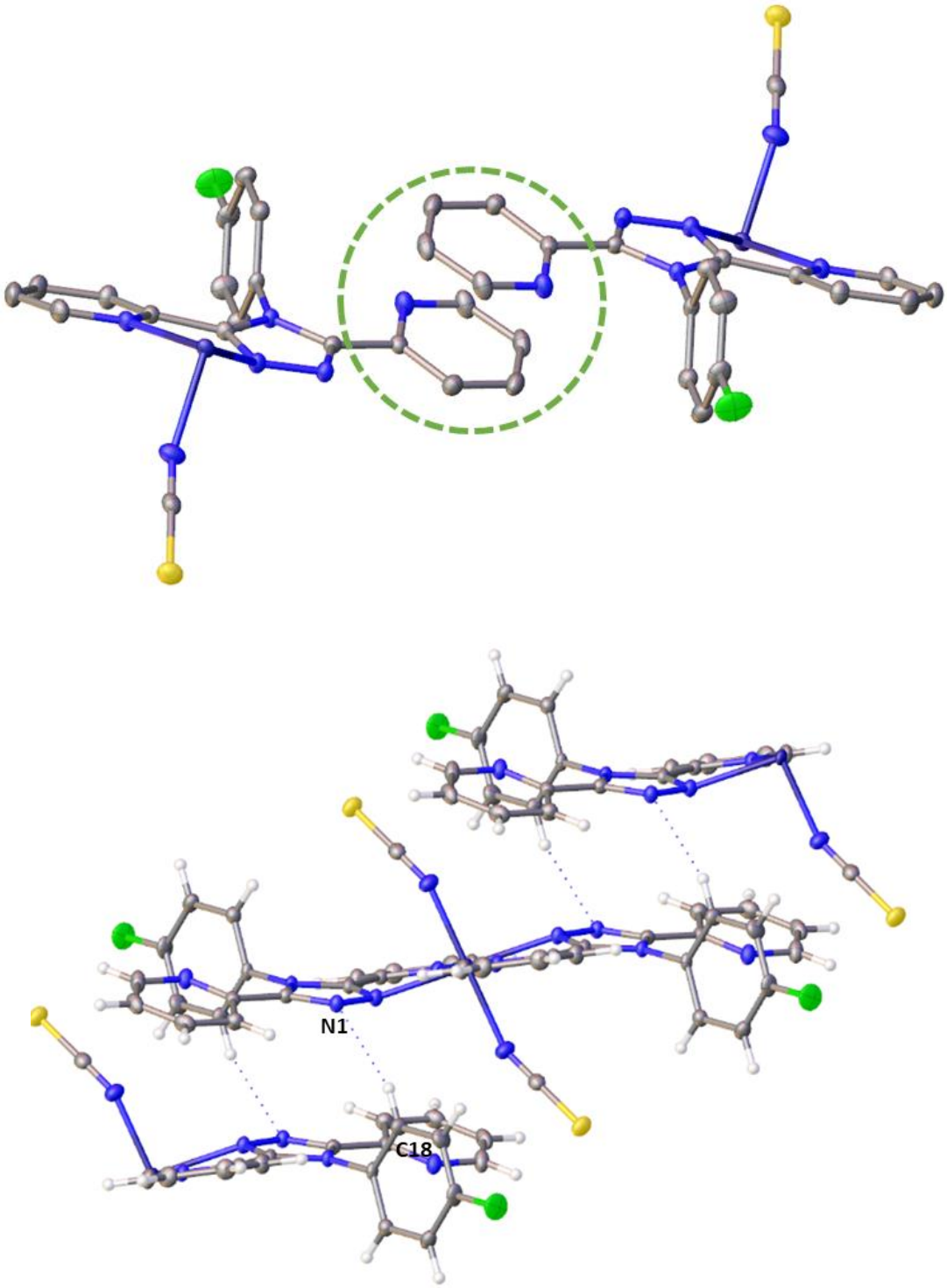

Figure 7.23. Image displaying the weak interactions in the crystal structure of **35** in the form of π-π interactions (top) and hydrogen bonding (bottom).

A [Fe(**16**)$_2$(NCS)$_2$] mononuclear structure containing **16** ligand was not obtained, it would have been a good comparison to the structures obtained in chapter 4, with the hydrogen bonding and π-π stacking present in these systems it would be a prime candidate for spin crossover. Attempts to synthesis this system was conducted multiple times utilising multiple crystallisation techniques.

Suitable single crystals of **36** were grown from an evaporation crystallisation, an ethyl acetate solution containing iron perchlorate and **16** was stirred for 5 hours at room temperature. Ventilation holes were added to the sample vial before being left for several weeks, after which nucleation had started, single crystals were observed after another week. These crystals were removed from the sample and placed into inert perfluoro poly ether oil, *Fomblin-YR 1800*, on a glass slide to allow manipulation and observation under a microscope. A orange block single crystal was selected for analysis by SC-XRD.

Structure solution was performed by SHELXT via intrinsic phasing in the Olex2 GUI2 which confirmed a triclinic space group setting of *P*-1. The structure reached convergence as implied by a shift/ESD of 0.001. The minimum unaccounted electron density was -0.5 $eÅ^{-3}$ and the maximum 0.6 $eÅ^{-3}$ located near S5. The final refined structure was 99% complete to 0.81 Å, with an R_1 = 4.40% and wR_2 = 12.91% suggesting the data was good quality. The final refinement results are shown in figure 7.24

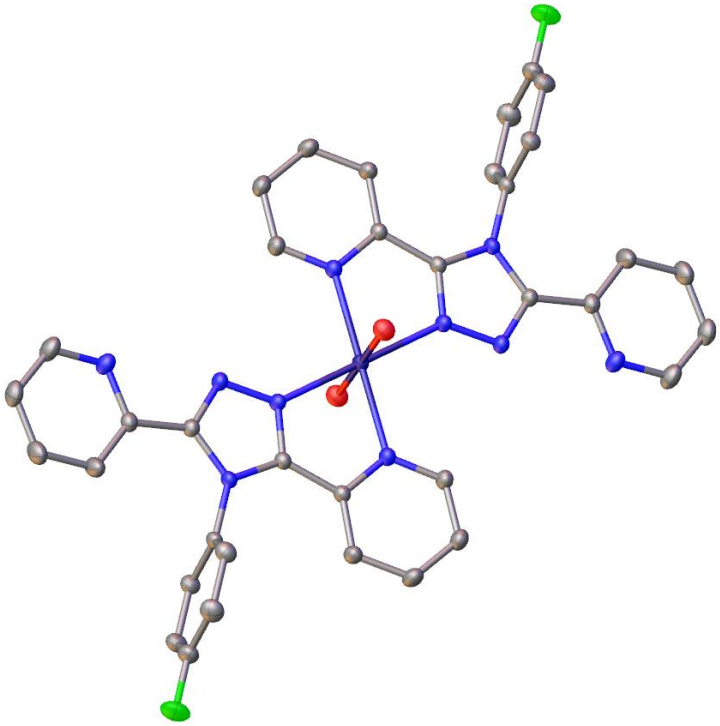

Figure 7.24. A symmetry expanded view of the crystallographic model of **36**, anisotropic displacement parameters of all non-hydrogen atoms are shown at 50% probability. Hydrogens, counter ions and solvent omitted for clarity.

The final refinement yielded a complex with a iron(II) metal centre coordinated in a bidentate fashion to two compounds of **16**, there are two coordinated trans oxygen molecules. The structure contains two perchlorate counter ions and an acetic acid solvent molecule. Ethyl acetate degrades into acetic acid and ethylene over time which is what appears to have happened with this sample.[6] The coordination sphere of N_4O_2 occurs in the literature for SCO systems but is not the optimal N6. The bond lengths of the iron centre investigated, Fe – N ranged from 2.14 – 2.18 Å and Fe – O bonds were 2.12 Å, these bond lengths indicate the system occupies a fully high spin state. The N2 – Fe1 – N3 bite angle is 76.05(7)˚

The crystal packing of **36** is displayed in figure 7.25, stacks of metal complex form along the 100 direction, these stacks are separated by perchlorate counter ions and the acetic acid. There is OH - O hydrogen bonding present between the coordinated water molecule and one of the perchlorate counter ions distance = 1.968(17) Å.

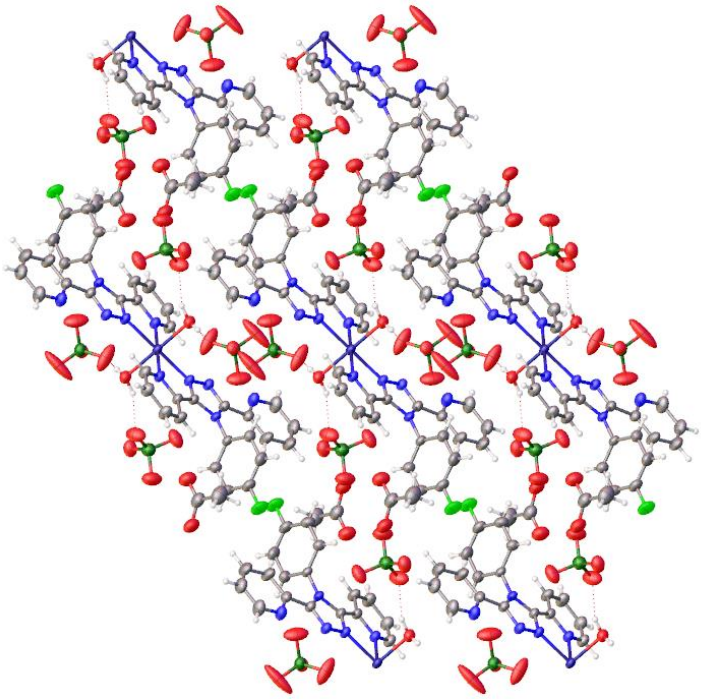

Figure 7.25. Image representing the packing of metal complex and counter ions present in the crystal structure of **36** viewed along the *a* axis.

A new single crystal of this sample was selected for low temperature experimentation on XIPHOS I. The sample was mounted to a sharpened graphite rod using a minimal amount of epoxy resin glue (Loctite^{TM} double bubble), known to be a good thermal conductor to hold the crystal in place while mounted vertically in the cold head. Full data collection was performed at 2 K, data integration and structure solution performed in the same manner as the 150 K data set. The structure solution yielded the same asymmetric unit, interrogation of the bond lengths revealed they were almost identical ranging from 2.15-2.18 Å remaining in a HS state. Due to this crystal structure belonging to a triclinic space group setting and the limitations of the XIPOHS I set up the data completeness was low and data quality impacted.

Suitable single crystals of **37** were grown from an evaporation crystallisation, a methanol solution containing cobalt bromide and **16** was stirred for 4 h before ventilation holes added to the sample vial and left to crystallise. After a week crystals had started to nucleate on the side of the sample vial, after another week crystals of an appropriate size had formed on the interface, these crystals were removed from the sample and placed into inert perfluoro poly ether oil, *Fomblin-YR 1800*, on a glass slide to allow manipulation and observation under a microscope. A large pink block-shaped single was selected for analysis by SC-XRD.

Structure solution was performed by SHELXT via intrinsic phasing in the Olex2 GUI2 which confirmed a triclinic space group setting of *P*-1. The structure reached convergence as implied by a shift/ESD of 0.001. The minimum unaccounted electron density was -0.9 eÅ^{-3} and the maximum 0.7 eÅ^{-3} located near the Br counterion. The final refined structure was 99% complete to 0.81 Å, with an R_1 = 5.63% and wR_2 = 17.14% suggesting the data was good quality. The final refinement results are shown in figure 7.26.

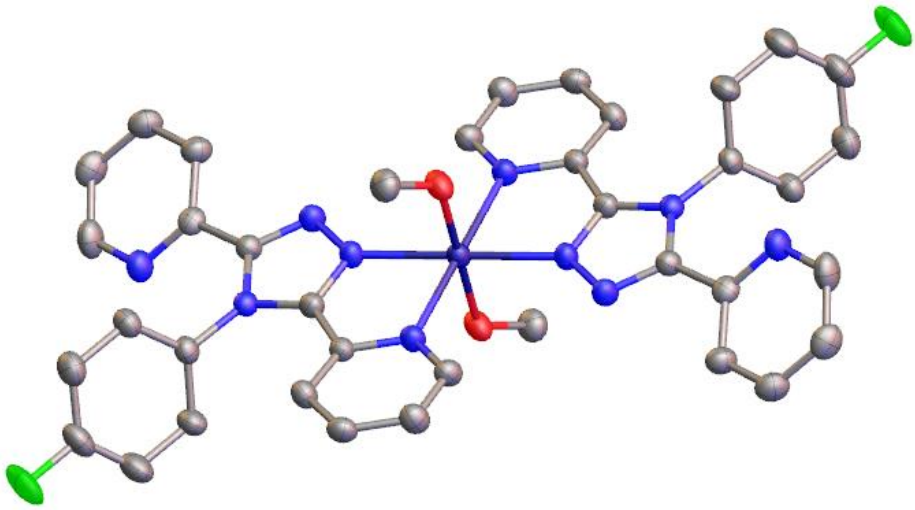

Figure 7.26. A symmetry expanded view of the crystallographic model of **37**. The anisotropic displacement parameters of all non-hydrogen atoms are shown at 50% probability. Hydrogens omitted for clarity

The final refinement yielded a structure containing a cobalt(II) metal centre, coordinated to two copies of **16** through nitrogen atoms N2 and N3 and coordinated to two methanol molecules, there were 2 uncoordinated bromine counter ions. The bond lengths were investigated and ranged from 2.09 – 2.13 Å suggesting a high spin state. The N4O2 coordination sphere was not optimal for SCO systems.

The Crystal packing of **37** displayed in figure 7.27, shows the formations of stacks in the 100 crystallographic direction, Fe – Fe distances in the stack are 7.4682(6) Å. There is hydrogen bonding within the stacks, the bromine at the centre of these interactions, hydrogen bonding occurs through CH-Br and OH-Br interactions shown in figure 7.28. CH-Br = 2.805, 2.870 Å, OH- Br = 2.245 Å.

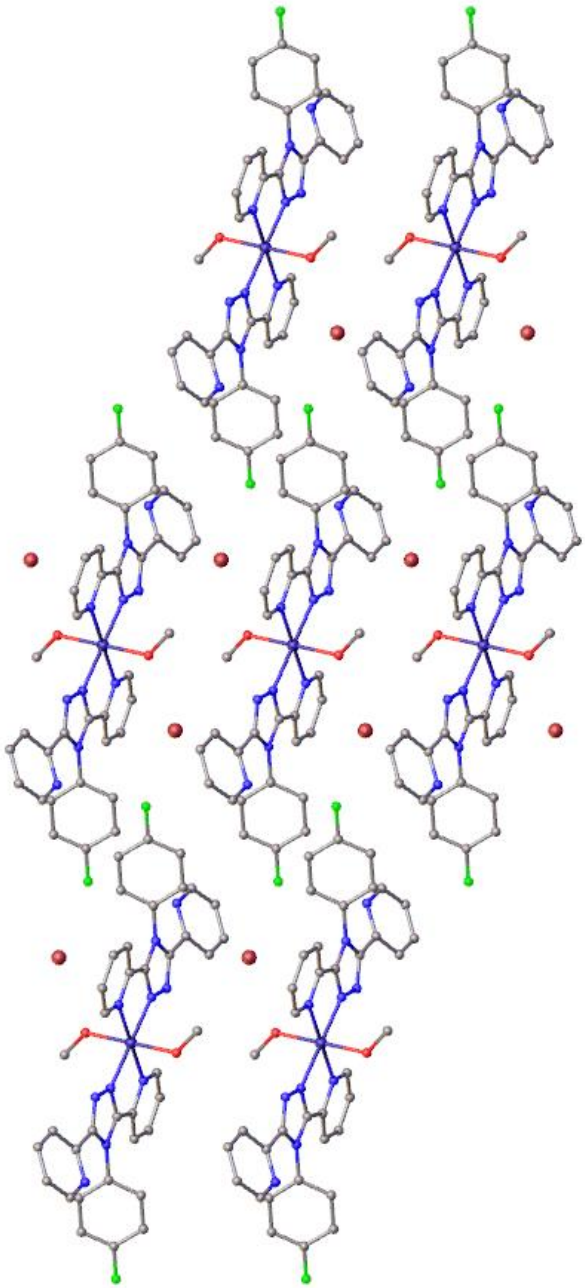

Figure 7.27. Image representing the packing of metal complexes and counter ions present in the crystal structure of **37** viewed along the *b* axis.

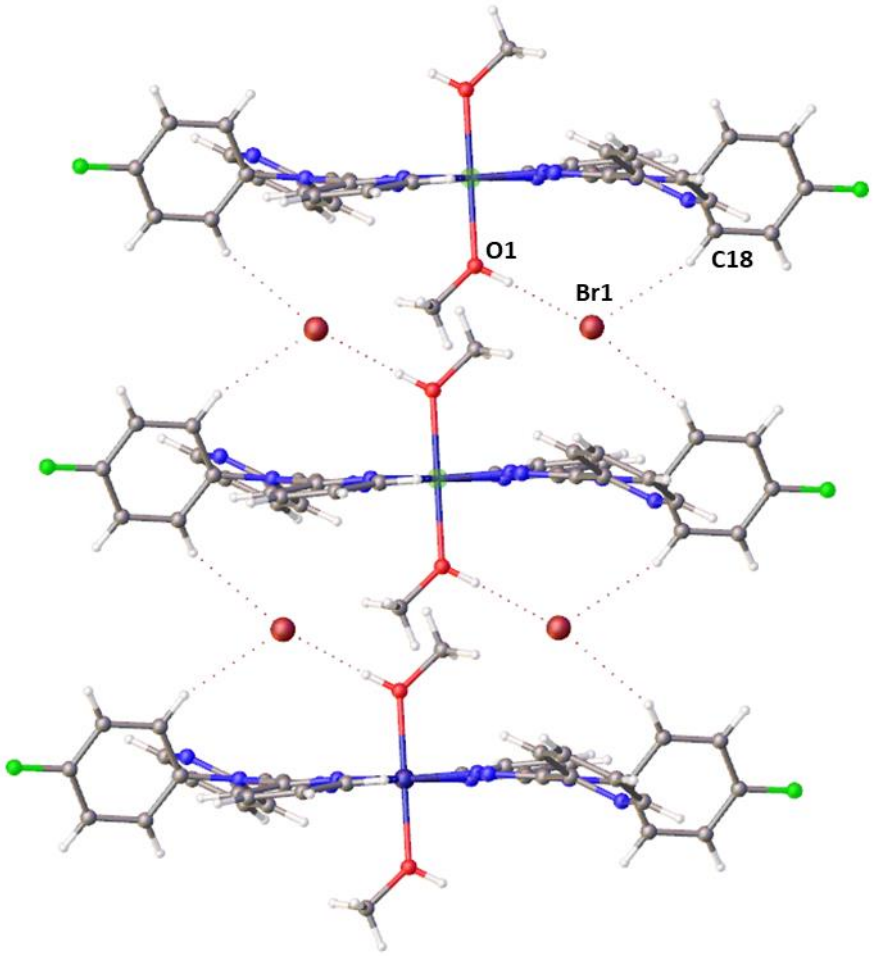

Figure 7.28. Image of the hydrogen bonding interactions observed in the crystal structure of **37**.

Crystals of this sample were on the waiting list for extreme low temperature studies however were low priority due to the N_4O_2 coordination sphere and Co(II). In the future this should be studied at low temperature for potential SCO.

Suitable single crystals of **38** were grown from a layered crystallisation, a ethanol:water 1:1 solution containing cobalt bromide was injected slowly with a microlance needle under a methanol solution containing **16**. After a ~4 days nucleation had started at the interface, after a week crystals of an appropriate size had formed on the interface, these crystals were removed from the sample and placed into inert perfluoro poly ether oil, *Fomblin-YR 1800*, on a glass slide to allow manipulation and observation under a microscope. A large pink block-shaped single was selected for analysis by SC-XRD.

Structure solution was performed by SHELXT via intrinsic phasing in the Olex2 GUI2 which confirmed a monoclinic space group setting of $P2_1/n$. The structure reached convergence as implied by a shift/ESD of 0.001. The minimum unaccounted electron density was -1.9 $eÅ^{-3}$ and the maximum 1.5 $eÅ^{-3}$ located near the Br counterion. The

final refined structure was 99.2% complete to 0.81 Å, with an R_1 = 8.37% and wR_2 = 25.67% suggesting the data was okay quality. The final refinement results are shown in figure 7.29.

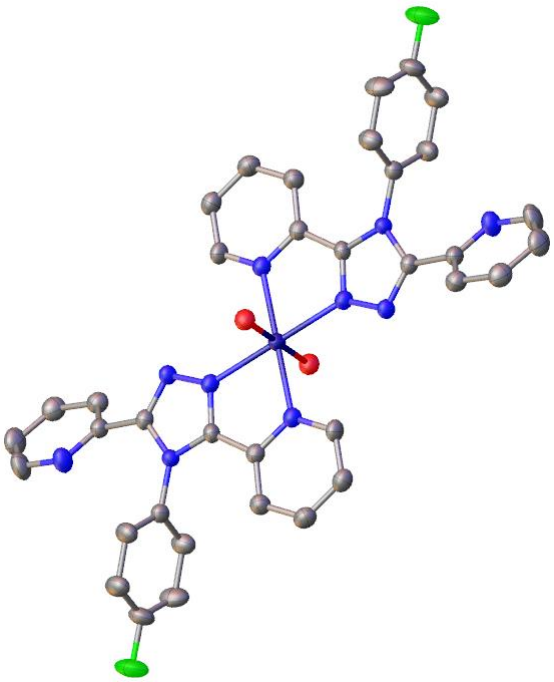

Figure 7.29. A symmetry expanded view of the crystallographic model of **38**. The anisotropic displacement parameters of all non-hydrogen atoms are shown at 50% probability. Hydrogens omitted for clarity.

The final refinement yielded a structure containing a cobalt(II) metal centre, coordinated to two copies of **16** through nitrogen atoms N2 and N3 and coordinated to two water molecules, there were 2 uncoordinated bromine counter ions and two uncoordinated ethanol molecules. The bond lengths were investigated and ranged from 2.09 – 2.14 Å suggesting a high spin state with an N_4O_2 coordination sphere.

The crystal packing of the structure shown in figure 7.30, stacks form on the 100 crystallographic direction, these stacks form inverted layers separated by the solvent and counter ion molecules.

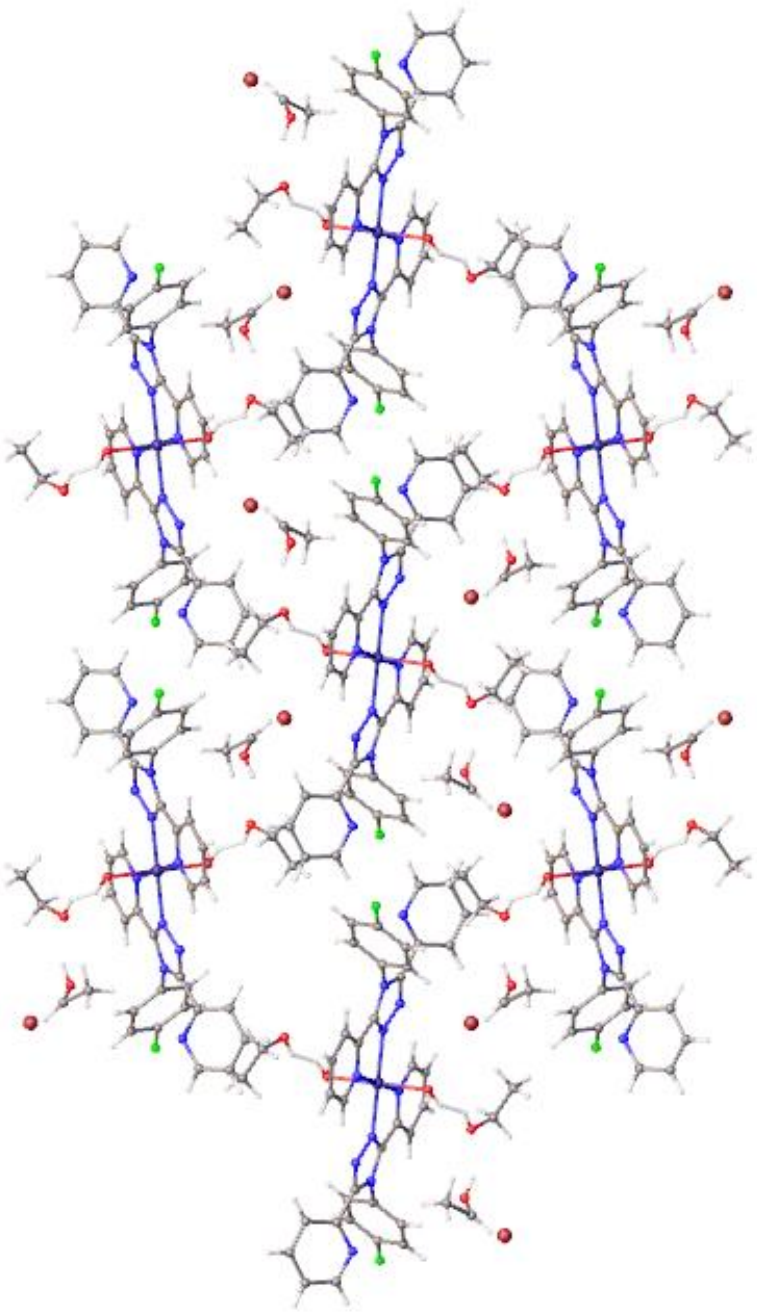

Figure 7.30. Image representing the packing of metal complexes, counter ions and solvent molecules present in the crystal structure of **38** viewed along the *a* axis.

There is Hydrogen bonding displayed in the structure between the metal complex and both counter ions and solvent molecules (figure 7.31). OH-Br hydrogen bonding between Br1 and O1, 12.3884(5) Å, A chain of hydrogen bonding displayed between the metal complex and 2 ethanol molecules with OH-O interactions of 1.904(3) between O1 and O2, 1.852(5) Å between O2 and O3. π-π stacking is displayed between coordinated 2-pyridyl rings, distance ca. 3.595 Å with a shift of 1.181 Å.

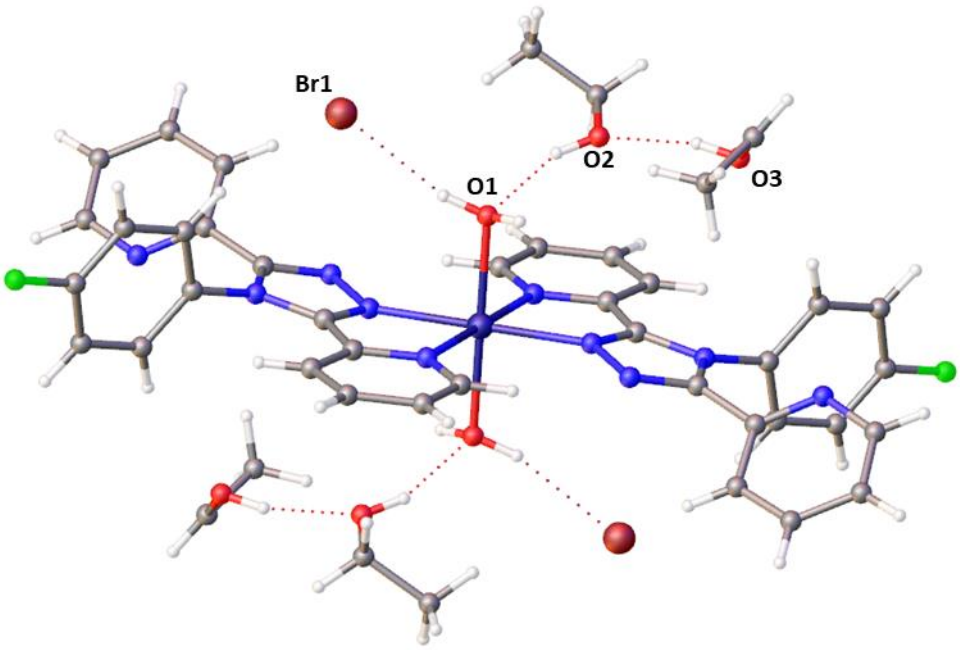

Figure 7.31. Image of the hydrogen bonding interactions displayed in crystal structure of **38**.

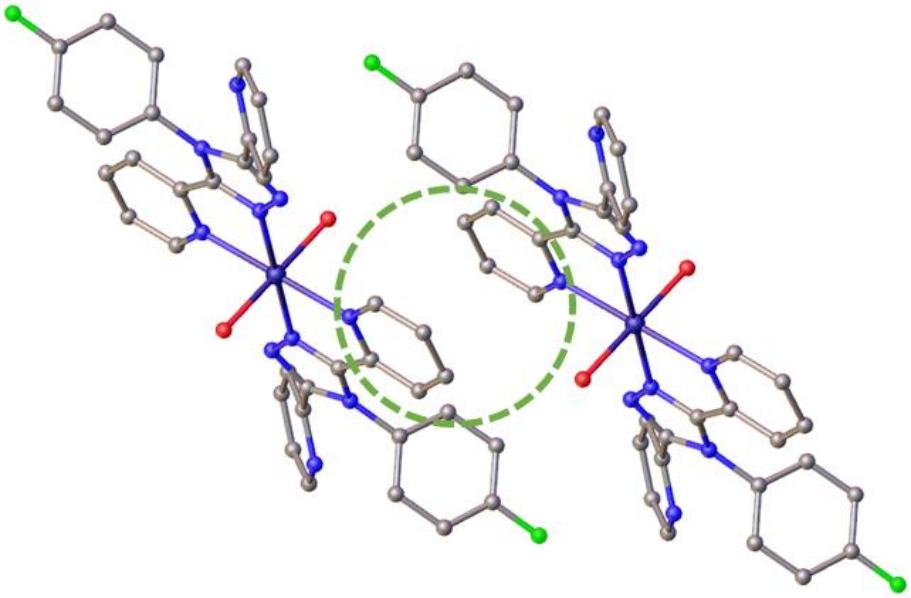

Figure 7.32. Image representing the π-π interactions present in the crystal structure of **38**.

Suitable single crystals of **39** were grown from a layered crystallisation, a methanol:water 1:1 solution containing cobalt bis-isothiocyanate was injected slowly with a microlance needle under a methanol solution containing **21**. After 4 days crystals of an appropriate size had formed on the interface, these crystals were removed from the sample and placed into inert perfluoro poly ether oil, *Fomblin-YR 1800*, on a glass

slide to allow manipulation and observation under a microscope. A pink plate-shaped single was selected for analysis by SC-XRD.

Structure solution was performed by SHELXT via intrinsic phasing in the Olex2 GUI2 which confirmed a triclinic space group setting of *P*-1. The structure reached convergence as implied by a shift/ESD of 0.001. The minimum unaccounted electron density was -0.6 $eÅ^{-3}$ and the maximum 0.3 $eÅ^{-3}$located along the C7-C8 bond. The final refined structure was 97.7% complete to 0.81 Å, with an R1 = 2.84% and wR2 = 7.82% suggesting the data was high quality. The final refinement results are shown in figure 7.33.

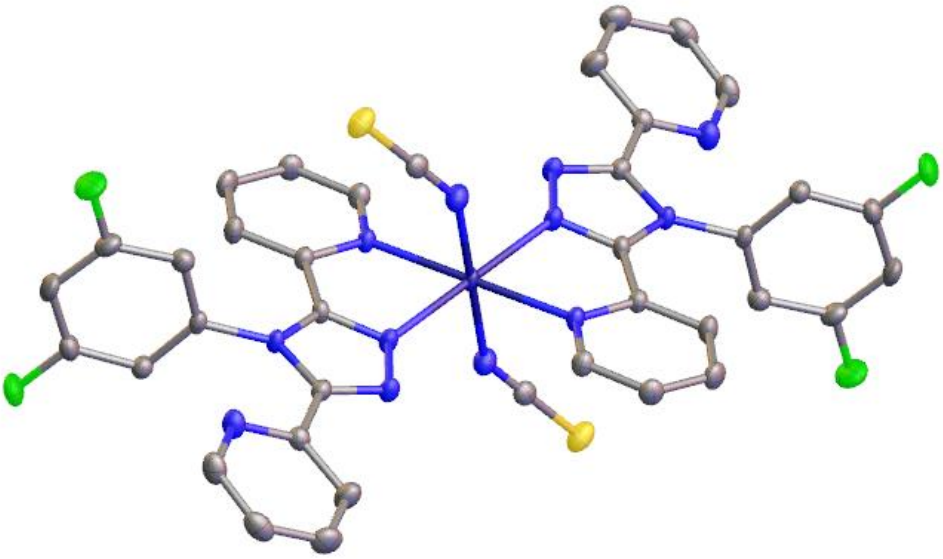

Figure 7.33. A symmetry expanded view of the crystallographic model of **39**. The anisotropic displacement parameters of all non-hydrogen atoms are shown at 50% probability. Hydrogens omitted for clarity.

The final refinement yielded a structure with a cobalt(II) centre coordinated to two 20 ligands via nitrogen atoms N2 and N3, two coordinated isothiocyanates and no further atoms in the cell. The N_6 coordination sphere was investigated for its bond lengths which ranged from 2.08 – 2.15 Å indicating the system occupied a HS state.

Crystal packing of the system is displayed in figure 7.34, stacks of metal complexes form in the 100 crystallographic plane.

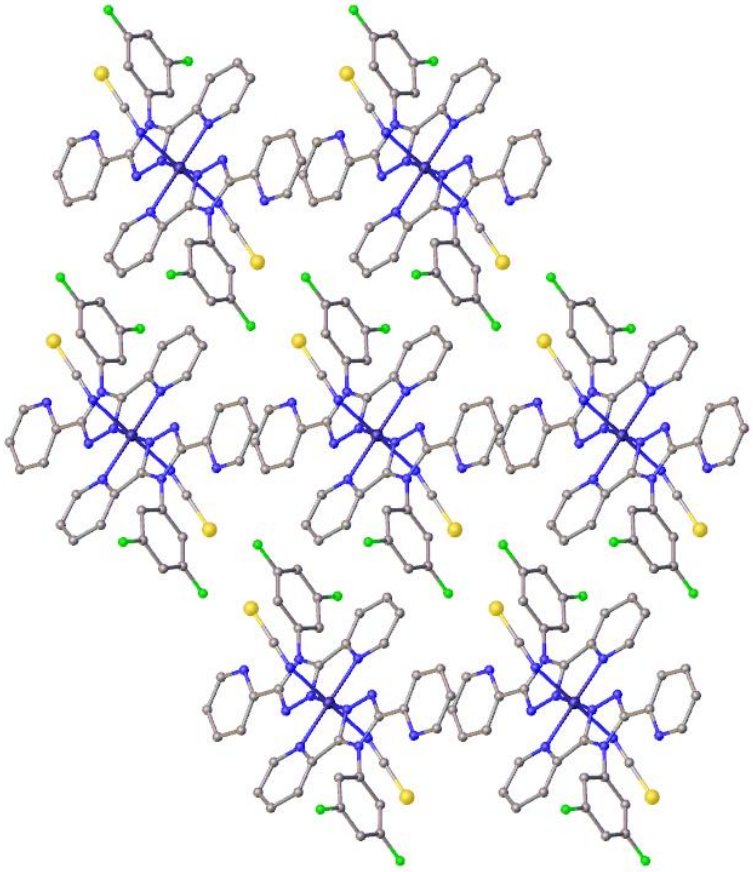

Figure 7.34. Image representing the packing of metal complexes and counter ions present in the crystal structure of **39** viewed along the *a* axis.

These planes display hydrogen bonding in the form of CH-N interactions between C14 and N1 of 2.4295(13) Å. There is also π-π stacking interactions in the crystal structure between the uncoordinated 2-pyridyl rings, 3.843(2) Å with a shift of 1.530(4) Å.

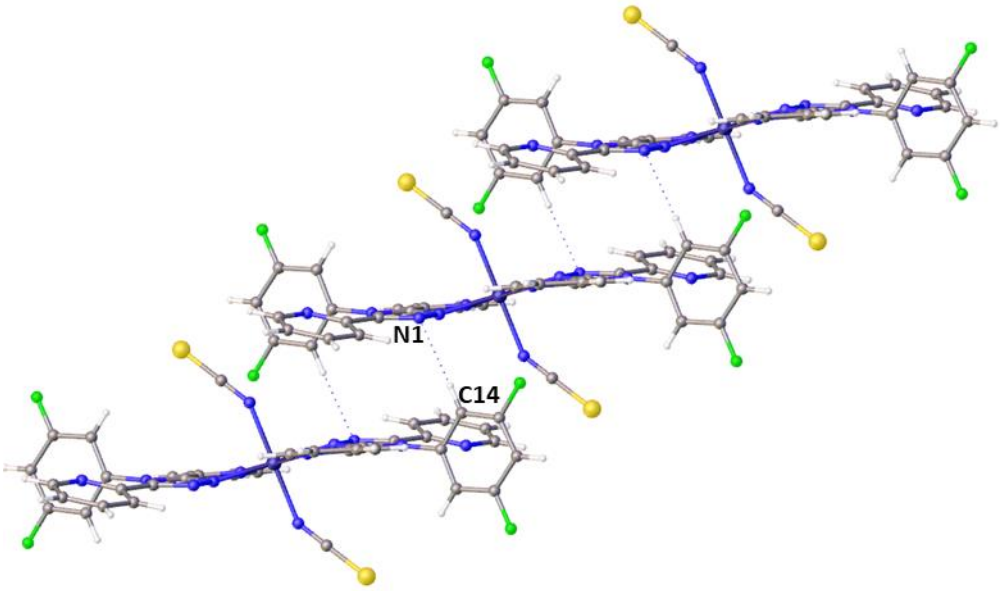

Figure 7.35. Image displaying the hydrogen bonding interactions present in the crystal structure of **39**.

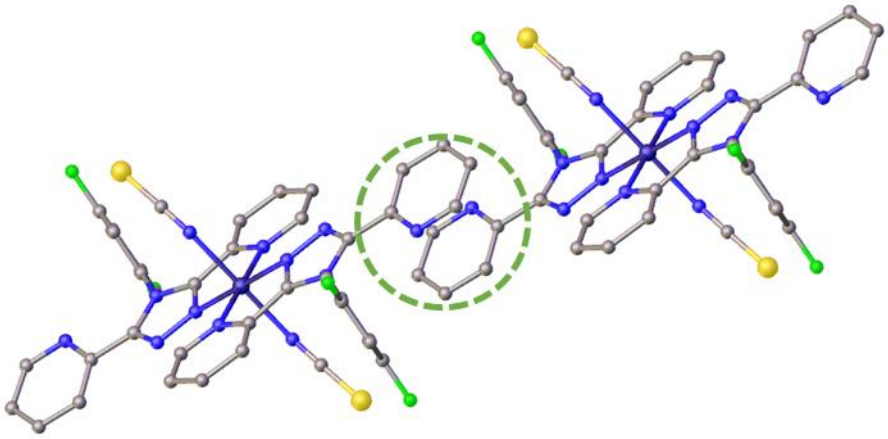

Figure 7.36. Image representing the π-π interactions present in the crystal structure of **39**.

Suitable single crystals of **40** were grown from a layered crystallisation, a methanol:water 1:1 solution containing cobalt bis-isothiocyanate was injected slowly with a microlance needle under a methanol solution containing **11**. After a week crystals of an appropriate size had formed on the interface, these crystals were removed from the sample and placed into inert perfluoro poly ether oil, *Fomblin-YR 1800*, on a glass slide to allow manipulation and observation under a microscope. A pink plate-shaped single was selected for analysis by SC-XRD.

Structure solution was performed by SHELXT via intrinsic phasing in the Olex2 GUI2 which confirmed a primitive monoclinic space group setting of $P2_1/c$. The structure

reached convergence as implied by a shift/ESD of 0.000. The minimum unaccounted electron density was -0.3 eÅ^{-3} and the maximum 0.2 eÅ^{-3} located near S1. The final refined structure was 100% complete to 0.81 Å, with an R_1 = 2.55% and wR_2 = 7.07% suggesting the data was high quality.

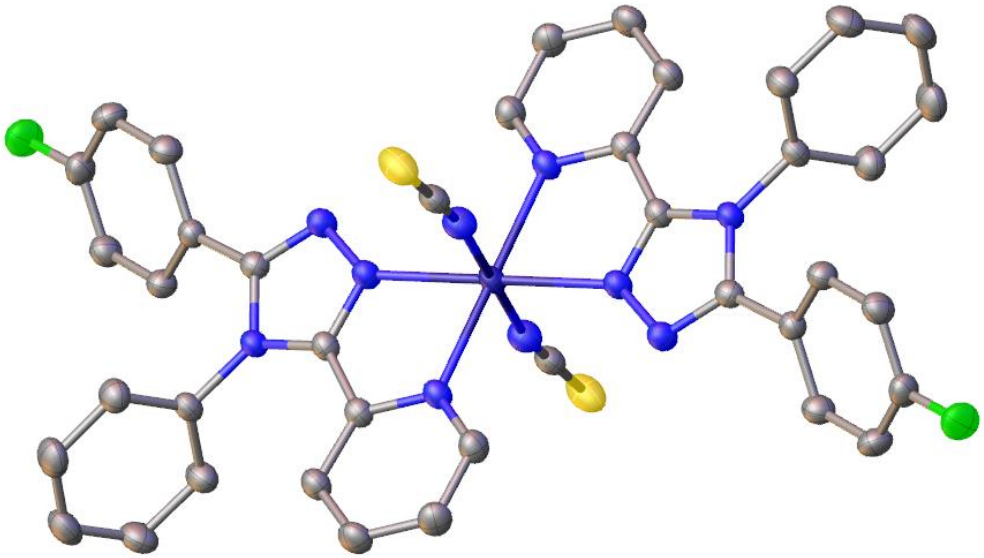

Figure 7.37. A symmetry expanded view of the crystallographic model of **40**. The anisotropic displacement parameters of all non-hydrogen atoms are shown at 50% probability. Hydrogens omitted for clarity.

The final refinement yielded a structure containing a cobalt(II) metal centre coordinated to two copies of **11** in a bidentate manner through nitrogen atoms N2 and N3, two coordinated trans isothiocyanates. The structure was interrogated for its structural properties, the bond lengths of the N_6 coordinated sphere ranged from 2.08 – 2.14 Å indicating the metal ion occupied a HS state.

The crystal packing is shown in figure 7.38, stacks of metal complexes form in the 100 crystallographic direction and are shown to form layers with channels in between. Hydrogen bonding is displayed between metal complexes in this system, CH-S hydrogen is displayed between S1 and C4 and C10 at 2.8529(4) and 2.8612(4) Å. Further hydrogen bonding is displayed from F1 to C19 at 2.3237(9) Å. π-π stacking is displayed in the system through an overlap of the 4-fluorophenyl ring on one metal complex overlapping with the 2-pyridyl of another metal complex at a distance of 3.874 Å with a shift of 1.289 Å.

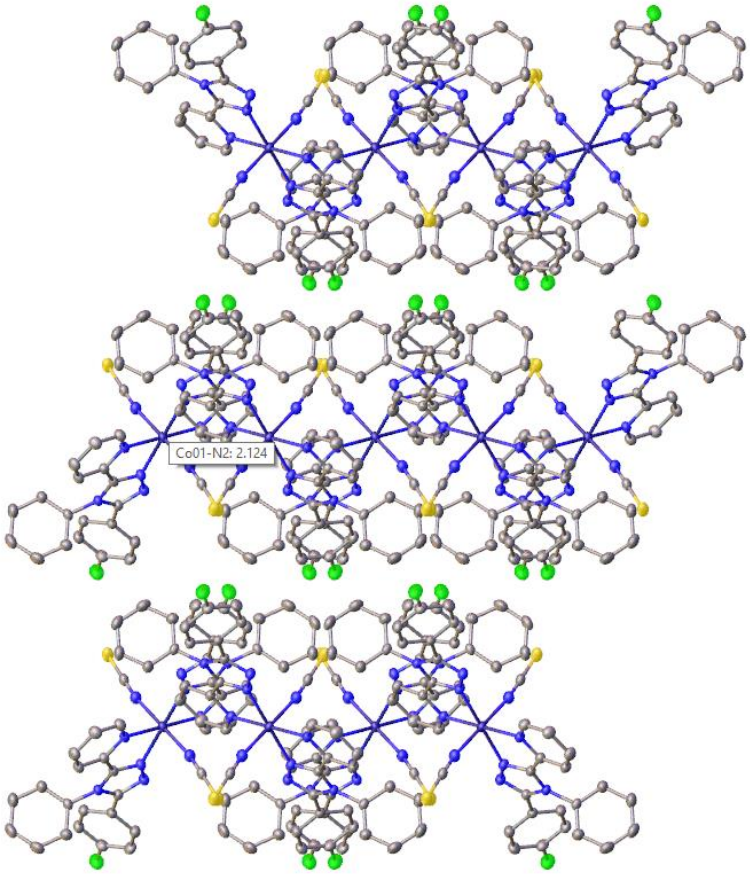

Figure 7.38. Image representing the packing of metal complexes and counter ions present in the crystal structure of **40** viewed along the *c* axis.

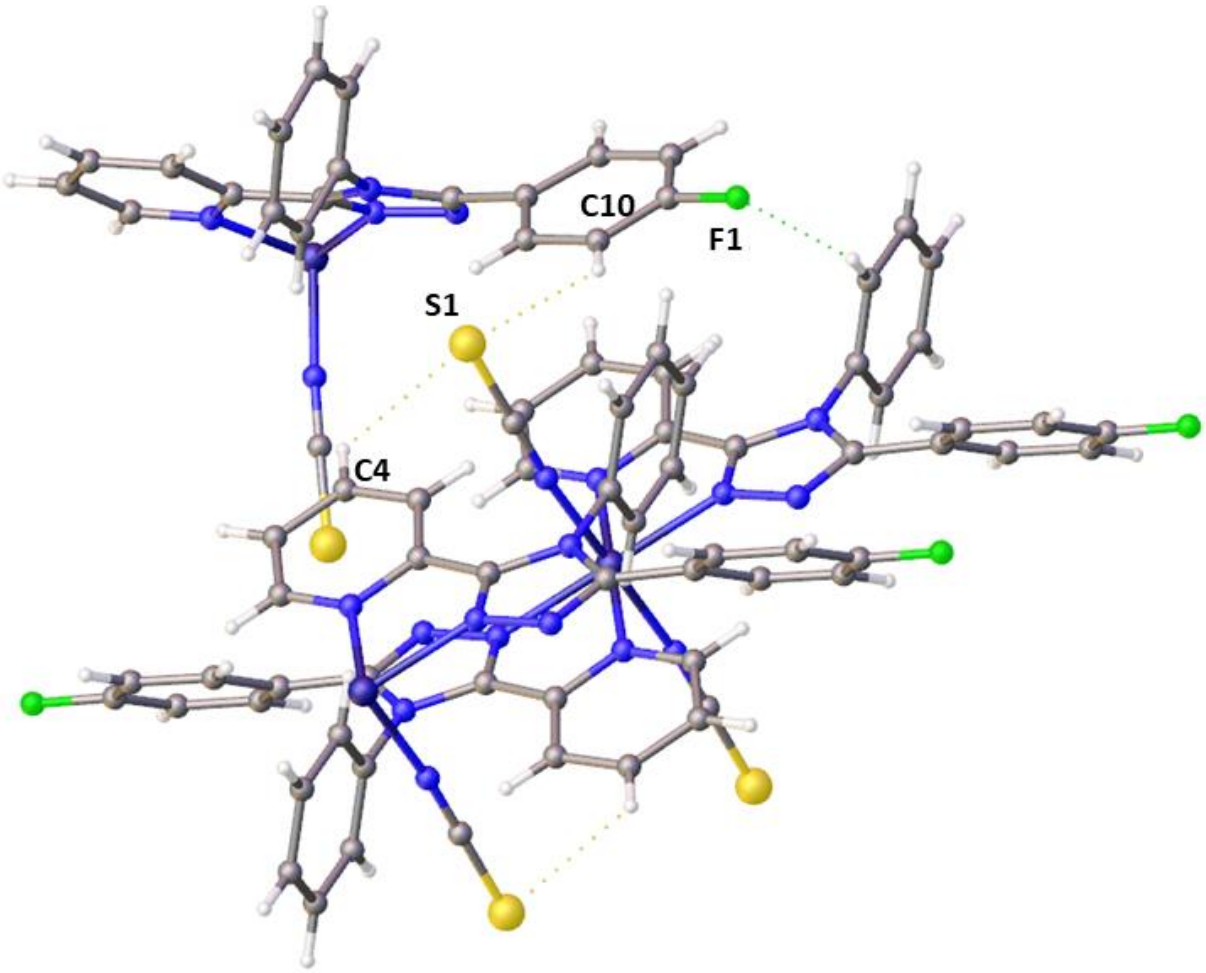

Figure 7.39. Image displaying the hydrogen bonding interactions present in the crystal structure of **40**.

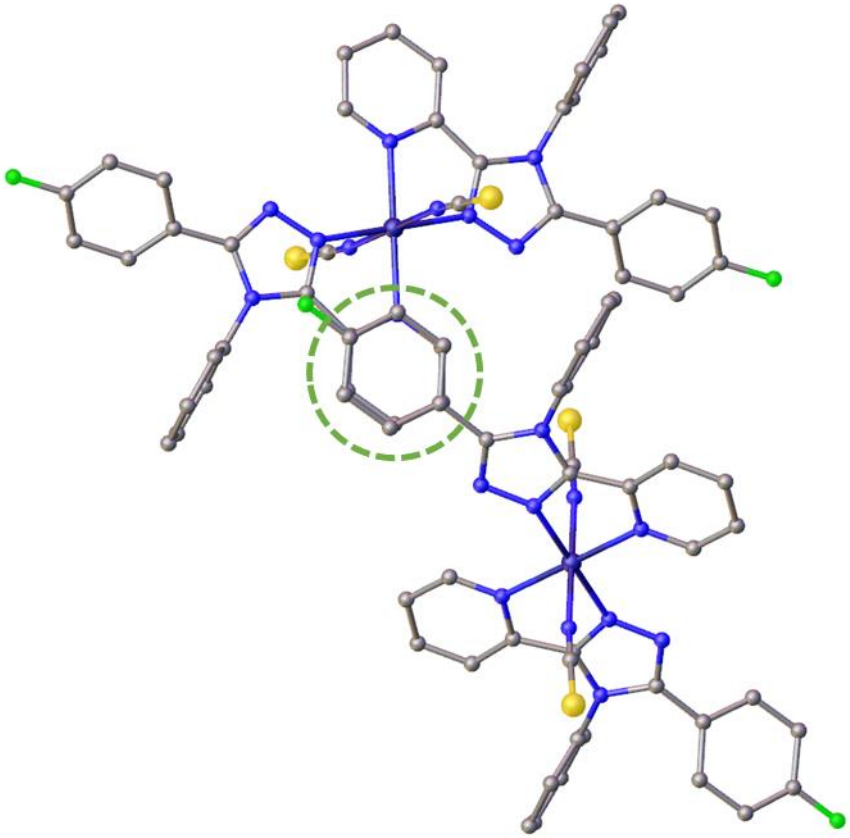

Figure 7.40. Image representing the π-π interactions present in the crystal structure of **40.**

Suitable single crystals of **41** were grown from a layered crystallisation, a methanol:water 1:1 solution containing cobalt bis-isothiocyanate was injected slowly with a microlance needle under a methanol solution containing **17**. After ~6 days crystals of an appropriate size had formed on the interface, these crystals were removed from the sample and placed into inert perfluoro poly ether oil, *Fomblin-YR 1800*, on a glass slide to allow manipulation and observation under a microscope. A pink plate-shaped single was selected for analysis by SC-XRD.

Structure solution was performed by SHELXT via intrinsic phasing in the Olex2 GUI2 which confirmed a primitive orthorhombic space group setting of *Pbca*. The structure reached convergence as implied by a shift/ESD of -0.001. The minimum unaccounted electron density was -0.3 eÅ^{-3} and the maximum 0.2 eÅ^{-3} located near the 4-fluorophenyl. The final refined structure was 99.8% complete to 0.81 Å, with an R_1 = 2.90% and wR_2 = 8.30% suggesting the data was high quality. Final refinement results are shown in figure 7.41.

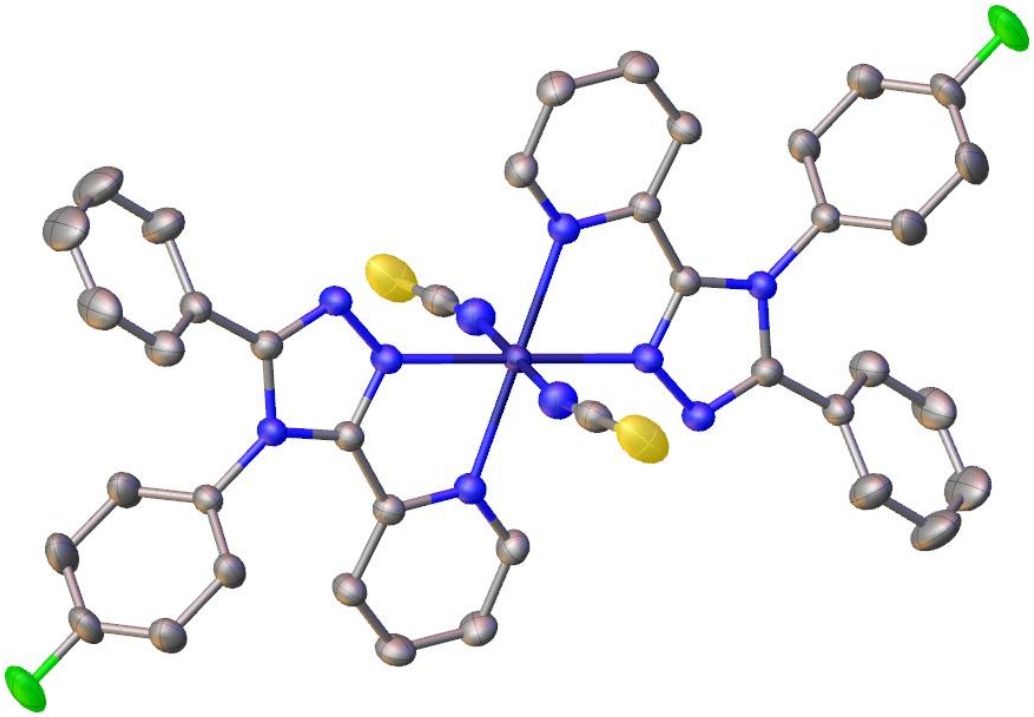

Figure 7.41. A symmetry expanded view of the crystallographic model of **41** at 200 K. The anisotropic displacement parameters of all non-hydrogen atoms are shown at 50% probability. Hydrogens omitted for clarity.

The final refinement yielded a structure containing a Co(II) metal centre coordinated to two copies of **17** in a bidentate manner through nitrogen atoms N2 and N3. Two isothiocyanate counter ions coordinated trans. The structural properties were investigated, the N6 coordination sphere bond lengths ranged from 2.08-2.16 Å indicating the metal ion occupied a HS state.

The crystal packing displayed in figure 7.42 is similar to many of the previous structures with stacks of metal complex forming in the 100 crystallographic direction, these stacks forming layers of metal complexes with a channel running between them. Hydrogen bonding is displayed between metal complexes in the crystal structure. Between S1 and C4, 2.9401(5) Å and between F1 and C15, 3.1673(19) Å.

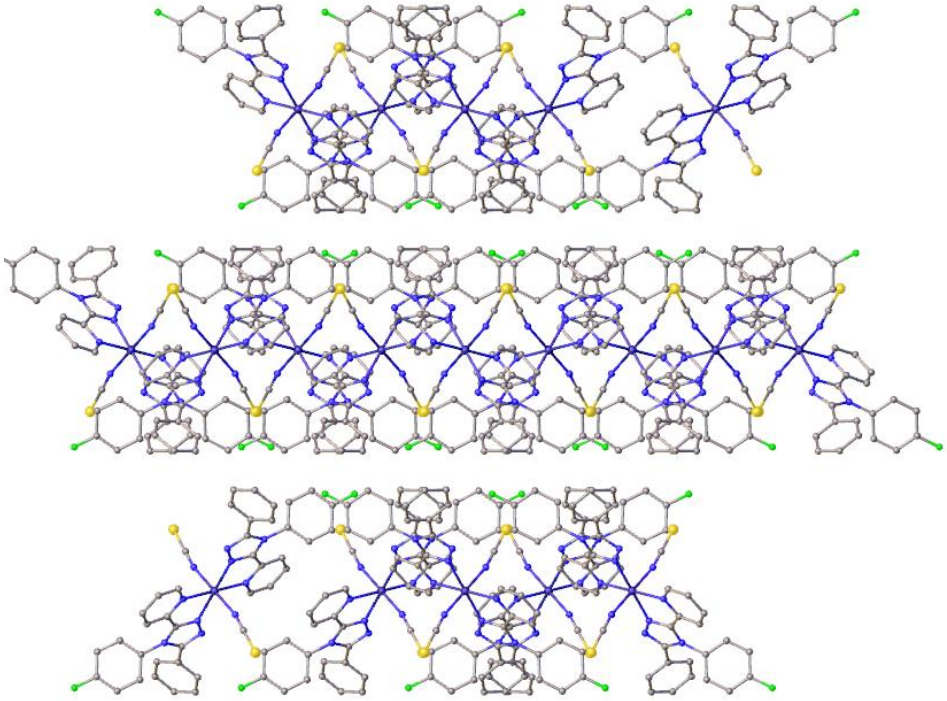

Figure 7.42. Image representing the packing of metal complexes present in the crystal structure of **41** viewed along the *b* axis.

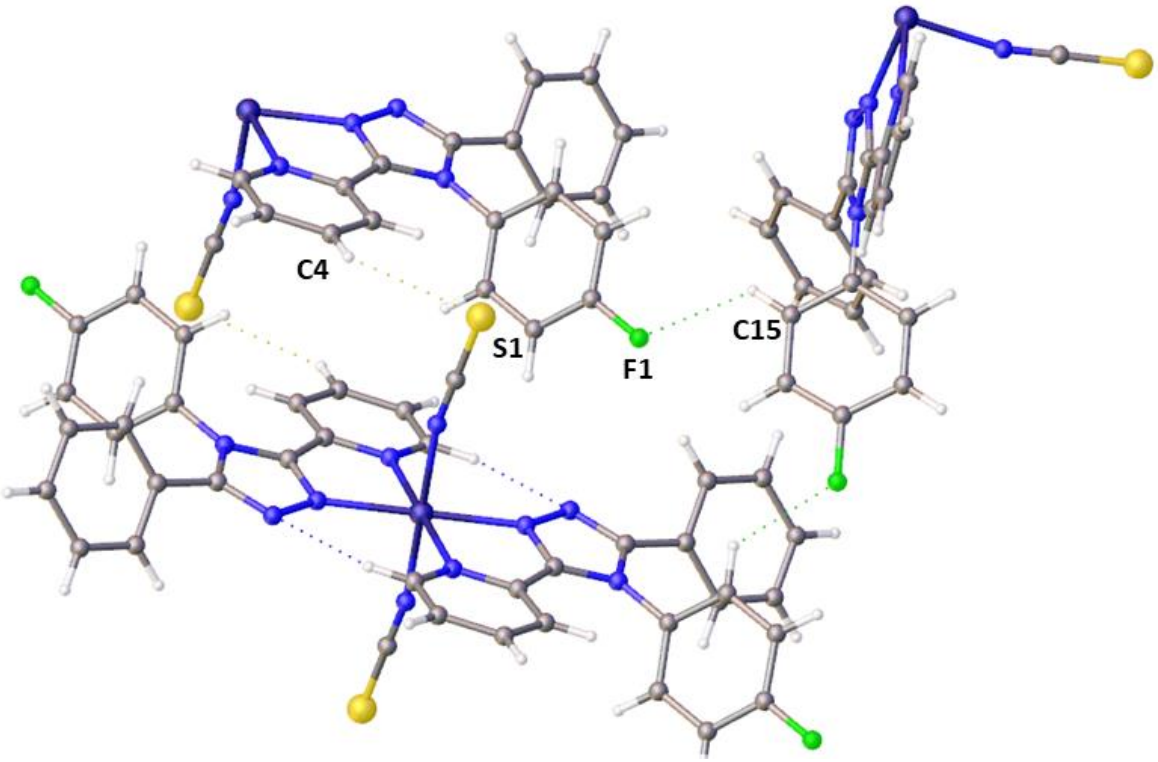

Figure 7.43. Image displaying the hydrogen bonding interactions present in the crystal structure of **41**.

Suitable single crystals of **42** were grown from a layered crystallisation, a methanol:water 1:1 solution containing cobalt(II) bis-isothiocyanate was injected slowly with a microlance needle under a methanol solution containing **5**. After a ~4 days crystals of an appropriate size had formed on the interface, these crystals were removed from the sample and placed into inert perfluoro poly ether oil, *Fomblin-YR 1800*, on a glass slide to allow manipulation and observation under a microscope. A pink block-shaped single was selected for analysis by SC-XRD.

Structure solution was performed by SHELXT via intrinsic phasing in the Olex2 GUI2 which confirmed a triclinic space group setting of *P*-1. The structure reached convergence as implied by a shift/ESD of 0.000. The minimum unaccounted electron density was -0.7 $eÅ^{-3}$ and the maximum 0.4 $eÅ^{-3}$ located near S1. The final refined structure was 98.1% complete to 0.81 Å, with an R_1 = 6.14% and wR_2 = 17.41% suggesting the data was of reasonable quality. The final refinement results are shown in figure 7.44.

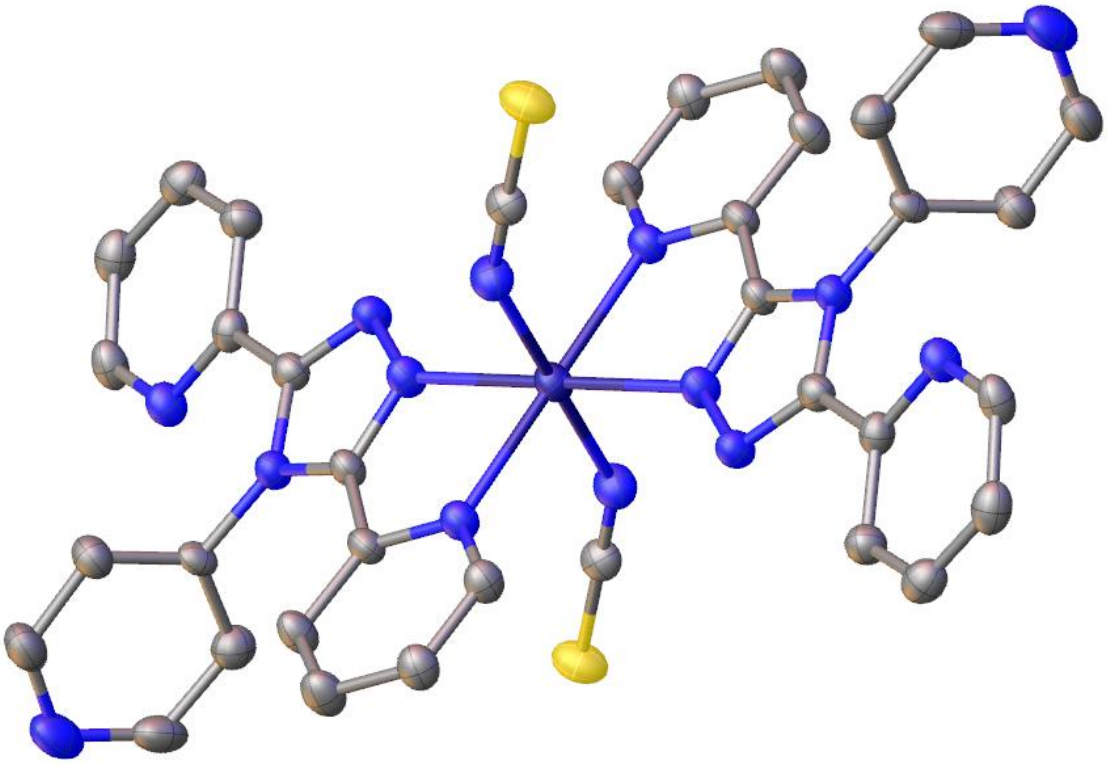

Figure 7.44. A symmetry expanded view of the crystallographic model of **42**. The anisotropic displacement parameters of all non-hydrogen atoms are shown at 50% probability. Hydrogens omitted for clarity.

The final refinement yielded a species with a Co(II) centre coordinated two copies of **5** in a bidentate fashion through N2 and N3, two iso-thiocyanates trans to one another. The bond lengths of the N_6 coordination sphere were investigated and ranged from 2.07 – 2.14 Å indicating a high spin state.

The packing of **42** displayed in figure 7.45, contains stacks of molecules with slight overlap forming along the 100 crystallographic direction. There are weak interactions in the form of hydrogen bonding in the structure, the first of these is from S1 to the hydrogen located on C4 on another metal complex at 2.9036(10) Å, the second set of interactions form with another metal complex through N1 and the hydrogen located on C17 at 2.484(3) Å.

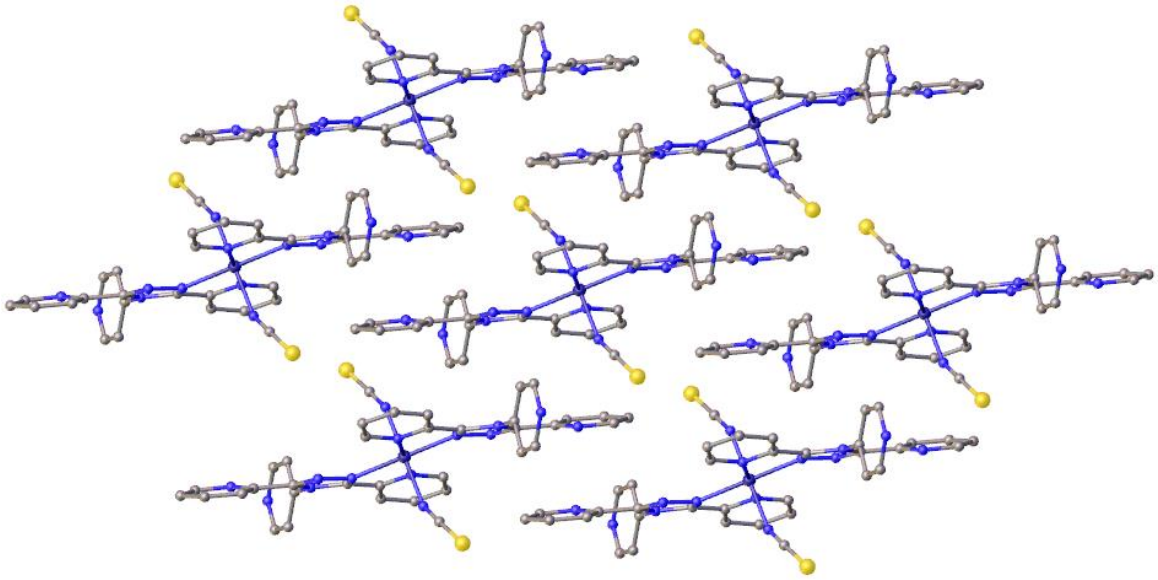

Figure 7.45. Image representing the packing of metal complexes in the crystal structure of **42**.

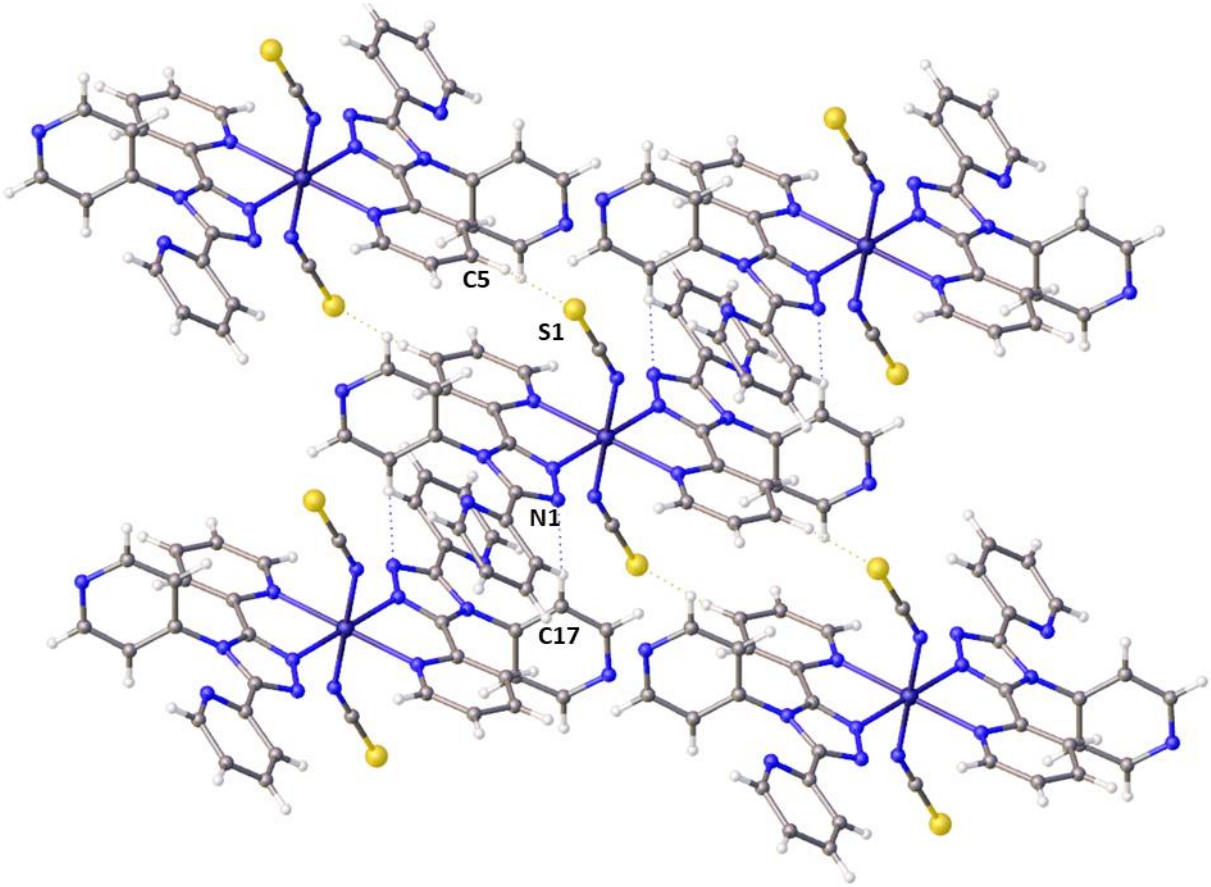

Figure 7.46. Image displaying the hydrogen bonding interactions present in the crystal structure of **42**.

There are also π-π interactions between uncoordinated 2-pyridyl rings on different metal complexes as displayed in figure 7.47, the centroid-centroid distance is 3.678(9) Å with a shift of 1.406(11) Å.

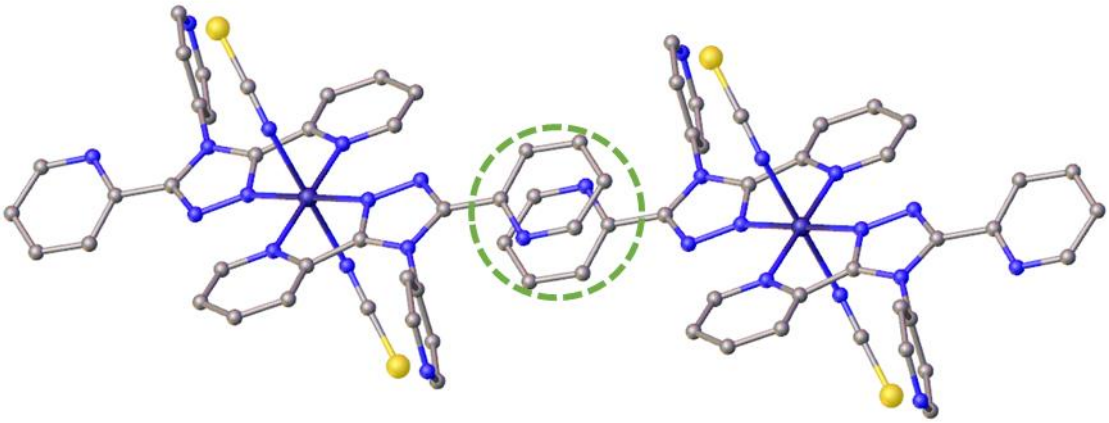

Figure 7.47. Image representing the π-π interactions present in the crystal structure of **42**.

In contrast to the iron metal complexes **24a** and **24b** discovered and discussed in chapter 5, the ligand **5** has coordinated to a metal bis-isothiocyanate salt without a rearrangement of the 4-pyridyl ring occurring. Experiments in attempts to force this rearrangement included heating of the sample and use of various other solvents, none of these further experimentations produced crystals of another structure.

Suitable single crystals of **43** were grown from a layered crystallisation, a methanol:water 1:1 solution containing cobalt(II) bis-isothiocyanate was injected slowly with a microlance needle under a methanol solution containing **1**. After a week crystals of an appropriate size had formed on the interface, these crystals were removed from the sample and placed into inert perfluoro poly ether oil, *Fomblin-YR 1800*, on a glass slide to allow manipulation and observation under a microscope. A pink block-shaped single was selected for analysis by SC-XRD.

Structure solution was performed by SHELXT via intrinsic phasing in the Olex2 GUI2 which confirmed a triclinic space group setting of *P*-1. The structure reached convergence as implied by a shift/ESD of 0.001. The minimum unaccounted electron density was -0.7 eÅ^{-3} and the maximum 0.4 eÅ^{-3} located near S1. The final refined structure was 97.6% complete to 0.83 Å, with an R_1 = 5.48% and wR_2 = 16.02% suggesting the data was of okay quality. The final refinement results are shown in figure 7.48.

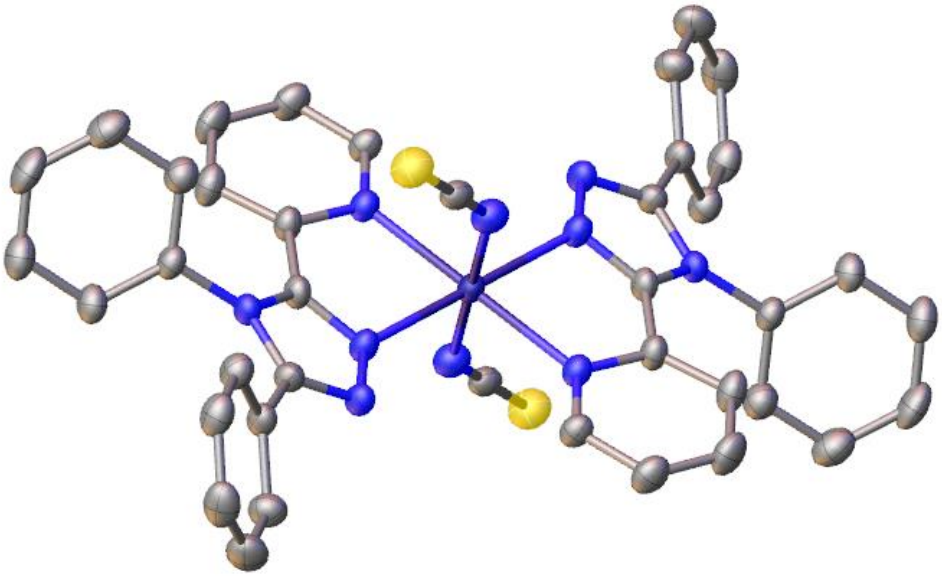

Figure 7.48. A symmetry expanded view of the crystallographic model of **43**. The anisotropic displacement parameters of all non-hydrogen atoms are shown at 50% probability. Hydrogens omitted for clarity.

The final refinement yield a Co(II) structure, the metal centre was coordinated to two copies of **1** in a bidentate fashion through nitrogen atoms N2 and N3, two isothiocyanates trans to one another. There is one methanol solvent molecule present in the structure. The N_6 coordination sphere was investigated for its bond lengths which ranged from 2.12 – 2.14 Å indicating a fully high spin state.

The crystal packing on this structure shown in figure 7.49, has layers of metal complex which have formed stacks. There are weak interactions in the form of hydrogen bonding in this structure as shown in figure 7.50, intramolecular between N1 and the hydrogen modelled to C13 at 2.591(2) Å and bonding between metal complex through N5 to the hydrogen on C4 at 2.579(3) Å.

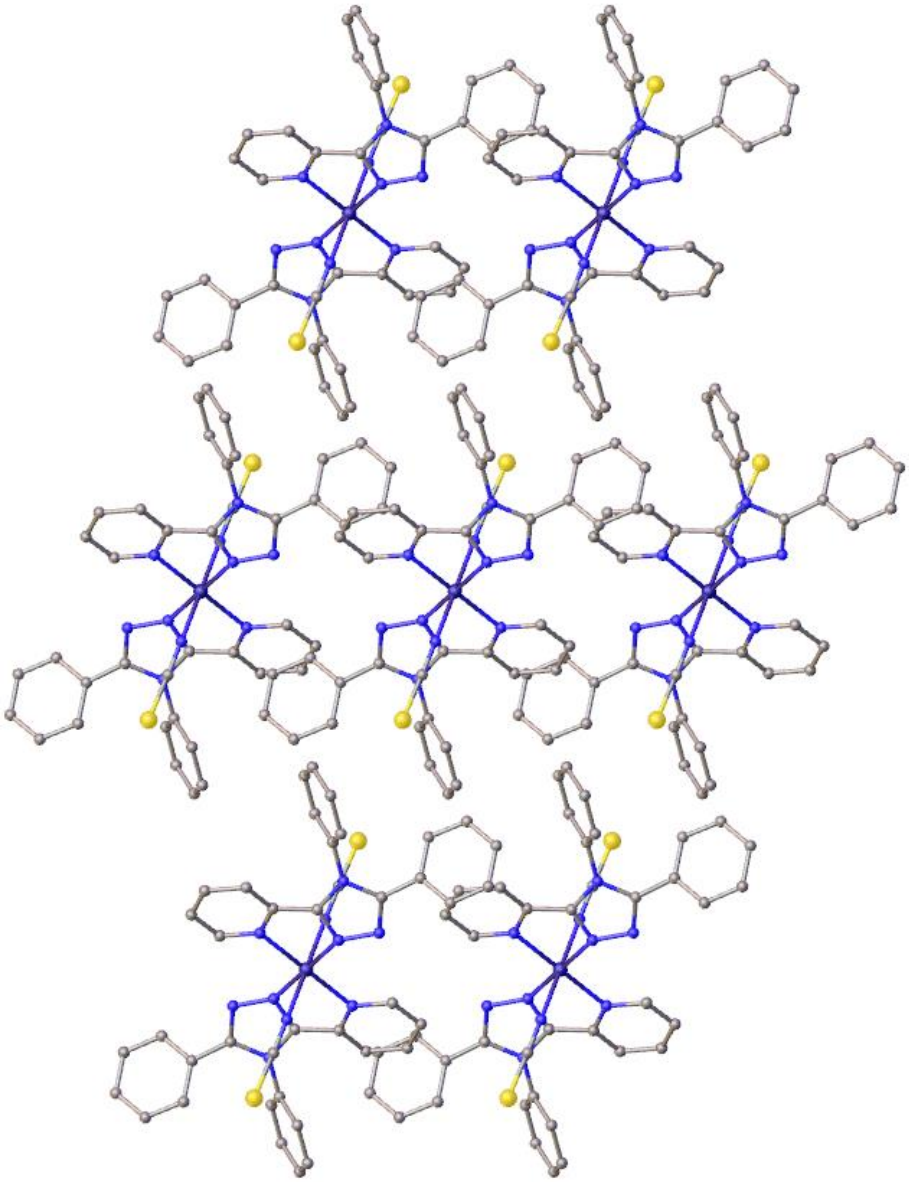

Figure 7.49. Image representing the packing of metal complexes in the crystal structure of **43**.

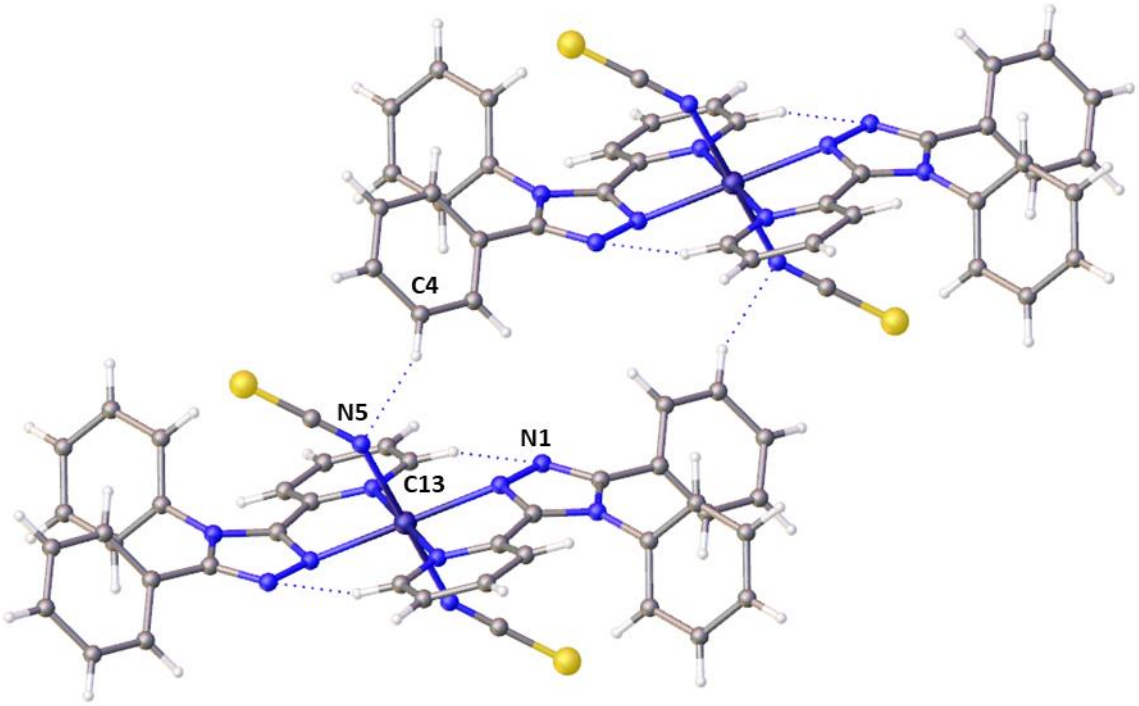

Figure 7.50. Image displaying the hydrogen bonding interactions present in the crystal structure of **43**.

Suitable single crystals of **44** were grown from a layered crystallisation, a methanol:water 1:1 solution containing cobalt(II) bis-isothiocyanate was injected slowly with a microlance needle under a methanol solution containing **4**. After a week crystals of an appropriate size had formed on the interface, these crystals were removed from the sample and placed into inert perfluoro poly ether oil, *Fomblin-YR 1800*, on a glass slide to allow manipulation and observation under a microscope. A pink block-shaped single was selected for analysis by SC-XRD.

Structure solution was performed by SHELXT via intrinsic phasing in the Olex2 GUI2 which confirmed an orthorhombic space group setting of *Pbca*. The structure reached convergence as implied by a shift/ESD of -0.001. The minimum unaccounted electron density was -0.3 $eÅ^{-3}$ and the maximum 0.3 $eÅ^{-3}$ located near S1. The final refined structure was 98.6% complete to 0.81 Å, with an R_1 = 4.26% and wR_2 = 11.43% suggesting the data was of good quality. The final refinement results are shown in figure 7.51.

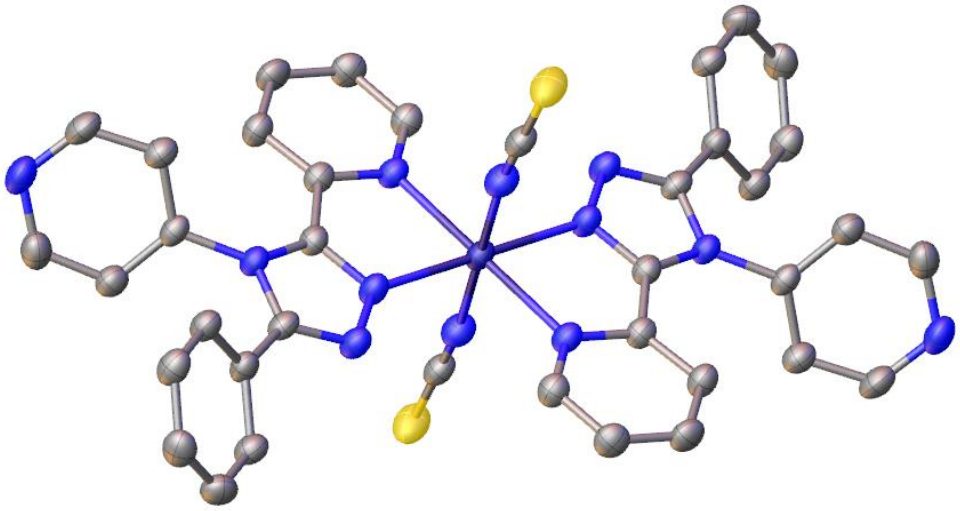

Figure 7.51. A symmetry expanded view of the crystallographic model of **44**. The anisotropic displacement parameters of all non-hydrogen atoms are shown at 50% probability. Hydrogens omitted for clarity.

The final refinement yielded a structure containing a Co(II) metal centre coordinated to two copies of **4** in a bidentate fashion through N2 and N3, two isothiocyanates trans to one another. The N_6 coordination sphere was investigated for it's bond lenghts which ranged from 2.07 – 2.16 Å indicating a fully high spin state.

Crystal packing of **44** shown in figure 7.52, shows reminiscent patterns to many of the previous structures with stacks of metal complexes form in the 100 crystallographic direction forming separate layers. There are weak interactions in the structure in the form of hydrogen bonding and π-π interactions. The first hydrogen bonding interaction occurs between S1 and the hydrogen modelled to C11 at 2.9181(8) Å, the next interaction is between N5 and C18 at 2,472(2) Å.

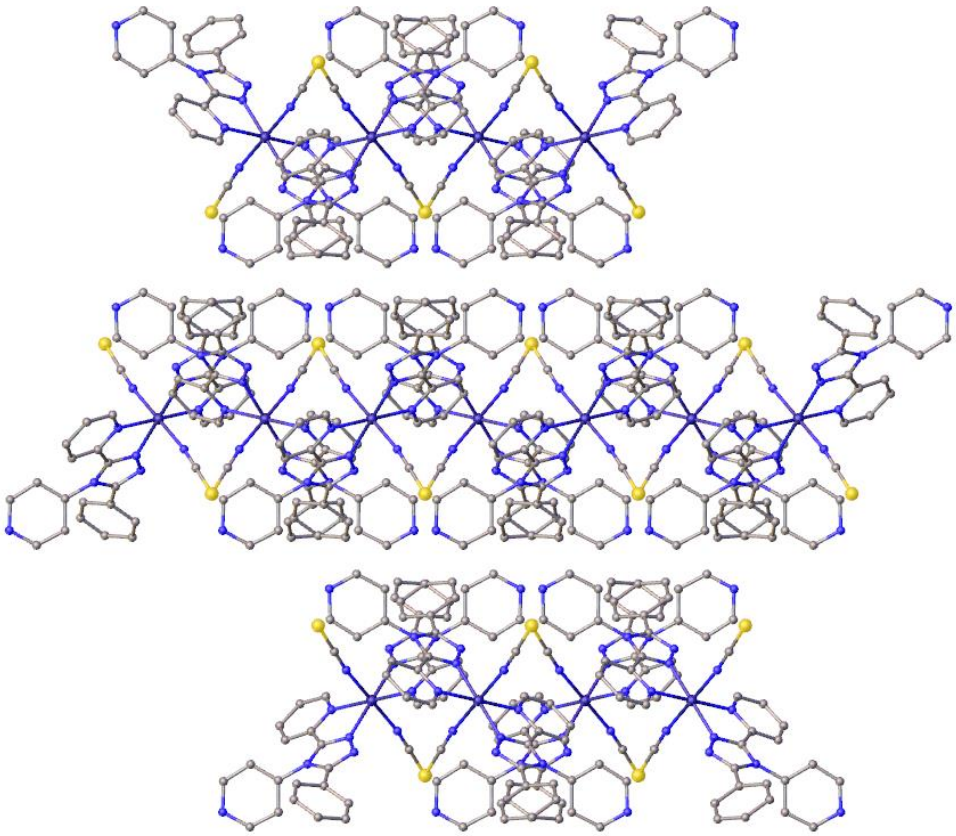

Figure 7.52. Image representing the packing of metal complexes present in the crystal structure of **44** viewed along the *b* axis.

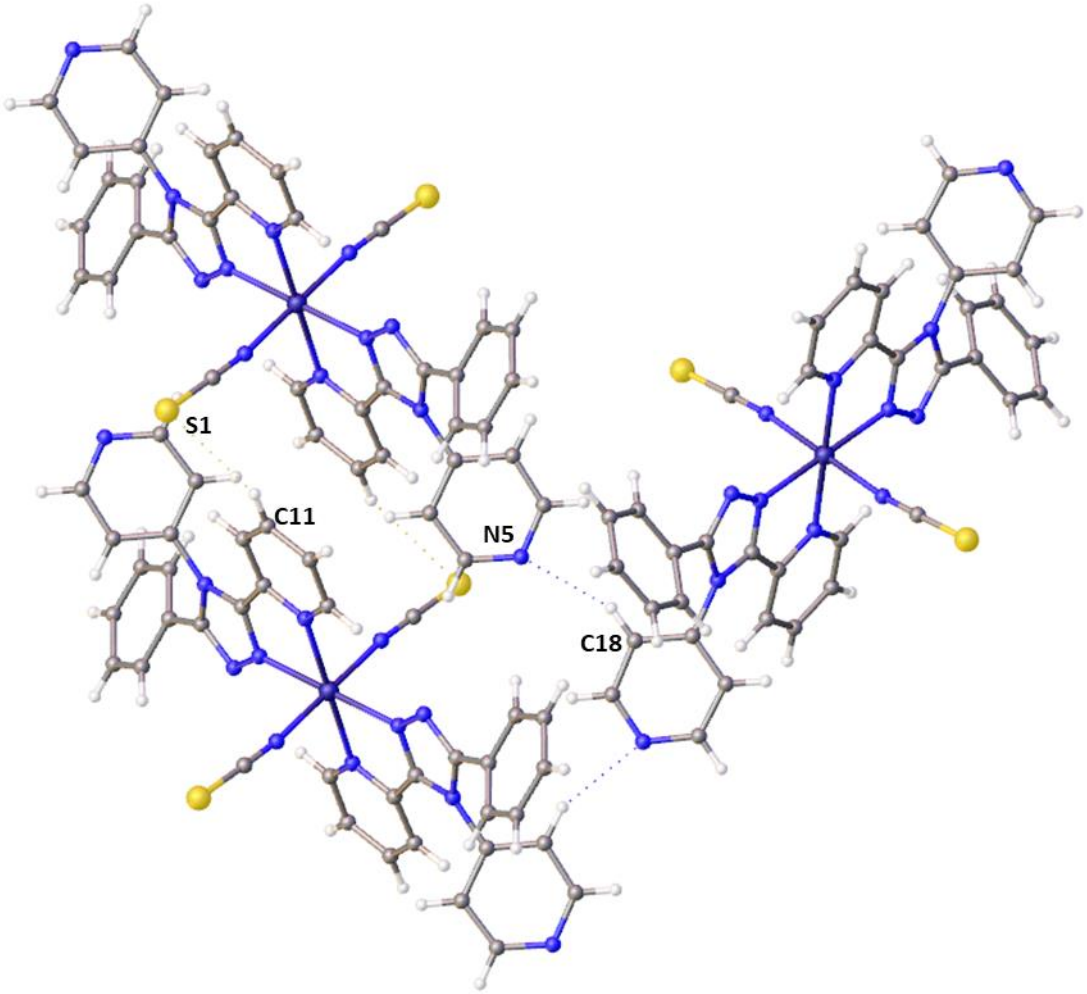

Figure 7.53. Image displaying the hydrogen bonding interactions present in the crystal structure of **44**.

The π-π interactions occur between the coordinated 2-pyridyl of one metal complex overlapping with the uncoordinated phenyl ring of another metal complex at 3.798 Å with a shift of 1.292 Å, see figure 7.54.

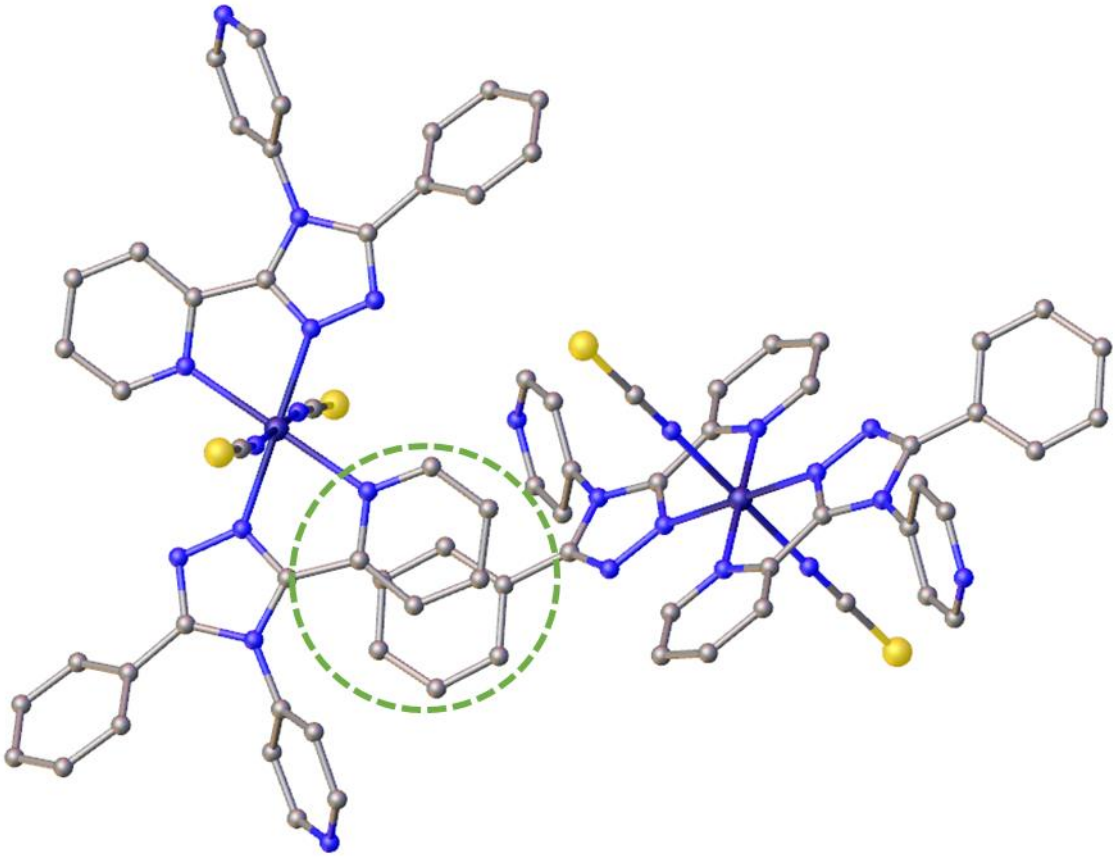

Figure 7.54. Image representing the π-π interactions present in the crystal structure of **44**.

Suitable single crystals of **45** were grown from a slow evaporation crystallisation, a methanol: containing manganese(II) nitrate and **16** was stirred for 1 hour before the addition of potassium hexafluorophosphate stirred for a further 4 h before being filtered and adding ventilation holes to the sample tube and left. After a several weeks nucleation was noted after another week crystals of an appropriate size had formed on the interface, these crystals were removed from the sample and placed into inert perfluoro poly ether oil, *Fomblin-YR 1800*, on a glass slide to allow manipulation and observation under a microscope. A pink plate-shaped single was selected for analysis by SC-XRD.

Structure solution was performed by SHELXT via intrinsic phasing in the Olex2 GUI2 which confirmed a triclinic space group setting of *P*-1. The structure reached convergence as implied by a shift/ESD of 0.001. The minimum unaccounted electron density was -0.5 eÅ^{-3} and the maximum 0.9 eÅ^{-3} located near the coordinated nitrate. The final refined structure was 99% complete to 0.81 Å, with an R_1 = 5.55% and wR_2 = 17.13% suggesting the data was okay quality.

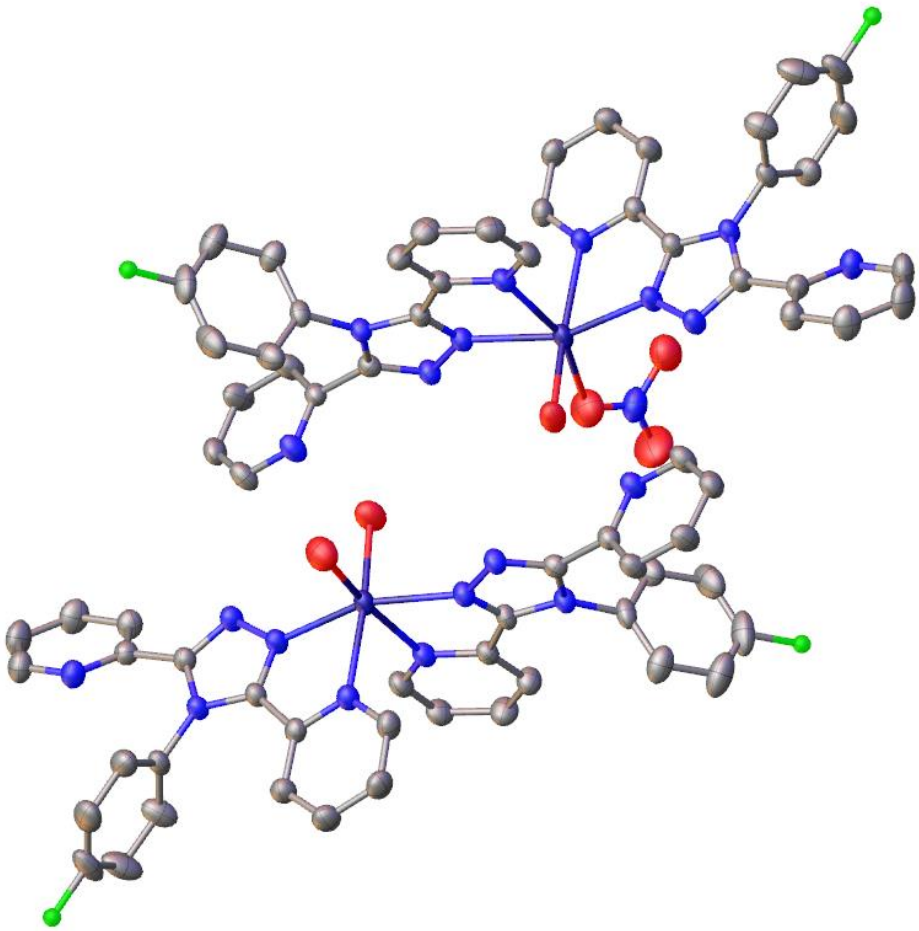

Figure 7.55. Image of the Crystallographic model of **45**. The anisotropic displacement parameters of all non-hydrogen atoms are shown at 50% probability. Hydrogens and counter ions omitted for clarity.

The final refinement results yielded a structure with two mononuclear units, each with a managanese(II) metal centre, the first of these metal ions to coordinated to two copies of **16** in a bidentate fashion through nitrogen atoms N2 and N3, it also has two coordinated water molecules in a cis configuration. The second manganese is coordinated to two copies of **16** in the same manner and one water molecule cis to a coordinated nitrate. The crystal structure also contains an uncoordinated nitrate and water molecule alongside two hexafluorophosphate counter ions. The bond lengths of the N_4O_2 coordination spheres were investigated for their bond lengths which ranged from 2.13 – 2.29 Å for Mn1 and 2.13 – 2.33 Å for Mn2. Indicating both metal ions occupied a high spin state.

The packing of the structure displayed in figure 7.56, forms layers of metal complexes with the nitrate and water molecule between the two metal centres with the PF_6 counter ions separating the other layers of metal complexes.

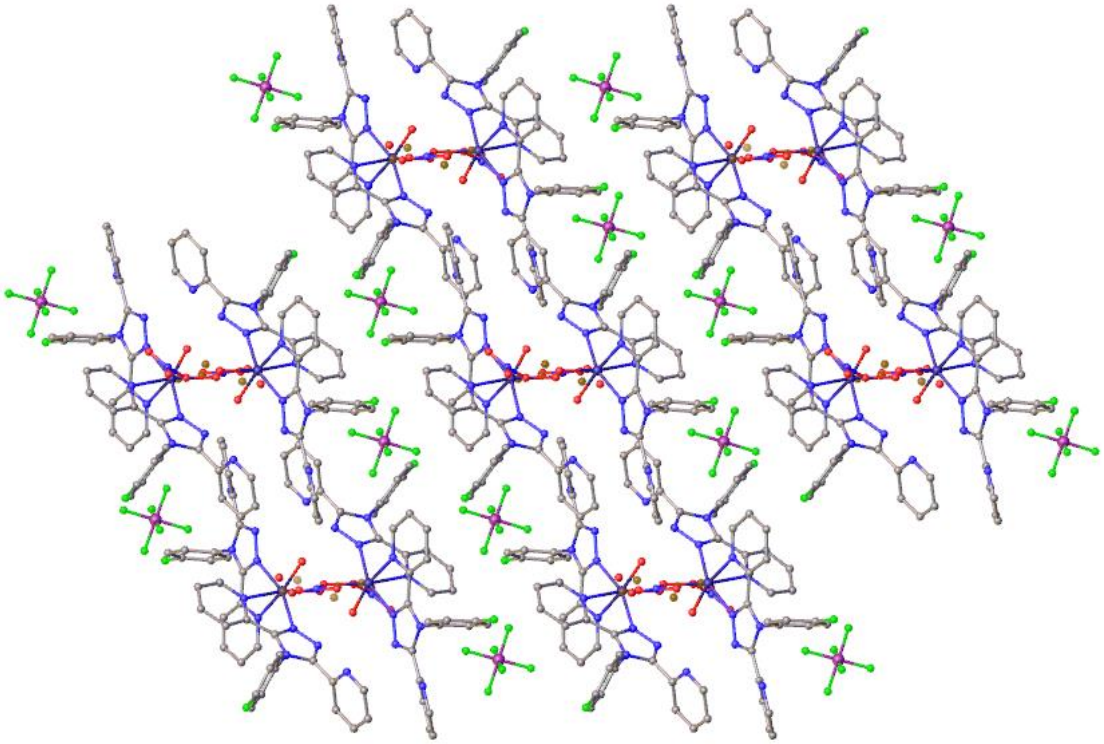

Figure 7.56. Image representing the packing of metal complexes, counter ions and solvent molecules present in the crystal structure of **45** viewed along the *a* axis.

There is vast number of weak interactions in the crystal structure in the form of hydrogen bonding shown in figure 7.60. The two metal complexes have hydrogen bonding between directly and via the water molecule. The direct hydrogen bonds are from N10 – O4 (2.031(2) Å), N11 – C30 (2.526(2) Å) and N20 – O6 (2.078(2) Å). There is then indirect hydrogen bonding through the uncoordinated water molecule between atoms O1 – O10 – O6 (2.270(3) and 2.361(3) Å). The free nitrate counter ion has 3 interactions with the hydrogen on O4 from O8, O9 and N22 (2.442(3), 2.084(3), 2.607(3) Å). Hydrogen bonding occurs between the layers of metal complexes through the PF_6 counter ions, C5 – F14 – C4 (2.519(2) and 2.508(2) Å) this same interaction occurs twice between the metal complexes as seen in figure 7.60.

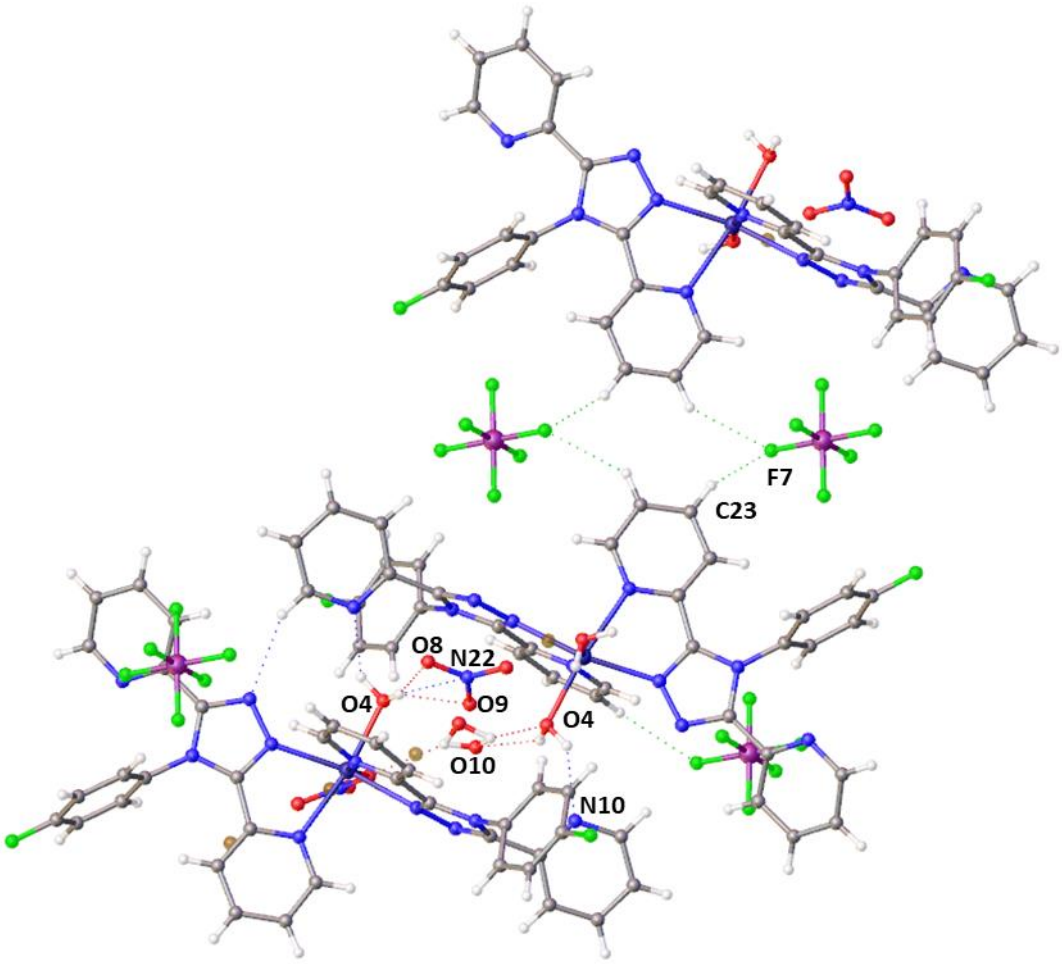

Figure 7.57. Image displaying the hydrogen bonding interactions present in the crystal structure of **45**.

The structure also displays π-π interactions, the overlap of both uncoordinated 2-pyridyl rings causes π-π interactions displayed in figure 7.58, the first 2-pyridyl ring (N10, C26-30) overlaps with its counterpart from another metal complex in the layer at 3.470(13) Å with a shift of 0.748(11) Å. The second 2-pyridyl (N20, C62-66) again overlaps with its counterpart from another metal complex in the layer at 3.518(9) Å and shift of 0.975(10) Å.

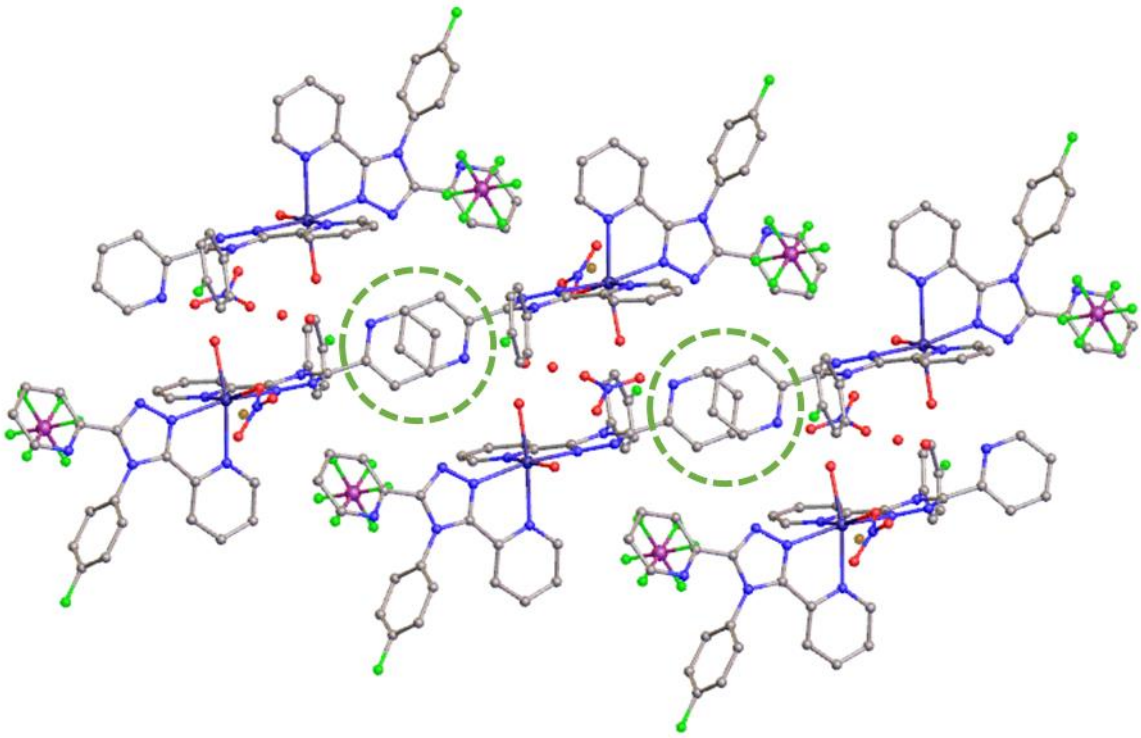

Figure 7.5855. Image representing the π-π interactions present in the crystal structure of **45**.

The final crystal structure discussed in this body of work is a structure identical to **45** with the exception of a change in counter ion. Suitable single crystals of **46** were grown from a slow evaporation crystallisation, a methanol: containing manganese(II) nitrate and **16** was stirred for 1 hour before the addition of sodium perchlorate stirred for a further 4 h before being filtered and adding ventilation holes to the sample tube and left. After a several weeks nucleation was noted after another week crystals of an appropriate size had formed on the interface, these crystals were removed from the sample and placed into inert perfluoro poly ether oil, *Fomblin-YR 1800*, on a glass slide to allow manipulation and observation under a microscope. A pink plate-shaped single was selected for analysis by SC-XRD.

Structure solution was performed by SHELXT via intrinsic phasing in the Olex2 GUI2 which confirmed a triclinic space group setting of *P*-1. The structure reached near convergence as implied by a shift/ESD of 0.010. The minimum unaccounted electron density was -1.2 eÅ^{-3} and the maximum 1.1 eÅ^{-3} located near one of the perchlorate counter ions. The final refined structure was 99% complete to 0.81 Å, with an R_1 = 7.78% and wR_2 = 23.72% suggesting the data was okay quality.

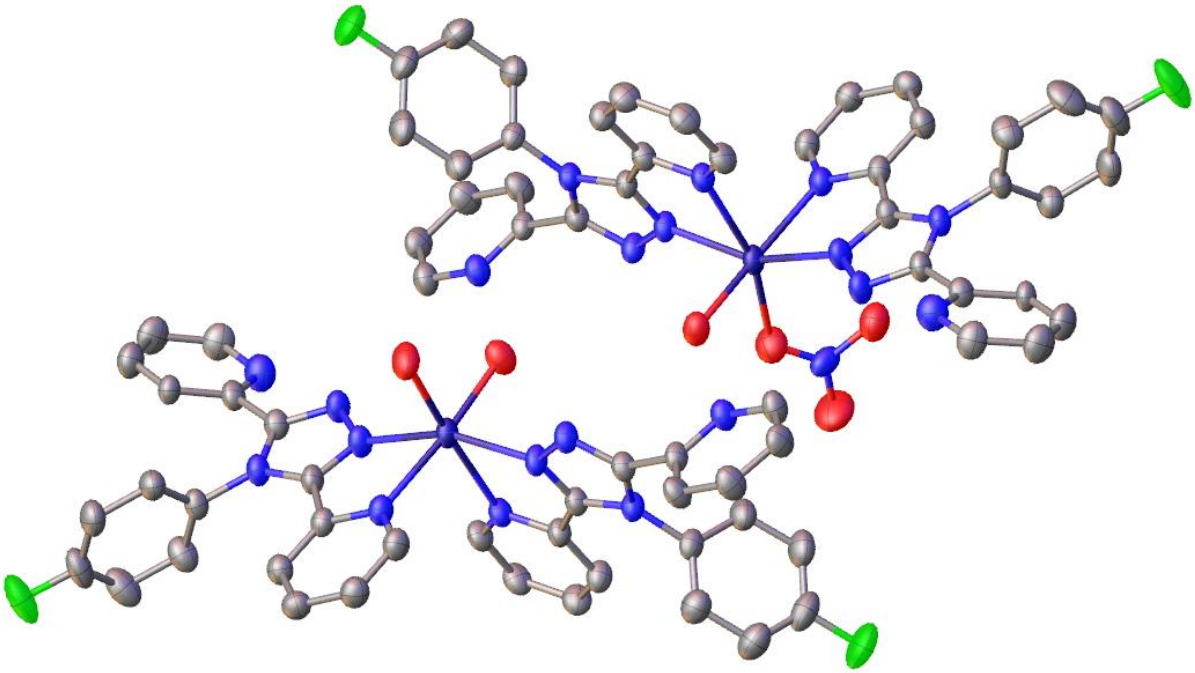

Figure 7.59. Image of the Crystallographic model of **46**. The anisotropic displacement parameters of all non-hydrogen atoms are shown at 50% probability. Hydrogens and counter ions omitted for clarity.

The final refinement displayed almost identical results to the previous structure **45**. Two manganese(II) metal centres, the first coordinated two **16** ligands in a bidentate fashion via nitrogen atoms N_2 and N_3, two water molecules are coordinated in a cis configuration. The second metal centre has two **16** ligands coordinated in the same manner, with one water molecule and one nitrate coordinated cis. There is one free water molecule in the structure and two perchlorate counter ions. The bond lengths of the N_4O_2 coordination spheres were investigated for their bond lengths which ranged from 2.15 – 2.30 Å for Mn1 and 2.13 – 2.34 Å for Mn2. Indicating both metal ions occupied a high spin state.

The packing of the structure as shown in figure 7.60, is almost identical to the previous structure with layers of metal complex form with some overlap, the uncoordinated water and nitrate molecules remain between the two units and the perchlorates in similar positions the hexafluorophosphate occupied on the outside between layers of metal complexes.

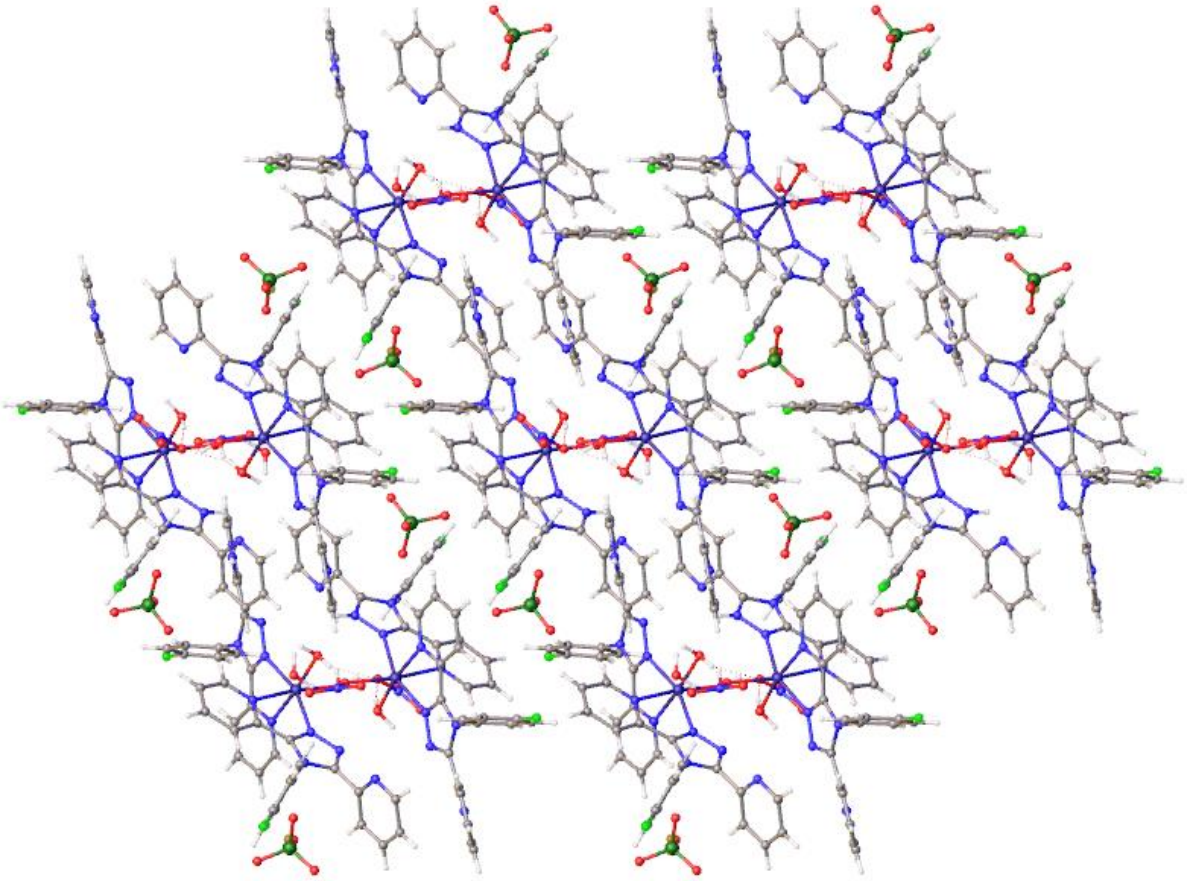

Figure 7.60. Image representing the packing of metal complexes, counter ions and solvent molecules present in the crystal structure of **46** viewed along the *a* axis.

There are weak interactions in the crystal structure in the form of hydrogen bonding, the first of these interactions are directly between metal complexes between N6 – C48 (2.619(3) Å) and N16 – C12 (2.495(3) Å). The second set of interactions are a series of interactions between the metal complexes through the nitrate between them, O1 and O2 both show interactions with the nitrate (O1 – O8, 1.865(3) Å and O2 – O7, 2.016(2) Å), the nitrate then has final interaction with the other metal complex (O6 – O7, 1,905(3) Å). There is a single interaction between one the metal complexes and a perchlorate counter ion, (C9 – O16, 2.566(4) Å) the final interaction is between a nitrate in a neighbouring cell and one of the metal complexes (C10 – O9, 2.463(3) Å and C11 – O9, 2.445(3) Å).

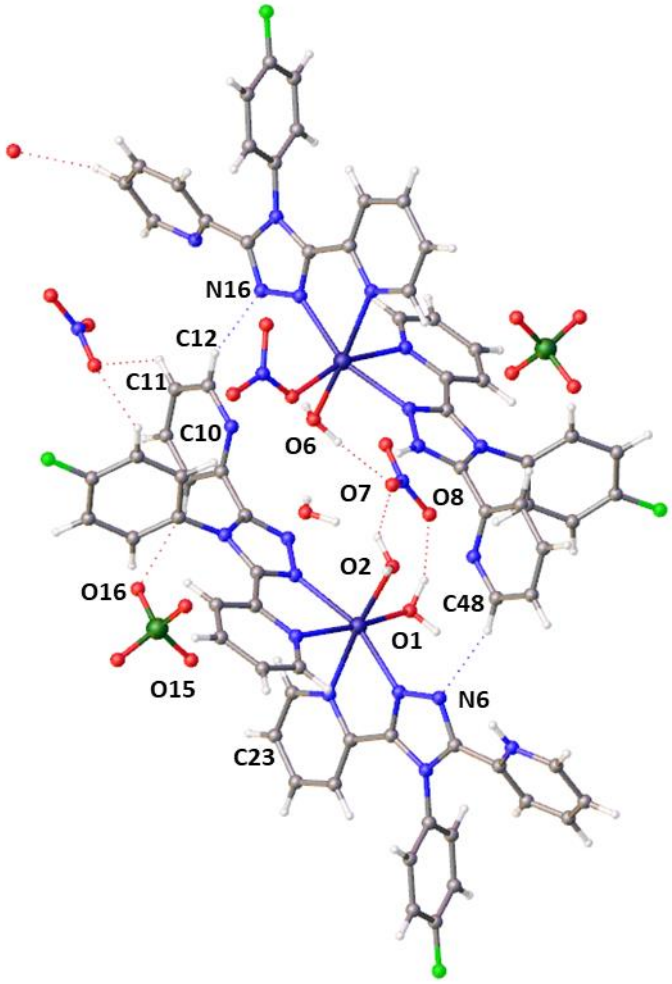

Figure 7.61. Image displaying the hydrogen bonding interactions present in the crystal structure of **46**.

There are also π-π interactions observed in the crystal structure for these systems similar to those in the structure of **45**, the first is the overlap of two uncoordinated 2-pyridyls (N5 C8-12) from different metal complexes overlapping at a 3.549(8) Å with a shift of 1.106(8) Å. The second case is the other uncoordinated 2-pyridyl (N15, C44-48) ring on the metal complex overlapping with its counterpart from a neighbouring cell at 3.470(7) Å with a shift of 0.851(10) Å.

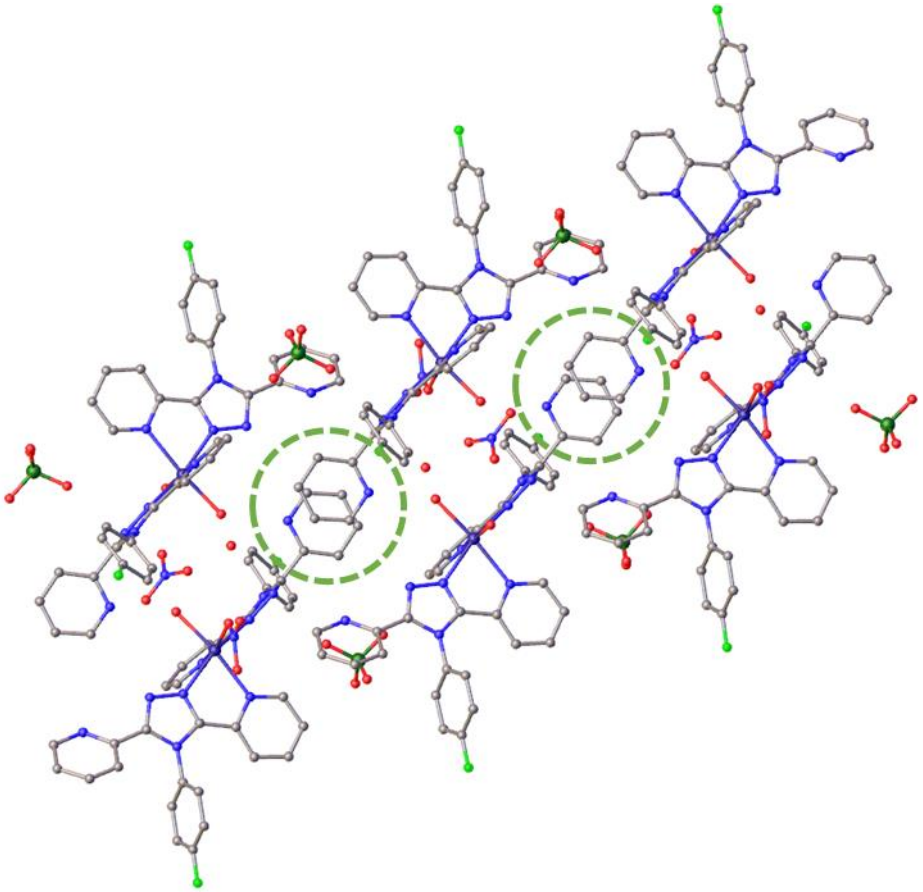

Figure 7.62. Image representing the π-π interactions present in the crystal structure of **46**.

Other than these 20 crystal structures discussed, various other novel crystal structures were observed however, due to issues such as low data quality they have not been presented and would need to be regrown and data recollected.

Of the 22 ligands synthesised, some did not produce crystals or appear to undergo coordination at all. These include the ligand **15**, this ligand was used in many coordination experiments, none of which produced single crystals of a metal complex. With the majority of other 1,2,4-triazoles used for this study, a colour change at interface in layered crystallisations was usually observed, in experiments with **15** this was never seen. Other experimental parameters which were utilised but never yielded concrete results include the use of $NCSe^-$ and $TCNQ^-$ as a counter ions.

7.5 Conclusion

This chapter has discussed the crystal structures for 19 new complexes that were generated during the course of study. Many of these new complexes contain ligands which were novel prepared for this thesis, the discussion of the synthesis of the 1,2,4-triazole ligands can be located in chapter 3. The crystal structures have been

investigated for their structural properties including their metal – ligand coordination sphere bond lengths, that can be used to determine the spin state of the metal complex. Some of these crystal structures had further measurements conducted on them in the form of variable temperature or high-pressure study. While it cannot be determined if any of the metal complexes discussed display SCO behaviour there are several promising candidates that require further study. These include compounds **32** and **33**, isomorphous structures of **23a** and **23b** respectively. Unfortunately, due to time constraints these systems were not able to be further characterised.

During the course of this study there were several notable observations. The first of these observations was the quick coordination and crystallisation of metal complexes containing Co(II) bis-isothiocyanate. During layered crystallisations often crystals useable for single crystal X-ray diffraction would appear within a few days, much quicker than their Fe(II) and Mn(II) counterparts which often took several weeks or evaporation of the solution to produce crystals of appropriate quality. This observation is apparent in this chapter with the large amount of Co(II) crystal structures obtained.

The samples were given a priority for further experimentation such as low temperature and high pressure. Higher priorities were awarded to Fe(II) structures due to this being the primary targeted metal ion for the research. Crystal structures containing coordination spheres of six nitrogen atoms were given higher priority. Crystal structures containing large amounts of hydrogen bonding and π-π interactions were given higher priority.

There are many more possible metal complexes to be generated with the library of 1,2,4-triazoles synthesised. Further coordination and crystallisation experiments are required to obtain these other metal complexes and fully explore the effects these ligands can have on SCO behaviour.

7.6 References

1. Bruker AXS Inc., Apex3, Bruker AXS Inc., Madison, Wisconsin, USA. *Bruker AXS Inc., Apex3, Bruker AXS Inc., Madison, Wisconsin, USA, 2015* (2015).

2. Sheldrick, G. M. SHELXT - Integrated space-group and crystal-structure determination. *Acta Crystallogr. Sect. A Found. Crystallogr.* **71**, 3–8 (2015).

3. Dolomanov, O. V, Bourhis, L. J., Gildea, R. J., Howard, J. A. K. & Puschmann, H. {\it OLEX2}: a complete structure solution, refinement and analysis program. *J. Appl. Crystallogr.* **42**, 339–341 (2009).

4. Sheldrick, G. M. Crystal structure refinement with SHELXL. *Acta Crystallogr. Sect. C Struct. Chem.* **71**, 3–8 (2015).

5. Piermarini, G. J., Block, S., Barnett, J. D. & Forman, R. A. Calibration of the pressure dependence of the R1 ruby fluorescence line to 195 kbar. *J. Appl. Phys.* **46**, 2774–2780 (1975).

6. Vargas, D. C., Salazar, S., Mora, J. R., Van Geem, K. M. & Almeida Streitwieser, D. Experimental and theoretical study of the thermal decomposition of ethyl acetate during fast pyrolysis. *Chem. Eng. Res. Des.* **157**, 153–161 (2020).

8 Conclusion and Future work

The primary aim of this project was to create and analyse metal complexes which displayed the phenomenon spin crossover. The first success in this study was the successful analysis of polymorph D of $[Fe(abpt)_2(NCS)_2]$ by high pressure revealing the possibility to access transitions not observed with variable temperature analysis. The second iron centre that does not undergo transition when the sample is cooled was successfully converted to the low spin state in pressures more than 15 kbar. This result demonstrates that there are states previously thought to be inaccessible for known compounds that can be accessed with advanced experimental techniques, modifying the physical conditions of the sample via such technologies as diamond anvil cells. This observation then opens the possibility of analysing old samples in the literature that could potentially lead to new applications. Following successes came in the form of **23a** and **25** two metal complexes generated from ligands synthesised in this body of work. Both systems display SCO behaviour, each paired with a unique attribute. **23a** indicates that a methanol solvent molecule in the structure plays a vital role leading to the belief that the transition between spin states is solvent mediated. The second system **25**, undergoes a migration of the 4-pyridyl in the ligand as seen in **24a**, **24b**.

The secondary aim was to explore the effects of adjusting the electronics of ligands on spin crossover complexes. Synthesising 1,2,4-tirazoles with a range of different substituents including fluorinated, methoxy and cyano - phenyl groups, and pyridines. These ligands were coordinated to various metal salts creating a range of metal complexes that could potentially display the spin crossover phenomenon when analysed by variable temperature single crystal X-ray diffraction. This study was highly successful, with a large number of metal complexes from various metal salts being generated. However, few displayed SCO behaviour and those that did were not able to be directly related to indicate the effects caused by different coordinated ligands, making conclusions based on the electronic influence of the ligands difficult to solidify.

The first of these systems **23a**, a Fe(II) system coordinated to isothiocyanate and **20**, displayed SCO behaviour when analysed by variable temperature SC-XRD. An analysis of unit cell parameters revealed a gradual transition centred around ~ 175 K. This system followed the formula $[Fe(X)_2(NCS)_2]$ (X = 1,2,4-triazole) after the successful work with polymorph D of $[Fe(abpt)_2(NCS)_2]$. Allowing comparisons to be made between the two, however the one other factor differentiating **23a** was the fact

the sample is a methanol solvate. This methanol molecule proves to be vital to the ability to undergo SCO, desolvating the sample generates **23b** which displays no SCO behaviour with variable temperature.

The indication that the SCO behaviour is solvent mediated is extremely interesting but makes direct comparisons to the four polymorphs of $[Fe(abpt)_2(NCS)_2]$ less impactful. The comparisons that can be made are the intermolecular interactions observed in the four polymorphs such as hydrogen bonding and π-π stacking are also observed in **23a**.

The other success **25**, while being a unique novel system suffers from similar issues. The complex displays SCO behaviour centred around a similar temperature ~185 K. The system undergoes a migration of the 4-pyridyl ligand from nitrogen atom N4 to N1 on the central triazole, like that observed in **24a** and **24b**. The ligand then coordinates through the nitrogen on the 4-pyridyl leading to a change in coordination motif. While this result is remarkable with both the migration and SCO being observed it means comparisons to **23a** are significantly different due a change in the coordination to the central metal ion leading to four ligands coordinating in a monodentate manner compared to the bidentate motif seen in the majority of the previous substituted triazole metal complexes.

8.2 Future work

Further to the detailed analyses highlighted in Chapters 2 – 6, many new organometallic species were generated throughout this work and are outlined in Chapter 7. All of these compounds had preliminary studies completed on their structures, analysed through SC-XRD. However, most of these compounds were not subjected to detailed variable temperature studies. This was principally due to time constraints and the prioritisation of work onto samples that appeared more likely to display SCO behaviour following initial structural investigation. Initial future work, resultant from this thesis, would involve further investigations into the various candidates for SCO from those structures realised but as yet not fully studied in Chapter 7. This work should be conducted to analyse variable temperature and pressure data collections, to determine if there are any further examples of interesting phenomena present in this library of compounds.

Furthermore, due to the impact of the global COVID 19 pandemic, it was not possible for the magnetic properties of the samples to be investigated, to detail their behaviour beyond structural characterisation. Originally these studies were planned through

collaborative work however this remained unrealised as restraints on travel and interactions outside of research bubbles remained in place over a large proportion of these studies. Given the interesting structural characteristics highlighted for several of the compounds formed during these studies the completion of the magnetic studies on these systems would be highly beneficial to supplement the work and the research literature.

The studies, for samples displaying interesting phenomena in this thesis, in particular compounds **23a** and **25**, were limited to variable temperature and pressure data. These systems would also benefit from exploration using light irradiation in the low spin states to observe if any metastable HS states i.e. if the systems additionally display the LIESST phenomena. An array of high-powered light emitting diodes was constructed using 3D printing to investigate this, but studies were curtailed due to limitations on laboratory time.

Finally, the results shown in this thesis indicate that the use of 1,2,4-triazole derivatives can indeed lead to new materials that display the SCO phenomena and there is a rich structural diversity that as yet remains unexplored for these systems. Therefore, the synthesis of new 1,2,4-triazoles derivatives should be considered an active avenue for future research to enable the increase the size of the library of these compounds and to further enable the impacts of minor structural modifications on the ligand backbone to the properties of the resultant materials' SCO behaviour.

9 Experimental

All reactions were carried out under a nitrogen atmosphere in glassware dried in the oven overnight (>75 °C) or under high vacuum by a heat-gun unless otherwise stated. Solvents were obtained anhydrous from Sigma or another appropriate chemical supplier and use as supplied.

Reagents were used as supplied unless otherwise stated.

Analytical thin layer chromatography (TLC) was performed using precoated aluminium or glass-backed plates (silica gel 60Å F_{254}) and visualised by UV radiation at 254 nm, or by staining with phosphomolybdic acid in ethanol or potassium permanganate in water.

All melting points were determined using a Gallenkamp melting point apparatus and are uncorrected.

Infrared spectra of solids were recorded using a Varian 800 FT-IR Scimitar Series spectrometer.

^{1}H NMR spectra were recorded in deutero solvent on Bruker Avance III 300, Bruker Avance II 400, Bruker Avance III HD 500 or Bruker Avance III HD 700 instruments and are reported as follows; chemical shift δ (ppm) (number of protons, multiplicity, coupling constant *J* (Hz), assignment). Residual protic solvent $CHCl_3$ (δ_H = 7.26) or DMSO (δ_H = 2.50) were used as the internal reference. ^{13}C NMR spectra were recorded using the central resonance of $CDCl_3$ (δ_C = 77.0 ppm) or DMSO (δ_C = 39.5 ppm) as the internal reference. All chemical shifts are quoted in parts per million relative to tetramethylsilane (δ_H = 0.00 ppm) and coupling constants are given in Hertz to the nearest 1 Hz. Assignment of spectra were carried out using COSY, HSQC, HMBC and NOESY experiments. Gas chromatography-mass spectra (EI) were obtained using a Thermo TRACE mass spectrometer. Electrospray mass spectra (ES) were obtained on a Micromass LCT mass spectrometer. High resolution mass spectra were obtained using a Thermo LTQ mass spectrometer (ES) at the University of Durham.

Single crystal X-ray diffraction experiments were carried out on a Bruker D8 Venture unless otherwise stated. Temperature control of the sample was controlled by an Oxford Cryosystems Cryostream cooling device for diffraction experiments between 100 – 400 K. Datasets below 100 K were conducted using an Oxford CryosystemsHeliX.[1,2] Both these devices utilise open-flow gas streams, the

Cryostream using nitrogen and the HeliX uses nitrogen or helium. The detector is a Bruker APEX-II CCD and is equipped with both a Cu-Kα (λ = 1.54178 Å) and a Ag-Kα (λ = 0.56086 Å) electron source.

Ultra-low temperature single crystal X-ray diffraction experiments were carried out on XIPHOS I. A custom-built diffractometer for ultra-low temperature studies, it is equipped with a Bruker Mo-Kα (λ = 0.71073 Å) source. Temperature control of the sample is monitored by a lakeshore 340 controller and a Lakeshore DT-470-CO-13 diode inside the cold head and cooled by a modified APD 202E displex. It is equipped with a Bruker APEX II CCD area detector.

High-Pressure single crystal X-ray diffraction experiments were carried out on XIPHOS II. A custom-built diffractometer for high pressure studies, it is equipped with a Incoatec Ag-Kα (λ = 0.56086 Å) ImS source and has no cooling device. Equipped with a Bruker APEX II CCD area detector.

General procedure

A round bottom flask was charged with a carboimidothioate and 1.2 equivalence of a hydrazide in BuOH, the solution was refluxed at 130 ˚C for 48h. The solution was cooled to room temperature before left at -4 ˚C for 48 h before the 1,2,4-triazole precipitated from the solution. This precipitate was washed with diethyl ether before being air dried. Compounds **1** – **9** (1,2,4-triazoles reported previously in the literature) were prepared using this method and analysed by ^{1}H NMR to verify the successful synthesis of the product.

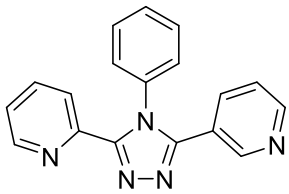

2-(4-phenyl-5-(pyridine-3-yl)-4*H*-1,2,4-triazol-3-yl)pyridine (10)

A 25 ml round bottom flask was charged with ethyl (Z)-*N*-phenylpyridine-2-carbimidothioate (0.50 g, 2.07 mmol) and 1.2 eq nicotinohydrazide (0.34 g 2.48 mmol) with BuOH (20 ml), the solution was refluxed at 130 ˚C for 48 h. The solution was cooled to -4˚C for 3 days before the title compounded precipitated from the solution affording a pale yellow solid (1.98 g, 0.66 mmol 32%); m.p. 200-202 °C; υ_{max} (ATR) 1584, 1567, 1496, 1442, 1458, 1396, 1169, 973, 774, 705, 604, 409 cm^{-1}; δ_H (300

MHz, $CDCl_3$); 8.64 (1H, dd, Ar-H), 8.59 (1H, dd, Ar-H), 8.33 (1H, dq, Ar-H), 8.14 (1H, dt, Ar-H), 7.79 (2H, qd, Ar-H), 7.43 (4H, m, Ar-H), 7.25 (3H, m, Ar-H), δ_C (300 MHz, $CDCl_3$) 150.53 (Ar-C), 149.11 (Ar-C), 136.68 (Ar-C), 136.02 (Ar-C), 129.49 (Ar-C), 127.90 (Ar-C), 124.33 (Ar-C), 124.08 (Ar-C), 123.23 (Ar-C), quaternary carbon signals not observed ;*m/z* (300); HRMS (ES^+) Found MH^+, 300.1974 ($C_{18}H_{13}N_5$ requires 300.1965);

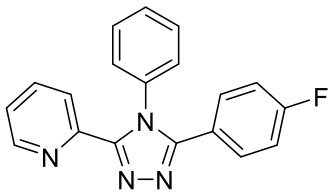

2-(5-(4-fluorophenyl)-4-phenyl-4*H*-1,2,4-triazol-3-yl)pyridine - 11

A 25 ml round bottom flask was charged with ethyl (Z)-*N*-phenylpyridine-2-carbimidothioate (0.50 g 2.05 mmol) and 1.2 eq 4-flurorbenzohydrazide (0.38 g 2.5 mmol) with BuOH (20 ml), the solution was refluxed at 130 ˚C for 48 h. The solution was cooled to -4˚C for 2 days before the title compounded precipitated from the solution affording a cream coloured powder (2.86 g, 0.9 mmol 44%); m.p. 238-239 °C; υ_{max} (ATR) 1603, 1526, 1497, 1468, 1450, 1228, 1160, 1096, 974, 843, 772, 691, 590, 406 cm^{-1}; δ_H (300 MHz, $CDCl_3$) 8.33 (1H, dq, Ar-H), 8.11 (1H, dt, Ar-H), 7.76 (1H, td, Ar-H), 7.41 (5H, m, Ar-H), 7.21 (3H, m, Ar-H), 6.98 (2H, t, Ar-H) ;δ_C (300 MHz, $CDCl_3$) 148.95 (Ar-C), 1461.61 (Ar-H), 130.95 (Ar-H), 130.83 (Ar-H), 129.26 (Ar-H), 128.00 (Ar-H), 124.32 (Ar-H), 123.91 (Ar-H), 115.79 (Ar-H), 115.50 (Ar-H) quaternary carbon signals not observed ; δ_f (300 MHz, $CDCl_3$) -110 (s); *m/z* (317); HRMS (ES^+) Found MH^+, 317.1384 ($C_{19}H_{13}FN_4$ requires 317.12);

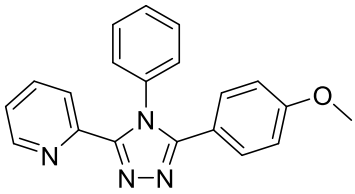

2-(5-(4-methoxyphenyl)-4-phenyl-4*H*-1,2,4-triazol-3-yl)pyridine - 12

A 25 ml round bottom flask was charged with ethyl (Z)-*N*-phenylpyridine-2-carbimidothioate (0.50 g 2.14 mmol) and 1.2 eq 3-methoxybenzohydrazide (0.42 g 2.55 mmol) with BuOH (20 ml), the solution was refluxed at 130 ˚C for 48 h. The solution was cooled to -4˚C for 3 days before the title compounded precipitated from the solution affording a pale yellow solid (0.20 g, 0.62 mmol 29%); m.p. 190-192 °C; υ_{max} (ATR) 1607, 1584, 1467, 1441, 1254, 1183, 1112, 1033, 832, 775, 696, 597, 534 cm^{-1}; δ_H (300 MHz, $CDCl_3$) ; 8.33 (1H, dt, Ar-H), 8.09 (1H, dt, Ar-H), 7.74 (2H, td, Ar-

H), 7.39 (6H, m, Ar-H), 7.22 (3H, m, Ar-H), 3.79 (3H, s, MeO-H), δ_C (300 MHz, $CDCl_3$)160.63 (Ar-C), 155.47 (Ar-C), 153.56 (Ar-C), 148.91 (Ar-C), 147.15 (Ar-C), 136.30 (Ar-C), 130.28 (Ar-C), 129.08 (Ar-C), 128.07 (Ar-C), 124.28 (Ar-C), 123.76 (Ar-C), 119.24 (Ar-C), 118.86 (Ar-C), 55.25 (MeO-C) quaternary carbon signals not observed;

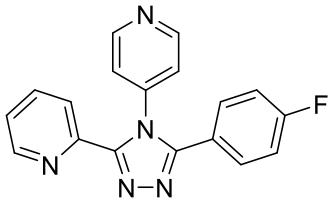

2-(5-(4-fluorophenyl)-4-(pyridine-4-yl)-4*H*-1,2,4-triazol-3-yl)pyridine - 13

A 25 ml round bottom flask was charged with ethyl (Z)-*N*-(pyridine-4-yl)lpyridine-2-carbimidothioate (0.52 g 2.16 mmol) and 1.2 eq 4-fluorobenzohydrazide (0.39 g 2.52 mmol) with BuOH (20 ml), the solution was refluxed at 130 ˚C for 48 h. The solution was cooled to -4˚C for 2 days before the title compounded precipitated from the solution affording pale brown solid (0.23 g, 0.69 mmol 32%); m.p. 195-196 °C; υ_{max} (ATR) 1604, 1567, 1505, 1466, 1239, 1157, 989, 841, 736, 596, 526, 405 cm^{-1}; δ_H (300 MHz, $CDCl_3$) 8.69 (2H, dd, Ar-H), 8.26 (2H, m, Ar-H), 7.80 (2H, m, Ar-H), 7.40 (2H, m, Ar-H) 7.09 (4H, m. (Ar-H); δ_C (300 MHz, $CDCl_3$) 151.12 (Ar-C), 148.79 (Ar-C), 143.71 (Ar-C), 136.96 (Ar-C), 131.10 (Ar-C), 130.98 (Ar-C), 129.33 (Ar-C), 129.21 (Ar-C), 124.34 (Ar-C), 124.14 (Ar-C), 122.85 (Ar-C), 116.15 (Ar-C), 115.96 (Ar-C), 115.86 (Ar-C), 115.67 (Ar-C) quaternary carbon signals not observed; δ_f (300 MHz, $CDCl_3$) -109.26 (s); *m/z* (ES) 318 (MH+); HRMS (ES) Found MH+, 318.1161 ($C_{18}H_{13}N_5F$ requires 318.1155);

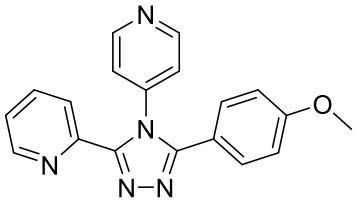

2-(5-(4-methoxyphenyl)-4-(pyridine-4-yl)-4*H*-1,2,4-triazol-3-yl)pyridine - 14

A 25 ml round bottom flask was charged with ethyl (Z)-*N*-(pyridine-4-yl)lpyridine-2-carbimidothioate (0.14 g 0.61 mmol) and 1.2 eq 4-methoxybenzohydrazide (0.12 g 0.72 mmol) with BuOH (20 ml), the solution was refluxed at 130 ˚C for 48 h. The solution was cooled to -4˚C for 2 days before the title compounded precipitated from the solution affording a pale yellow solid (0.06 g, 30%); m.p. 140-2 °C; υ_{max} (ATR) 1609, 1586, 1469, 1443, 1258, 1177, 1028, 988, 834, 739, 601, 539, 496, 410 cm^{-1};

δ_H (300 MHz, $CDCl_3$) 8.68 (1H, m, Ar-H), 8.28, (2H, m, Ar-H), 8.17 (1H, dd, Ar-H), 7.90 (1H, td, Ar-H), 7.80 (1H, td, Ar-H), 7.72 (1H, m, Ar-H), 7.33 (1H, m, Ar-H), 7.17 (1H, dd, Ar-H), 7.04 (1H, dd, Ar-H), 6.93 (1H, dd, Ar-H), 6.84 (1H, dd, Ar-H), 3.80 (3H, s, MeO-H);

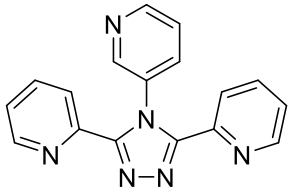

2,2'-(4-(pyridine-3-yl)-4*H*-1,2,4-triazole-3,5-diyl)dipyridine - 15

A 25 ml round bottom flask was charged with (Z)-*N*-(pyridine-3-yl)lpyridine-2-carbimidothioate (0.63 g 2.58 mmol) and 1.2 eq picolinohydrazide (0.44 g 3.22 mmol) with BuOH (20 ml), the solution was refluxed at 130 ˚C for 48 h. The solution was cooled to -4˚C for 2 days before the title compounded precipitated from the solution affording a bright yellow solid (0.11 g, 14%); m.p. 86-88 °C; υ_{max} (ATR) 1584, 1501, 1462, 1416, 1341, 1215, 1187, 993, 770, 728, 702, 616, 568, cm^{-1}; δ_H (300 MHz, $CDCl_3$) 8.96 (1H, d, Ar-H), 8.86 (1H, ddd, Ar-H), 8.77 (1H, dt, Ar-H), 8.58 (1H, dd, Ar-H), 8.52 (2H, dd, Ar-H), 7.91 (2H, td, Ar-H), 7.51 (2H, ddd, Ar-H), 7.40 (2H, dd, Ar-H); δ_C (300 MHz, $CDCl_3$) 147.21 (Ar-C), 146.67 (Ar-C), 144.39 (Ar-C), 137.68 (Ar-C), 129.46(Ar-C), 126.42 (Ar-C), 124.82 (Ar-C), 123.30(Ar-C) quaternary carbon signals not observed; *m/z* (ES) 301.1202; HRMS (ES) Found MH+, 301.1202 ($C_{17}H_{12}N_6$ requires 301.1202);

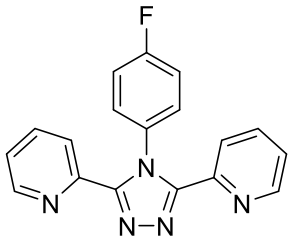

2,2'-(4-(4-fluorophenyl)-4*H*-1,2,4-triazole-3,5-diyl)dipyridine - 16

A 25 ml round bottom flask was charged with ethyl (Z)-*N*-(4-fluorophenyl)lpyridine-2-carbimidothioate (0.5087 g 1.95 mmol) and 1.2 eq picolinohydrazide (0.3293 g 2.4 mmol) with BuOH (20 ml), the solution was refluxed at 130 ˚C for 48 h. The solution was cooled to -4˚C for 2 days before the title compounded precipitated from the solution affording orange-brown solid (0.3285 g, 1.04 mmol 53%); m.p 144-156 °C; υ_{max} (ATR) 1585, 1512, 1462, 1430, 1221, 1167, 996, 844, 801, 621, 599, 403 cm^{-1}; δ_H (300 MHz, $CDCl_3$) 8.39 (2H, dq, Ar-H), 8.14 (2H, dt, Ar-H), 7.80 (2H, td, AR-H), 7.27(4H, m, Ar-H), 7.06 (2H, t, Ar-H); δ_C (300 MHz, $CDCl_3$) 163.96 (Ar-C), 160.67 (Ar-

C), 154.46 (Ar-C), 149.02 (Ar-C), 149.37 (Ar-C), 146.82 (Ar-C), 137.34 (Ar-C), 136.63 (Ar-C), 132,45 (Ar-C), 129.96 (Ar-C), 129.84 (Ar-C), 126.47 (Ar-C), 124.52 (Ar-C), 124.04 (Ar-C), 122.20 (Ar-C), 115.50 (Ar-C), 115.19 (Ar-C), some quaternary carbon signals not observed; δ_f (300 MHz, $CDCl_3$) -113 (s) ; *m/z* (318); HRMS (ES) Found MH+, 318.1140 ($C_{18}H_{12}FN_5$ requires 318.1155);

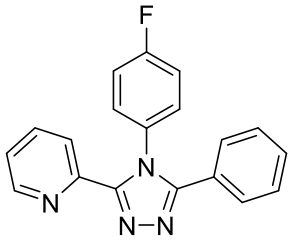

2-(4-(4-fluorophenyl)-5-phenyl-4*H*-1,2,4-triazole-3-yl)pyridine - 17

A 25 ml round bottom flask was charged with ethyl (Z)-*N*-(4-fluorophenyl)lpyridine-2-carbimidothioate (0.50 g 1.91 mmol) and 1.2 eq benzohydrazide (0.31 g 2.23 mmol) with BuOH (20 ml), the solution was refluxed at 130 ˚C for 48 h. The solution was cooled to -4˚C for 5 days before the title compounded precipitated from the solution affording orange-brown solid (0.24 g, 0.77 mmol 40%); m.p. 234-236 °C; υ_{max} (ATR) 1601, 1583, 1510, 1451, 1225, 1153, 844, 718, 694, 621, 520, 404 cm^{-1}; δ_H (300 MHz, $CDCl_3$) 8.34 (1H, dq, Ar-H), 8.17 (1H. dt, Ar-H), 7.78 (1H, td, Ar-H), 7.45 (2H dd, Ar-H), 7.33 (3H, m, Ar-H), 7.22 (4H, m, Ar-H), 7.08 (2H, t, Ar-H); δ_C (300 MHz, $CDCl_3$) 148.86 (Ar-C), 136.70 (Ar-C), 129.86 (Ar-C), 128.88 (Ar-C), 128.51 (Ar-C), 125.35 (Ar-C), 123.96 (Ar-C), 116.30 (Ar-C), 116.00 (Ar-C) quaternary carbon signals not observed; δ_f (300 MHz, $CDCl_3$) 114.44 (s); *m/z* (317); HRMS (ES) Found MH+, 317.1212 ($C_{19}H_{14}N_4F$ requires 317.1202);

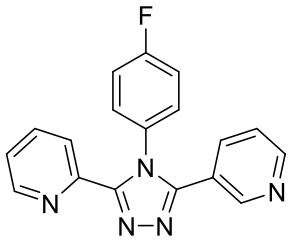

2-(4-(4-fluorophenyl)-5-(pyridin-3-yl)-4*H*-1,2,4-triazole-3-yl)pyridine – 18

A 50 ml round bottom flask was charged with ethyl (Z)-*N*-(4-fluorophenyl)lpyridine-2-carbimidothioate (0.48 g 1.85 mmol) and 1.2 eq nicotinohydrazide (0.30 g 2.22 mmol) with BuOH (35 ml), the solution was refluxed at 130 ˚C for 48 h. The solution was cooled to -4˚C for 2 days before the title compounded precipitated from the solution affording orange-brown solid (0.17 g, 0.52 mmol 28%); m.p.155-156 °C; υ_{max} (ATR) 1671, 1594, 1543, 1426, 1338, 1191, 951, 833, 705, 628, 418 cm^{-1}; δ_H (300 MHz,

$CDCl_3$) 8.97 (1H, dd, Ar-H), 8.69 (1H, dd, Ar-H), 8.61 (1H, m, Ar-H), 8.36 (1H, m, Ar-H), 8.16 (1H, dt, Ar-H). 8.09, (1H, dt, Ar-H), 7.96, (1H, td, Ar-H), 7.77, (1H. dt, Ar-H), 7.51, (2H, m, Ar-H), 7.41, (1H, m, Ar-H), 7.28, (1H, t, Ar-H); δ_C (300 MHz, $CDCl_3$) 164.80 (Ar-C), 152.23 (Ar-C), 151.04 (Ar-C), 149.52 (Ar-C), 149.41 (Ar-C), 148.54 (Ar-C), 137.77 (Ar-C), 136.64 (Ar-C), 135.14 (Ar-C), 131.10 (Ar-C), 130.89 (Ar-C), 129.36 (Ar-C), 124.99 (Ar-C), 124.57 (Ar-C), 123.97 (Ar-C), 116.69 (Ar-C), 116.11 (Ar-C) some quaternary carbon signals not observed; δ_f (300 MHz, $CDCl_3$) -111.56 (s);

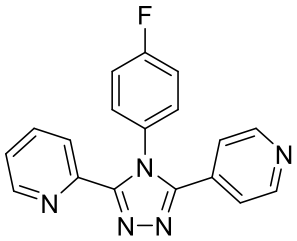

2-(4-(4-fluorophenyl)-5-(pyridin-4-yl)-4*H*-1,2,4-triazole-3-yl)pyridine - 19

A 20 ml round bottom flask was charged with ethyl (Z)-*N*-(4-fluorophenyl)lpyridine-2-carbimidothioate (0.48 g 1.85 mmol) and 1.2 eq nicotinohydrazide (0.31 g 2.21 mmol) with BuOH (20 ml), the solution was refluxed at 130 ˚C for 48 h. The solution was cooled to -4˚C for 2 days before the title compounded precipitated from the solution affording orange-brown solid (0.19 g, 0.61 mmol 33%); m.p. 161-163 °C; υ_{max} (ATR) 1664, 1553, 1512, 1412, 1333, 1222, 1142, 993, 846, 673, 605, 503, 404 cm^{-1}; δ_H (300 MHz, $CDCl_3$) 8.76 (1H, dd, Ar-H), 8.59 (2H, dd, Ar-H), 8.33 (1H, m, Ar-H), 8.20 (1H, dt, Ar-H), 7.80 (1H, td, Ar-H), 7.60 (1H, dd, Ar-H), 7.35 (2H, dd, Ar-H), 7.26 (2H, m, Ar-H), 7.15 (1H, m, Ar-H); δ_f (300 MHz, $CDCl_3$) -111.89 (s);

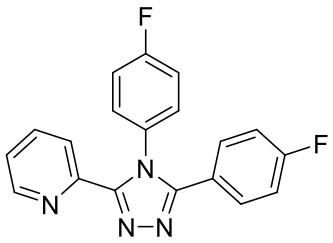

2-(4,5-bis(4-fluorophenyl)-4*H*-1,2,4-triazol-3-yl)pyridine - 20

A 25 ml round bottom flask was charged with ethyl (Z)-*N*-(4-fluorophenyl)lpyridine-2-carbimidothioate (0.52 g 2.00 mmol) and 1.2 eq 4-fluorobenzohydrazide (0.37 g 2.41 mmol) with BuOH (20 ml), the solution was refluxed at 130 ˚C for 48 h. The solution was cooled to -4˚C for 2 days before the title compounded precipitated from the solution affording orange-brown solid (0.43 g, 1.36 mmol 68%); m.p. 162-163 °C ; υ_{max} (ATR) 1651, 1602, 1510, 1451, 1227, 1159, 1001, 844, 536, 588, 406 cm^{-1}; δ_H (300 MHz, $CDCl_3$) 8.3 (1H, ddd, Ar-H), 8.16 (2H, dt, Ar-H), 7.78 (2H, m, Ar-H), 7.43 (2H, m,

Ar-H), 7.22 (2H, m, Ar-H), 7.10 (2H, m, Ar-H), 7.01 (2H, m, Ar-H ; δ_C (300 MHz, $CDCl_3$) 148.88 (Ar-C, 136.73 (Ar-C), 130.90(Ar-C), 129.91(Ar-C), 129.32 (Ar-C), 124.17 (Ar-C) quaternary carbon signals not observed;δ_f (300 MHz, $CDCl_3$) -111.18 s, -109.97 s ; *m/z* (ES) 335 (MH+) ; HRMS (ES) Found MH+,335.1111 ($C_{19}H_{13}N_4F_2$ requires 335.1108);

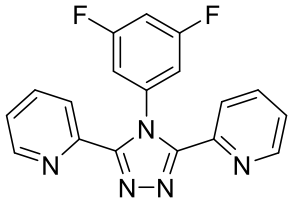

2,2'-(4-(3,5-difluorophenyl)-4*H*-1,2,4-triazole-3,5-diyl)dipyridine - 21

A 25 ml round bottom flask was charged with ethyl (Z)-*N*-(3,5-difluorophenyl)lpyridine-2-carbimidothioate (0.30 g 1.09 mmol) and 1.2 eq picolinohydrazide (0.21 g 1.53 mmol) with BuOH (20 ml), the solution was refluxed at 130 ˚C for 48 h. The solution was cooled to -4˚C for 2 days before the title compounded precipitated from the solution affording a brown solid (0.14 g, 0.43 mmol 39%); m.p. 230-232 °C; υ_{max} (ATR) 1608, 1483, 1348, 1235, 1125, 989, 848, 747, 677, 616, 541, 403 cm^{-1}; δ_H (300 MHz, $CDCl_3$) 8.41 (2H, dq, Ar-H), 8.30 (2H, dt, Ar-H), 7.86 (2H, td,Ar-H), 7.34 (1H dd, Ar-H), 7.32 (1H, dd, Ar-H), 6.92 (3H, m, Ar-H); δ_C (300 MHz, $CDCl_3$) 154.07 (Ar-C), 149.02 (Ar-C), 146.47 (Ar-C), 136.78 (Ar-C), 124.42 (Ar-C), 124,24 (Ar-C), 112.48 (Ar-C), 112.12 (Ar-C), 104.69 (Ar-C), 104.02 (Ar-C); δ_f (300 MHz, $CDCl_3$) -108 (s); *m/z* (336); HRMS (ES) Found MH+, 336.1061 ($C_{18}H_{12}N_5F_2$ requires 336.1061);

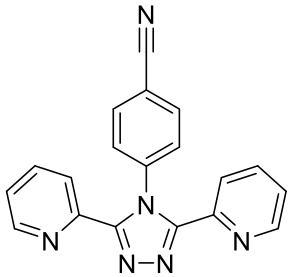

4-(3,5-di(pyridine-2-yl)-4*H*-1,2,4,-triazol-4-yl)benzonitrile - 22

A 25 ml round bottom flask was charged with ethyl (Z)-*N*-(4-cyanophenyl)lpyridine-2-carbimidothioate (0.16 g 0.59 mmol) and 1.2 eq picolinohydrazide (0.10 g 0.76 mmol) with BuOH (20 ml), the solution was refluxed at 130 ˚C for 48 h. The solution was cooled to -4˚C for 2 days before the title compounded precipitated from the solution affording a pale brown solid (0.10 g, 51%); m.p. 192-193 °C; υ_{max} (ATR) 2228 (CΞN), 1604, 1585, 1485, 1433, 1282, 1176, 1003, 853, 790, 740, 602, 405 cm^{-1}; δ_H (300 MHz, $CDCl_3$) 8.26 (4H, m, Ar-H), 7.80 (2H, td, Ar-H), 7.67 (2H, m, Ar-H), 7.39 (2H, d,

Ar-H), 7.25 (2H. m, Ar-H) ; δ_C (300 MHz, $CDCl_3$) 154.02 (Ar-C), 148.83 (Ar-C), 146.42 (Ar-C), 141.10 (Ar-C), 136.86 (Ar-C), 132.26 (Ar-C), 129.27 (Ar-C), 124.33 (Ar-C), 118.30 (Ar-C), 112.35 (CN-C); *m/z* (325) ; HRMS (ES) Found MH^+, 324.1207 ($C_{19}H_{12}N_6$ requires 324.1202);

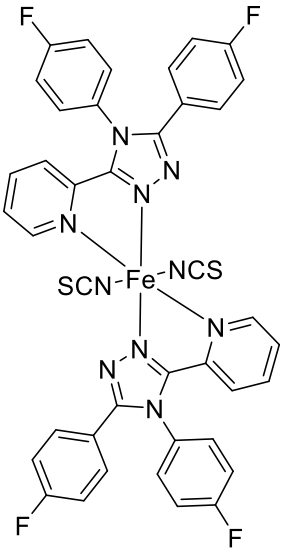

[Fe(2-(4,5-bis(4-fluorophenyl)-4H-1,2,4-triazol-3-yl)pyridine)$_2$(NCS)$_2$].MeOH – 23a

A methanol solution containing **20** (20 mg 0.006 mmol) was loaded into a sample vial, a methanol:water (1:1) solution containing iron(II) bis-isothiocyanate (0.003 mmol) was slowly injected using a microlance hypodermic needle and syringe under the clear ligand containing solution to avoid disruption of the interface. After several weeks red-orange single crystals had formed.

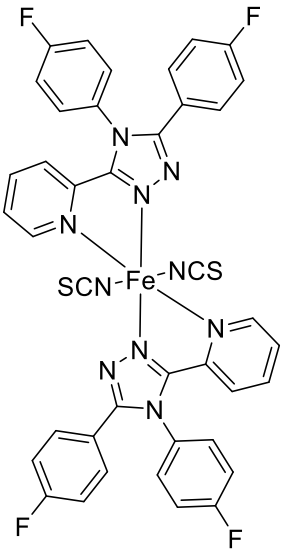

[Fe(2-(4,5-bis(4-fluorophenyl)-4H-1,2,4-triazol-3-yl)pyridine)$_2$(NCS)$_2$]– 23b

A methanol solution containing **20** (10 mg 0.003 mmol) and **7** (10 mg 0.003 mmol) and was loaded into a sample vial, a methanol:water (1:1) solution containing iron(II) bis-isothiocyanate (0.003 mmol) was slowly injected using a microlance hypodermic

needle and syringe under the clear ligand containing solution to avoid disruption of the interface. After several weeks dark red single crystals had formed.

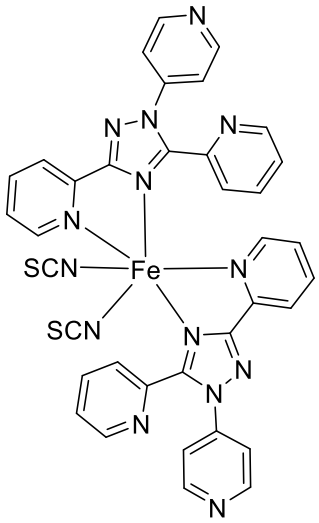

[Fe(2,2'-(1-(pyridine-4-yl)-1H-1,2,4-triazole-3,5-diyl)dipryrdine)$_2$(NCS)$_2$].H2O – 24a

A methanol solution containing **5** (20 mg 0.006 mmol) was loaded into a sample vial, a methanol:water (1:1) solution containing iron(II) bis-isothiocyanate (0.003 mmol) was slowly injected using a microlance hypodermic needle and syringe under the clear ligand containing solution to avoid disruption of the interface. After several weeks yellow plate single crystals had formed.

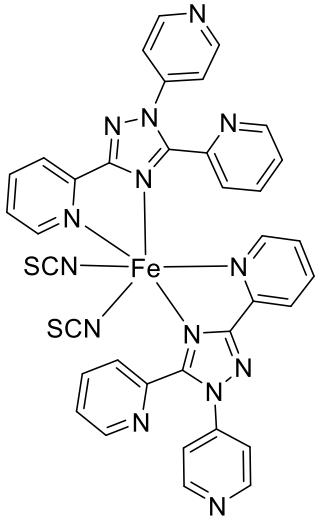

[Fe(2,2'-(1-(pyridine-4-yl)-1H-1,2,4-triazole-3,5-diyl)dipryrdine)$_2$(NCS)$_2$].MeOH – 24b

A methanol solution containing **5** (20 mg 0.006 mmol) was loaded into a sample vial, a methanol:water (1:1) solution containing iron(II) bis-isothiocyanate (0.003 mmol) was slowly injected using a microlance hypodermic needle and syringe under the ligand containing solution to avoid disruption of the interface. After several weeks red plate single crystals had formed.

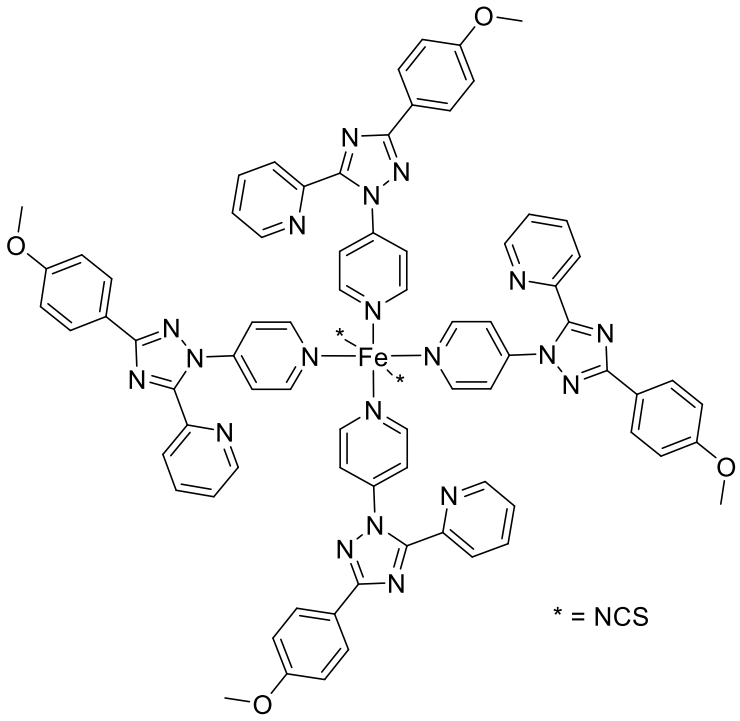

[Fe(2-(3-(4-methoxyphenyl)-1-(pyridine-4-yl)-1H-1,2,4-triazol-5-yl)pyridine)$_2$(NCS)$_2$] – 25

A methanol solution containing (40 mg 0.012 mmol) was loaded into a sample vial, the solution was heated at 50 °C for 1 hour. Before a heated (50 °C) methanol:water (1:1) solution containing iron(II) bis-isothiocyanate (0.003 mmol) was slowly injected using a microlance hypodermic needle and syringe under the clear ligand containing solution to avoid disruption of the interface. After several weeks no crystals had formed so ventilation holes were added to the sample vial and left for a further 3 weeks for single crystals to form.

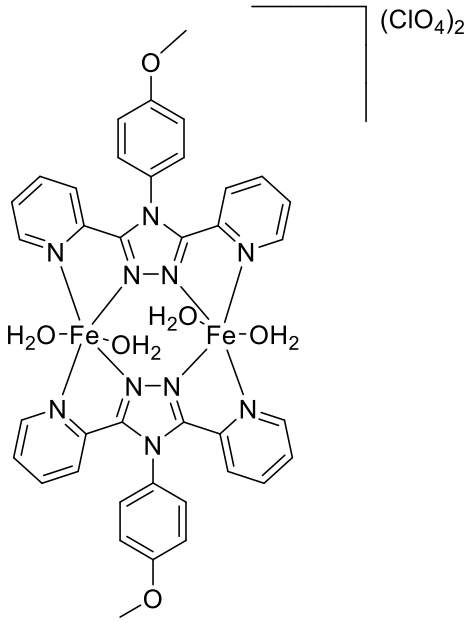

26

A sample vial was loaded with a methanol solution containing iron(II) perchlorate and ~3 equivalents of **8** and was stirred at room temperature for 2 h. Ventilation holes were added to the sample vial and left undisturbed. After three weeks single crystals of **26** were present.

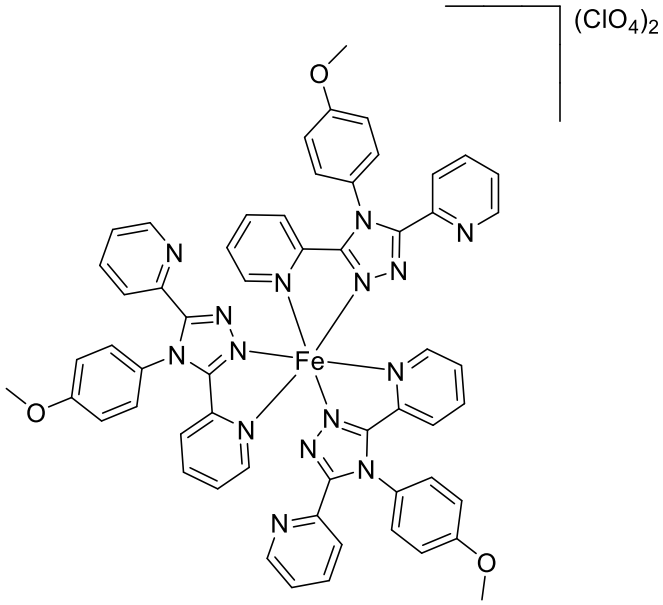

27

A sample vial was loaded with supersaturated methanol solution containing iron(II) perchlorate and ~4 equivalents of **8** and was stirred at room temperature for 2 h. Ventilation holes were added to the sample vial and left undisturbed. After three weeks single crystals of **27** were present.

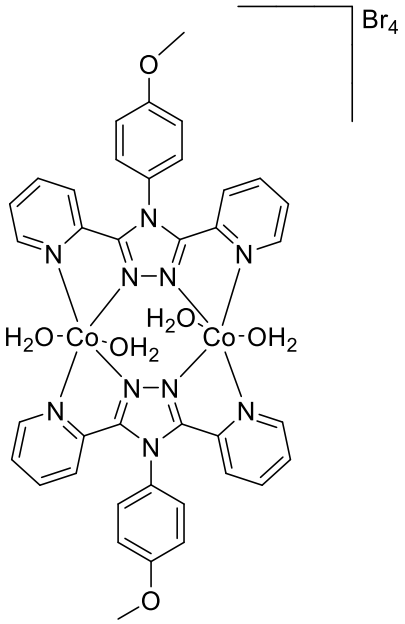

28

A sample vial was loaded with a methanol solution containing **8**, a methanol:water (1:1) solution containing cobalt(II) bromide was slowly injected using a microlance hypodermic needle and syringe under the ligand containing solution to avoid disruption of the interface. After two days, pink single crystals had formed at the interface.

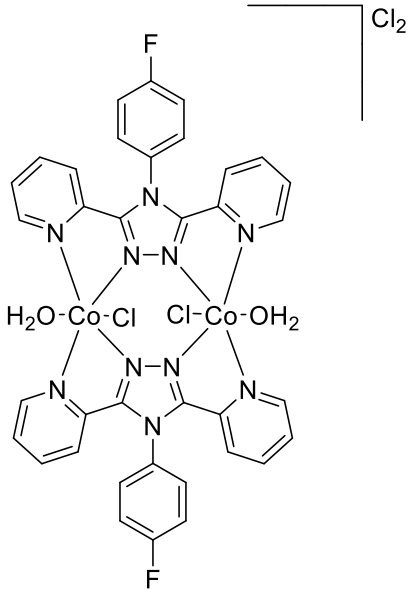

29

A sample vial was loaded with a methanol solution containing **16**, a methanol:water (1:1) solution containing cobalt(II) chloride was slowly injected using a microlance hypodermic needle and syringe under the ligand containing solution to avoid disruption of the interface. After five days, orange single crystals had formed at the interface.

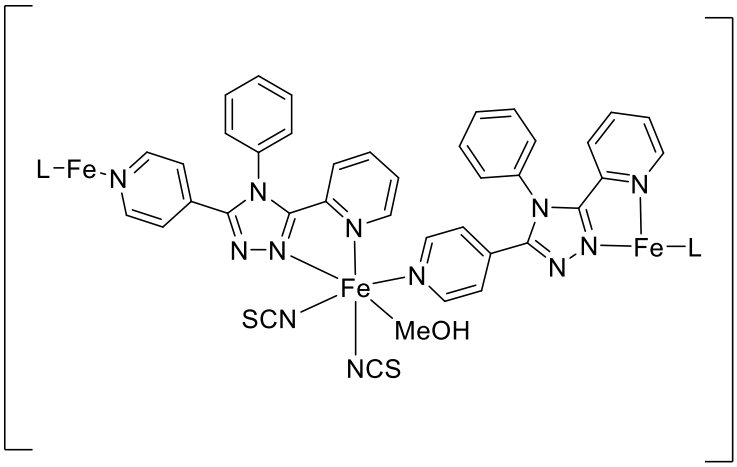

30

A sample vial was loaded with a methanol solution containing **3**, a methanol:water (1:1) solution containing cobalt(II) bis-isothiocyanate was slowly injected using a microlance hypodermic needle and syringe under the ligand containing solution to avoid disruption of the interface. After three days, pink single crystals had formed at the interface.

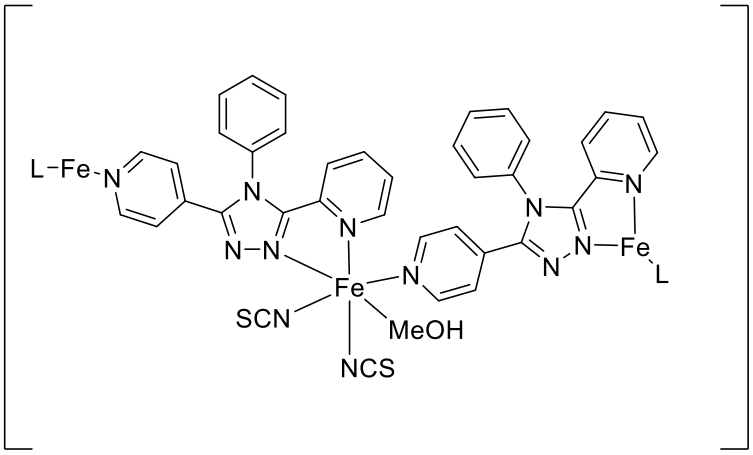

31

A sample vial was loaded with a methanol solution containing **3**, a methanol:water (1:1) solution containing cobalt(II) bis-isothiocyanate was slowly injected using a microlance hypodermic needle and syringe under the ligand containing solution to avoid disruption of the interface. After two weeks, red single crystals had formed at the interface.

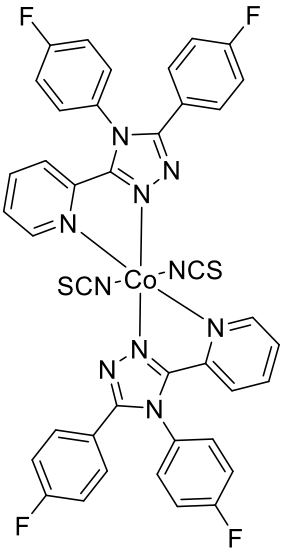

32

A methanol solution containing **20** (20 mg 0.006 mmol) was loaded into a sample vial, a methanol:water (1:1) solution containing cobalt(II) bis-isothiocyanate (0.003 mmol) was slowly injected using a microlance hypodermic needle and syringe under the clear ligand containing solution to avoid disruption of the interface. After a week red single crystals had formed.

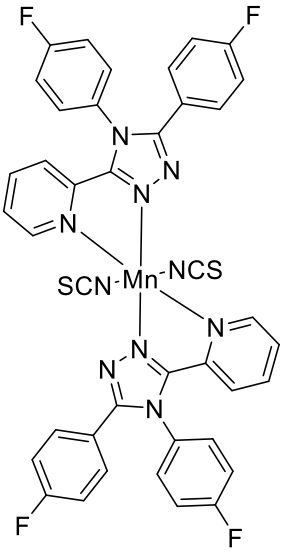

33

A methanol solution containing **20** (20 mg 0.006 mmol) was loaded into a sample vial, a methanol:water (1:1) solution containing manganese(II) bis-isothiocyanate (0.003 mmol) was slowly injected using a microlance hypodermic needle and syringe under the clear ligand containing solution to avoid disruption of the interface. After two weeks light pink single crystals had formed.

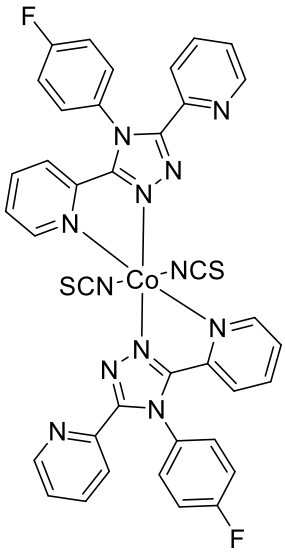

34

A methanol solution containing **16** was loaded into a sample vial, a methanol:water (1:1) solution containing cobalt(II) bis-isothiocyanate was slowly injected using a microlance hypodermic needle and syringe under the clear ligand containing solution to avoid disruption of the interface. After a week pink single crystals had formed.

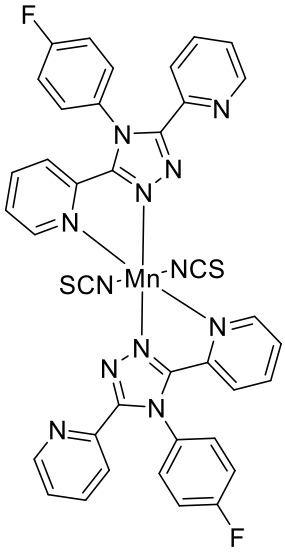

35

A methanol solution containing **20** (17 mg 0.010 mmol) was loaded into a sample vial, a methanol:water (1:1) solution containing manganese(II) bis-isothiocyanate (0.005 mmol) was slowly injected using a microlance hypodermic needle and syringe under the clear ligand containing solution to avoid disruption of the interface. After a week light clear single crystals had formed.

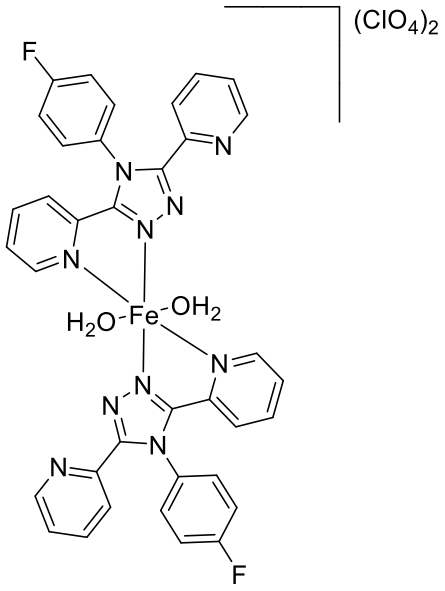

36

A sample vial was loaded with a saturated ethyl acetate solution containing iron(II) perchlorate and **16** was stirred for 5 hours at room temperature. Ventilation holes were added to the lid of the sample vial and left undisturbed for several weeks before single crystals were present in the vial.

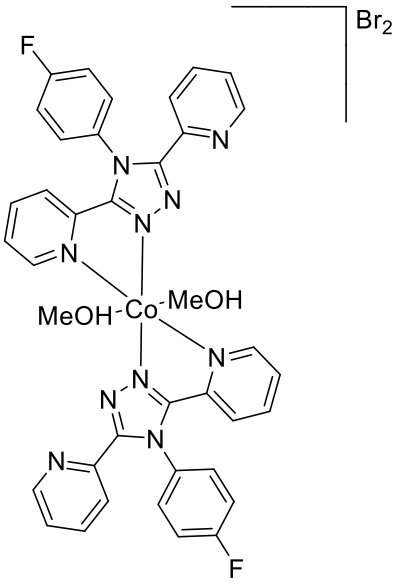

37

A sample vial was loaded with a saturated methanol solution containing cobalt(II) bromide and **16** was stirred for 5 hours at room temperature. Ventilation holes were added to the lid of the sample vial and left undisturbed for several weeks before pink single crystals were present in the vial.

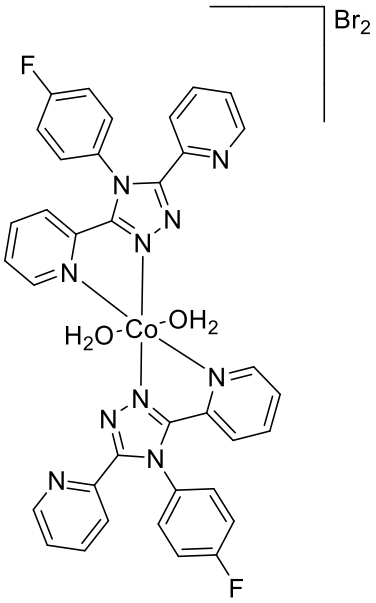

38

A ethanol solution containing **16** was loaded into a sample vial, an ethanol:water (1:1) solution containing cobalt(II) bromide was slowly injected using a microlance hypodermic needle and syringe under the clear ligand containing solution to avoid disruption of the interface. After a 4 days pink single crystals had formed.

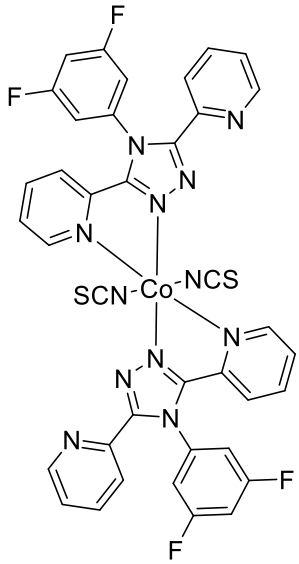

39

A methanol solution containing **21** was loaded into a sample vial, a methanol:water (1:1) solution containing colbat(II) bis-isothiocyanate was slowly injected using a microlance hypodermic needle and syringe under the clear ligand containing solution to avoid disruption of the interface. After 4 days single crystals had formed.

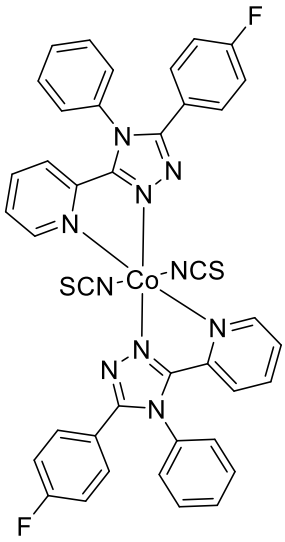

40

A methanol solution containing **11** was loaded into a sample vial, a methanol:water (1:1) solution containing colbat(II) bis-isothiocyanate was slowly injected using a microlance hypodermic needle and syringe under the clear ligand containing solution to avoid disruption of the interface. After a week single crystals had formed.

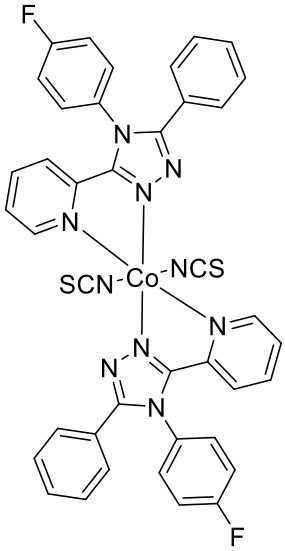

41

A methanol solution containing **17** was loaded into a sample vial, a methanol:water (1:1) solution containing colbat(II) bis-isothiocyanate was slowly injected using a microlance hypodermic needle and syringe under the clear ligand containing solution to avoid disruption of the interface. After 6 days pink single crystals had formed.

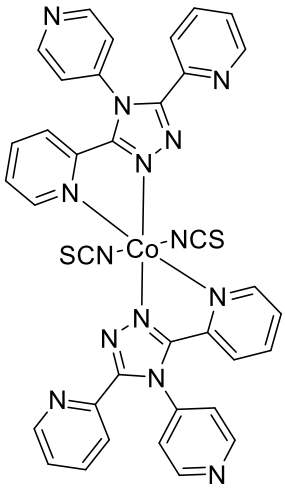

42

A methanol solution containing **5** was loaded into a sample vial, a methanol:water (1:1) solution containing colbat(II) bis-isothiocyanate was slowly injected using a microlance hypodermic needle and syringe under the clear ligand containing solution to avoid disruption of the interface. After 4 days single crystals had formed.

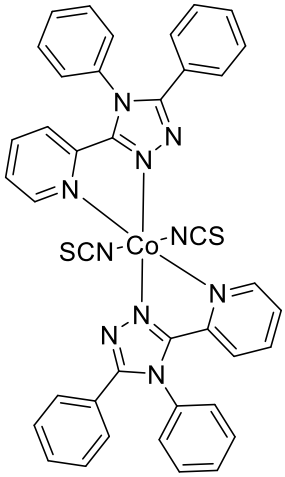

43

A methanol solution containing **1** was loaded into a sample vial, a methanol:water (1:1) solution containing colbat(II) bis-isothiocyanate was slowly injected using a microlance hypodermic needle and syringe under the clear ligand containing solution to avoid disruption of the interface. After a week single crystals had formed.

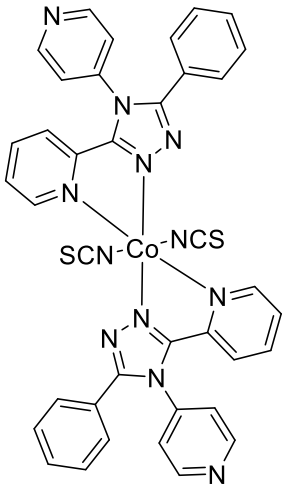

44

A methanol solution containing **4** was loaded into a sample vial, a methanol:water (1:1) solution containing colbat(II) bis-isothiocyanate was slowly injected using a microlance hypodermic needle and syringe under the clear ligand containing solution to avoid disruption of the interface. After a week pink single crystals had formed.

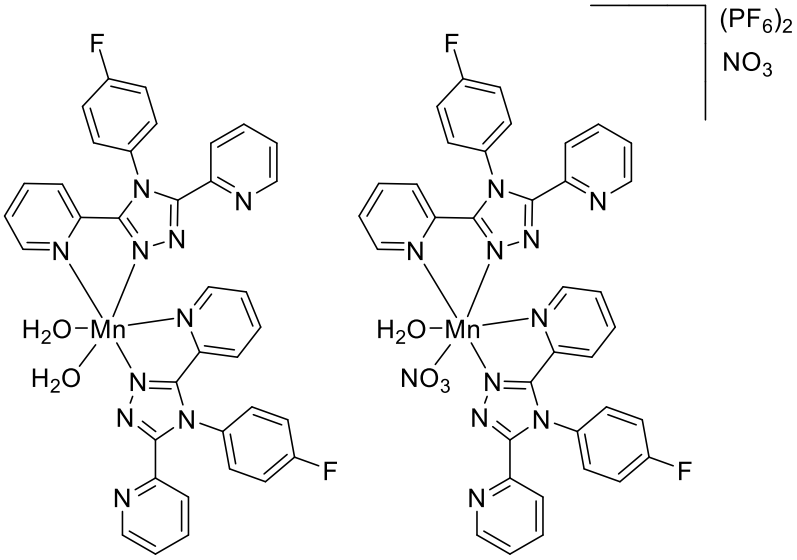

45

A 10 ml round bottom flask was loaded with 5 ml of methanol solution containing **16** (0.0663 g 0.21 mmol) and manganese(II) nitrate (0.019 g 0.07 mmol) and stirred for 1 hour. Potassium hexafluorophosphate (0.0258 g 0.14 mmol) was added to the solution and stirred at room temperature for a further 4 hours. The solution was filtered, before transferred to a sample vial with ventilation holes and left to evaporate for several weeks till clear single crystals had formed.

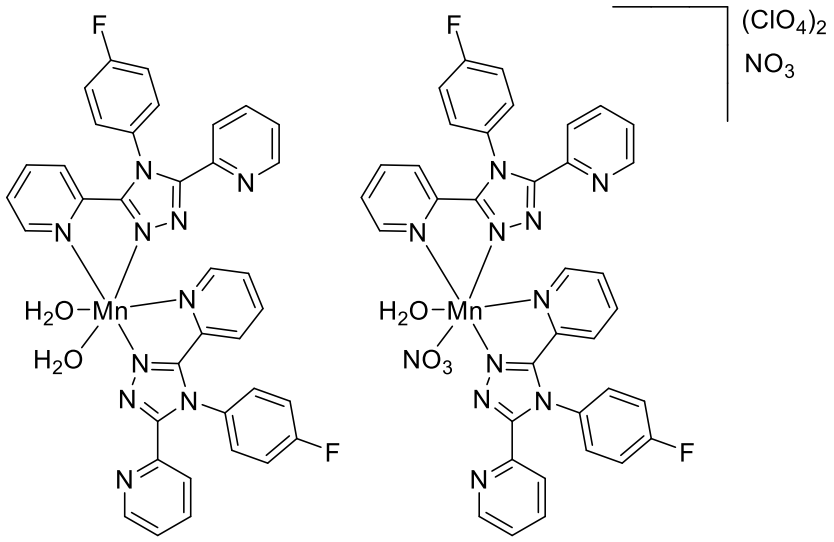

46

A 10 ml round bottom flask was loaded with 5 ml of methanol solution containing **16** (0.0659 g 0.20 mmol) and manganese(II) nitrate (0.019 g 0.007 mmol) and stirred for 1 hour. Sodium perchlorate (0.0171 g 0.14 mmol) was added to the solution and stirred at room temperature for a further 4 hours. The solution was filtered, before transferred to a sample vial with ventilation holes and left to evaporate for several weeks till clear single crystals had formed.

10. Appendix

Table 10.1. Crystal data and refinement table for Polymorph D high pressure experiments.

Identification code	**Ambient start**	**1.8(2) kbar**	**7.5(2) kbar**	**9.6(2) kbar**	**12.0(2) kbar**	**15.0(2) kbar**	**Ambient end**
Empirical formula	$C_{26}H_{20}N_{14}S_2Fe$	$C_{26}H_{20}N_{14}S_2Fe$	$C_{26}H_{20}N_{14}S_2Fe$	$C_{26}H_{20}N_{14}S_2Fe$	$C_{26}H_{20}FeN_{14}S_2$	$C_{26}H_{20}N_{14}S_2Fe$	$C_{26}H_{20}N_{14}S_2Fe$
Formula weight	648.53	648.53	648.53	648.53	648.53	648.53	648.53
Temperature/K	296.15	296.15	296.15	296.15	296.15	296.15	296.15
Crystal system	monoclinic	monoclinic	monoclinic	monoclinic	monoclinic	monoclinic	monoclinic
Space group	$P2_1/c$	$P2_1/c$	$P2_1/c$	$P2_1/c$	$P2_1/c$	$P2_1/c$	$P2_1/c$
a/Å	10.7819(15)	10.760(2)	10.7361(7)	10.6923(8)	10.6433(7)	10.4607(17)	10.777(2)
b/Å	15.870(4)	15.808(6)	15.4827(17)	15.3683(18)	15.3285(16)	15.203(4)	15.859(5)
c/Å	17.415(3)	17.253(4)	16.6888(11)	16.4865(12)	16.4392(11)	16.348(3)	17.450(5)
α/°	90	90	90	90	90	90	90
β/°	106.875(10)	106.721(12)	107.567(4)	107.682(4)	107.475(4)	105.886(11)	106.734(12)
γ/°	90	90	90	90	90	90	90
Volume/Å^3	2851.7(9)	2810.5(14)	2644.7(4)	2581.1(4)	2558.2(4)	2500.7(9)	2856.2(13)
Z	4	4	4	4	4	4	4
ρ_{calc}g/cm^3	1.511	1.533	1.629	1.669	1.684	1.723	1.508
μ/mm^{-1}	0.377	0.382	0.409	0.416	0.420	0.430	0.376
F(000)	1328.0	1328.0	1328.0	1328.0	1328.0	1328.0	1328.0
Crystal size/mm^3	0.18 × 0.14 × 0.12	0.18 × 0.14 × 0.12	0.18 × 0.14 × 0.12	0.18 × 0.14 × 0.12	0.18 × 0.14 × 0.12	0.18 × 0.14 × 0.12	0.18 × 0.14 × 0.12
Radiation	AgKα (λ = 0.56086)	AgKα (λ = 0.56086)	AgKα (λ = 0.56086)	AgKα (λ = 0.56086)	AgKα (λ = 0.56086)	AgKα (λ = 0.56086)	AgKα (λ = 0.56086)
2θ range for data collection/°	2.796 to 39.206	3.118 to 39.072	2.896 to 39.048	2.926 to 39.064	2.932 to 39.018	2.94 to 39.182	2.794 to 38.994
Index ranges	-12 ≤ h ≤ 12, -14 ≤ k ≤ 15, -19 ≤ l ≤ 19	-12 ≤ h ≤ 12, -13 ≤ k ≤ 13, -19 ≤ l ≤ 18	-12 ≤ h ≤ 12, -14 ≤ k ≤ 14, -17 ≤ l ≤ 19	-12 ≤ h ≤ 12, -14 ≤ k ≤ 14, -17 ≤ l ≤ 19	-12 ≤ h ≤ 12, -14 ≤ k ≤ 14, -18 ≤ l ≤ 17	-12 ≤ h ≤ 12, -14 ≤ k ≤ 14, -16 ≤ l ≤ 16	-12 ≤ h ≤ 12, -16 ≤ k ≤ 15, -18 ≤ l ≤ 18
Reflections collected	15847	23079	23039	22491	22284	13610	24875
Independent reflections	2524 [R_{int} = 0.0858, R_{sigma} = 0.0948]	2717 [R_{int} = 0.0567, R_{sigma} = 0.0436]	2697 [R_{int} = 0.0562, R_{sigma} = 0.0426]	2669 [R_{int} = 0.0599, R_{sigma} = 0.0403]	2601 [R_{int} = 0.0545, R_{sigma} = 0.0352]	2354 [R_{int} = 0.0727, R_{sigma} = 0.0687]	2832 [R_{int} = 0.0610, R_{sigma} = 0.0428]
Data/restraints/parameters	2524/346/403	2717/351/407	2697/346/403	2669/346/403	2601/346/393	2354/346/393	2832/350/407
Goodness-of-fit on F^2	1.047	1.059	1.100	1.084	1.112	1.085	1.063
Final R indexes [I>=2σ (I)]	R_1 = 0.0821, wR_2 = 0.1916	R_1 = 0.0396, wR_2 = 0.0925	R_1 = 0.0467, wR_2 = 0.1124	R_1 = 0.0498, wR_2 = 0.1220	R_1 = 0.0466, wR_2 = 0.1111	R_1 = 0.0735, wR_2 = 0.1762	R_1 = 0.0455, wR_2 = 0.1204
Final R indexes [all data]	R_1 = 0.1318,	R_1 = 0.0604,	R_1 = 0.0649,	R_1 = 0.0705,	R_1 = 0.0642,	R_1 = 0.1088,	R_1 = 0.0700,

	wR_2 = 0.2231	wR_2 = 0.1028	wR_2 = 0.1234	wR_2 = 0.1343	wR_2 = 0.1213	wR_2 = 0.1986	wR_2 = 0.1354
Largest diff. peak/hole / e $Å^{-3}$	0.48/-0.42	0.26/-0.24	0.28/-0.27	0.31/-0.34	0.30/-0.27	0.46/-0.52	0.23/-0.28

Table 10.2 Crystal data and structure refinement for 14_150K_1_0m

Identification code	14_150K_1_0m
Empirical formula	$C_{19}H_{15}N_5O$
Formula weight	329.36
Temperature/K	150.01
Crystal system	monoclinic
Space group	$P2_1/c$
a/Å	8.1333(13)
b/Å	5.6070(9)
c/Å	34.556(5)
α/°	90
β/°	96.018(4)
γ/°	90
Volume/Å^3	1567.2(4)
Z	4
ρ_{calc}g/cm^3	1.396
μ/mm^{-1}	0.737
F(000)	688.0
Crystal size/mm^3	0.258 × 0.108 × 0.081
Radiation	CuKα (λ = 1.54178)
2Θ range for data collection/°	5.142 to 133.338
Index ranges	-9 ≤ h ≤ 9, -6 ≤ k ≤ 6, -41 ≤ l ≤ 41
Reflections collected	28825
Independent reflections	2767 [R_{int} = 0.0193, R_{sigma} = 0.0115]
Data/restraints/parameters	2767/0/275
Goodness-of-fit on F^2	1.062
Final R indexes [I>=2σ (I)]	R_1 = 0.0304, wR_2 = 0.0758
Final R indexes [all data]	R_1 = 0.0307, wR_2 = 0.0761
Largest diff. peak/hole / e Å^{-3}	0.19/-0.20

Table 10.3 Crystal data and structure refinement for 15_150K_0m.

Identification code	15_I_Diamond_100K	15_II_150K_0m
Empirical formula	$C_{17}H_{12}N_6$	$C_{17}H_{12}N_6$
Formula weight	300.33	300.33
Temperature/K	100.0(2)	150.01
Crystal system	monoclinic	triclinic
Space group	$P2_1/n$	P-1
a/Å	5.65430(10)	8.0924(7)
b/Å	15.6170(4)	9.3088(8)
c/Å	15.8854(4)	10.7598(9)
α/°	90	95.530(3)
β/°	97.1920(10)	100.309(3)
γ/°	90	113.839(3)
Volume/Å^3	1391.70(6)	716.49(11)
Z	4	2
ρ_{calc}g/cm^3	1.433	1.392
μ/mm^{-1}	0.087	0.719
F(000)	624.0	312.0
Crystal size/mm^3	0.196 × 0.031 × 0.016	0.174 × 0.052 × 0.033
Radiation	Synchrotron (λ = 0.6889)	CuKα (λ = 1.54178)
2Θ range for data collection/°	3.558 to 58.026	10.578 to 145.652
Index ranges	-7 ≤ h ≤ 7, -21 ≤ k ≤ 21, -22 ≤ l ≤ 22	-10 ≤ h ≤ 10, -11 ≤ k ≤ 11, -13 ≤ l ≤ 13
Reflections collected	16464	24315
Independent reflections	4050 [R_{int} = 0.0547, R_{sigma} = 0.0487]	2765 [R_{int} = 0.0564, R_{sigma} = 0.0336]
Data/restraints/parameters	4050/0/208	2765/0/209
Goodness-of-fit on F^2	1.172	1.131
Final R indexes [I>=2σ (I)]	R_1 = 0.0532, wR_2 = 0.1477	R_1 = 0.0790, wR_2 = 0.2212
Final R indexes [all data]	R_1 = 0.0571, wR_2 = 0.1511	R_1 = 0.0853, wR_2 = 0.2289
Largest diff. peak/hole / e Å^{-3}	0.68/-0.38	0.39/-0.34

Table 10.4 Crystal data and structure refinement for 16_150K_0m.

Identification code	16_150K_0m
Empirical formula	$C_{18}H_{12}FN_5$
Formula weight	317.33
Temperature/K	149.96
Crystal system	triclinic
Space group	P-1
a/Å	10.3416(4)
b/Å	11.1309(4)
c/Å	14.7363(6)
α/°	71.3240(10)
β/°	81.2970(10)
γ/°	68.8860(10)
Volume/Å^3	1497.87(10)
Z	4
ρ_{calc}g/cm^3	1.407
μ/mm^{-1}	0.798
F(000)	656.0
Crystal size/mm^3	0.358 × 0.326 × 0.266
Radiation	CuKα (λ = 1.54178)
2Θ range for data collection/°	6.336 to 144.22
Index ranges	-12 ≤ h ≤ 12, -13 ≤ k ≤ 13, -18 ≤ l ≤ 18
Reflections collected	38463
Independent reflections	5789 [R_{int} = 0.0369, R_{sigma} = 0.0317]
Data/restraints/parameters	5789/0/437
Goodness-of-fit on F^2	1.083
Final R indexes [I>=2σ (I)]	R_1 = 0.0417, wR_2 = 0.1013
Final R indexes [all data]	R_1 = 0.0418, wR_2 = 0.1014
Largest diff. peak/hole / e Å^{-3}	0.22/-0.39

Table 10.5 Crystal data and structure refinement for 17_150K.

Identification code	17_150K
Empirical formula	$C_{19}H_{13}FN_4$
Formula weight	316.33
Temperature/K	150.02
Crystal system	monoclinic
Space group	$P2_1/n$
a/Å	5.8344(3)
b/Å	16.1932(9)
c/Å	15.7275(9)
α/°	90
β/°	94.951(2)
γ/°	90
Volume/Å^3	1480.35(14)
Z	4
ρ_{calc}g/cm^3	1.419
μ/mm^{-1}	0.785
F(000)	656.0
Crystal size/mm^3	0.167 × 0.105 × 0.103
Radiation	CuKα (λ = 1.54178)
2Θ range for data collection/°	7.852 to 145.172
Index ranges	-7 ≤ h ≤ 7, -20 ≤ k ≤ 20, -19 ≤ l ≤ 19
Reflections collected	27425
Independent reflections	2898 [R_{int} = 0.0159, R_{sigma} = 0.0091]
Data/restraints/parameters	2898/0/217
Goodness-of-fit on F^2	1.075
Final R indexes [I>=2σ (I)]	R_1 = 0.0411, wR_2 = 0.1068
Final R indexes [all data]	R_1 = 0.0412, wR_2 = 0.1069
Largest diff. peak/hole / e Å^{-3}	0.43/-0.41

Table 10.6 Crystal data and structure refinement for 19_150K_0m.

Identification code	19_150K_0m
Empirical formula	$C_{18}H_{12}N_5F$
Formula weight	317.33
Temperature/K	149.98
Crystal system	monoclinic
Space group	$P2_1/n$
a/Å	5.7910(2)
b/Å	15.8069(6)
c/Å	15.8092(6)
α/°	90
β/°	94.2330(10)
γ/°	90
Volume/Å^3	1443.19(9)
Z	4
ρ_{calc}g/cm^3	1.460
μ/mm^{-1}	0.828
F(000)	656.0
Crystal size/mm^3	0.249 × 0.066 × 0.044
Radiation	CuKα (λ = 1.54178)
2Θ range for data collection/°	7.92 to 133.646
Index ranges	-6 ≤ h ≤ 6, -18 ≤ k ≤ 18, -18 ≤ l ≤ 18
Reflections collected	25158
Independent reflections	2538 [R_{int} = 0.0530, R_{sigma} = 0.0256]
Data/restraints/parameters	2538/0/218
Goodness-of-fit on F^2	1.047
Final R indexes [I>=2σ (I)]	R_1 = 0.0341, wR_2 = 0.0905
Final R indexes [all data]	R_1 = 0.0385, wR_2 = 0.0941
Largest diff. peak/hole / e Å^{-3}	0.22/-0.18

Table 10.7 Crystal data and structure refinement for 20_150K_0m.

Identification code	20150K_0m
Empirical formula	$C_{19}H_{12}F_2N_4$
Formula weight	334.33
Temperature/K	150.01
Crystal system	monoclinic
Space group	$P2_1/n$
a/Å	5.8180(2)
b/Å	16.4274(6)
c/Å	15.8786(6)
α/°	90
β/°	95.1720(10)
γ/°	90
Volume/Å^3	1511.41(9)
Z	4
ρ_{calc}g/cm^3	1.469
μ/mm^{-1}	0.901
F(000)	688.0
Crystal size/mm^3	0.346 × 0.206 × 0.186
Radiation	CuKα (λ = 1.54178)
2Θ range for data collection/°	7.76 to 145.1
Index ranges	-7 ≤ h ≤ 7, -20 ≤ k ≤ 20, -19 ≤ l ≤ 19
Reflections collected	22624
Independent reflections	2950 [R_{int} = 0.0544, R_{sigma} = 0.0360]
Data/restraints/parameters	2950/391/278
Goodness-of-fit on F^2	1.076
Final R indexes [I>=2σ (I)]	R_1 = 0.0667, wR_2 = 0.1719
Final R indexes [all data]	R_1 = 0.0678, wR_2 = 0.1729
Largest diff. peak/hole / e Å^{-3}	0.24/-0.35

Table 10.8 Crystal data and structure refinement for 21_150K_0m.

Identification code	21_150K_0m
Empirical formula	$C_{18}H_{11}F_2N_5$
Formula weight	335.32
Temperature/K	149.96
Crystal system	orthorhombic
Space group	$P2_12_12_1$
a/Å	5.3897(3)
b/Å	14.5854(9)
c/Å	19.0815(11)
α/°	90
β/°	90
γ/°	90
Volume/Å^3	1500.01(15)
Z	4
ρ_{calc}g/cm^3	1.485
μ/mm^{-1}	0.930
F(000)	688.0
Crystal size/mm^3	0.187 × 0.164 × 0.079
Radiation	CuKα (λ = 1.54178)
2Θ range for data collection/°	7.628 to 144.728
Index ranges	-6 ≤ h ≤ 6, -18 ≤ k ≤ 18, -23 ≤ l ≤ 23
Reflections collected	60515
Independent reflections	2964 [R_{int} = 0.0889, R_{sigma} = 0.0275]
Data/restraints/parameters	2964/0/226
Goodness-of-fit on F^2	1.095
Final R indexes [I>=2σ (I)]	R_1 = 0.0752, wR_2 = 0.2221
Final R indexes [all data]	R_1 = 0.0788, wR_2 = 0.2252
Largest diff. peak/hole / e Å^{-3}	0.56/-0.35
Flack parameter	0.13(5)

Table 10.9 Crystal data and structure refinement for 22_150K_0m.

Identification code	22_150K_0m
Empirical formula	$C_{14}H_{11.5}N_{4.5}O_{0.5}$
Formula weight	250.78
Temperature/K	149.99
Crystal system	triclinic
Space group	P-1
a/Å	8.0538(6)
b/Å	12.6170(10)
c/Å	14.4229(11)
α/°	113.381(3)
β/°	91.433(4)
γ/°	106.859(4)
Volume/Å^3	1270.94(17)
Z	4
ρ_{calc}g/cm^3	1.311
μ/mm^{-1}	0.691
F(000)	524.0
Crystal size/mm^3	0.183 × 0.030 × 0.013
Radiation	CuKα (λ = 1.54178)
2Θ range for data collection/°	6.764 to 144.98
Index ranges	-9 ≤ h ≤ 9, -15 ≤ k ≤ 15, -17 ≤ l ≤ 17
Reflections collected	38043
Independent reflections	4908 [R_{int} = 0.1175, R_{sigma} = 0.0720]
Data/restraints/parameters	4908/0/346
Goodness-of-fit on F^2	1.117
Final R indexes [I>=2σ (I)]	R_1 = 0.0966, wR_2 = 0.2711
Final R indexes [all data]	R_1 = 0.1437, wR_2 = 0.3069
Largest diff. peak/hole / e Å^{-3}	0.62/-0.46

Table 10.10. Crystal data and structure refinement for **23a.**

Identification code	**23a**_150 K	**23a**_293 K	**23a** _100 K	**23a**_2 K
Empirical formula	$C_{20.5}H_{14}F_2Fe_{0.5}N_5OS$	$C_{20.5}H_{14}F_2Fe_{0.5}N_5OS$	$C_{20.5}H_{14}F_2Fe_{0.5}N_5OS$	$C_{20.5}H_{14}F_2Fe_{0.5}N_5OS$
Formula weight	444.35	444.35	444.35	444.35
Temperature/K	150.0	293.1	100.0	2.25
Crystal system	monoclinic	monoclinic	monoclinic	monoclinic
Space group	C2/c	C2/c	C2/c	C2/c
a/Å	27.2696(11)	27.8650(16)	27.2374(14)	27.1142(12)
b/Å	8.9975(4)	9.1320(5)	8.9222(5)	8.9057(4)
c/Å	16.0663(6)	16.1065(13)	16.0938(12)	16.0743(9)
α/°	90	90	90	90
β/°	91.041(2)	90.902(4)	91.153(3)	91.380(2)
γ/°	90	90	90	90
Volume/Å^3	3941.3(3)	4098.0(5)	3910.3(4)	3880.4(3)
Z	8	4	4	4
ρ_{calc}g/cm^3	1.498	1.400	1.486	1.494
μ/mm^{-1}	4.666	0.533	0.559	0.565
F(000)	1816.0	1764.0	1812.0	1784.0
Crystal size/mm^3	0.163 × 0.103 × 0.072	0.96 × 0.65 × 0.144	0.96 × 0.65 × 0.144	0.96 × 0.65 × 0.144
Radiation	CuKα (λ = 1.54)	MoKα (λ = 0.71073)	MoKα (λ = 0.71073)	MoKα (λ = 0.71073)
2Θ range for data collection/°	6.484 to 145.03	2.924 to 50.302	2.992 to 50.364	3.004 to 50.09
Index ranges	-33 ≤ h ≤ 33, -10 ≤ k ≤ 10, -19 ≤ l ≤ 19	-33 ≤ h ≤ 33, -10 ≤ k ≤ 10, -12 ≤ l ≤ 12	-32 ≤ h ≤ 32, -10 ≤ k ≤ 10, -11 ≤ l ≤ 11	-32 ≤ h ≤ 32, -10 ≤ k ≤ 10, -15 ≤ l ≤ 15
Reflections collected	51161	17748	16509	31030
Independent reflections	3881 [R_{int} = 0.0582, R_{sigma} = 0.0301]	2776 [R_{int} = 0.0519, R_{sigma} = 0.0337]	2620 [R_{int} = 0.0512, R_{sigma} = 0.0343]	3045 [R_{int} = 0.0474, R_{sigma} = 0.0231]
Data/restraints/parameters	3881/0/279	2776/0/279	2620/246/279	3045/0/279
Goodness-of-fit on F^2	1.195	1.105	1.103	1.104
Final R indexes [I>=2σ (I)]	R_1 = 0.0839, wR_2 = 0.2003	R_1 = 0.0450, wR_2 = 0.1213	R_1 = 0.0498, wR_2 = 0.1277	R_1 = 0.0441, wR_2 = 0.1182

Final R indexes [all data]	R_1 = 0.0851, wR_2 = 0.2007	R_1 = 0.0562, wR_2 = 0.1383	R_1 = 0.0541, wR_2 = 0.1362	R_1 = 0.0472, wR_2 = 0.1268
Largest diff. peak/hole / e Å^{-3}	0.90/-1.31	0.51/-0.38	0.87/-1.12	0.75/-0.79

Table 4.3. Crystal data and structure refinement for **23a.**

Identification code	**23a**_150 K	**23a**_293 K	**23a** _100 K	**23a**_
Empirical formula	$C_{20.5}H_{14}F_2Fe_{0.5}N_5OS$	$C_{20.5}H_{14}F_2Fe_{0.5}N_5OS$	$C_{20.5}H_{14}F_2Fe_{0.5}N_5OS$	$C_{20.5}$
Formula weight	444.35	444.35	444.35	444.3
Temperature/K	150.0	293.1	100.0	2.25
Crystal system	monoclinic	monoclinic	monoclinic	mono
Space group	C2/c	C2/c	C2/c	C2/c
a/Å	27.2696(11)	27.8650(16)	27.2374(14)	27.1
b/Å	8.9975(4)	9.1320(5)	8.9222(5)	8.905
c/Å	16.0663(6)	16.1065(13)	16.0938(12)	16.0
α/°	90	90	90	90
β/°	91.041(2)	90.902(4)	91.153(3)	91.38
γ/°	90	90	90	90
Volume/Å^3	3941.3(3)	4098.0(5)	3910.3(4)	3880
Z	8	4	4	4
ρ_{calc}g/cm^3	1.498	1.400	1.486	1.494
μ/mm^{-1}	4.666	0.533	0.559	0.565
F(000)	1816.0	1764.0	1812.0	1784
Crystal size/mm^3	0.163 × 0.103 × 0.072	0.96 × 0.65 × 0.144	0.96 × 0.65 × 0.144	0.96
Radiation	CuKα (λ = 1.54178)	MoKα (λ = 0.71073)	MoKα (λ = 0.71073)	MoK
2Θ range for data collection/°	6.484 to 145.03	2.924 to 50.302	2.992 to 50.364	3.004
Index ranges	-33 ≤ h ≤ 33, -10 ≤ k ≤ 10, -19 ≤ l ≤ 19	-33 ≤ h ≤ 33, -10 ≤ k ≤ 10, -12 ≤ l ≤ 12	-32 ≤ h ≤ 32, -10 ≤ k ≤ 10, -11 ≤ l ≤ 11	-32 ≤ 10, -
Reflections collected	51161	17748	16509	3103
Independent reflections	3881 [R_{int} = 0.0582, R_{sigma} = 0.0301]	2776 [R_{int} = 0.0519, R_{sigma} = 0.0337]	2620 [R_{int} = 0.0512, R_{sigma} = 0.0343]	3045 R_{sigm}
Data/restraints/parameters	3881/0/279	2776/0/279	2620/246/279	3045
Goodness-of-fit on F^2	1.195	1.105	1.103	1.104
Final R indexes [I>=2σ (I)]	R_1 = 0.0839, wR_2 = 0.2003	R_1 = 0.0450, wR_2 = 0.1213	R_1 = 0.0498, wR_2 = 0.1277	R_1 = 0.118
Final R indexes [all data]	R_1 = 0.0851, wR_2 = 0.2007	R_1 = 0.0562, wR_2 = 0.1383	R_1 = 0.0541, wR_2 = 0.1362	R_1 = 0.120
Largest diff. peak/hole / e Å^{-3}	0.90/-1.31	0.51/-0.38	0.87/-1.12	0.75/

Table 4.4. Crystal data and structure refinement for **23b.**

Identification code	23b_30K	23b_250K
Empirical formula	$C_{40}H_{24}N_{10}F_4S_2Fe$	$C_{40}H_{24}N_{10}F_4S_2Fe$
Formula weight	872.7	840.66
Temperature/K	30	288.31
Crystal system	monoclinic	monoclinic

Space group	$P2_1/c$	$P2_1/c$
a/Å	13.019(4)	13.292(5)
b/Å	9.136(3)	9.158(3)
c/Å	15.831(5)	16.014(5)
α/°	90	90
β/°	105.732(9)	105.125(9)
γ/°	90	90
Volume/Å^3	1812.3(10)	1881.9(10)
Z	2	2
ρ_{calc}g/cm^3	1.599	1.484
μ/mm^{-1}	0.318	0.305
F(000)	892	856
Crystal size/mm^3	0.187 × 0.137 × 0.119	0.187 × 0.185 × 0.09
Radiation	AgKα (λ = 0.56086)	AgKα (λ = 0.56086)
2Θ range for data collection/°	4.354 to 39.228	4.312 to 39.062
Index ranges	-15 ≤ h ≤ 14, -10 ≤ k ≤ 10, -18 ≤ l ≤ 18	-15 ≤ h ≤ 15, -10 ≤ k ≤ 10, -19 ≤ l ≤ 19
Reflections collected	15117	24112
Independent reflections	3225 [R_{int} = 0.0925, R_{sigma} = 0.0693]	3321 [R_{int} = 0.1067, R_{sigma} = 0.0574]
Data/restraints/parameters	3225/0/259	3321/243/259
Goodness-of-fit on F^2	1.033	1.028
Final R indexes [I>=2σ (I)]	R_1 = 0.0508, wR_2 = 0.1167	R_1 = 0.0530, wR_2 = 0.1252
Final R indexes [all data]	R_1 = 0.0772, wR_2 = 0.1324	R_1 = 0.0944, wR_2 = 0.1497
Largest diff. peak/hole / e Å^{-3}	0.45/-0.73	0.28/-0.49

Table 10.11 Crystal data and structure refinement for 24a and 24b.

Identification code	24a_150 K	24b_120 K	22b_120 K_nomask
Empirical formula	C36H36FeN14O6S2	C40H40N12S2FeO0.13	C40H40N12S2FeO0.13
Formula weight	880.76	810.81	810.81
Temperature/K	150.02	119.9	119.9
Crystal system	monoclinic	orthorhombic	orthorhombic
Space group	P21/n	Pnma	Pnma
a/Å	14.6433(5)	18.9788(7)	18.9788(7)
b/Å	17.1629(6)	29.8588(12)	29.8588(12)
c/Å	16.4837(6)	16.9124(6)	16.9124(6)
α/°	90	90	90
β/°	104.5070(10)	90	90
γ/°	90	90	90
Volume/Å3	4010.6(2)	9584.0(6)	9584.0(6)
Z	4	8	8
ρcalcg/cm3	1.459	1.124	1.124
μ/mm-1	4.533	3.646	3.646
F(000)	1824	3384	3384
Crystal size/mm3	0.102 × 0.154 × 0.167	0.113 × 0.108 × 0.077	0.113 × 0.108 × 0.077
Radiation	CuKα (λ = 1.54178)	CuKα (λ = 1.54178)	CuKα (λ = 1.54178)
2Θ range for data collection/°	7.564 to 133.252	7 to 133.582	7 to 133.582
Index ranges	-17 ≤ h ≤ 17, -20 ≤ k ≤ 20, -19 ≤ l ≤ 19	-21 ≤ h ≤ 22, -34 ≤ k ≤ 35, -20 ≤ l ≤ 18	-21 ≤ h ≤ 22, -34 ≤ k ≤ 35, -20 ≤ l ≤ 18
Reflections collected	36722	75401	75401
Independent reflections	6999 [Rint = 0.0322, Rsigma = 0.0286]	8675 [Rint = 0.0797, Rsigma = 0.0401]	8675 [Rint = 0.0797, Rsigma = 0.0401]
Data/restraints/parameters	6999/0/550	8675/0/1	8675/0/1
Goodness-of-fit on F2	1.093	1.043	2.757
Final R indexes [I>=2σ (I)]	R1 = 0.0560, wR2 = 0.1635	R1 = 0.0689, wR2 = 0.2063	R1 = 0.2194, wR2 = 0.5718
Final R indexes [all data]	R1 = 0.0572, wR2 = 0.1643	R1 = 0.0828, wR2 = 0.2172	R1 = 0.2415, wR2 = 0.5959
Largest diff. peak/hole / e Å-3	1.22/-0.97	0.42/-0.42	7.14/-1.06

Table 10.12 Crystal data and structure refinement for 25

Identification code	25_150K	25_90K	25_250K
Empirical formula	$C_{39}H_{30}Fe_{0.5}N_{11}O_2S$	$C_{39}H_{30}Fe_{0.5}N_{11}O_2S$	$C_{39}H_{30}Fe_{0.5}N_{11}O_2S$
Formula weight	840.81	818.72	744.72
Temperature/K	149.97	90.22	250
Crystal system	orthorhombic	orthorhombic	orthorhombic
Space group	Pbcn	Pbcn	Pbcn
a/Å	22.1189(6)	22.071(5)	22.3820(6)
b/Å	14.3226(4)	14.202(3)	14.4750(4)
c/Å	22.5829(6)	22.550(5)	22.7741(7)
α/°	90	90	90
β/°	90	90	90
γ/°	90	90	90
Volume/Å^3	7154.3(3)	7068(3)	7378.3(4)
Z	8	8	8
ρ_{calc}g/cm^3	1.561	1.539	1.341
μ/mm^{-1}	4.948	4.997	2.711
F(000)	3504	3376	3088
Crystal size/mm^3	0.336 × 0.092 × 0.088	0.244 × 0.138 × 0.138	0.244 × 0.138 × 0.138
Radiation	CuKα (λ = 1.54178)	CuKα (λ = 1.54178)	CuKα (λ = 1.54178)
2Θ range for data collection/°	7.352 to 144.664	7.402 to 144.788	7.272 to 136.622
Index ranges	-26 ≤ h ≤ 27, -17 ≤ k ≤ 17, -27 ≤ l ≤ 22	-27 ≤ h ≤ 24, -17 ≤ k ≤ 17, -27 ≤ l ≤ 26	-26 ≤ h ≤ 25, -17 ≤ k ≤ 15, -26 ≤ l ≤ 27
Reflections collected	59267	68378	49789
Independent reflections	7045 [R_{int} = 0.0260, R_{sigma} = 0.0129]	6976 [Rint = 0.0293, Rsigma = 0.0164]	6752 [R_{int} = 0.0319, R_{sigma} = 0.0160]
Data/restraints/parameters	7045/0/488	6976/0/488	6752/0/492
Goodness-of-fit on F^2	1.097	1.062	1.048
Final R indexes [I>=2σ (I)]	R_1 = 0.0512, wR_2 = 0.1351	R1 = 0.0397, wR2 = 0.1104	R_1 = 0.0443, wR_2 = 0.1273
Final R indexes [all data]	R_1 = 0.0539, wR_2 = 0.1369	R1 = 0.0417, wR2 = 0.1121	R_1 = 0.0535, wR_2 = 0.1355
Largest diff. peak/hole / e Å^{-3}	0.47/-0.69	0.63/-1.18	0.55/-0.84

Table 10.13 Crystal data and structure refinement for 26_150K_0m.

Identification code	26_150K_0m
Empirical formula	$C_{19}H_{19}Cl_2FeN_5O_{11}$
Formula weight	620.14
Temperature/K	149.99
Crystal system	monoclinic
Space group	$P2_1/c$
a/Å	10.3041(4)
b/Å	16.1411(6)
c/Å	14.9795(5)
α/°	90
β/°	103.7620(10)
γ/°	90
Volume/Å^3	2419.86(15)
Z	4
ρ_{calc}g/cm^3	1.702
μ/mm^{-1}	7.671
F(000)	1264.0
Crystal size/mm^3	0.144 × 0.184 × 0.277
Radiation	CuKα (λ = 1.54178)
2Θ range for data collection/°	8.182 to 144.876
Index ranges	$-12 \leq h \leq 12$, $-19 \leq k \leq 19$, $-18 \leq l \leq 18$
Reflections collected	40770
Independent reflections	4779 [R_{int} = 0.0249, R_{sigma} = 0.0142]
Data/restraints/parameters	4779/10/392
Goodness-of-fit on F^2	1.065
Final R indexes [I>=2σ (I)]	R_1 = 0.0331, wR_2 = 0.0904
Final R indexes [all data]	R_1 = 0.0333, wR_2 = 0.0905
Largest diff. peak/hole / e Å^{-3}	0.95/-0.50

Table 10.14 Crystal data and structure refinement for 27_150k_0m.

Identification code	27_150k_0m
Empirical formula	$C_{42.75}H_{33.75}Cl_{1.5}Fe_{0.75}N_{11.25}O_{8.25}$
Formula weight	932.12
Temperature/K	150.04
Crystal system	trigonal
Space group	R-3
a/Å	36.7861(6)
b/Å	36.7861(6)
c/Å	24.4870(5)
α/°	90
β/°	90
γ/°	120
Volume/Å^3	28696.8(11)
Z	24
ρ_{calc}g/cm^3	1.294
μ/mm^{-1}	3.235
F(000)	11520.0
Crystal size/mm^3	0.094 × 0.219 × 0.363
Radiation	CuKα (λ = 1.54178)
2Θ range for data collection/°	4.552 to 121.646
Index ranges	$-29 \leq h \leq 29$, $-29 \leq k \leq 29$, $-27 \leq l \leq 27$
Reflections collected	53599
Independent reflections	6615 [R_{int} = 0.0329, R_{sigma} = 0.0178]
Data/restraints/parameters	6615/727/779
Goodness-of-fit on F^2	1.769
Final R indexes [I>=2σ (I)]	R_1 = 0.1108, wR_2 = 0.3488
Final R indexes [all data]	R_1 = 0.1153, wR_2 = 0.3557
Largest diff. peak/hole / e Å^{-3}	3.04/-0.43

Table 10.15 Crystal data and structure refinement for 28_150K_0m

Identification code	28_150K_0m
Empirical formula	$C_{19}H_{26}Br_2CoN_5O_6$
Formula weight	639.20
Temperature/K	149.97
Crystal system	triclinic
Space group	P-1
a/Å	10.4587(4)
b/Å	10.8916(4)
c/Å	11.8506(4)
α/°	71.6880(10)
β/°	80.7530(10)
γ/°	81.7430(10)
Volume/Å^3	1258.65(8)
Z	2
ρ_{calc}g/cm^3	1.687
μ/mm^{-1}	9.441
F(000)	640.0
Crystal size/mm^3	0.078 × 0.190 × 0.402
Radiation	CuKα (λ = 1.54178)
2Θ range for data collection/°	8.594 to 144.816
Index ranges	$-11 \leq h \leq 12$, $-13 \leq k \leq 13$, $-14 \leq l \leq 14$
Reflections collected	53803
Independent reflections	4889 [R_{int} = 0.0354, R_{sigma} = 0.0184]
Data/restraints/parameters	4889/0/310
Goodness-of-fit on F^2	1.033
Final R indexes [I>=2σ (I)]	R_1 = 0.0261, wR_2 = 0.0695
Final R indexes [all data]	R_1 = 0.0262, wR_2 = 0.0696
Largest diff. peak/hole / e Å^{-3}	0.87/-0.67

Table 10.16 Crystal data and structure refinement for 29_2K

Identification code	29_2K
Empirical formula	$C_{36}H_{28}Cl_4Co_2F_2N_{10}O_2$
Formula weight	930.34
Temperature/K	2.2
Crystal system	monoclinic
Space group	C2/c
a/Å	16.3024(4)
b/Å	14.2655(4)
c/Å	17.1314(4)
α/°	90
β/°	102.1910(10)
γ/°	90
Volume/Å^3	3894.26(17)
Z	4
ρ_{calc}g/cm^3	1.587
μ/mm^{-1}	1.184
F(000)	1880.0
Crystal size/mm^3	0.057 × 0.164 × 0.240
Radiation	MoKα (λ = 0.71073)
2Θ range for data collection/°	4.866 to 52.806
Index ranges	$-20 \leq h \leq 20$, $-15 \leq k \leq 15$, $-21 \leq l \leq 21$
Reflections collected	18570
Independent reflections	3503 [R_{int} = 0.0372, R_{sigma} = 0.0280]
Data/restraints/parameters	3503/0/262
Goodness-of-fit on F^2	1.074
Final R indexes [I>=2σ (I)]	R_1 = 0.0393, wR_2 = 0.1119
Final R indexes [all data]	R_1 = 0.0431, wR_2 = 0.1144
Largest diff. peak/hole / e Å^{-3}	1.04/-0.84

Table 10.17 Crystal data and structure refinement for 30_150K_0m.

Identification code	30_150K_0m
Empirical formula	$C_{42}H_{30}Co_2N_{14}O_2S_4$
Formula weight	1008.90
Temperature/K	150.01
Crystal system	triclinic
Space group	P-1
a/Å	8.7051(4)
b/Å	10.5816(5)
c/Å	13.6033(6)
α/°	71.458(2)
β/°	76.828(2)
γ/°	67.811(2)
Volume/Å^3	1091.71(9)
Z	1
ρ_{calc}g/cm^3	1.535
μ/mm^{-1}	8.199
F(000)	514.0
Crystal size/mm^3	0.144 × 0.243 × 0.309
Radiation	CuKα (λ = 1.54178)
2Θ range for data collection/°	10.09 to 145.352
Index ranges	$-10 \leq h \leq 10$, $-11 \leq k \leq 12$, $-16 \leq l \leq 16$
Reflections collected	42534
Independent reflections	4205 [R_{int} = 0.0528, R_{sigma} = 0.0301]
Data/restraints/parameters	4205/240/299
Goodness-of-fit on F^2	1.158
Final R indexes [I>=2σ (I)]	R_1 = 0.0741, wR_2 = 0.2298
Final R indexes [all data]	R_1 = 0.0753, wR_2 = 0.2336
Largest diff. peak/hole / e Å^{-3}	0.61/-1.21

Table 10.18 Crystal data and structure refinement for 31_150K_0m

Identification code	31_150K_0m
Empirical formula	$C_{20.47}H_{14.09}FeN_7OS_{1.96}$
Formula weight	492.58
Temperature/K	149.96
Crystal system	triclinic
Space group	P-1
a/Å	8.7340(5)
b/Å	10.6601(6)
c/Å	13.5920(8)
α/°	71.545(2)
β/°	77.047(3)
γ/°	67.990(2)
Volume/Å^3	1104.88(11)
Z	2
ρ_{calc}g/cm^3	1.481
μ/mm^{-1}	7.436
F(000)	502.0
Crystal size/mm^3	0.095 × 0.145 × 0.184
Radiation	CuKα (λ = 1.54178)
2Θ range for data collection/°	6.906 to 145.614
Index ranges	$-10 \leq h \leq 10$, $-13 \leq k \leq 13$, $-16 \leq l \leq 16$
Reflections collected	50703
Independent reflections	4305 [R_{int} = 0.0540, R_{sigma} = 0.0284]
Data/restraints/parameters	4305/0/305
Goodness-of-fit on F^2	1.117
Final R indexes [I>=2σ (I)]	R_1 = 0.0522, wR_2 = 0.1380
Final R indexes [all data]	R_1 = 0.0555, wR_2 = 0.1404
Largest diff. peak/hole / e Å^{-3}	0.51/-0.82

Table 10.19 Crystal data and structure refinement for 32_150k_0m.

Identification code	32_150k_0m
Empirical formula	$C_{41}H_{27}CoF_4N_{10}O_{0.5}S_2$
Formula weight	866.77
Temperature/K	149.98
Crystal system	monoclinic
Space group	C2/c
a/Å	27.3008(9)
b/Å	9.0742(3)
c/Å	15.9729(5)
α/°	90
β/°	91.220(2)
γ/°	90
Volume/Å^3	3956.1(2)
Z	4
ρ_{calc}g/cm^3	1.455
μ/mm^{-1}	4.946
F(000)	1768.0
Crystal size/mm^3	0.102 × 0.124 × 0.273
Radiation	CuKα (λ = 1.54178)
2Θ range for data collection/°	6.476 to 121.804
Index ranges	$-30 \leq h \leq 30$, $-10 \leq k \leq 10$, $-17 \leq l \leq 17$
Reflections collected	24920
Independent reflections	2976 [R_{int} = 0.0387, R_{sigma} = 0.0213]
Data/restraints/parameters	2976/0/274
Goodness-of-fit on F^2	1.124
Final R indexes [I>=2σ (I)]	R_1 = 0.0590, wR_2 = 0.1567
Final R indexes [all data]	R_1 = 0.0632, wR_2 = 0.1590
Largest diff. peak/hole / e Å^{-3}	0.54/-0.45

Table 10.20 Crystal data and structure refinement for 33_150K_0m.

Identification code	33_150K_0m
Empirical formula	$C_{40}H_{24}F_4MnN_{10}S_2$
Formula weight	839.75
Temperature/K	150.0
Crystal system	monoclinic
Space group	$P2_1/c$
a/Å	13.1997(3)
b/Å	9.2522(2)
c/Å	15.9084(3)
α/°	90
β/°	105.0060(10)
γ/°	90
Volume/Å^3	1876.58(7)
Z	2
ρ_{calc}g/cm^3	1.486
μ/mm^{-1}	4.463
F(000)	854.0
Crystal size/mm^3	0.106 × 0.157 × 0.210
Radiation	CuKα (λ = 1.54178)
2Θ range for data collection/°	6.932 to 144.736
Index ranges	$-16 \leq h \leq 16$, $-11 \leq k \leq 11$, $-19 \leq l \leq 19$
Reflections collected	35090
Independent reflections	3709 [R_{int} = 0.0196, R_{sigma} = 0.0104]
Data/restraints/parameters	3709/0/259
Goodness-of-fit on F^2	1.042
Final R indexes [I>=2σ (I)]	R_1 = 0.0232, wR_2 = 0.0653
Final R indexes [all data]	R_1 = 0.0239, wR_2 = 0.0660
Largest diff. peak/hole / e Å^{-3}	0.25/-0.20

Table 10.21 Crystal data and structure refinement for 34_150K_0m.

Identification code	34_150K_0m
Empirical formula	$C_{38}H_{24}CoF_2N_{12}S_2$
Formula weight	809.74
Temperature/K	149.99
Crystal system	triclinic
Space group	P-1
a/Å	8.8808(7)
b/Å	9.2658(8)
c/Å	10.9460(9)
α/°	76.654(2)
β/°	77.913(3)
γ/°	86.738(2)
Volume/Å^3	856.93(12)
Z	1
ρ_{calc}g/cm^3	1.569
μ/mm^{-1}	5.583
F(000)	413.0
Crystal size/mm^3	0.136 × 0.162 × 0.297
Radiation	CuKα (λ = 1.54178)
2Θ range for data collection/°	8.476 to 144.882
Index ranges	$-10 \leq h \leq 10$, $-11 \leq k \leq 11$, $-13 \leq l \leq 13$
Reflections collected	20776
Independent reflections	3326 [R_{int} = 0.0518, R_{sigma} = 0.0360]
Data/restraints/parameters	3326/0/250
Goodness-of-fit on F^2	1.082
Final R indexes [I>=2σ (I)]	R_1 = 0.0329, wR_2 = 0.0959
Final R indexes [all data]	R_1 = 0.0329, wR_2 = 0.0958
Largest diff. peak/hole / e Å^{-3}	0.32/-0.59

Table 10.22 Crystal data and structure refinement for 35_150K_0m.

Identification code	35_150K_0m
Empirical formula	$C_{38}H_{24}F_2MnN_{12}S_2$
Formula weight	805.75
Temperature/K	150.0
Crystal system	triclinic
Space group	P-1
a/Å	8.8965(4)
b/Å	9.2920(4)
c/Å	11.0397(5)
α/°	76.8840(10)
β/°	76.8250(10)
γ/°	87.0160(10)
Volume/Å^3	865.41(7)
Z	1
ρ_{calc}g/cm^3	1.546
μ/mm^{-1}	4.743
F(000)	411.0
Crystal size/mm^3	0.290 × 0.434 × 0.485
Radiation	CuKα (λ = 1.54178)
2Θ range for data collection/°	10.212 to 144.862
Index ranges	$-10 \leq h \leq 10$, $-11 \leq k \leq 11$, $-13 \leq l \leq 13$
Reflections collected	33446
Independent reflections	3334 [R_{int} = 0.0282, R_{sigma} = 0.0190]
Data/restraints/parameters	3334/0/250
Goodness-of-fit on F^2	1.093
Final R indexes [I>=2σ (I)]	R_1 = 0.0266, wR_2 = 0.0746
Final R indexes [all data]	R_1 = 0.0266, wR_2 = 0.0746
Largest diff. peak/hole / e Å^{-3}	0.25/-0.62

Table 10.23 Crystal data and structure refinement for 36_150K_0m.

Identification code	36_150K_0m
Empirical formula	$C_{44}Cl_2F_2FeN_8O_{20}H$
Formula weight	1126.28
Temperature/K	150.0
Crystal system	triclinic
Space group	P-1
a/Å	9.3821(15)
b/Å	9.8568(15)
c/Å	14.937(2)
α/°	90.953(5)
β/°	98.885(4)
γ/°	112.972(5)
Volume/Å^3	1252.0(3)
Z	1
ρ_{calc}g/cm^3	1.494
μ/mm^{-1}	4.225
F(000)	559.0
Crystal size/mm^3	0.098 × 0.123 × 0.224
Radiation	CuKα (λ = 1.54178)
2Θ range for data collection/°	6.01 to 145.334
Index ranges	$-11 \leq h \leq 11$, $-12 \leq k \leq 12$, $-18 \leq l \leq 18$
Reflections collected	51901
Independent reflections	4879 [R_{int} = 0.0494, R_{sigma} = 0.0269]
Data/restraints/parameters	4879/8/435
Goodness-of-fit on F^2	1.134
Final R indexes [I>=2σ (I)]	R_1 = 0.0440, wR_2 = 0.1288
Final R indexes [all data]	R_1 = 0.0443, wR_2 = 0.1291
Largest diff. peak/hole / e Å^{-3}	0.55/-0.47

Table 10.24 Crystal data and structure refinement for 37_150K_0m.

Identification code	37_150K_0m
Empirical formula	$C_{38}H_{32}Br_2CoF_2N_{10}O_2$
Formula weight	917.48
Temperature/K	149.97
Crystal system	triclinic
Space group	P-1
a/Å	7.4682(6)
b/Å	8.2019(7)
c/Å	15.7293(13)
α/°	79.247(2)
β/°	84.428(3)
γ/°	81.066(3)
Volume/Å^3	932.77(13)
Z	1
ρ_{calc}g/cm^3	1.633
μ/mm^{-1}	6.622
F(000)	461.0
Crystal size/mm^3	0.092 × 0.240 × 0.302
Radiation	CuKα (λ = 1.54178)
2Θ range for data collection/°	5.734 to 145.492
Index ranges	$-9 \leq h \leq 8$, $-10 \leq k \leq 10$, $-19 \leq l \leq 19$
Reflections collected	54125
Independent reflections	3644 [R_{int} = 0.0494, R_{sigma} = 0.0254]
Data/restraints/parameters	3644/3/255
Goodness-of-fit on F^2	1.230
Final R indexes [I>=2σ (I)]	R_1 = 0.0563, wR_2 = 0.1704
Final R indexes [all data]	R_1 = 0.0568, wR_2 = 0.1714
Largest diff. peak/hole / e Å^{-3}	0.67/-0.91

Table 10.25 Crystal data and structure refinement for 38_150K_0m.

Identification code	38_150K_0m
Empirical formula	$C_{22}H_{25}BrCo_{0.5}FN_5O_3$
Formula weight	535.84
Temperature/K	150.01
Crystal system	monoclinic
Space group	$P2_1/n$
a/Å	8.6655(3)
b/Å	16.9779(6)
c/Å	16.4856(6)
α/°	90
β/°	95.146(2)
γ/°	90
Volume/Å^3	2415.62(15)
Z	4
ρ_{calc}g/cm^3	1.473
μ/mm^{-1}	5.261
F(000)	1094.0
Crystal size/mm^3	0.235 × 0.375 × 0.487
Radiation	CuKα (λ = 1.54178)
2Θ range for data collection/°	7.49 to 145.616
Index ranges	$-10 \leq h \leq 10$, $-20 \leq k \leq 21$, $-20 \leq l \leq 20$
Reflections collected	47068
Independent reflections	4730 [R_{int} = 0.0552, R_{sigma} = 0.0297]
Data/restraints/parameters	4730/0/301
Goodness-of-fit on F^2	1.177
Final R indexes [I>=2σ (I)]	R_1 = 0.0837, wR_2 = 0.2504
Final R indexes [all data]	R_1 = 0.0870, wR_2 = 0.2566
Largest diff. peak/hole / e Å^{-3}	1.53/-1.89

Table 10.26 Crystal data and structure refinement for 39_150K_0m.

Identification code	39_150K_0m
Empirical formula	$C_{38}H_{22}CoF_4N_{12}S_2$
Formula weight	845.72
Temperature/K	149.94
Crystal system	triclinic
Space group	P-1
a/Å	9.1219(3)
b/Å	9.4776(3)
c/Å	10.6981(4)
α/°	78.9110(10)
β/°	77.7620(10)
γ/°	84.3480(10)
Volume/Å^3	885.39(5)
Z	1
ρ_{calc}g/cm^3	1.586
μ/mm^{-1}	5.516
F(000)	429.0
Crystal size/mm^3	0.140 × 0.252 × 0.662
Radiation	CuKα (λ = 1.54178)
2Θ range for data collection/°	9.94 to 144.956
Index ranges	$-10 \leq h \leq 10$, $-11 \leq k \leq 11$, $-13 \leq l \leq 13$
Reflections collected	32241
Independent reflections	3395 [R_{int} = 0.0347, R_{sigma} = 0.0233]
Data/restraints/parameters	3395/0/259
Goodness-of-fit on F^2	1.098
Final R indexes [I>=2σ (I)]	R_1 = 0.0284, wR_2 = 0.0782
Final R indexes [all data]	R_1 = 0.0284, wR_2 = 0.0782
Largest diff. peak/hole / e Å^{-3}	0.26/-0.59

Table 10.27 Crystal data and structure refinement for 40_150K_0m.

Identification code	40_150K_0m
Empirical formula	$C_{20}H_{13}Co_{0.5}FN_5S$
Formula weight	403.88
Temperature/K	150.01
Crystal system	monoclinic
Space group	$P2_1/c$
a/Å	13.0235(10)
b/Å	9.2141(7)
c/Å	16.1018(12)
α/°	90
β/°	105.699(2)
γ/°	90
Volume/Å^3	1860.1(2)
Z	4
ρ_{calc}g/cm^3	1.442
μ/mm^{-1}	5.126
F(000)	826.0
Crystal size/mm^3	0.088 × 0.152 × 0.339
Radiation	CuKα (λ = 1.54178)
2Θ range for data collection/°	7.05 to 144.926
Index ranges	$-15 \leq h \leq 16$, $-11 \leq k \leq 11$, $-19 \leq l \leq 19$
Reflections collected	31937
Independent reflections	3670 [R_{int} = 0.0259, R_{sigma} = 0.0167]
Data/restraints/parameters	3670/0/250
Goodness-of-fit on F^2	1.071
Final R indexes [I>=2σ (I)]	R_1 = 0.0255, wR_2 = 0.0705
Final R indexes [all data]	R_1 = 0.0258, wR_2 = 0.0707
Largest diff. peak/hole / e Å^{-3}	0.20/-0.26

Table 10.28 Crystal data and structure refinement for 41_200K_0m.

Identification code	41_200K_0m
Empirical formula	$C_{40}H_{26}CoF_2N_{10}S_2$
Formula weight	807.76
Temperature/K	200.01
Crystal system	orthorhombic
Space group	Pbca
a/Å	9.0962(3)
b/Å	15.7990(4)
c/Å	26.2177(7)
α/°	90
β/°	90
γ/°	90
Volume/Å^3	3767.77(19)
Z	4
ρ_{calc}g/cm^3	1.424
μ/mm^{-1}	5.062
F(000)	1652.0
Crystal size/mm^3	0.036 × 0.199 × 0.416
Radiation	CuKα (λ = 1.54178)
2Θ range for data collection/°	6.742 to 144.67
Index ranges	$-10 \leq h \leq 10$, $-18 \leq k \leq 14$, $-32 \leq l \leq 31$
Reflections collected	21116
Independent reflections	3667 [R_{int} = 0.0299, R_{sigma} = 0.0235]
Data/restraints/parameters	3667/0/250
Goodness-of-fit on F^2	1.046
Final R indexes [I>=2σ (I)]	R_1 = 0.0290, wR_2 = 0.0807
Final R indexes [all data]	R_1 = 0.0315, wR_2 = 0.0830
Largest diff. peak/hole / e Å^{-3}	0.19/-0.30

Table 10.29 Crystal data and structure refinement for 42_150k_0m

Identification code	42_150k_0m
Empirical formula	$C_{36}H_{24}FeN_{14}S_2$
Formula weight	788.66
Temperature/K	149.98
Crystal system	triclinic
Space group	P-1
a/Å	8.9797(8)
b/Å	9.5029(8)
c/Å	10.3197(9)
α/°	76.715(3)
β/°	77.629(3)
γ/°	85.487(3)
Volume/Å^3	836.75(13)
Z	1
ρ_{calc}g/cm^3	1.565
μ/mm^{-1}	5.249
F(000)	404.0
Crystal size/mm^3	0.087 × 0.233 × 0.401
Radiation	CuKα (λ = 1.54178)
2Θ range for data collection/°	8.99 to 144.648
Index ranges	$-11 \leq h \leq 11$, $-10 \leq k \leq 11$, $-12 \leq l \leq 12$
Reflections collected	17302
Independent reflections	3188 [R_{int} = 0.0445, R_{sigma} = 0.0375]
Data/restraints/parameters	3188/0/241
Goodness-of-fit on F^2	1.172
Final R indexes [I>=2σ (I)]	R_1 = 0.0614, wR_2 = 0.1719
Final R indexes [all data]	R_1 = 0.0620, wR_2 = 0.1741
Largest diff. peak/hole / e Å^{-3}	0.43/-0.73

Table 10.30 Crystal data and structure refinement for 43_150K_0m.

Identification code	43_150K_0m
Empirical formula	$C_{42}H_{28}CoN_{10}O_2S_2$
Formula weight	827.79
Temperature/K	150.0
Crystal system	triclinic
Space group	P-1
a/Å	8.9046(6)
b/Å	9.3103(6)
c/Å	13.4151(9)
α/°	96.196(3)
β/°	107.616(2)
γ/°	110.526(3)
Volume/Å^3	963.76(11)
Z	1
ρ_{calc}g/cm^3	1.426
μ/mm^{-1}	4.926
F(000)	425.0
Crystal size/mm^3	0.227 × 0.246 × 0.267
Radiation	CuKα (λ = 1.54178)
2Θ range for data collection/°	11.014 to 137.012
Index ranges	$-10 \leq h \leq 10$, $-11 \leq k \leq 11$, $-16 \leq l \leq 16$
Reflections collected	32289
Independent reflections	3460 [R_{int} = 0.0453, R_{sigma} = 0.0280]
Data/restraints/parameters	3460/0/259
Goodness-of-fit on F^2	1.204
Final R indexes [I>=2σ (I)]	R_1 = 0.0548, wR_2 = 0.1596
Final R indexes [all data]	R_1 = 0.0554, wR_2 = 0.1607
Largest diff. peak/hole / e Å^{-3}	0.39/-0.69

Table 10.31 Crystal data and structure refinement for 44_150K_0m_sx.

Identification code	44_150K_0m_sx
Empirical formula	$C_{25.33}H_{17.33}Co_{0.67}N_8S_{1.33}$
Formula weight	515.84
Temperature/K	149.99
Crystal system	orthorhombic
Space group	Pbca
a/Å	9.2193(2)
b/Å	15.8276(4)
c/Å	24.3385(7)
α/°	90
β/°	90
γ/°	90
Volume/Å^3	3551.46(16)
Z	6
ρ_{calc}g/cm^3	1.447
μ/mm^{-1}	5.277
F(000)	1588.0
Crystal size/mm^3	0.078 × 0.142 × 0.378
Radiation	CuKα (λ = 1.54178)
2Θ range for data collection/°	7.264 to 144.872
Index ranges	$-9 \leq h \leq 11$, $-18 \leq k \leq 17$, $-26 \leq l \leq 27$
Reflections collected	26989
Independent reflections	3430 [R_{int} = 0.0657, R_{sigma} = 0.0397]
Data/restraints/parameters	3430/0/241
Goodness-of-fit on F^2	1.045
Final R indexes [I>=2σ (I)]	R_1 = 0.0426, wR_2 = 0.1085
Final R indexes [all data]	R_1 = 0.0541, wR_2 = 0.1143
Largest diff. peak/hole / e Å^{-3}	0.31/-0.30

Table 10.32 Crystal data and structure refinement for 45_150K_0m.

Identification code	45_150K_0m
Empirical formula	$C_{36}H_{28}F_8MnN_{11}O_5P$
Formula weight	932.60
Temperature/K	149.98
Crystal system	triclinic
Space group	P-1
a/Å	12.5532(4)
b/Å	15.7162(5)
c/Å	20.6494(6)
α/°	75.684(2)
β/°	88.176(2)
γ/°	89.205(2)
Volume/Å^3	3945.3(2)
Z	4
ρ_{calc}g/cm^3	1.570
μ/mm^{-1}	3.968
F(000)	1892.0
Crystal size/mm^3	0.084 × 0.287 × 0.408
Radiation	CuKα (λ = 1.54178)
2Θ range for data collection/°	4.418 to 145.456
Index ranges	-15 ≤ h ≤ 15, -19 ≤ k ≤ 19, -25 ≤ l ≤ 25
Reflections collected	205966
Independent reflections	15437 [R_{int} = 0.0754, R_{sigma} = 0.0344]
Data/restraints/parameters	15437/8/1133
Goodness-of-fit on F^2	1.113
Final R indexes [I>=2σ (I)]	R_1 = 0.0555, wR_2 = 0.1627
Final R indexes [all data]	R_1 = 0.0664, wR_2 = 0.1713
Largest diff. peak/hole / e Å^{-3}	0.92/-0.51

Table 10.33 Crystal data and structure refinement for 46_150K_0m.

Identification code	46_150K_0m
Empirical formula	$C_{36}H_{29}ClF_2MnN_{11}O_9$
Formula weight	888.09
Temperature/K	149.99
Crystal system	triclinic
Space group	P-1
a/Å	12.7545(6)
b/Å	15.3929(8)
c/Å	20.0823(10)
α/°	78.106(2)
β/°	87.926(2)
γ/°	89.741(2)
Volume/Å^3	3855.5(3)
Z	4
ρ_{calc}g/cm^3	1.530
μ/mm^{-1}	4.122
F(000)	1816.0
Crystal size/mm^3	0.172 × 0.326 × 0.492
Radiation	CuKα (λ = 1.54178)
2Θ range for data collection/°	4.5 to 145.542
Index ranges	-15 ≤ h ≤ 15, -19 ≤ k ≤ 19, -24 ≤ l ≤ 24
Reflections collected	170133
Independent reflections	15032 [R_{int} = 0.0877, R_{sigma} = 0.0448]
Data/restraints/parameters	15032/0/1088
Goodness-of-fit on F^2	1.133
Final R indexes [I>=2σ (I)]	R_1 = 0.0779, wR_2 = 0.2335
Final R indexes [all data]	R_1 = 0.0872, wR_2 = 0.2472
Largest diff. peak/hole / e Å^{-3}	1.09/-1.16